UNIVERSITY OF OKLAHOMA

GRADUATE COLLEGE

INTEGRATED STUDIES ON WOODFORD SHALE NATURAL FRACTURE ATTRIBUTES, ORIGIN, AND THEIR RELATION TO HYDRAULIC FRACTURING

A DISSERTATION

SUBMITTED TO THE GRADUATE FACULTY

in partial fulfillment of the requirements for the

Degree of

DOCTOR OF PHILOSOPHY

By

SAYANTAN GHOSH
Norman, Oklahoma
2017

INTEGRATED STUDIES ON WOODFORD SHALE NATURAL FRACTURE ATTRIBUTES, ORIGIN, AND THEIR RELATION TO HYDRAULIC FRACTURING

A DISSERTATION APPROVED FOR THE
CONOCOPHILLIPS SCHOOL OF GEOLOGY AND GEOPHYSICS

BY

_____
Dr. Roger M. Slatt, Chair

_____
Dr. Brett Carpenter

_____
Dr. Xiaowei Chen

_____
Dr. Ahmad Ghassemi

_____
Dr. Seth Busetti

DEDICATION

To my parents, my wife, my brother, and my friends for their patience, continuous support, and encouragement through the duration of my studies.

ACKNOWLEDGEMENTS

I would like to express my sincere gratitude to my advisor Dr. Roger M. Slatt for his continuous support of my Ph.D. study and research. He has been an inspiration.

I would like to thank Dr. Ze'ev Reches, Dr. Ahmad Ghassemi, Dr. Brad Wallet, Dr. Seth Busetti, Dr. John Hooker, Dr. Julia Gale, and Dr. Stephen Laubach for their help with various equipment, technical difficulties, and concepts. Thanks to Dr. Xiaowei Chen and Dr. Brett Carpenter for serving on my committee. Sincere thanks to the industry consortium for continued funding to the Institute of Reservoir Characterization at the University of Oklahoma during the low oil prices prevailing in the last four years.

Thanks to Dr. Jennifer Miskimmins for providing Carl Neuhaus' thesis, which served a source of data for my dissertation. Thanks to Mr. Caleb P. Bontempi, Mr. Benmadi Milad, Mr. Henry Galvis, Ms. Daniela Becerra, and Ms. Colleen Klockow for their help with field work and other aspects of my research. Thanks to Mr. Herman Burrough for helping me obtain permissions to visit private lands and for helping with field measurements. Thanks to Dr. Andrew Madden and Dr. Megan Elwood Madden for allowing me to use their laboratory for mineralogy measurements.

I would like to thank Mr. Ron Gillihan, Mrs. Evelyn Gillihan and Mr. Josh Gillihan (owners of Arbuckle Wilderness Outcrop) for allowing me to use their land (outcrop) for the study. Thanks to Mr. Jessie Wyche (owner of Wyche Shale Pit) and Mr. Randy Jennings (owner of Jennings Stone Co.) for letting me use their quarries for the study.

Sincere thanks to Golder Associates for providing me the FracMan^{TM} Software license. Thanks to Mr. Rusty King and Mr. Neal Josephson for helping me obtain the software.

TABLE OF CONTENTS

LIST OF TABLES

LIST OF FIGURES

ABSTRACT

The Woodford Shale is a prolific hydrocarbon producing formation in Oklahoma. It is a silica and TOC rich, fractured reservoir and source rock. The natural fractures present within this formation, even though vital for fluid transport, have not been rigorously studied.

This dissertation presents Woodford Shale fracture related studies from several different outcrop locations in Southern Oklahoma, covering the Criner Hills and the central and eastern Arbuckle Mountains. These areas have varying degrees of tilting and folding, ranging from almost flat beds to overturned beds. Addition of fold related fracture sets with progressive folding and tilting of beds (from one outcrop to the other) were visualized and documented. These observations gave a clear picture of the fracture sets that existed before folding and that developed during folding. The presence and absence of bitumen, silica, and calcite as fracture fill also serve as clues to fracture origin timing.

These outcrops present opportunities for rigorous field measurements on fracture stratigraphic intensity variation, which helps in deciding the optimum landing spots for horizontal wells. Besides, relatively large surfaces on the quarry floor and quarry walls exposing the length, aperture, and height of relatively large fractures allowed quantification of these fracture parameters. These parameters then were used as inputs into a discrete fracture network model. This model, containing the discrete fractures and log-derived rock properties provided a complete static geomechanical model.

This model was then used to simulate the stimulated rock volumes using field treatment parameters. The simulated geometries were matched with field microseismic geometries for three stages. Several simulations under different subsurface and treatment conditions explain the control of natural fractures on hydraulic fracture propagation and natural fracture reactivation.

INTRODUCTION

This dissertation includes three chapters each focusing on three different aspects of natural fractures in the Woodford Shale in Oklahoma. The application of Chapter 1 is to show the control of natural fractures on artificial stimulation in shales. The focus of Chapter 2 is the timing of natural fracture origin in the Woodford Shale in Oklahoma. The emphasis of Chapter 3 is the stratigraphic natural fracture density variation along an entire Woodford Shale section.

Chapter 1 includes discussion of fracture size in the Hunton Group, in addition to the Woodford Shale. The fracture dimensions discussed in this chapter include natural fracture apertures, heights, and lengths of large fractures that have significant control on the fluid flow during artificial hydraulic fracturing. Fracture sizes in both the Woodford Shale and the Hunton Group are needed to build the geologic model for hydraulic fracture simulations, as the field microseismicity is not confined to the Woodford Shale only. The geologic/geomechanical model in Chapter 1 was built using FracMan^{TM} software. For the hydraulic fracture simulation in Chapter 1, the microseismic geometry and treatment pumping (parameters) were obtained from a treatment well in the western edge of the Arkoma Basin. The simulated and field microseismic geometry match gives insight into the properties of the Woodford Shale and underlying/overlying formations. Sensitivity analyses showing the effect of several parameters on the microseismic geometries were also performed.

Even though cementation and bed mineralogy constitute major parts of both Chapters 2 and 3, the focus of these chapters is fracture origin timing and stratigraphic fracture density variation respectively. Detailed discussions on the fracture cement and

crosscutting relationships have been used to interpret fracture origins. Discussion on bed mineral composition and thickness has been related to fracture intensity variation. The discussion on fracture size in Chapter 2 and Chapter 3 mainly focuses on joint apertures in the Woodford Shale.

The chapters are organized in such a way that the discussion on the least deformed/tilted outcrops occurs first, and that of the most deformed/tilted outcrops occurs last. This helps in demonstrating the occurrence of additional natural fracture sets with successive phases of deformation. The field study areas constitute the south-central parts of Oklahoma. The Clarita and Lawrence Uplift areas are the focus of Chapter 1; the Criner Hills area is the focus of Chapter 2; the Arbuckle Mountain area is the focus of Chapter 3.

The main aims of this dissertation are to investigate: a) aperture-size distributions of fractures (joints) ranging from microscopic (smallest) to bed scale to a couple of tens of meters long (largest), b) height distribution of the large natural fractures, c) natural fracture length-height relationships, d) natural fracture aperture-length relationships, e) natural fracture sets related to overpressure, f) natural fracture sets related to structural bending, g) dominant fracture sets that control the subsurface fluid flow, h) preferential orientation of natural fractures based on lithology, i) timing of natural fracture origin, j) lithologic dependence of fracture density, k) number of natural fracture growth stages and cement fill in the Woodford Shale, l) macro- and microfracture spacing patterns, m) bed thickness-fracture intensity relationships, n) fracture intensity-bed mineralogy relationship, o) average natural fracture relative permeabilities of different formations, p) suitable zones for landing horizontal wells in

the Woodford Shale based on field measurements, q) fracture fluid efficiency during hydraulic fracturing (using simulation), and r) theoretical effects (using simulation) of well landing location, strain accumulation due to previous stages, net pressure on fracture walls, rate of fracture fluid pressure drop, and natural fracture intensity on the stimulated volume (or geometry) during hydraulic fracturing.

CHAPTER 1: PREDICTION OF HYDRAULIC FRACTURE STIMULATED ROCK VOLUME GEOMETRIES IN THE WOODFORD SHALE IN ARKOMA BASIN USING DISCRETE FRACTURE NETWORK MODELS

Abstract

Natural fracture parameters obtained at shale and carbonate outcrops/quarries were used to understand artificial hydraulic fracture propagation in both lithologies. The outcrop fracture parameters were used as inputs into FracMan^{TM} software to build a discrete fracture network model. Field hydraulic fracture treatment parameters were applied on the model to match the microseismic geometries of three stages. The Arkoma Basin well located 20-25 miles east of the studied outcrops. The simulator and field microseismic geometry match gives insight into the properties of the Woodford Shale and underlying/overlying formations.

The outcrops reveal relatively long and continuous fractures in the Woodford Shale compared to the Hunton Group Limestone. The Woodford Shale has two predominant fracture sets (E-W, NE-SW), and the Hunton Group Limestone has three to four predominant sets (E-W, NE-SW to N-S, and NW-SE). In the shale, the E-W average fracture height is almost twice that of the NE-SW fractures, considering fractures with height > 1 m. However, the average NE-SW set aperture (for fractures with height > 1 m) is nearly twice that of the E-W fractures. In the carbonates, there is much lower variability in the dimensions of different fracture sets. Most of the fracture dimension exhibit exponential and lognormal, followed by a power-law best fits.

The simulator predicts that halving the number and doubling final storage apertures of natural fractures leads to high fluid efficiency (increases from 1.4% to 27%), or lower leak off ratio, in areas where fluid was restricted from flowing in non-

dilatable fractures. In stages with high fluid mobility due to flow through non-dilatable fractures, high efficiency was not obtainable. With increased fluid efficiency (using fluid loss additives or increasing viscosity), even though more horizontal growth (across wellbore) of the hydraulic fracture (new surface area) was obtained within all formations, most growth happens out of the target zone (Woodford Shale), reducing the effectiveness of the hydraulic fracture job. In addition, a 15% lower stimulated volume was obtained when the fluid pressure-drop slope within fractures was increased from 0.1 to 1.0. A high pressure-drop slope value usually results from using a high viscosity, a high-density fluid or both. Therefore, reactivation of natural fractures should be prioritized (resulting from low viscosity/low-density fluid and without additives) over increasing fluid efficiency (usually resulting from high viscosity fluid, using fluid loss additives, or both).

Pumping at a higher net pressure (ISIP increased from 6500 psi to 7000 psi) was found to reduce the stimulation volume (8% to 52% depending on stage) and opening of more non-dilatable fractures closer to the wellbore. Higher net pressure also causes more stimulation downward and out of the target zone in the studied area. However, when a high slurry rate is applied for better proppant placement, the horizontal well should be placed high in the Woodford Shale due to downward reactivation of natural fractures. Shifting the well locations within the Woodford Shale into zones of relatively high or low horizontal stresses did not affect the overall microseismic cloud geometry considerably (6% or less change in the stimulated volume). Only, a corresponding shift in the stimulation volume with the well location was observed. However, a minor increase in the minimum strain (1.5e-5 or 5e-6 depending on stage), leading to an

increase in Shmin with successive stages, showed a considerable change in the microseismic cloud geometry, and higher stimulation volume in the layers closer to the wellbore. A 14% to 23% change in stimulation volume was observed depending on the stage.

1.1 Introduction

The Arkoma Basin (Figure 1.1) is a prolific petroleum producing basin in North America (Suneson, 2012). The type of hydrocarbon is mainly gas. Historically, production in this basin has taken place from several formations such as the Red Oak Sandstone, the Shapiro Sandstone, the Wapanuchka Limestone, and the Bigfork Chert (Suneson, 2012). However, with advanced horizontal drilling technology, the Woodford Shale, which is both the source and reservoir rock, is one of the main targets (e.g., Vulgamore et al., 2007; Keller, 2010). As of 2016, the Woodford Shale in the Arkoma Basin in Oklahoma has produced 1.3 million barrels of oil and ~ 2.5 TCF of gas.

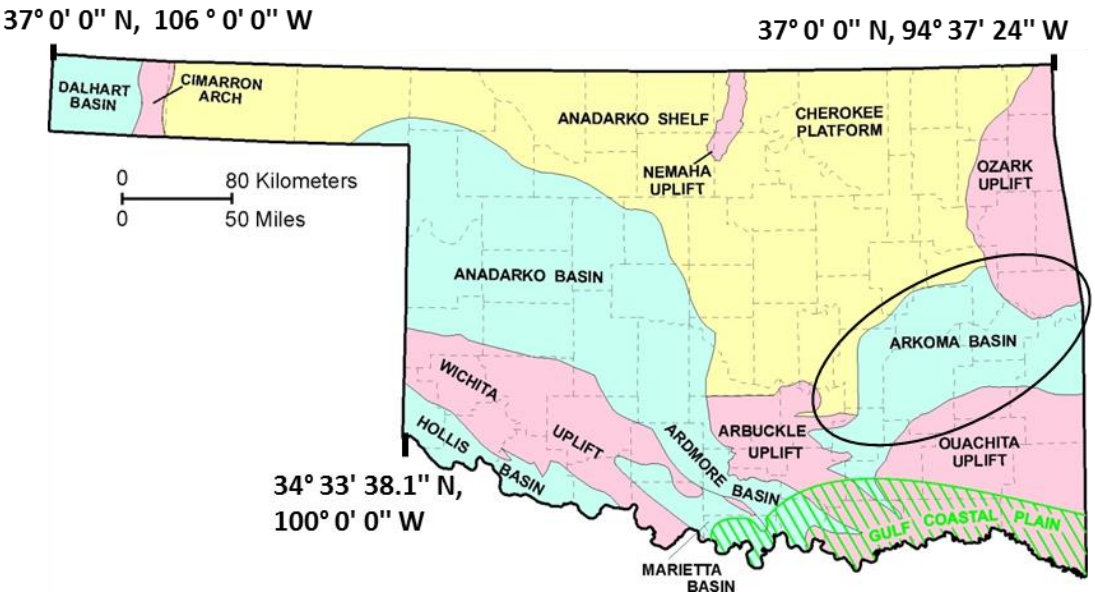

Modified from www.ogs.ou.edu/MapsBasic/Provinces.jpg

Figure 1.1: Geologic provinces of Oklahoma. Arkoma Basin is circled.

Although subsurface faults within the Arkoma Basin have been extensively studied and documented using well and outcrop data (e.g., Arbenz, 1984; Hardie, 1988, Andrews 2008; Arbenz, 2008; Allison et al., 2012; Suneson 2012) there is a dearth of literature regarding joint (Mode I fracture) studies in the Arkoma Basin. This is mainly because image logs are not readily available, likely due to the extra cost associated with running/obtaining these logs. Seismic imaging has helped delineate large structures, however, smaller structures that influence engineering activities remain hidden (Fairhurst, 2013). However, given the importance of natural fractures in hydrocarbon production from unconventional reservoirs, it is necessary to understand their characteristics, because they affect hydraulic fracture propagation (Cipolla et al., 2008b; Li et al., 2015).

Hydraulic fracturing in unconventional reservoirs has become an essential operation because production is not profitable due to low matrix permeabilities (Milad, 2013). One way to understand hydraulic fracture propagation in the presence of natural fractures is to perform computer simulations. Simulations on the effect of hydraulic fracture propagation in the presence of natural fractures were conducted by several researchers. Riahi and Damjanac (2013), using hypothetical scenarios, concluded that as the connectivity of the DFN (discrete fracture network) decreases, the injection pressure and probability of hydraulic fracture propagation increases. Injection rate and effective fracture permeability combined are important in determining the formation response to fluid pumping (Riahi and Damjanac, 2013). Pirayeghar and Duesseault (2014), using several hypothetical scenarios, concluded that fracture branching increases with lower

stress anisotropy. Fairhurst (2013) showed that the asymmetry in the fracture propagation depends on how the natural fractures are oriented on both sides of a wellbore. If an initiated hydraulic fracture encounters an unfavorably-oriented natural fracture on one side of a wellbore, the hydraulic fracture on the other side of the wellbore will receive more fluid and grow in that direction. Though the earlier works discussed here are informative, a common drawback among these models is that they are either 2D or use hypothetical scenarios or both.

However, the models (using FracMan^{TM}) built for study are three-dimensional and based on field (outcrop) and microseismic data. Therefore, they are more realistic compared to the hypothetical and 2D simulations. In the field (subsurface), several factors interact, and therefore, different stages within the same well behave in a dissimilar manner. Some of these factors are variation in fracture abundance, connectivity, permeability and changing stress heterogeneity with subsequent stages. Therefore, through hydraulic fracture simulation, the reasons behind the differences in the microseismic cloud (MC) geometries between different stages in a well were investigated. Subsequently, the MC geometries were predicted under different geologic and treatment conditions.

In this study, due to non-availability of image logs or seismic data, the discrete fracture network model was built using natural fracture parameters obtained from three outcrops located 20-25 miles from the treatment well. Essential natural fracture parameters, such as aperture, length, height, and intensities for both shale and carbonate natural fractures were obtained. Statistical analysis and correlations between these parameters were also obtained. Following this, several discrete fracture network

realizations were made in FracMan™ software with the intention of matching the hydraulic fracture geometry outlined by microseismic recordings. The best 3D matches between the field MC geometries for three stages could only be obtained under certain conditions of formation permeabilities, horizontal stress magnitudes, presence/absence of different fracture sets, simulator grid sizes, and fluid pumping timesteps. Therefore, the model parameters used here are well constrained, especially given the fact that hydraulic fracturing is not an "exact science" (Fairhurst, 2013). Shuttle et al. (2000), Dershowitz (2006), Dershowitz et al. (2010), and Rogers et al. (2014) conducted simulations using the FracMan™ software for hydraulic fracturing and grouting purposes.

Outcrop data is used in this study because core, image logs, and seismic data are not available. Even with the availability of these data, the outcrops are important. Due to limited visibility of fractures in core and image logs, outcrops studies are useful for studying natural fractures (Gross, 1993; Hanks et al., 1997; Ahmadhadi et al., 2008; Fischer et al., 2009; Barbier et al., 2012a; Beaudoin et al., 2012). The purpose of this part of the study is also to bridge the gap between structural geologists and engineers studying natural and hydraulic fractures by i) quantifying parameters of the relevant fracture at the outcrops, ii) explaining the causes of the observed MC geometries by stages, iii) predicting the formation behavior under variable subsurface conditions and hydraulic fracture parameters.

1.2 Methods

1.2.1 Fracture parameters from outcrops

Definitions for fracture length, height, and kinematic aperture are shown in (Figure 1.2). The outcrops (Figures 1.3 through 1.8) were used for measuring both fracture intensities and dimensions. For fracture length vs. height correlations, several fracture faces (i.e., perpendicular to the strike of a particular set) were photographed. For example, photographs in the N-S direction were taken for the E-W fracture lengths and heights. This was done for all fracture sets. The photographs and the height-length interpretations for the Woodford Shale at the Wyche Shale Pit are shown in Figures 1.4A and 1.4B. Photographs and the height-length interpretations for the Hunton Group Limestone at the Jennings Quarry are shown in Figures 1.6A, 1.6B, and 1.6C.

There are several methods for measuring fracture abundance in outcrops, i.e., the scanline sampling, window sampling, and circular window sampling (Zeeb et al., 2013) methods. In the scanline sampling method, fracture intensities (P10) are measured bed by bed along scanlines. The fracture intensity (P10) is the number of fractures divided by the scanline length (e.g., Hooker et al., 2013). Mauldon et al. (2001) and Rohrbaugh et al. (2002) described the circular window sampling. In this method, the number of fracture intersections with a circle is divided by four times the circle radius to find the fracture intensity (P21) (Zeeb et al., 2013). Workers such as Pahl (1981) and Priest (1993) have described the window sampling method. In the window sampling method, the total length (m) of the fracture traces in an observed area (m^2) is divided by the area to get the fracture intensity (P21) in fractures/m (Zeeb et al., 2013).

In the Wyche Shale Pit (Figure 1.3) and the Jennings Quarry (Figure 1.5), the window method was used for measuring fracture intensities. The window method was chosen for several reasons. First, only the top 30-40 feet of the Woodford Shale and the Hunton Group Limestone were visible. Therefore, using the scanline method layer by layer was not a viable option. Therefore, an area method was needed, which means either the circular window sampling or the window sampling method could be used. However, the exposures, in either the Woodford Shale or the Hunton Group Limestone, were not big enough to draw enough circles with several intersecting fractures, for statistical analysis. Therefore, the window method was chosen between the two area methods. The photographs used for the window method in the Woodford Shale at Wyche Shale Pit are shown in Figures 1.4C through 1.4F. Photographs used for the window method in the Hunton Group Limestone at the Jennings Quarry are shown in Figures 1.6D through 1.6I. Priest (1993), similar to this study, used this method on a mine wall. Also, for the remaining formations (non-Woodford, non-Hunton), outcrops were not available. Therefore, a viable option was to take average fracture intensities of each fracture set for the Woodford Shale and the Hunton Group Limestone, and use them for other shale and limestone formations respectively.

There are some limitations to these measurements. The most obvious limitation in the fracture height measurement in a hierarchical distribution is the vertical truncation (invisibility) of some of the longer fractures, which transect more beds compared to the bed bounded ones. This hierarchical pattern has been observed in many carbonate and clastic rocks (Cooke et al., 2006, Bertotti et al., 2007; Zahm and Hennings, 2009). These high (large) fractures are more important, compared to the bed-

bounded ones, in a hierarchical fracture distribution because they can carry fluids across beds and increase overall vertical permeability. Hooker et al. (2013, p. 58) describe hierarchical fracture pattern along with other patterns of fracture termination. In the current study, due to the truncation limitations (upper cutoff bias), the statistical distributions (shown later) obtained should be used as DFN simulator inputs, rather than for geologic inferences such as fracture origin and growth conditions.

The quarry floor surfaces are generally covered with rock debris. However, certain spots in the Wyche Shale Pit, the Jennings Quarry, and the Clarita Shale Pit provide relatively cleaner surfaces for measuring fracture lengths and kinematic apertures (opening displacements). The Clarita Shale pit allowed measurements of the E-W fracture lengths and apertures in the Woodford Shale. However, at some places, a visual estimate was made as to whether some tens of feet long (used interchangeably with "large" in the text) fractures transect the debris cover, or are different fractures (e.g., Figure 1.8C). The Wyche Shale Pit allowed measurements of the NE-SW apertures on the quarry floor. The Jennings Quarry allowed measurements of the N-S and the E-W Hunton Group Limestone fracture apertures on the quarry floor. The fracture kinematic apertures (opening displacements) were interpreted to have been unaffected, or minimally affected, by the uplift, i.e., no clear displacement parallel to fracture faces was visible.

In addition to the lengths and opening displacements, the quarry floor fractures also provide a glimpse of the fracture timing and continuity. For example in the Clarita Shale Pit, even though the NE-SW and E-W fractures mostly are crosscutting (Figure 1.8B), sometimes large (long) NE-SW fractures also terminate on the E-W set (Figure

1.8A). This indicates the following sequence of timing in the Woodford Shale from the Clarita Shale Pit: E-W set → NE-SW set. Similarly, in the Jennings Quarry, at a few spots N-S fractures terminate at the E-W fractures (Figures 1.6J, and 1.6K), E-W fractures crosscut and terminate at NW-SE set, and N-S fractures terminate at the NW-SE fractures (Figures 1.6L and 1.6M), indicating the following fracture origin sequence in the Hunton Group Limestone from the Jennings Quarry: NW-SE set → E-W set → NE-SW and N-S set. This timing sequence, however, needs to be supported by evidence from other Hunton Group Limestone exposures. Figure 1.8A shows the long and relatively continuous nature of the shale fractures. Figure 1.6J shows the relatively discontinuous nature of the carbonate fractures compared to that in shales.

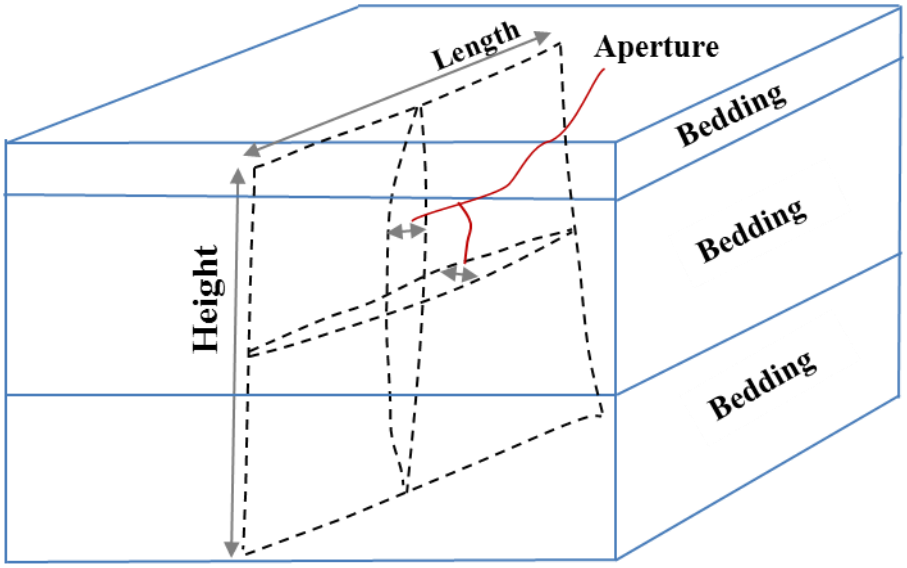

Figure 1.2: Cartoon depicting the fracture aperture, length, and height.

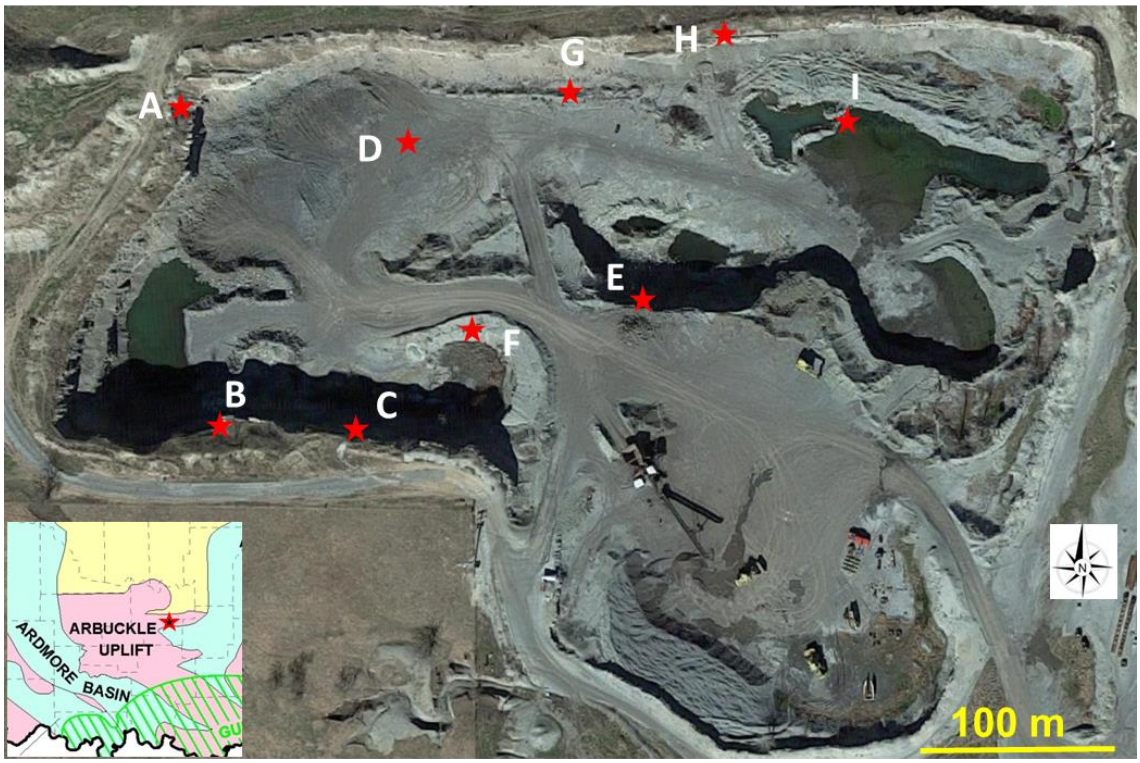

Figure 1.3: Plan view of the Wyche Shale Pit (34°40'22.7"N, 96°38'34.8"W). Beds dip ~ 10 degrees in the ENE direction (Ham and McKinley [1954]; revised by Johnson [1990]). The north and the western sides of the quarry have good exposures for measurements of fracture attributes. Marked are different spots at which measurements and observations were made. Spot D has a relatively clean quarry floor fracture trace exposure for aperture measurements.

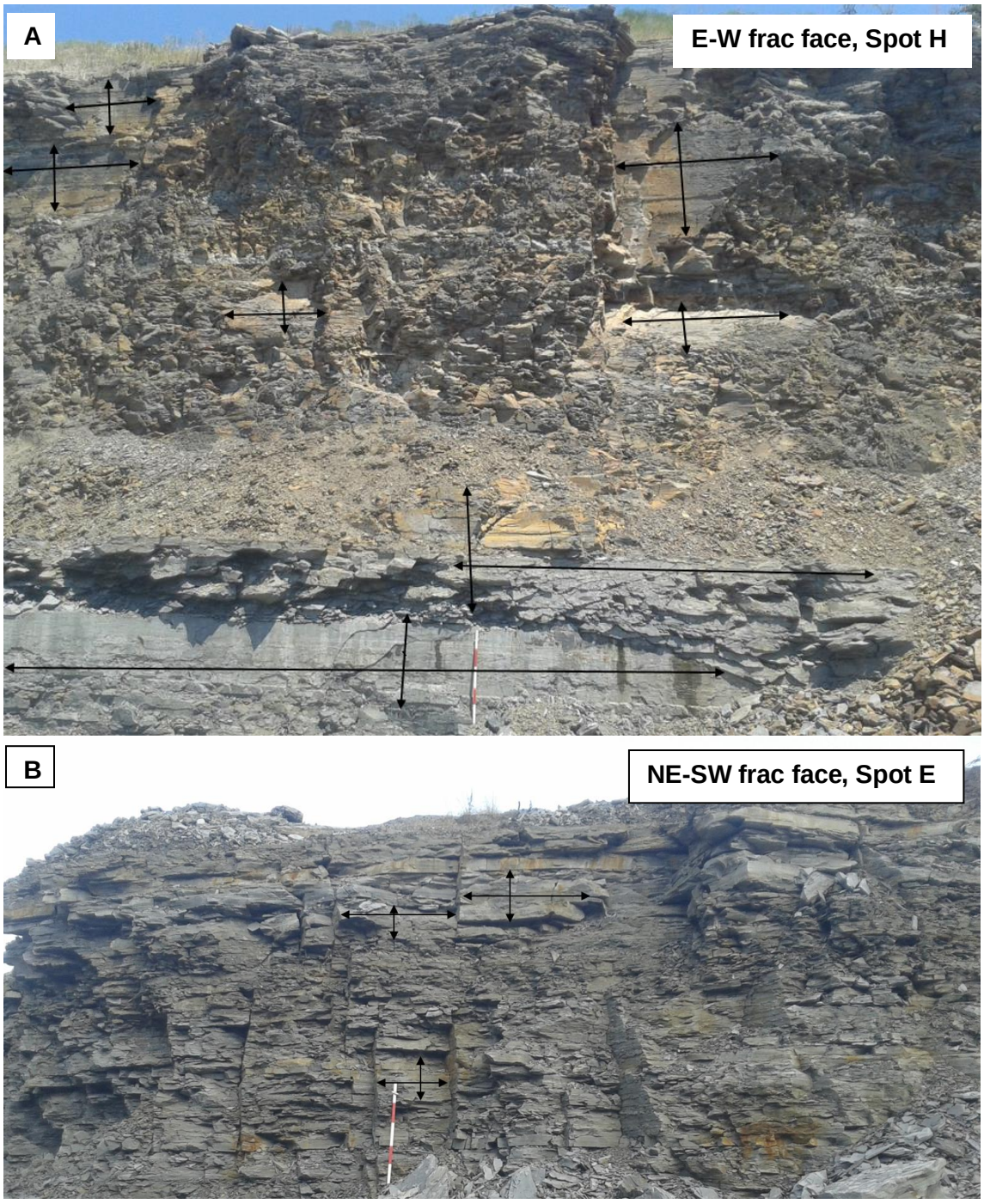
A
E-W frac face, Spot H
B
NE-SW frac face, Spot E

C

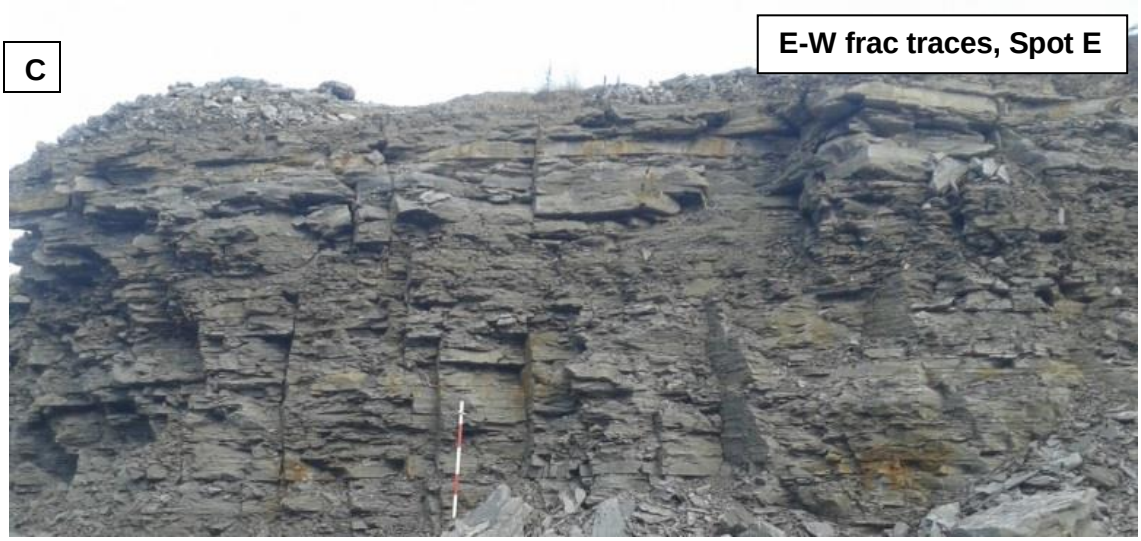

D

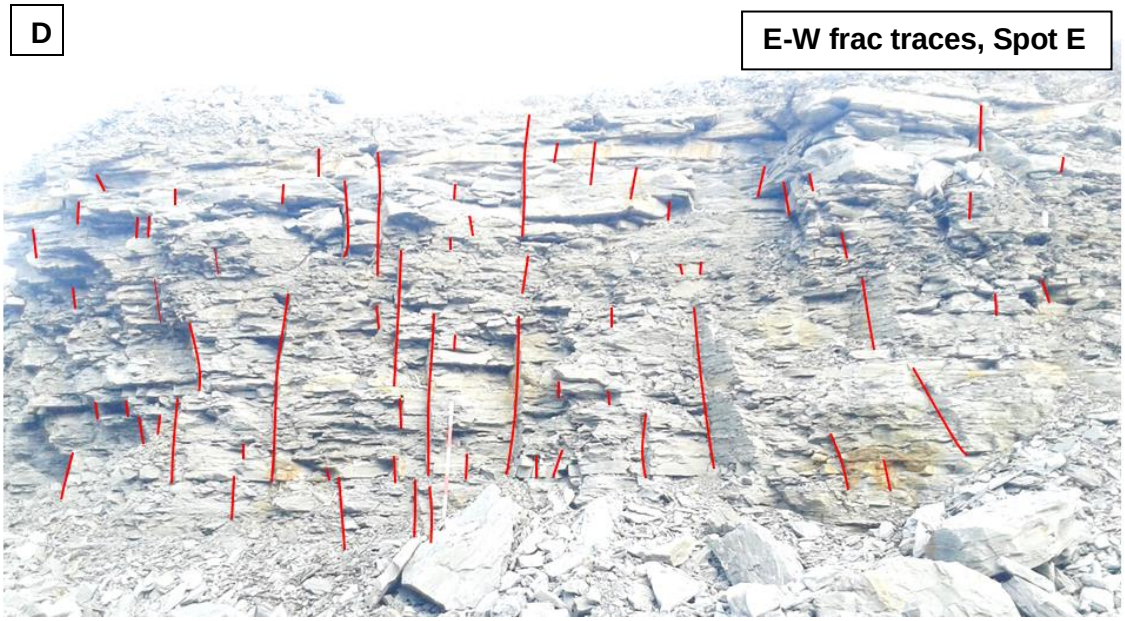

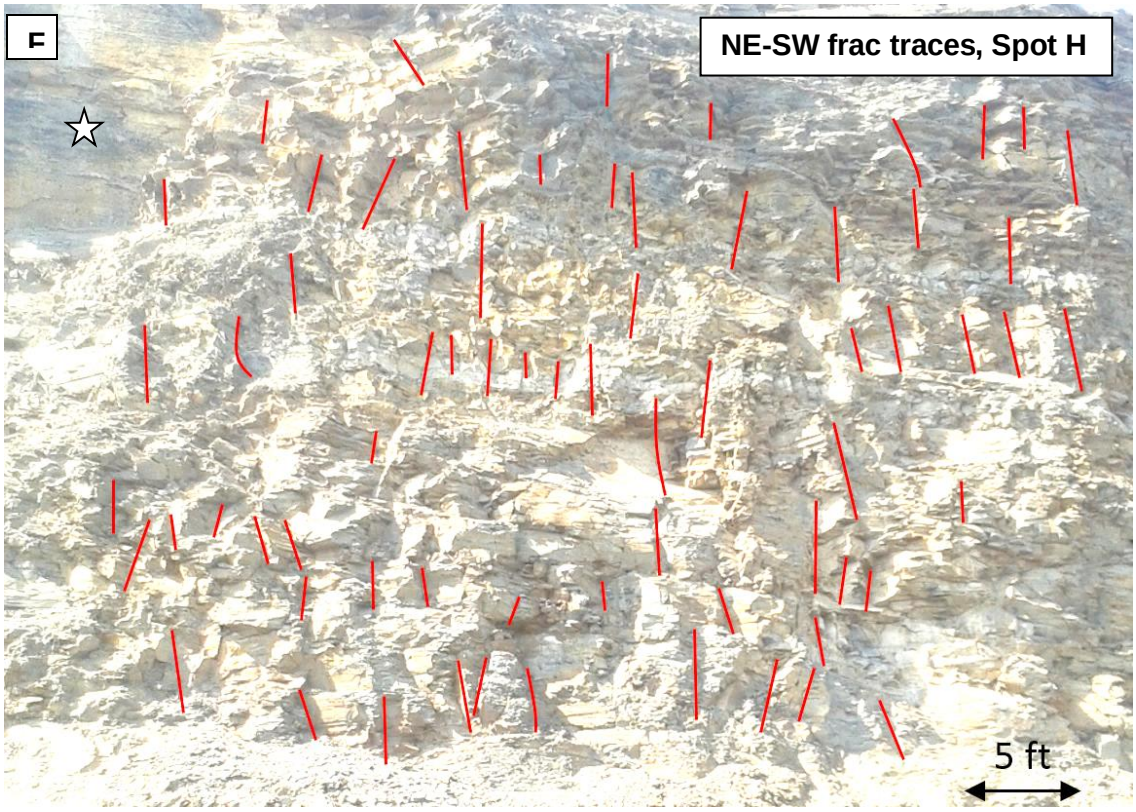

Figure 1.4: Fracture dimensions in the Woodford Shale. **A)** An example of length vs. height interpretation on the E-W fracture faces. Double-headed vertical and horizontal

arrows represent the height and length of each face respectively. **B)** An example of length vs. height interpretation on the NE-SW fracture faces. **C)** E-W fracture traces. **D)** E-W fracture trace interpretation. **E)** NE-SW fracture traces. A much larger E-W fracture face is seen on the top left (star). **F)** NE-SW fracture trace interpretation. Notice that the NE-SW trace interpretation is not as straightforward as the E-W trace interpretation because of shorter lengths and their occurrence in predominantly clay-rich beds.

Figure 1.5: Plan view of the Jennings Quarry (34°35'39.3"N, 96°39'01.2"W). The beds dip 5-15 degrees towards the NE direction at the measured spots. The west and south sides have well-exposed faces for fracture length and height measurements. In addition, locations such as Spot G and Spot I (dry during measurement) have quarry floor fracture exposures for aperture measurements.

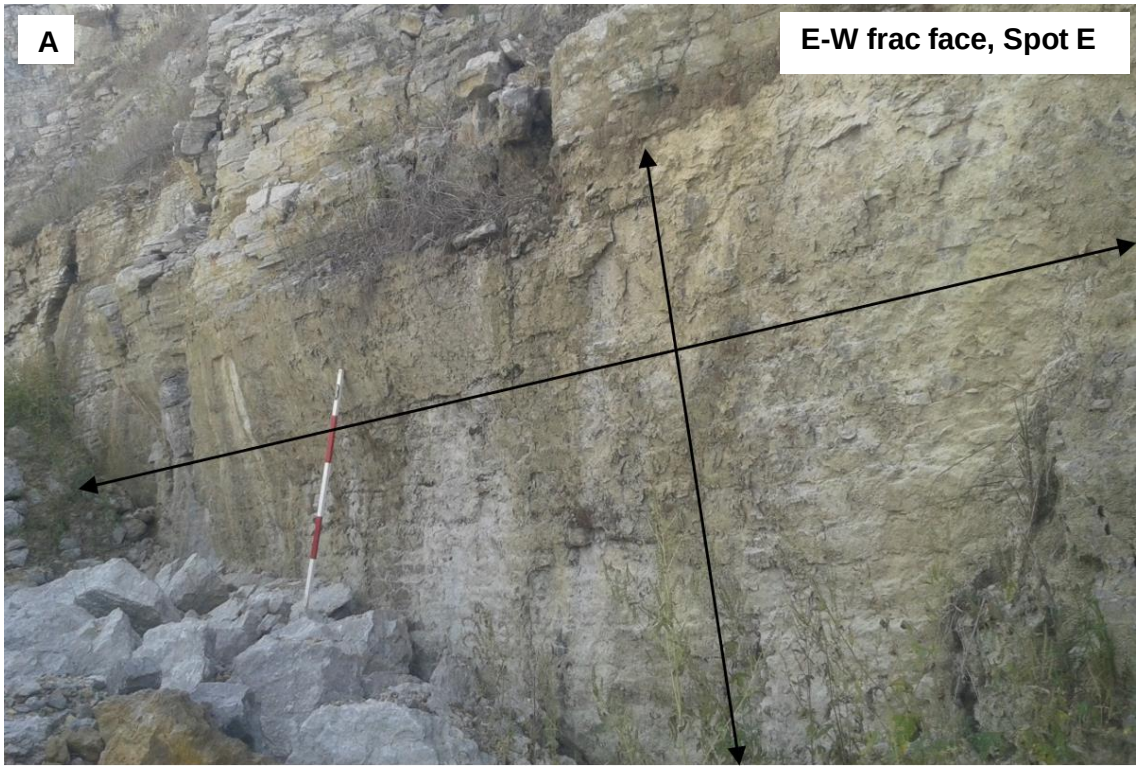
A
E-W frac face, Spot E

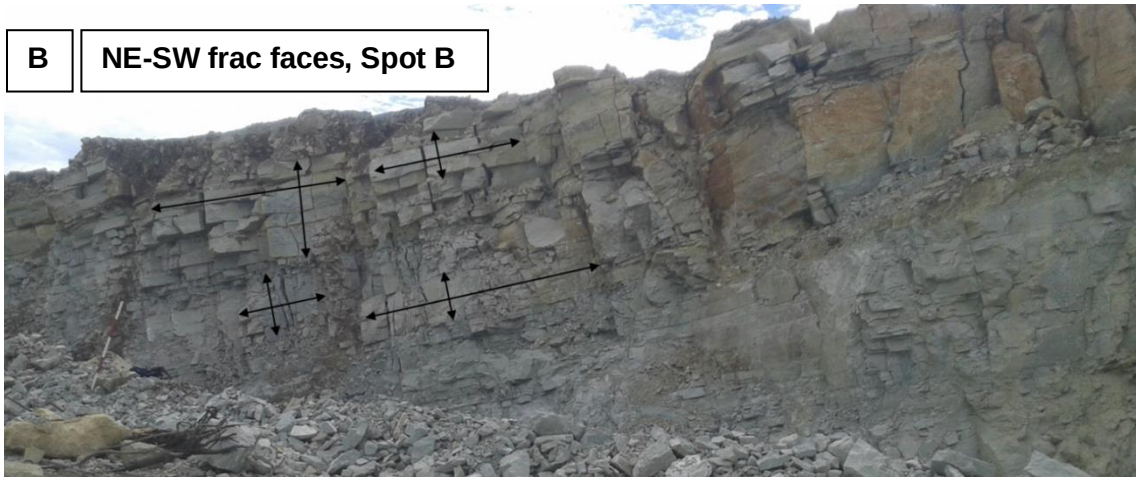
B
NE-SW frac faces, Spot B

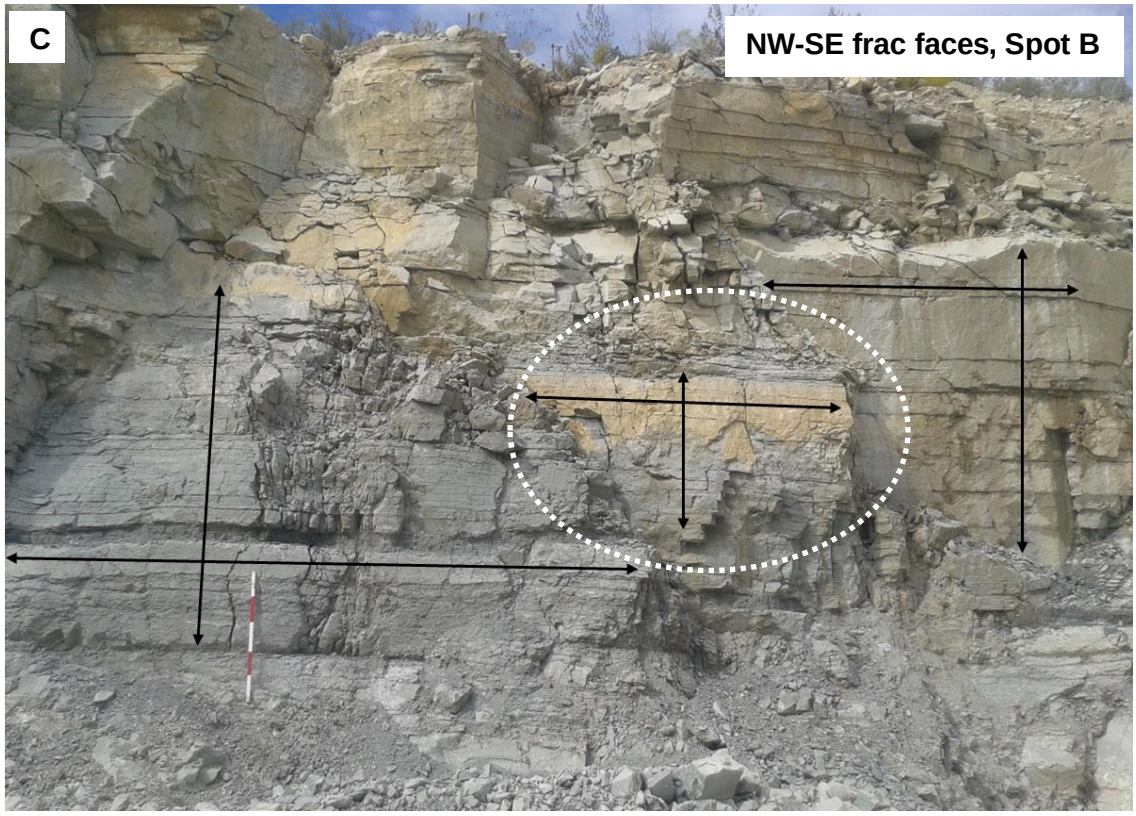
C
NW-SE frac faces, Spot B


D
E-W frac traces, Spot C

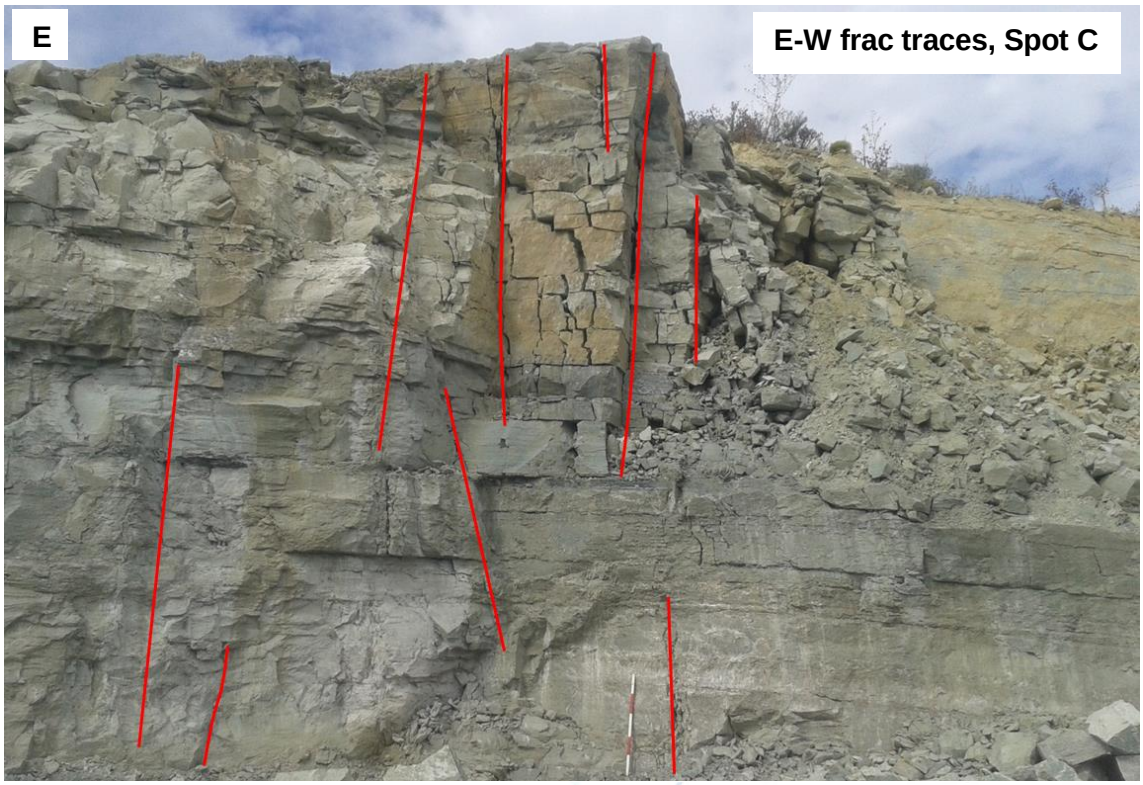
E
E-W frac traces, Spot C


F
NE-SW frac traces, Spot A

G **NE-SW frac traces, Spot A**

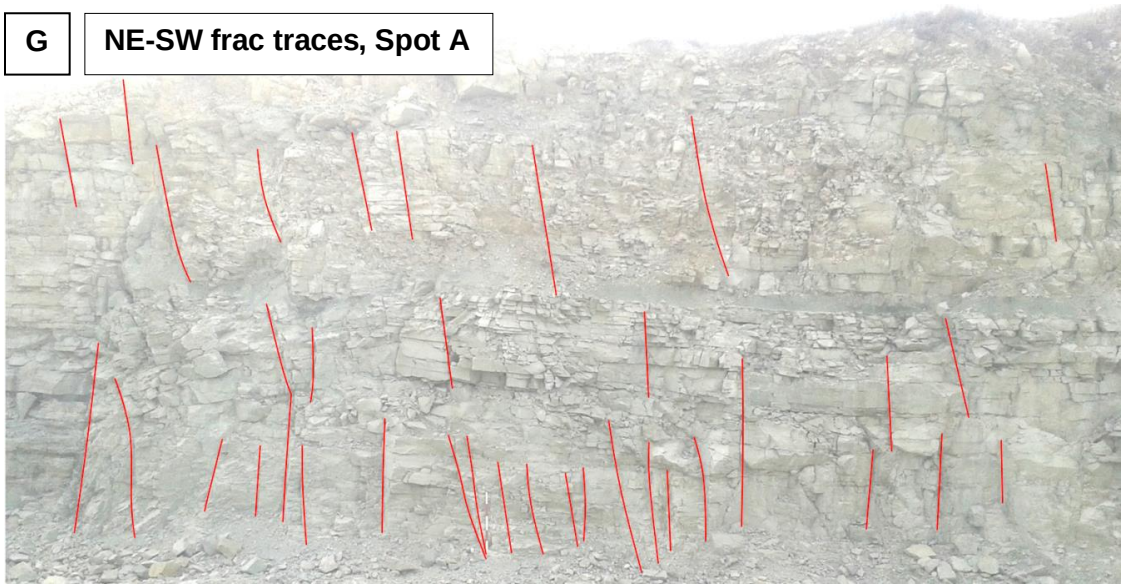

H **NW-SE frac traces, Spot B**

I **NW-SE frac traces, Spot B**

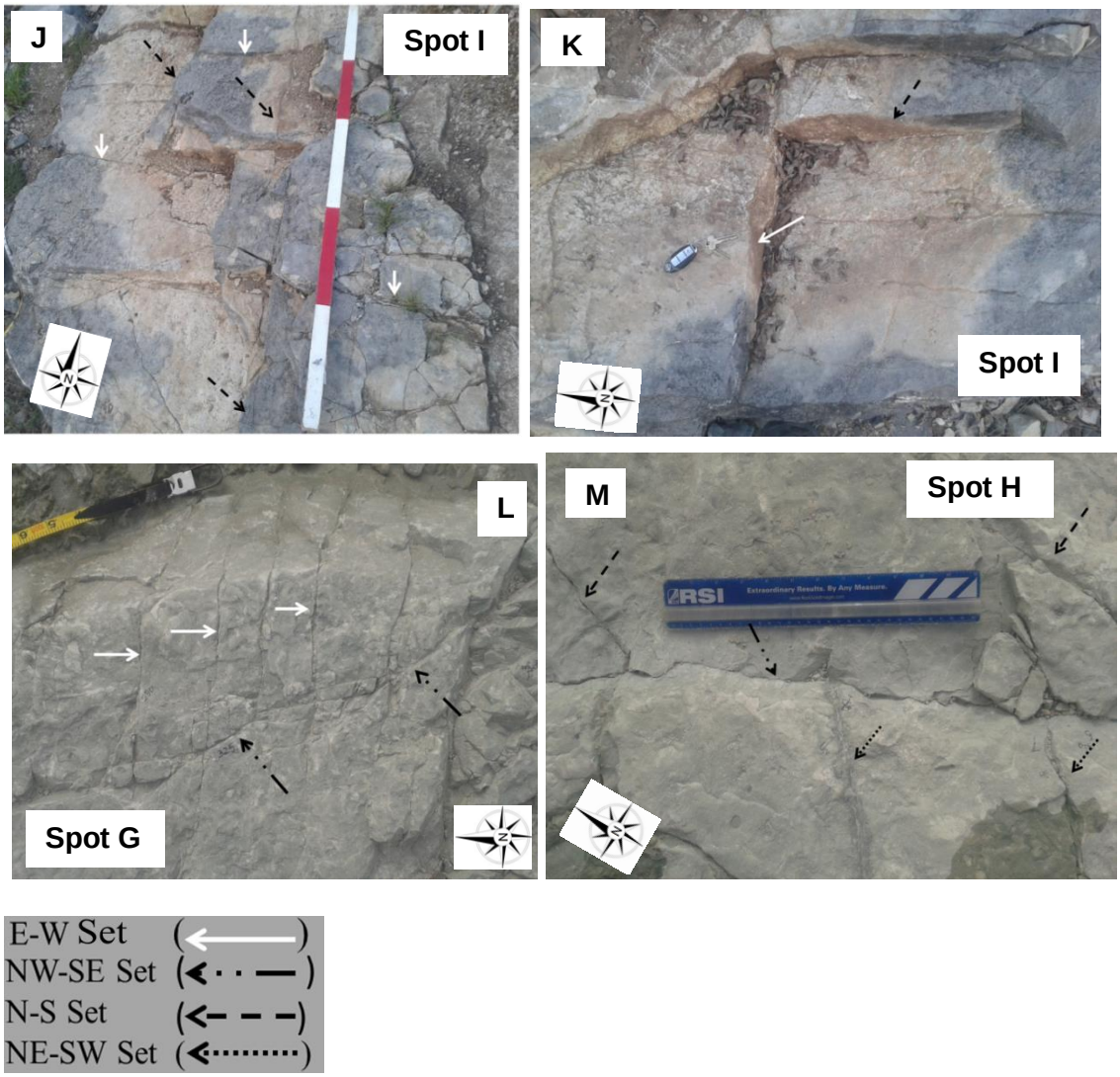

Figure 1.6: Fractures in the Jennings Quarry where the Hunton Group Limestone is exposed. **A)** An example of length vs. height interpretation on the E-W fracture faces. Double-headed vertical and horizontal arrows represent the height and length of each face respectively. **B)** An example of length vs. height interpretation on the NE-SW fracture faces. **C)** An example length vs. height interpretation on the NW-SE fracture faces. Notice that fracture face within the circle is likely obscured and probably extends below the matrix (towards the left), and artificially truncated to the right due to the absence of the matrix, i.e., the visible length is less than the real length of that fracture. This is true for all visible fractures in variable degrees. **D)** E-W fracture traces. **E**) E-W fracture trace interpretation. **F)** NE-SW fracture traces. **G)** NE-SW fracture trace interpretation. **H)** NW-SE fracture traces. **I)** NW-SE fracture trace interpretation. **J)** N-S fractures crosscutting and terminating at the E-W fractures. **K)** N-S fractures crosscutting and terminating at the E-W fractures. **L)** E-W fractures crosscutting and terminating at the NW-SE fractures. Notice E-W fractures terminating within the rock (top part of the picture). **M)** NE-SW and NS fractures terminating at NW-SE fractures.

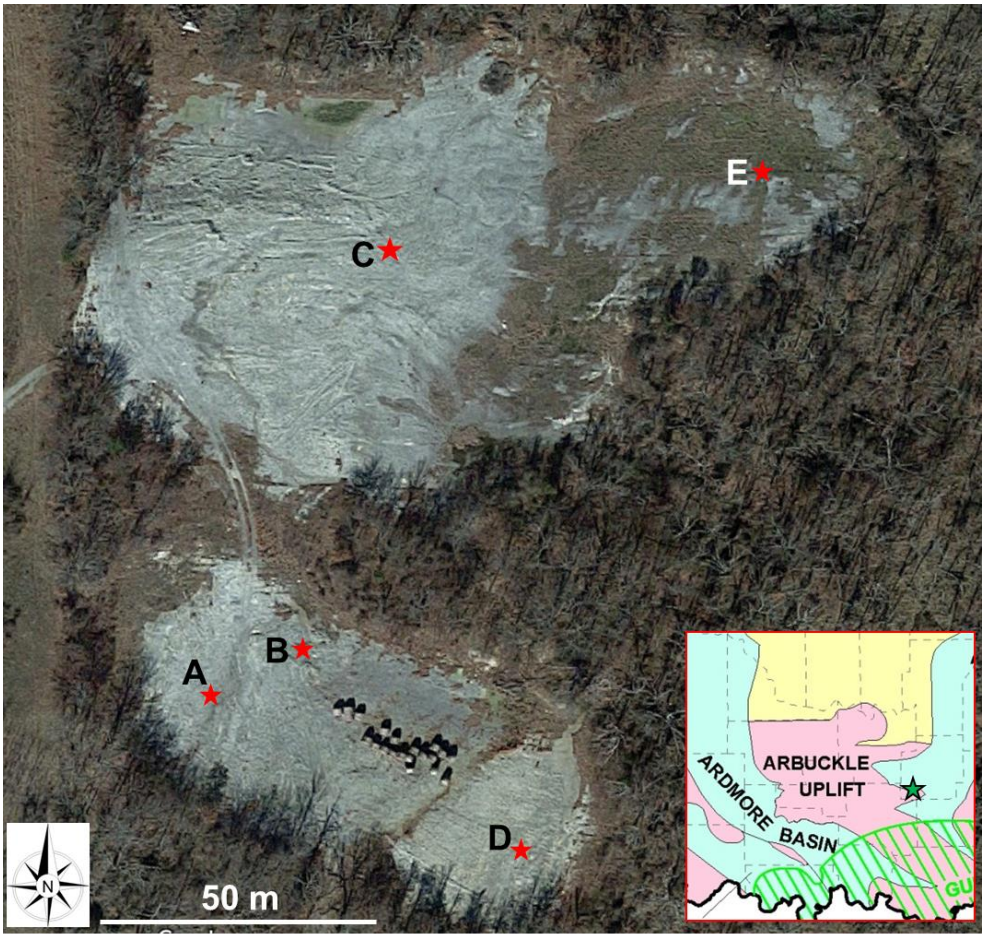

Figure 1.7: Plan view of the Clarita Shale pit (34°27'45.1"N, 96°27'21.8"W). Beds are oriented 015/06 (right-hand rule) (Ataman, 2008). Observation and measurements spots are marked. Spots C and D have relatively clean fracture trace exposures for aperture measurements.

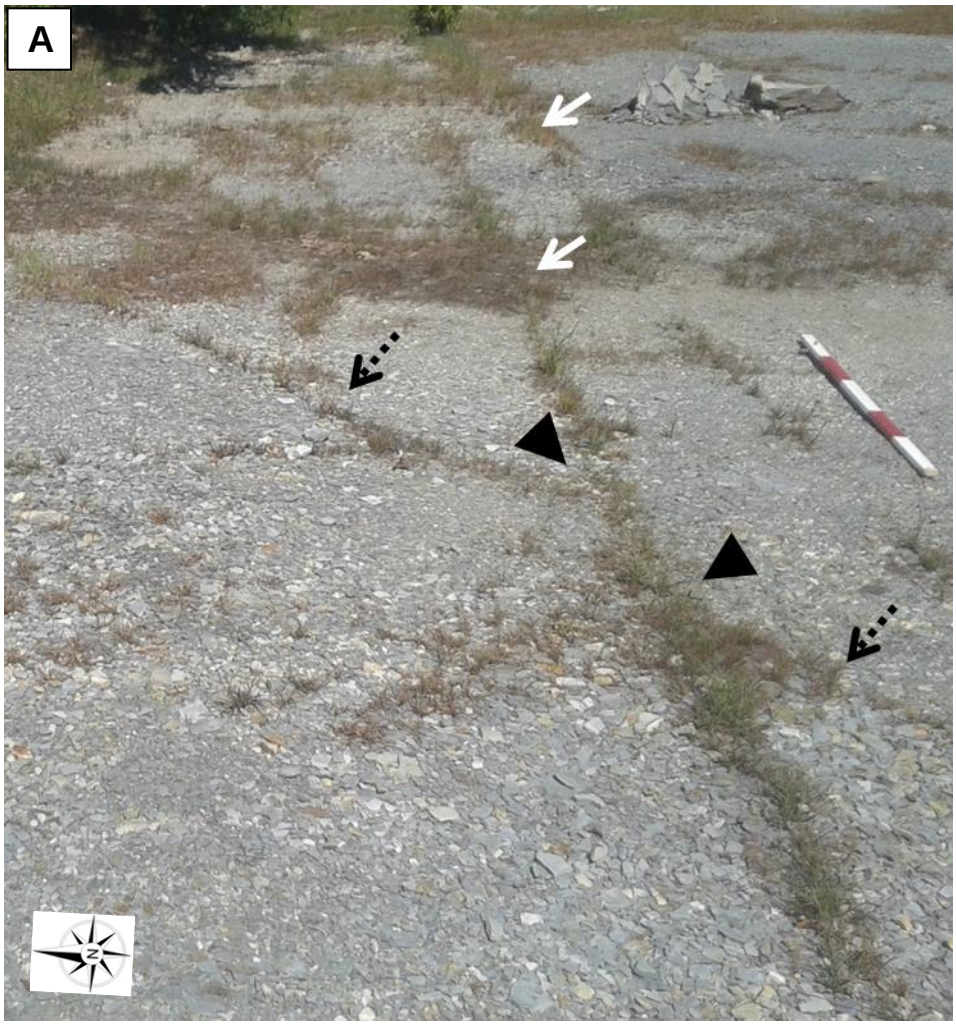
A

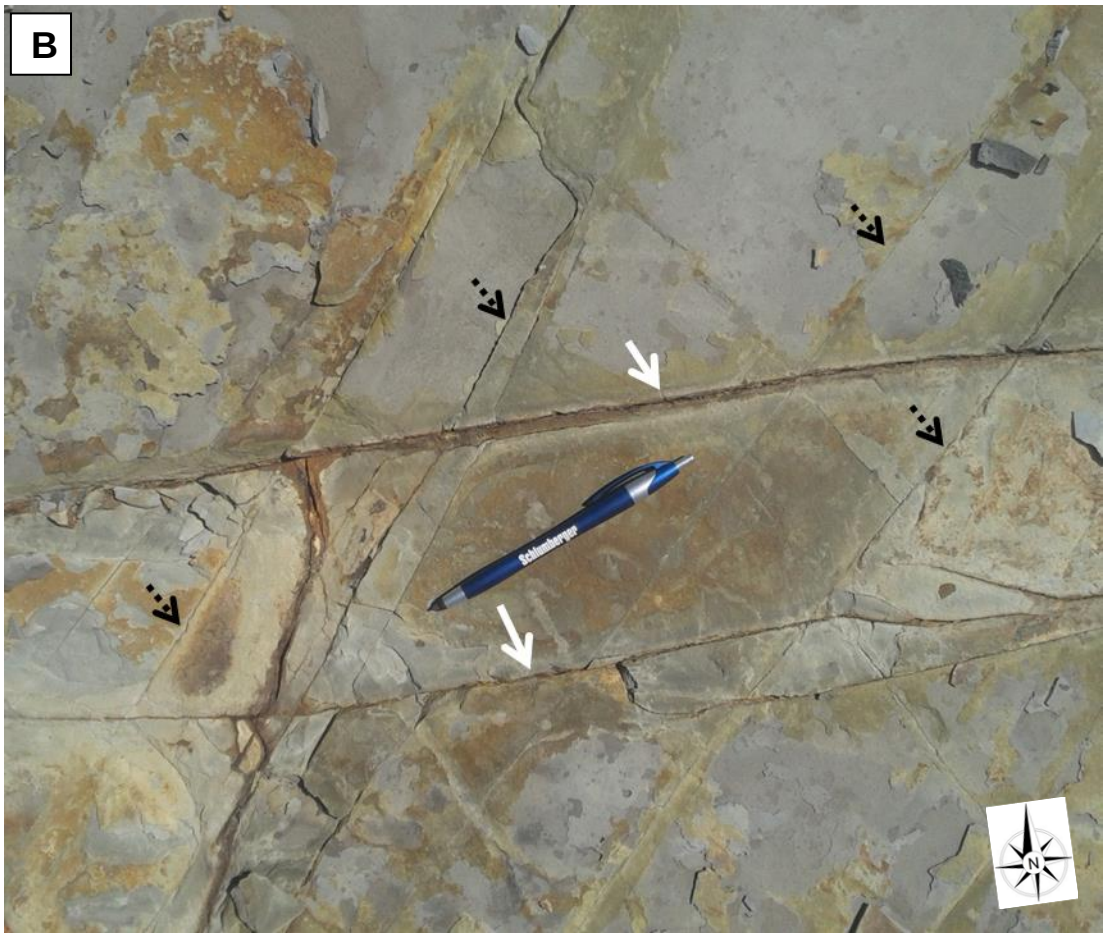
B
Schlumberger
N

Figure 1.8: Fractures in the Clarita Shale Pit. **A)** Vegetation growth showing the E-W and NE-SW striking fractures in the Clarita Shale Pit. Notice the NE-SW fractures terminating at the E-W fractures (triangles show intersections). **B)** NE-SW and E-W fractures crosscutting each other. **C)** Segmentation in the E-W fractures. The top two, and the lower three segments likely are two different fractures. However, due to a separation of only 4-5 inches between the two fractures, they may be mistaken as one fracture if the segmentation is hidden under rock debris.

1.2.2 Stimulated rock volume dimensions from field microseismic cloud

The outcrop fracture parameters (discussed earlier) were used to build a static DFN (discrete fracture network) model in FracMan^{TM} software. The static model was stimulated using the field treatment parameters resulting in stimulated (simulated) rock

volumes. However, to match the simulated geometry to the field MC (microseismic cloud) geometry, the latter needs to be defined first. Defining particular geometries given the complex and irregular field microseismic cloud (MC) shapes is a widely discussed topic. Sayers and Le Calvez (2010) developed a technique called the radius of gyration tensor. The radius of gyration tensor generates characteristic ellipsoids for a set of a given MC. The eigenvectors of the tensor coincide with the principal axes (3D) of the ellipsoid. The square roots of the eigenvalues are related to the lengths of the three ellipsoid axes. Therefore, the dimensions of the ellipsoid are a function of the horizontal stress ratios and fractures. The ellipsoid also requires defining confidence intervals, i.e., the percentage of microseisms within the ellipsoids. Choosing different confidence intervals changes the ellipse axes directions and dimensions. Therefore using this method of defining microseismic geometries is not just a question of choosing the confidence intervals, but also the availability of the field recorded microseismic data.

Shapiro (2008) mentioned using distance-square root time plots (linear relationship) to interpret a triggering front in an area from observations of different MC's. Using outer bound of the front, hydraulic diffusivities in three directions can be defined. Then the triggering front equation becomes the equation of an ellipsoid. The square roots of the principal diffusivities are related to the half axes lengths of the ellipse. However, defining a triggering front involves interpreting and eliminating events that are not related to the pore pressure diffusion using the distance-square root time plots. Therefore, this method also involves interpretational bias.

Therefore, both cases require 3D microseismic data and are subject to interpretational bias. However, for this study, only 2D photographs from 3 directions

for each stage is available from Neuhaus (2011). Therefore, a simplified method was used for defining the microseismic geometry for the three modeled stages. As mentioned by Sayers and Le Calvez (2010), the ellipsoids were defined in a way that maximizes the number of microseisms and reduces the amount of empty space within the ellipsoids. Eppheimer (2016) mentioned that as more points are included within the ellipsoids to increase the confidence interval, the empty space also increases, thus increasing uncertainty. Therefore, the ellipsoid dimension is a question of reasonable interpretation. The dimensional interpretations and corresponding FracMan^{TM} models are discussed later.

1.3 Geology

As subsurface analogs for the fracture model three quarries were studied on the eastern edge of the Arbuckle Mountains- the Wyche Shale Pit (exposes the Woodford and the Mayes Shales), the Jennings Quarry (exposes the Hunton Group Limestone), and the Clarita Shale Pit (exposes the Woodford Shale). The Wyche Shale Pit and the Clarita Shale Pit are both located on horst blocks, and the Jennings Quarry is located in a fault zone. The locations of these outcrops are shown in Figures 1.9 and 1.10A.

The Wyche Shale Pit is located south of the city of Ada. The structural position is east of the Arbuckle Mountains and west of the Arkoma Basin on a structure called the Lawrence Uplift/Horst. The Lawrence Horst is bounded by the Ahloso Fault to the north and by the Stonewall Fault to the south (Figure 1.9). The Franks Graben is located south of the Lawrence Horst. The rocks in the Lawrence Horst dip gently east, while those in the Franks Graben dip gently west, indicating Mode III or scissor type movement in the Stonewall Fault (Suneson, 1997). This also results in progressively

older rocks being exposed on the west side of the Lawrence Horst. The Lawrence Horst is located just outside (east) of the Southern Oklahoma Aulacogen, and therefore the rock units are thinner here compared to that in the aulacogen to the West (Suneson, 1997). The structure along the line DD' (Figure 1.10A) resembles a gently dipping monocline at the Woodford Shale exposure (Figure 1.10B).

The Jennings Quarry is located in the city of Fittstown, OK. The structural position is a faulted area known as the Franks fault zone (Suneson, 1997) (Figure 1.9). To the east of the Franks fault zone is the Franks Graben (which gradually merges with the Arkoma Basin further east), where mostly Middle-Upper Pennsylvanian rocks are exposed. To the west of the fault zone is the Hunton Anticline, which is approximately rectangular and exposes Lower-Middle Ordovician age rocks (Suneson, 1997).

The Clarita Shale Pit is located south of the city of Clarita and north of Bromide. The structural position is the Clarita Horst, which is bounded on the north by the Clarita Fault and to the south by the Bromide Fault (Figure 1.9). The Clarita Horst also dips slightly to the east, similar to that of the Lawrence Horst, exposing the older rocks to the west. Section FF' shows the cross-section line located near the Clarita Shale Pit (Figures 1.10A and 1.10B). The late Cambrian through early Mississippian deposits are thin compared to that of the Southern Oklahoma Aulacogen area (Suneson, 1997) indicating that the Clarita Horst is located outside the Aulacogen boundaries.

After Woodford-deposition, a major tectonic event, the Ouachita Orogeny, began around 350-330 mya (mid to late Mississippian) (Suneson, 1997). This was a major period of faulting and mountain building in southern Oklahoma and western Arkansas. The driving force behind this orogeny was the collision of the North

American and Gondwanan plates (Suneson, 2012). The Ouachita Orogeny also initiated the formation of the Arkoma Basin, which is an arcuate foreland basin (Byrnes and Lawyer, 1999). These Stonewall and Ahloso faults probably came into existence during the Savanna (Desmoinesian) Time (Barker, 1951), which was a time of major epeirogeny in Southern Oklahoma (Cooper, 1995). However, this area, including the Hunton Anticline is also thought to have been affected by the later mid-Virgilian Arbuckle Orogeny (Suneson, 1997).

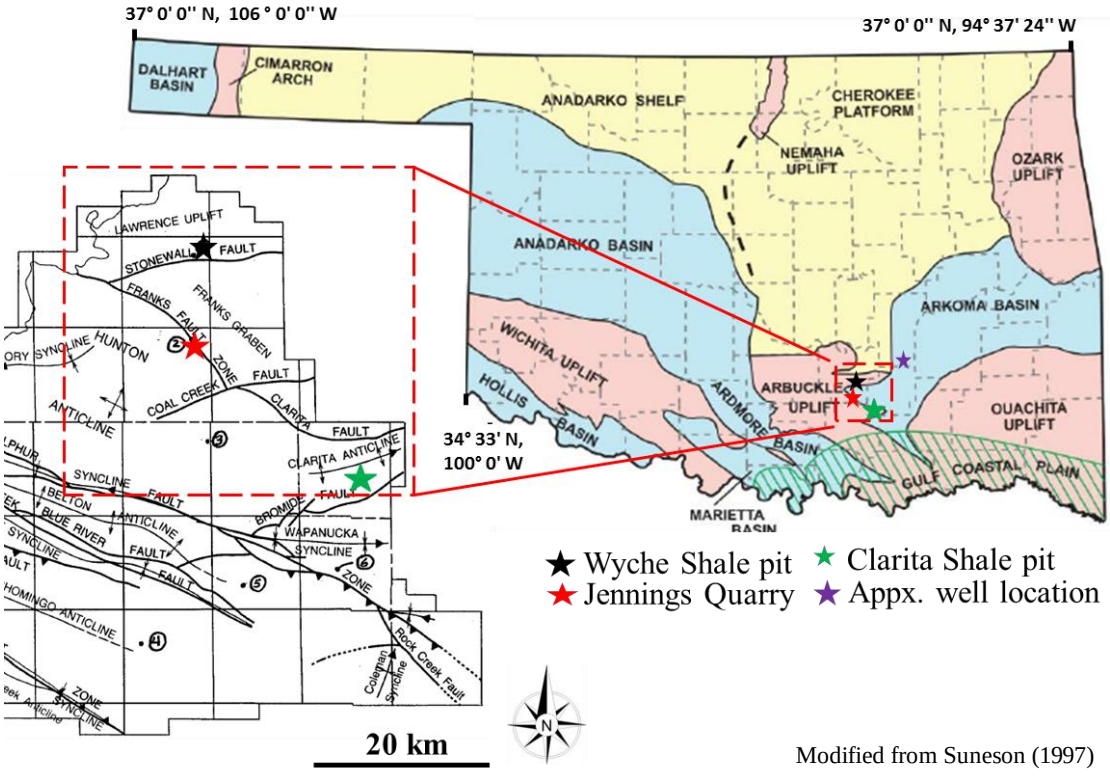

Modified from Suneson (1997)

Figure 1.9: Structural features of the field study areas are shown within the dashed rectangle. Star outside the rectangle is the approximate treatment well location.

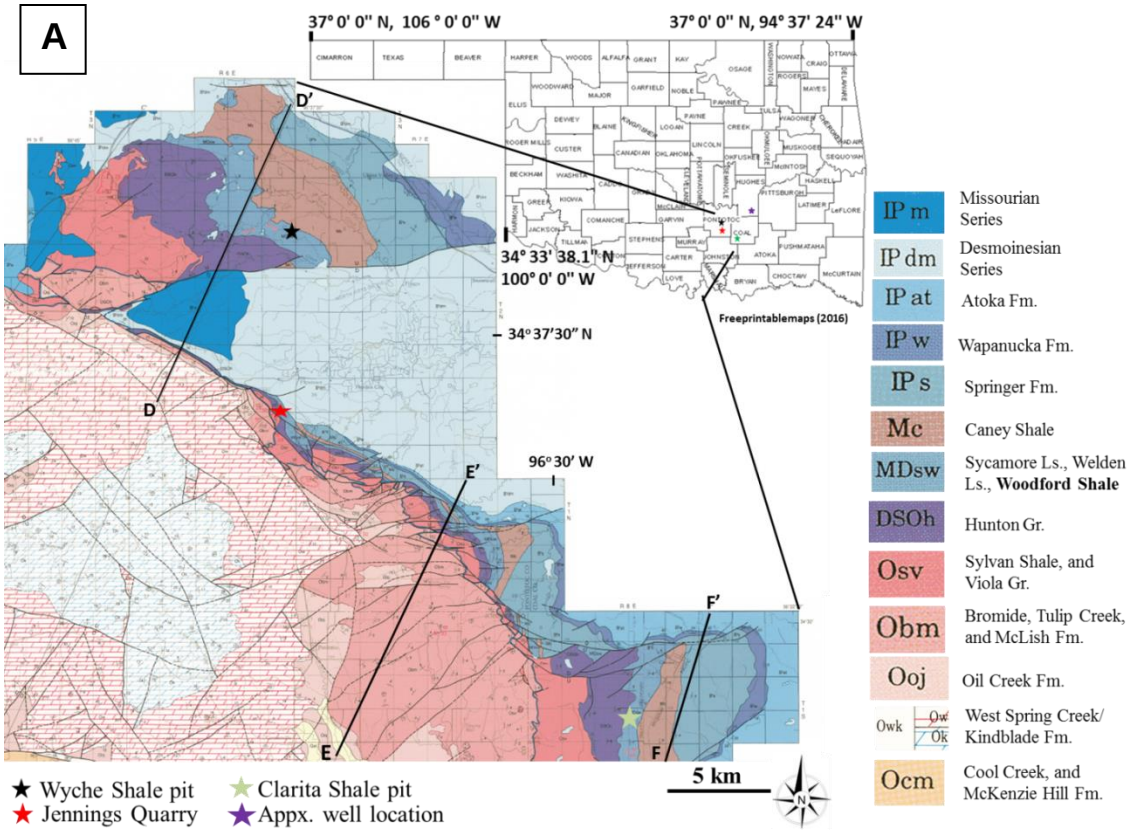

Modified from Ham and McKinley (1954); revised by Johnson (1990)

B

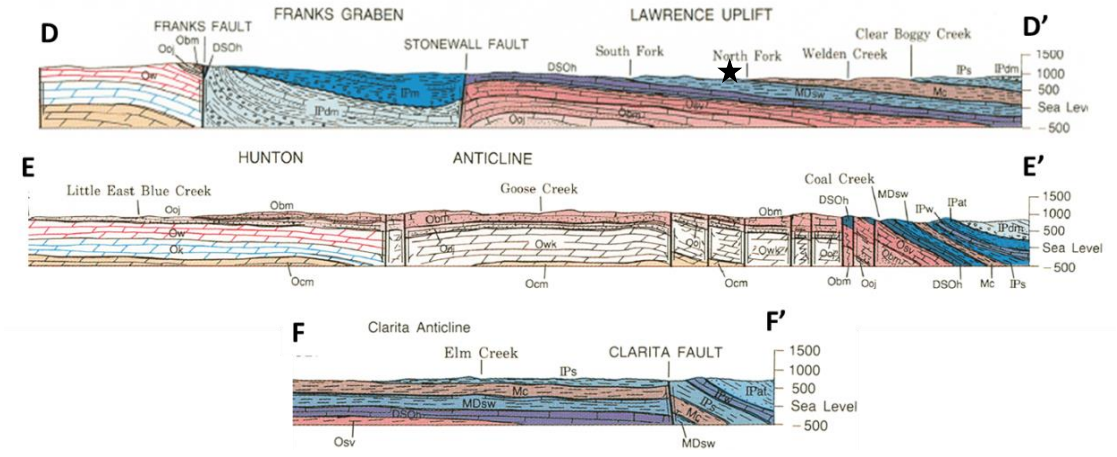

Modified from Ham and McKinley (1954); revised by Johnson (1990)

Figure 1.10: Geologic map of the eastern Arbuckle Mountains and the Lawrence Uplift. **A)** The Wyche Shale Pit, Jennings Quarry, and the Clarita Shale pit locations are marked both in the geologic map and on the map of Oklahoma in black, red, and green stars respectively. Notice the general NW-SE direction of bed strikes near the Wyche Shale Pit (dip < 10 degrees NE) and Jennings Quarry (variable dips), and N-S strike near the Clarita Shale pit (dip < 10 degrees E). Beds strike approximately N-S (at the treatment well location) and dip slightly towards the east. **B)** Cross sections along lines DD', EE', and FF'. Wyche Shale Pit is situated close to the DD' section and its approximate location in the cross section is shown using the black star shape.

The Cherokee Platform and the Ozark uplift to the north, and the Ouachita and the Arbuckle Uplifts to the south surround the Arkoma Basin in Oklahoma. As was shown in Figure 1.9, the well is located in the Arkoma Basin. The geologic formations confining the field microseismic cloud (shown later) are a subset of the ones shown in Figure 1.10A, i.e., the Caney Shale, Sycamore Limestone, Woodford Shale, Hunton Group Limestone, Sylvan Shale, Viola Group Limestone, and Bromide Formation. However, some researchers have referred to the formation just overlying the Caney Shale, i.e., the bottom-most part of the Springer Formation as the "False Caney" Formation (e.g., Andrews, 2003-2; Kamann, 2006) in the Arkoma Basin. Therefore,

both “Caney Shale” and “False Caney Shale” have been referred to as only “Caney Shale.” Additionally, only a few to a couple of tens of feet above the upper Woodford Shale and below the Sycamore Limestone is referred to as the “Welden Limestone”, “pre-Welden Shale”, “Welden Shale” etc. (e.g., Champlin, 1958; Kamann, 2006; Boardman et al., 2008; Puckette et al., 2010). These are not very well defined lithologic units and as mentioned earlier, referred to by different people under different names. Therefore, hereafter, only Sycamore Limestone and Woodford Shale are referred to without naming these intervening units.

Figure 1.11A shows the approximate elevation above mean sea level near the circled area (in arrow) in Fig 7B is nearly 700-800 ft. The top of the Hunton Group Limestone near the circle is approximately 7000 ft TVDSS. Adding the above values yield a value of 7700-7800 ft, which is close to the top of the Hunton Group Limestone. No other place in Hughes County matches the Hunton Group Limestone top this closely. Secondly, the Woodford Shale isopach thickness of 150 ft passes close to the circled area (Figure 1.11C). The Woodford Shale is approximately 150 ft thick near at the treatment well. Therefore, the well is most likely somewhere within or near the circled area. The Hunton Group Limestone (Figure 1.11D) and Sylvan Shale thicknesses (Figure 1.11E) are close to 90 and 100 ft respectively as seen from the contour lines.

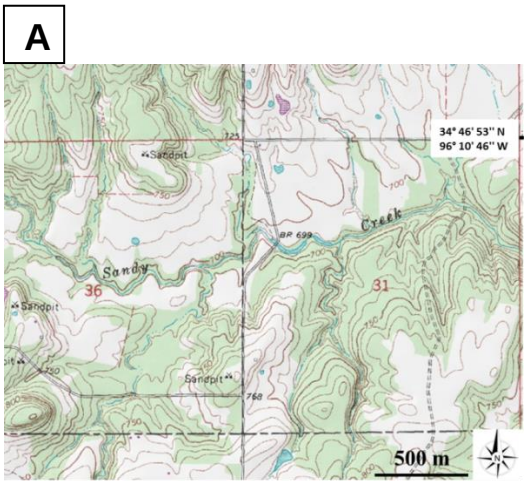

Mytopo (2016)

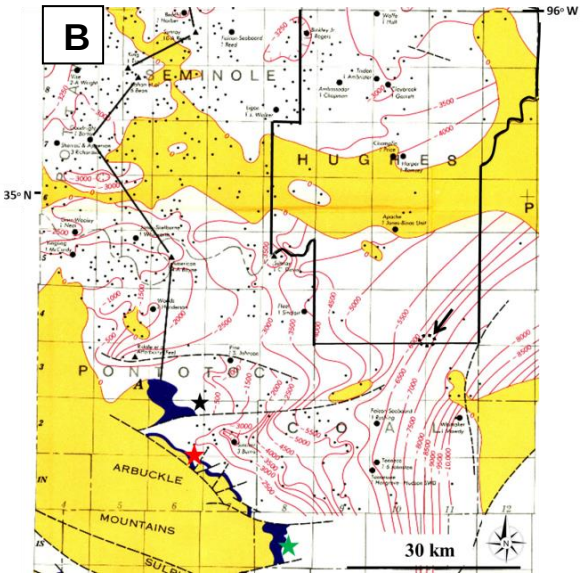

Modified from Amsden (1980-2)

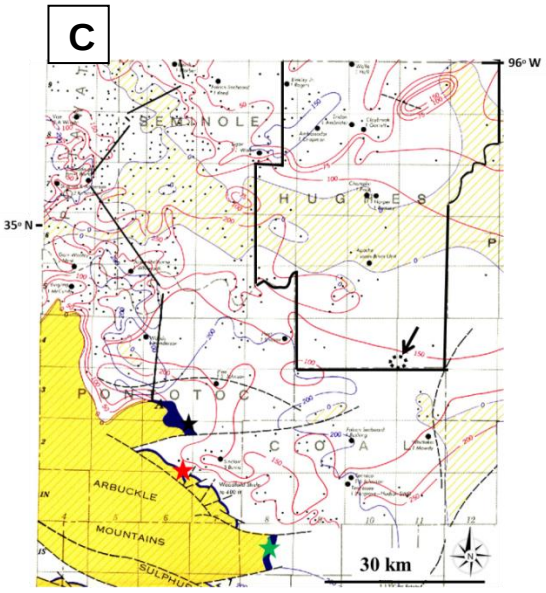

Modified from Amsden (1980-3)

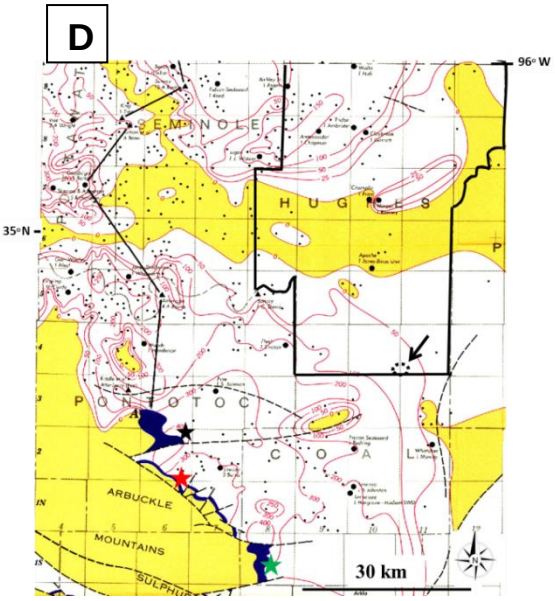

Modified from Amsden (1980-2)

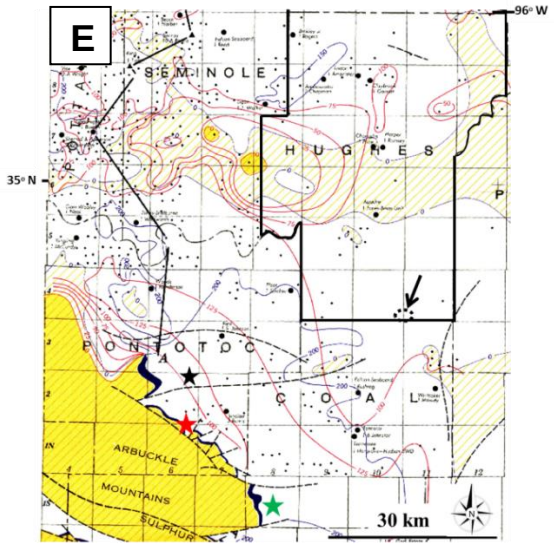

Modified from Amsden (1980-1)

Figure 1.11: Structure and isopach maps of the studied areas. **A)** Topographic map showing elevation above MSL (ft) in the area varies in the 700-800 ft range. **B)** Elevation (TVDSS) of the top of the Hunton Group Limestone. A likely location of the well is marked by the downward pointing arrow based on approximately 7900 ft TVD of the top of the Hunton Group Limestone in the treatment well. **C)** Woodford Shale thickness map. Notice that the Woodford Shale is nearly 150 ft thick at the well location. **D)** Hunton Group Limestone thickness map shows thickness between 50 and 100 ft near the circled area. **E)** Sylvan Shale thickness map shows thickness between 75 and 100 ft near the circled area.

1.4 Outcrop fracture parameterization

1.4.1 Fracture orientations

1.4.1.1 Shale

Portas (2009) measured outcrop Woodford Shale fracture orientations in the Wyche Shale Pit along two scanlines oriented along 318 degree and 005 degree azimuths on the floor in the Wyche Shale Pit. Most E-W fractures strike 075-090 degrees azimuth (histogram in Figure 1.12A). Some scatter is present on both sides of the 075-090 degrees fractures. Also, a peak in the NE direction (31-45) degree range is observed. However, the degree of scattering shown by Portas (2009) towards the NW direction (106-135 degrees) was not seen for the long (large) fractures in the Wyche

Shale Pit or the Clarita Shale Pit. At the Clarita Shale Pit, an average azimuth of 090 degrees along ten fractures was measured for the E-W fractures. In addition, Portas (2009) showed poles to fracture planes (Figure 1.12B) picked by software from image logs from a well nearby, which show two high pole density regions in the range of 030-055 and 075-095 degrees, similar to what was measured at the outcrop (Figure 1.12A). Partial quartz cementation was observed on all measured fractures. A few fractures had partial calcite cement as well.

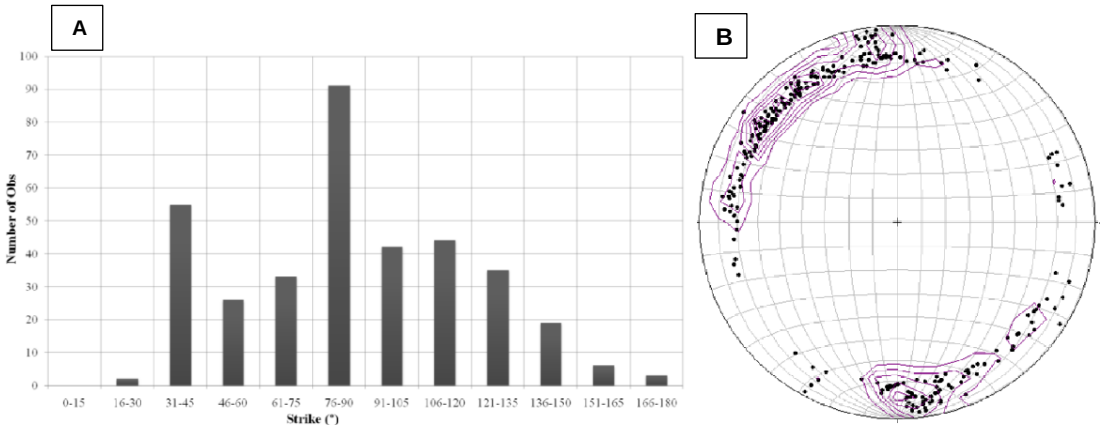

Portas (2009) Portas (2009)

Figure 1.12: Woodford Shale joint orientations. **A)** Fracture strikes measured in the Wyche Shale Pit (for the Woodford Shale) on the quarry floor using two scanlines by Portas (2009). **B)** Poles to fracture planes picked up by a software in an image log from a well near the Wyche Shale Pit (Portas, 2009).

1.4.1.2 Carbonate

Fracture orientations were measured along three scanlines exposed on the floor of the Jennings Quarry, two running along 320 degrees azimuth, and one running along 240 degrees azimuth. Figure 1.13A shows a rose diagram of the strikes. Unlike, the shale, three, perhaps four, sets are visible. The separation between the NW-SE and E-W sets is clear. A continuous range of fractures striking 000-035 degrees azimuth is also seen which can be considered two sets (N-S and a NE-SW) or one set, depending on the

interpreter. Poles to fracture planes are shown in Figure 1.13B. Since only fracture traces and not faces were available for measurements on the quarry floor, only fracture strikes were measured, i.e., fracture dips could not be measured. Therefore, the dips needed to represent the poles were randomly assigned between 75-90 degrees for better visualization on the stereonet in Figure 1.13B. Assigning 90 degrees dips to all fractures would result in poles plotting one above the other, making the distribution look uniform around the circumference of the stereonet. In the Hunton Group Limestone, all fractures are partial to fully cemented with calcite.

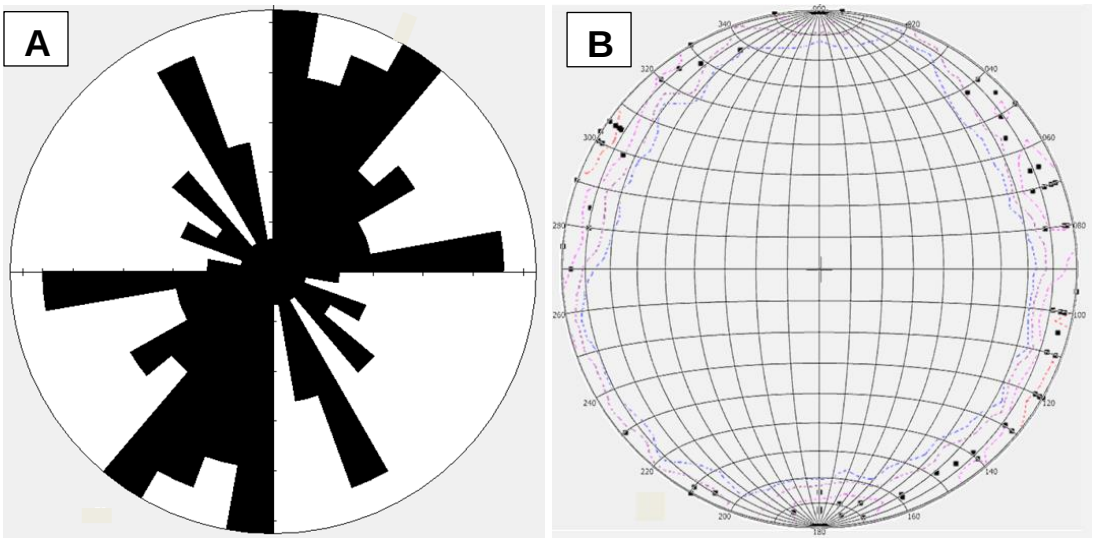

Figure 1.13: Hunton Group joint orientations. **A)** Fracture strikes measured in the Jennings Quarry (for the Hunton Group Limestone) on the quarry floor using three scanlines. **B)** Poles to fracture planes for same fractures in A. Note that the poles were randomly assigned between 75-90 degrees for clarity since fracture faces were not available for dip measurement.

1.4.2 Fracture sizes

This section describes the fracture heights, spacings, lengths, and aperture distribution from the outcrops.

1.4.2.1 Shale

The Wyche Shale Pit and the Clarita Shale Pit were studied for the shales, and the Jennings Quarry was studied for the carbonates/limestones. Examples of photographs for fracture heights and lengths were shown earlier (Figures 1.4A, 1.4B, 1.4D, 1.4F, 1.6A, 1.6B, 1.6C, 1.6E, 1.6G, and 1.6I).The length vs. height distribution contains fractures from all sets as not many well-exposed faces showing substantial lengths and heights were available. Fracture lengths vs. height relations were tested for best fit using either a linear or a power-law distribution. Other distributions did not fit the data as closely as the linear or power-law fits. The fit with the highest R^2 value (among linear and power-law fits) was chosen for deriving individual fracture lengths for a given height distribution. The power-law equation was chosen for the shales (Figure 1.14H). In the Woodford Shale, however, the R^2 values for the linear and power-law equations are almost identical.

For the Woodford Shale, the length vs. height relation derived from the equation: length = 2.83*height^0.8533 found at the Wyche Shale Pit walls, underpredicts the lengths based on the heights. For example, the maximum and average measured lengths of E-W fractures measured at the Clarita Shale Pit were 27.5 m, and 15.5 m respectively. However, the maximum length based on the measured height at the Wyche Shale Pit using equation length = 2.83*height^0.8533 give a maximum length of 11.3 m and an average of 5.5 m. Therefore, in this equation lengths (y-axis in Figure 1.14H) were multiplied by two to make the length values comparable to that in Clarita Shale Pit. The linear equation now becomes: length = 5.657*height^0.8533. The maximum and average heights now become 22.5 m and 11 m. The initial equation could

have been multiplied by 2.5 to get the length values closer to that of the Clarita Shale Pit. However, as discussed earlier, due to a possibility that some long (large) fractures that were interpreted to be transecting the debris cover could actually have been two different fractures led to only doubling the measured fracture lengths.

Except for the E-W set apertures in the Woodford Shale which show a power-law best fit (Figure 1.14E), all other sizes fit either an exponential (Figures 1.14B, 1.14D, 1.14F) or lognormal (Figures 1.14A, 1.14C, 1.14G) distribution, which are both categorized as characteristic size distributions (Hooker, 2014). The coefficient of variation ($C_v = \sigma_{spacing} \div \mu_{spacing}$) values is less than 1 in cases where spacing was measured, which is defined by Gillespie et al. (1999) as less than randomly spaced, (i.e., fractures are evenly spaced). The measured heights and calculated length distribution of the E-W and NE-SW fractures in shales show considerable differences in the mean and maximum values (Table 1.1).

Table 1.1: Fracture height, aperture, length, and spacing in the Woodford Shale. All fractures are bed-normal. The number of fractures (NF) used to calculate the parameters for both short and long (large) fractures are shown. **Abbreviations- FS:** fracture-size classification (long [large]: fractures with height > 1 m, short: fractures with height < 1 m), **ND:** normal distribution χ^2 error, **LND:** lognormal distribution χ^2 error, **PLD:** power-law distribution χ^2 error, **EXD:** exponential distribution χ^2 error **(**distribution showing the lowest χ^2 error [best fit] in each case is in bold), **PLD exp**: exponent of the power-law distribution, **EXD exp**: exponent of the exponential distribution, **NF:** number of fractures, **Int.**: areal intensity (fractures/m), **C_v:** coefficient of variation ($\sigma_{spacing} \div \mu_{spacing}$), **Loc.**: location, **WSP:** Wyche Shale pit, **CSP:** Clarita Shale pit, **Dash (-)**: not applicable or not available**.**

Shale	FS	ND	LND	PLD	EXD	PLD exp	EXD exp	NF	Int.	Mean (Aver.)	Stdev	Min	Max	Cv	Loc.
E-W height (m)	**Long**	0.07	**0.013**	0.39	0.11	-2.1	-1	74	0.256	2.19	0.893	1	5	-	WSP
	Short	0.9	0.337	0.36	**0.03**	-2.6	-4.6	54	0.33	0.517	0.19	0.302	1	-	WSP
NE-SW height (m)	**Long**	0.11	**0.06**	0.16	0.08	-5.4	-4.1	36	0.282	1.31	0.209	1	1.84	-	WSP
	Short	2.79	1.08	1.8	**0.3**	-3	-5.5	76	0.77	0.511	0.166	0.304	1	-	WSP
E-W aperture (mm)	**Long**	27.04	0.48	**0.4**	0.45	-1.6	-1.3	30	-	0.84	0.6	0.265	3.3	0.74 (1.2 ÷1.6)	CSP
	Short	-	-	-	-	-	-	-	-	-	-	-	-	-	-
NE-SW aperture (mm)	**Long**	3.60E+06	6.23	10.9	**0.6**	-0.87	-0.48	55	-	2.05	1.83	0.265	10	0.57 (0.15 ÷ 0.26)	WSP
	Short	11.7	**5.44**	15.3	6.54	-1.5	-7.7	21	-	0.22	0.099	0.075	0.5	0.54 (1.4÷ 2.6)	CSP
E-W lenght (measured)	**Long**	-	-	-	-	-	-	28	-	15.5	5.8	5.2	27.5	-	CSP
E-W lenght 2X(calculated)	**Long**	-	-	-	-	-	-	72	-	11	3.5	5.7	22.5	-	WSP
NE-SW length 2X(calculated)	**Long**	-	-	-	-	-	-		-	7.1	0.96	5.7	9.5	-	WSP

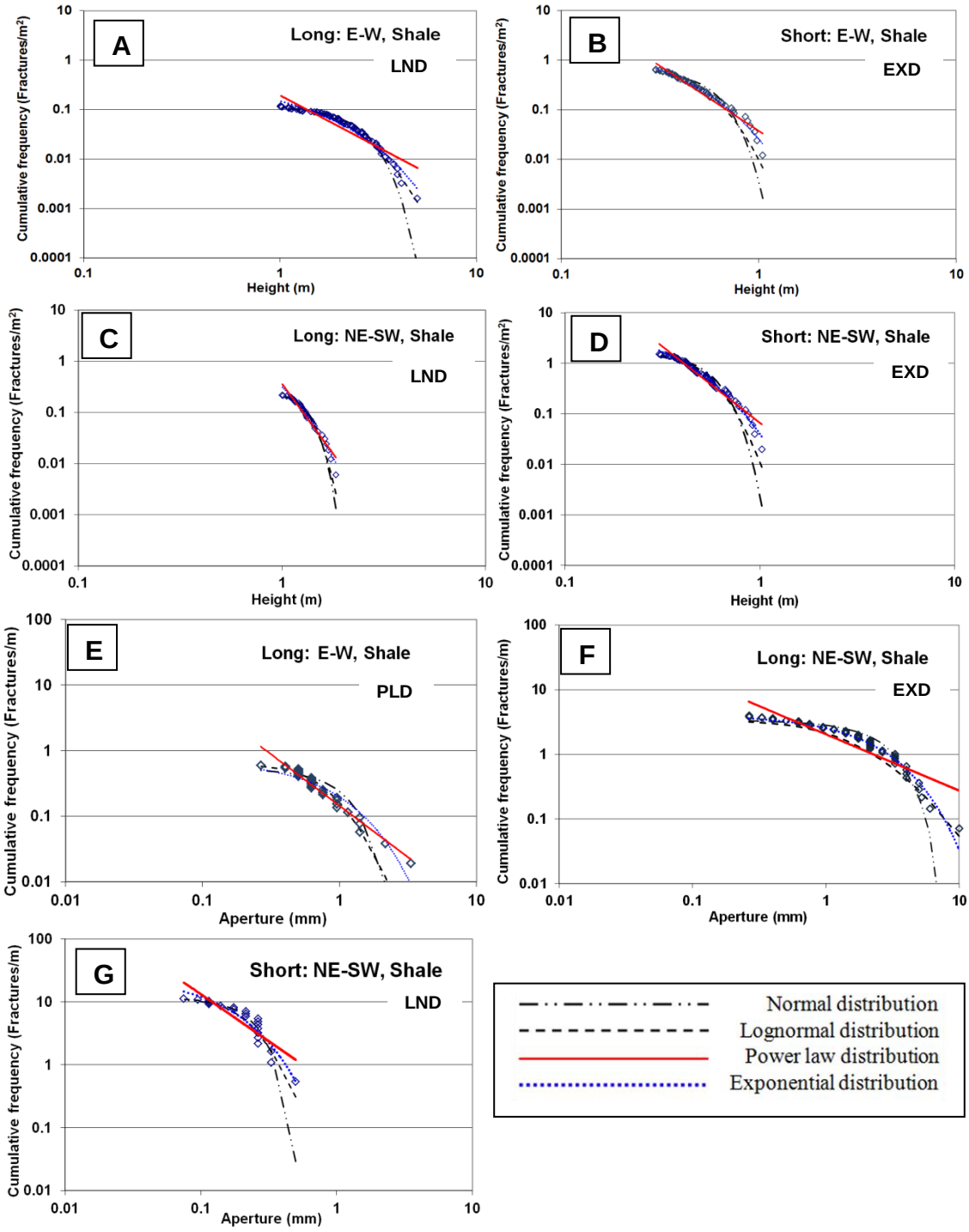
A
Long: E-W, Shale
LND
B
Short: E-W, Shale
EXD
C
Long: NE-SW, Shale
LND
D
Short: NE-SW, Shale
EXD
E
Long: E-W, Shale
PLD
F
Long: NE-SW, Shale
EXD
G
Short: NE-SW, Shale
LND
Cumulative frequency (Fractures/m²)
Cumulative frequency (Fractures/m)
Height (m)
Aperture (mm)
Normal distribution
Lognormal distribution
Power law distribution
Exponential distribution

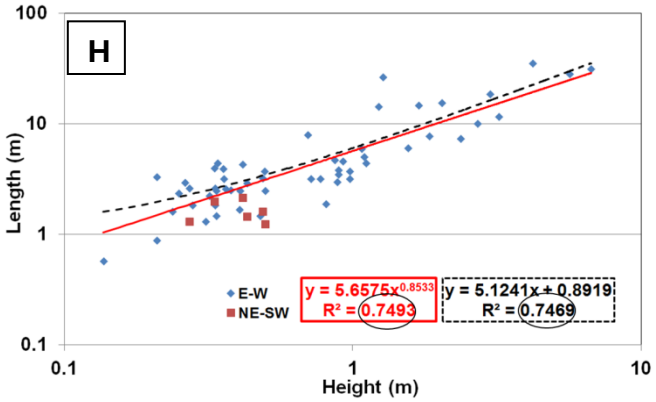

Figure 1.14: Height and aperture distributions measured in the Woodford Shale. Best fit cumulative distributions (**EXD**: exponential; **LND**: lognormal; **PLD**: power-law) are mentioned in the figures. **A)** Height distribution of E-W striking fractures with height > 1 m. **B)** Height distribution of E-W striking fractures with height < 1 m. **C)** Height distribution for NE-SW striking fractures with height > 1 m. **D)** Height distribution for NE-SW striking fractures with height < 1 m. **E)** Aperture distribution for E-W fractures with height > 1 m. **F)** Aperture distribution for NE-SW fractures with height > 1 m. **G)** Aperture distribution for NE-SW fractures with height < 1 m (not used in the simulation but shown). **H)** Corrected length vs. height distribution of the Woodford Shale fractures. The measured lengths at the Wyche Shale Pit were multiplied by two (for correction) to obtain length values closer to that measured in the Clarita Shale Pit. The R^2 values are almost the same for both power-law and linear fits.

Modified from Ataman (2008)

Figure 1.15: Long, continuous fractures in the Woodford Shale. Brunton for scale pointed by an arrow.

1.4.2.2 Carbonate

The Jennings Quarry was studied for the carbonates/limestones. Except NW-SE set heights in the Hunton Group Limestone, which shows both a power-law, as well as exponential best fit (Figure 1.16C, Table 1.2), all others fit an exponential distribution (Figures 1.16A, 1.16B, 1.16D, and 1.16E). The coefficient of variation ($C_v = \sigma_{spacing} \div \mu_{spacing}$) values, like those of shales, are < 1 in cases where spacing was measured, which as defined by Gillespie et al. (1999) as less evenly spaced or less than randomly spaced. The difference in the mean and maximum values in the measured heights and calculated lengths of the E-W, NE-SW (N-S), and NW-SE fractures in the Hunton Group Limestone do not show considerable differences (Table 1.2).

For the carbonates, unlike shales, the fracture lengths measured from the walls were not doubled because the limestone fractures are not as long and continuous as in the shales (Figure 1.17). The fit with the highest R^2 value was chosen, which is the linear equation for the carbonates (Figure 1.16F).

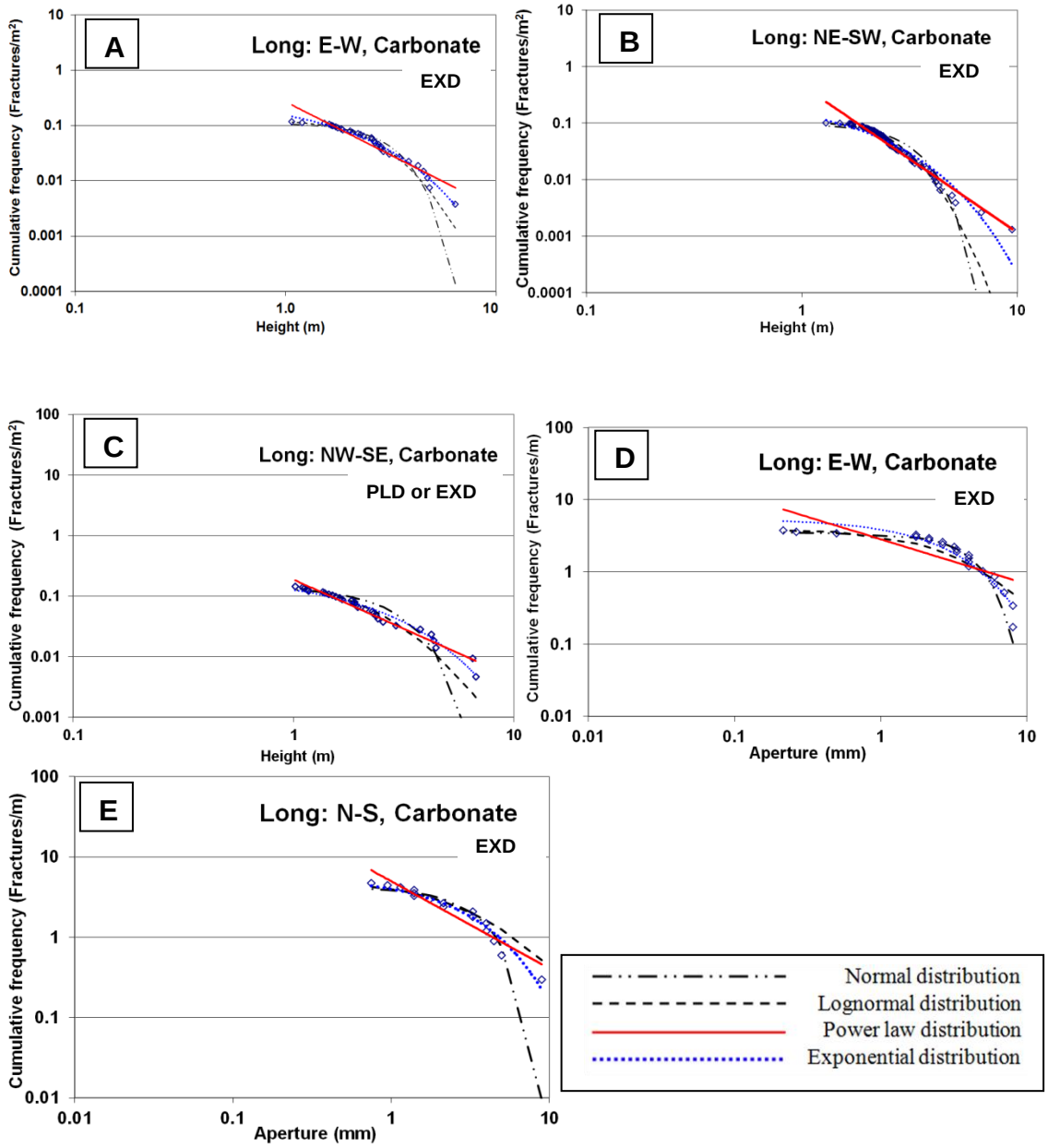

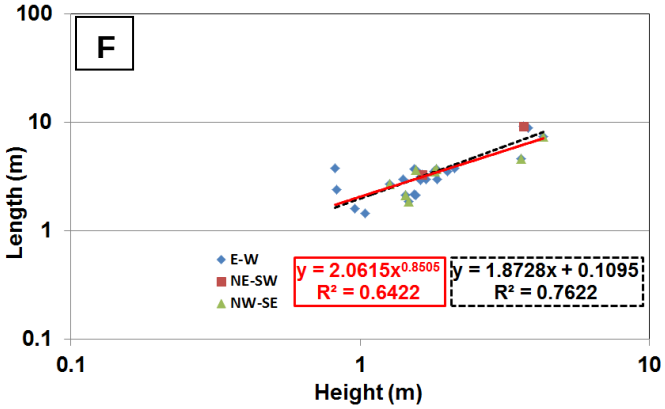

Figure 1.16: Height and aperture distribution measured in the Hunton Group Limestone. Best fit cumulative distributions (**EXD**: exponential; **PLD**: power-law) are mentioned in the figures. **A)** Height distribution for E-W striking fractures with height > 1 m. **B)** Height distribution of NE-SW striking fractures with height > 1 m. **C)** Height distribution of NW-SE striking fractures with height > 1m. **D)** Aperture distribution for E-W fractures with height > 1 m. **E)** Aperture distribution for N-S fractures with height > 1 m. **F)** Length vs. height distribution in the Hunton Group Limestone.

Table 1.2: Fracture height, aperture, length, and spacing in the Hunton Group Limestone. The number of fractures (**NF**) used to calculate the parameters for both short and long fractures are shown. **Abbreviations- FS:** fracture-size classification (long [large]: fractures with height > 1 m, short: fractures with height < 1 m), **ND:** Normal distribution χ^2 error, **LND:** Lognormal distribution χ^2 error, **PLD:** power-law distribution χ^2 error, **EXD:** exponential distribution χ^2 error **(**distribution showing the lowest χ^2 error [best fit] in each case is in bold), **PLD exp**: exponent of the power-law distribution, **EXD exp**: exponent of the exponential distribution, **NF:** number of fractures, **Int.**: areal intensity (fractures/m), **C_v:** coefficient of variation ($\sigma_{spacing} \div \mu_{spacing}$), **Loc.**: location, **JQ**: Jennings Quarry, **Dash (-)**: not applicable or not available.

Carbonate	FS	ND	LND	PLD	EXD	PLD exp	EXD exp	NF	Int.	Mean (Aver.)	Stdev	Min	Max	Cv	Loc.
E-W height (m)	**Long**	0.14	0.022	1.22	**0.017**	-1.9	-0.69	31	0.328	2.7	1.21	1.07	6.4	-	JQ
NE-SW height (m)	**Long**	855	0.253	0.17	**0.088**	-2.6	-0.22	77	0.279	2.79	1.21	1.3	9.48	-	JQ
NW-SE height (m)	**Long**	0.46	0.052	**0.0388**	**0.0384**	-1.6	-0.56	34	0.344	2.23	1.43	1	6.72	-	JQ
E-W aperture (mm)	**Long**	1.23	2.13	9.34	**1.61**	-0.6	-0.34	22	-	3.6	2.28	0.215	8	0.81 (0.74÷0.91)	JQ
N-S aperture (mm)	**Long**	9.35	1.02	6.58	**0.49**	-1.1	-0.36	16	-	2.88	2.12	0.75	9	0.63 (0.54÷0.85)	JQ
NW-SE aperture (mm)	**Long**	-	-	-	-	-	-	-	-	-	-	-	-	-	-
E-W aperture (mm)	**Short**	-	-	-	-	-	-	18	-	0.43	0.21	0.14	0.75	0.56 (0.09÷0.16)	JQ
NE-SW aperture (mm)	**Short**	-	-	-	-	-	-	31	-	0.41	0.33	0.095	1.4	0.71 (0.12÷0.16)	JQ
NW-SE aperture (mm)	**Short**	-	-	-	-	-	-	17	-	0.52	0.62	0.14	2.65	0.82 (0.09÷0.11)	JQ
E-W length (calculated)	**Long**	-	-	-	-	-	-	31	-	5.2	2.3	2.1	12.1	-	JQ
NE-SW lenght (calculated)	**Long**	-	-	-	-	-	-		-	5.3	2.3	2.5	17.8	-	JQ
NW-SE length (calculated)	**Long**	-	-	-	-	-	-	31	-	4.6	2.8	2	12.7	-	JQ

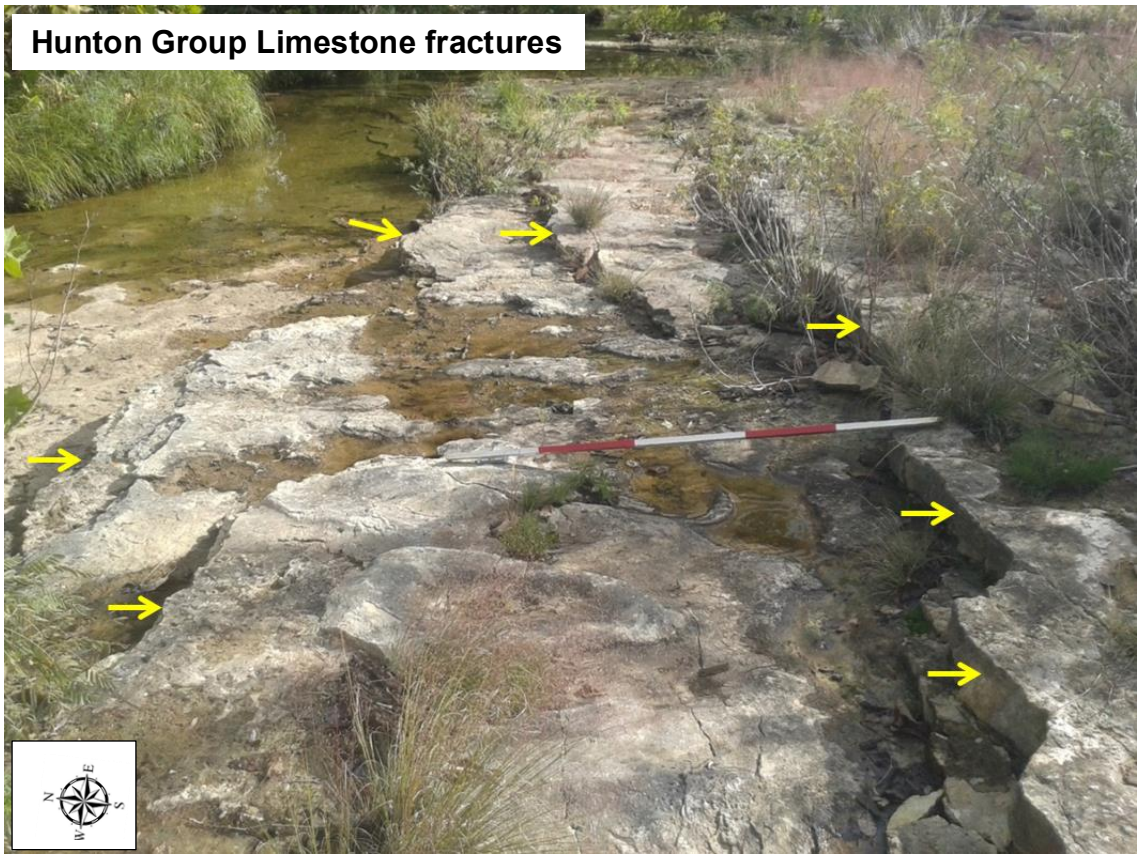

Figure 1.17: A Hunton Group Limestone exposure located 1 km south (34°39'43.5"N, 96°38'33.8"W) of the Wyche Shale Pit. Notice that the fractures (in arrows) are not as smooth and continuous as the shale fractures shown in Figure 1.15.

1.5 DFN static modeling in FracMan

1.5.1 Fracture orientation for static DFN model

1.5.1.1 Shales

For the Woodford Shale E-W fractures, the bivariate-normal distribution, with the parameters shown in Figure 1.18B, accommodates the scatter around an average strike of 085 degrees (mean pole orientation of 355 degrees). This distribution also accommodates dip scatter of ~ 10 degrees along both sides of the vertical. For the NE-SW fractures, an average strike of 043 degrees (mean pole orientation of 313 degrees) was chosen with the same bivariate normal parameters (Figure 1.18C) to accommodate

the scatter around the mean. The majority of the NE-SW striking fractures in the Clarita Shale Pit strike between 035-040 degrees. Contours in Figures 1.18B and 1.18C cover the high pole density areas in Figure 1.18A (same as Figure 1.12B), which were recorded by a software from image logs in a well near the Wyche Shale Pit.

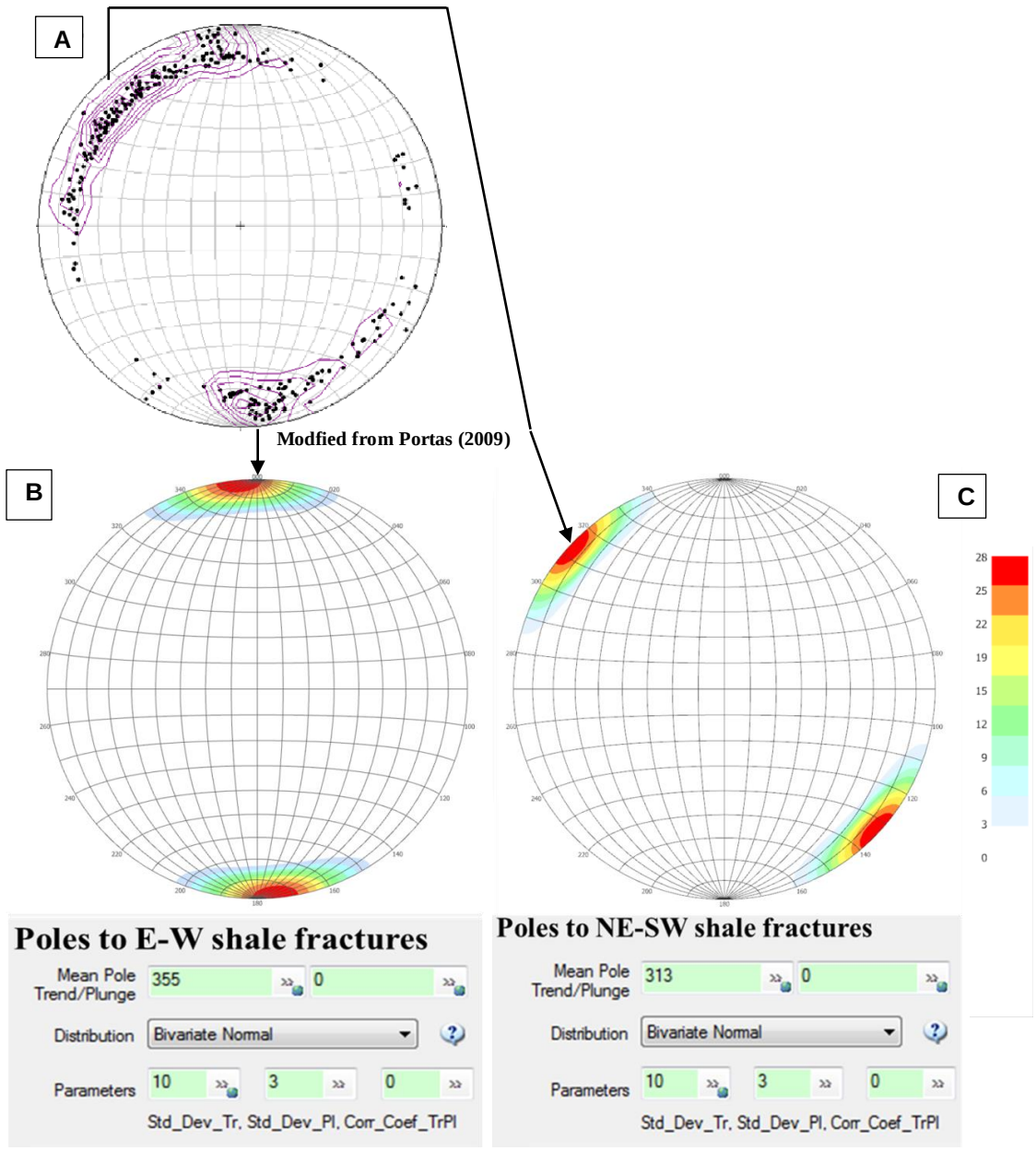

Figure 1.18: Comparison of measured and modeled fracture orientations in the Woodford Shale. **A)** Poles to fracture planes recorded near the Wyche Shale Pit. **B)** Steronet showing contours (Schmidt) of the poles to modeled E-W fracture set in FracMan^{TM}. **C)** Steronet showing contours (Schmidt) of the poles to the modeled NE-SW fracture set in FracMan^{TM}.

1.5.1.2 Carbonates

In the Hunton Group Limestone, the E-W and NW-SE fractures were assigned using different orientations but same bivariate normal distribution parameters used in the shales (Figure 1.19B and Figure 1.19D respectively). The N-S and NE-SW fractures were assigned at once, using a bivariate fisher distribution (Figure 1.19C). Figure 1.19C shows that the contours are oriented such that fracture strikes are scattered around means of 008 and 032 degrees azimuth. Figure 1.19D shows the contours of the poles to the NW-SE fractures. Same orientation was used for the Sylvan Shale NW-SE fractures. The contours showed in Figures 1.19B, 1.19C, and 1.19D approximately match the pole locations in Figure 1.19A (same as Figure 1.13B).

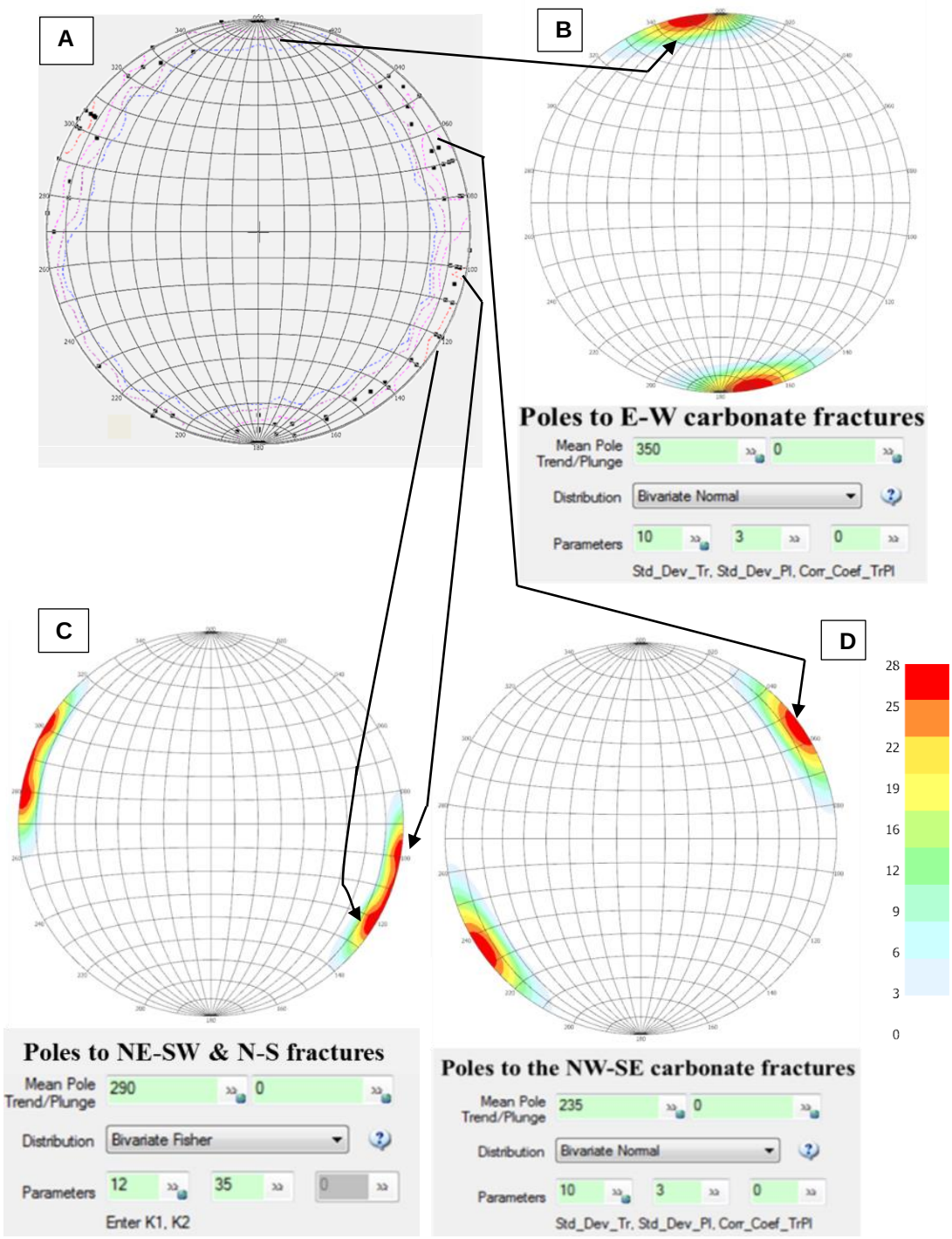

Figure 1.19: Comparison of measured and modeled fracture orientations in the Hunton Group Limestone. **A)** Same as Figure 1.13B, i.e., poles to fracture planes measured in the Jennings Quarry (for the Hunton Group Limestone) on the quarry floor. **B)** Seteronet showing contours (Schmidt) of the poles to the E-W fracture set used in FracMan^{TM}. **C)** Seteronet showing contours (Schmidt) of the poles to the NE-SW and N-S fracture set in FracMan^{TM}. **D)** Seteronet showing contours (Schmidt) of the poles to modeled NW-SE fracture set in FracMan^{TM}.

1.5.2 Fracture size for static DFN model

Ideally, it is preferable to measure each fracture set separately for each formation on flat outcrops, as close as possible to the well location. However, as mentioned earlier, only three such outcrops were available, two for the Woodford Shale and one for the Hunton Group Limestone. Therefore, shale and carbonate fracture intensities, apertures, heights, and length-height relations were assigned based on the measurements in the Woodford Shale and the Hunton Group Limestone observations. Additionally, NW-SE fracture sets were not observed in the Woodford Shale but are present in substantial number in the Hunton Group Limestone. The crosscutting relations studied at the Jennings Quarry floor, at a few places indicated that the NW-SE fractures could be older than the other sets. Therefore, possibly they are also present in the Sylvan Shale, located stratigraphically below the Hunton Group Limestone. Therefore, the NW-SE set was included in the Sylvan Shale with intensities similar to that in the E-W set in the Woodford Shale, and orientation similar to that in the Hunton Group Limestone.

Tables 1.3 and Table 1.4 show the input values of fracture sizes used in FracMan^{TM}. All distributions were assigned based on the distributions observed at the outcrops, except the E-W set apertures in the shales and NW-SE set heights in the limestones. In both cases, the power-law and the exponential $\chi 2$ errors are close to each other (Figure 1.14E and Figure 1.16C; Table 1.1 and Table 1.2). Except for these two distributions, all others follow either exponential or lognormal distributions. There was a low confidence on the power-law exponent for these two cases, and the software had trouble generating these fractures upon application of power-law distribution.

Therefore, exponential distribution, which has similar χ^2 errors as that of the power law, was chosen in both cases. Another, reason for using an exponential distribution is that even the fractures with height < 1m, which are not truncated, show closer fits with the exponential distribution (Figures 1.14B and 1.14D). Therefore, the possibility that the truncated fracture heights (i.e., fractures with height > 1m) might also be exponentially distributed is reasonable.

Table 1.3: FracMan^{TM} inputs used for long (or large) shale fractures (height > 1m).

Shale	**Long E-W**	**Long NE-SW**	**Long NW-SE (for Sylvan Sh. only)**
Fracture areal intensity (P32: fractures/m)	0.256	0.282	Same as E-W set
Fracture height (m)	**Distr.**: Lognormal **Mean**: 2.190 **Dev.** : 0.893 **Min.** : 1.000 **Max.** : 5.000	**Distr.**: Lognormal **Mean**: 1.310 **Dev.** : 0.209 **Min.** : 1.000 **Max.** : 1.840	Same as E-W set
Fracture length (m) formula	5.657*height^0.8533	5.657*height^0.8533	Same as E-W set
Fracture aperture (mm)	**Distr.**: Exponential **Mean**: 0.843 **Min.** : 0.265 **Max.** : 3.300	**Distr.**: Exponential **Mean**: 2.047 **Min.** : 0.265 **Max.** : 10.000	Same as E-W set

Table 1.4: FracMan^{TM} inputs used for long (or large) carbonate (limestone) fractures (height > 1 m).

Carbonate	**Long E-W**	**Long NE-SW and N-S**	**Long NW-SE (for Hunton Group, Viola Group, and Bromide Gr.; Sycamore Limestone excluded)**
Fracture areal intensity (P32: fractures/m)	0.328	0.279	0.344
Fracture height (m)	**Distr.**: Exponential **Mean**: 2.700 **Min.**: 1.070 **Max.**: 6.400	**Distr.**: Exponential **Mean**: 2.790 **Min.**: 1.300 **Max.**: 9.480	**Distr.**: Exponential **Mean**: 2.230 **Min.**: 1.000 **Max.**: 6.720
Fracture length (m) formula	1.873*height + 0.1095	1.873*height + 0.1095	1.873*height + 0.1095
Fracture aperture (mm)	**Distr.**: Exponential **Mean**: 3.630 **Min**: 0.215 **Max**: 8.000	**Distr.**: Exponential **Mean**: 2.880 **Min**: 0.750 **Max**: 9.000	Same as E-W set (since height parameters are closer to the EW set)

1.5.3 Static DFN model

Based on the information on fracture orientations and that presented in Tables 1.3 and 1.4, a DFN model was generated (Figures 1.20A and 1.20B). Both the west and north cross-section views are presented. Each color in the DFN represents a fracture set in the seven formations. This DFN model is used for understanding natural fracture connectivity to the wellbore and clusters present. It has also been used to perform microseismic cloud (MC) geometry matches in three hydraulic fracture stages. Subsequently, the effects of well location, tectonic strain (related to Shmin and SHmax), fracture fluid efficiency, ISIP (net pressure), pressure-drop slope, and fracture abundance (with half the intensity in the current model) on the reactivated fractures and accompanying hydraulic fractures have been simulated ("Dynamic Simulation" section).

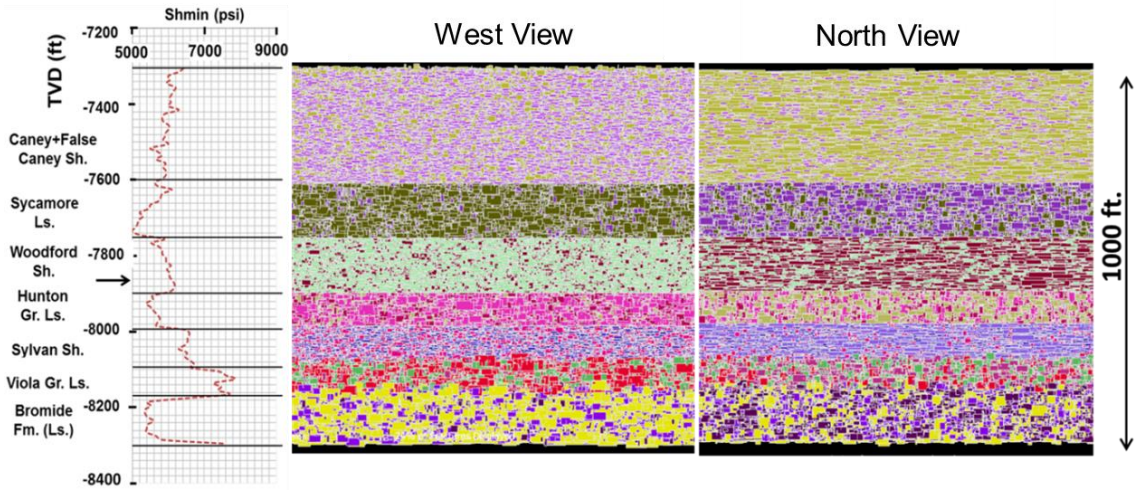

Figure 1.20: Static DFN model looking west and north. Notice that in carbonates, the fractures have lower aspect ratios (height ÷ length) compared to that in the shale. Fracture dimensions from Woodford Shale were applied to all shale, and fracture dimension from Hunton was applied to all carbonates.

1.5.4 Fracture clusters

Cluster analysis helps visualize compartmentalization in the DFN (discrete fracture network) model. Natural fracture cluster analysis was performed to assess the connectivity between the fractures themselves and that to the wellbore. In this study, both fracture sets in the Woodford Shale were included. Figure 1.21A shows the main cluster, with 1,908,961 fractures (Table 1.5), and several (13) barely visible smaller clusters of 20 or more fractures. Figure 1.21B shows the small clusters with the main cluster removed for better visibility. A connectivity analysis, performed for the fractures connected to the wellbore, also reveals the same main cluster with the same number of fractures (1,908,961). Performing cluster analysis for greater than 100 or 1000 fractures per cluster, only the main cluster (i.e., more than 1.9 million fractures) remains. Therefore, practically, there is only one cluster, i.e., the DFN can be considered fully connected.

The same analysis was also performed with fracture intensities halved in both sets. Figure 1.21C shows the 3237 clusters of 20 or more fractures in the Woodford Shale (compared to just 13 clusters of 20 more fractures in the base case). Figure 1.21D shows the same 3236 fracture clusters, i.e., without the main cluster (orange: 333,372 fractures) in Figure 1.21C. Figures 1.21E and 1.21F show the 395 clusters (of 100 or more fractures [Table 1.5]) and 17 clusters (of 1000 or more fractures [Table 1.5]), both without the main cluster for clear visualization. Figures 1.21G and 1.21H show the main cluster and the fractures connected to the wellbore. Both are the same entities, i.e., the main cluster is the one connected to the wellbore (same as the base case). Figures 1.21A and 1.21H show that if the intensity is reduced to half the original (base case), the DFN is not fully connected anymore, i.e., there are significant number of disconnected clusters containing more than 20 fractures (Figure 1.21C), with several of them containing hundreds and thousands of fractures.

Cluster analysis was performed for formations with more than two sets, i.e., those below the Woodford Shale. Considering the base case intensities, the formations below the Woodford Shale are fully connected due to the presence of 3-4 sets, considering a minimum of 20 fractures and more. Table 1.6 shows an example of cluster analysis performed at half the fracture intensity, in addition to the base case intensities, in the Hunton Group. For the half fracture intensity case, only four clusters of 20 or more fractures exist (Figures 1.21I and 1.21J). There is only one cluster of 100 or more fractures (Figure 1.21I), i.e., the one connected to the wellbore. Therefore, both the base case and the half intensity cases can be considered as fully connected DFNs when more than two fracture sets are present.

A

Woodford: Base case intensity (minimum of 20 fractures)

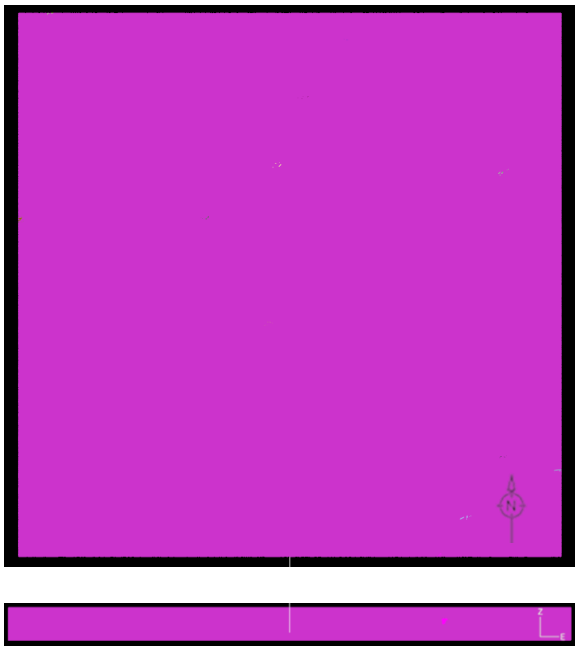

B

Woodford: Base case intensity (minimum of 20 fractures) without main cluster

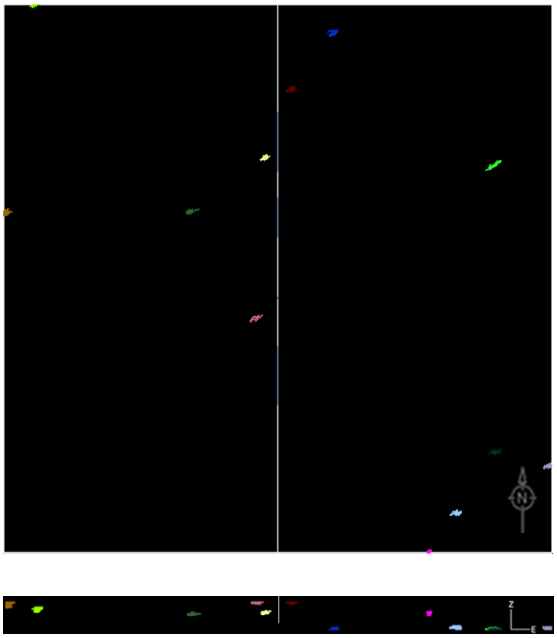

C

Woodford: Half intensity (minimum of 20 fractures)

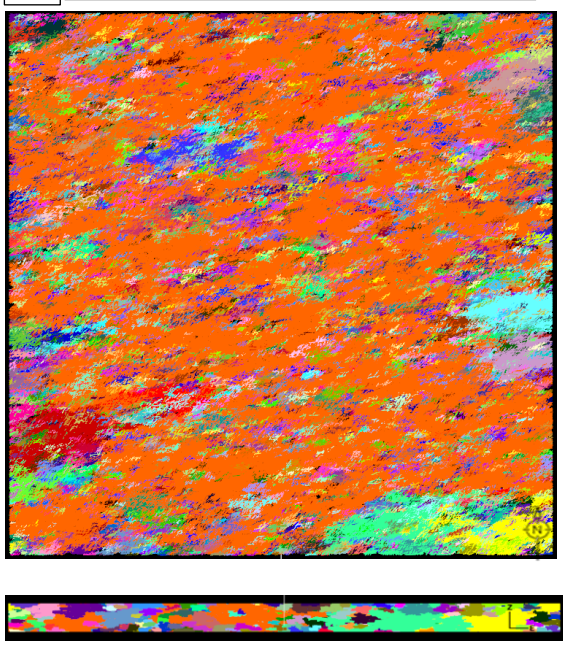

D

Woodford: Half intensity (minimum of 20 fractures) without main cluster

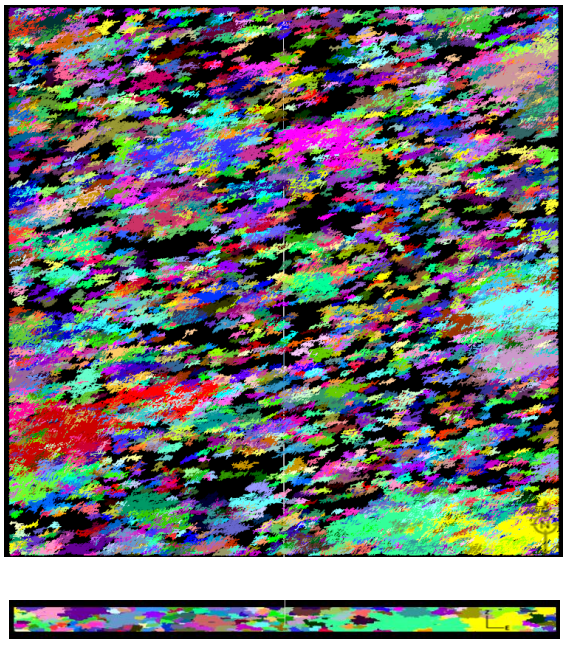

E Woodford: Half intensity (minimum of 100 fractures) without main cluster

F Woodford: Half intensity (minimum of 1000 fractures) without main cluster

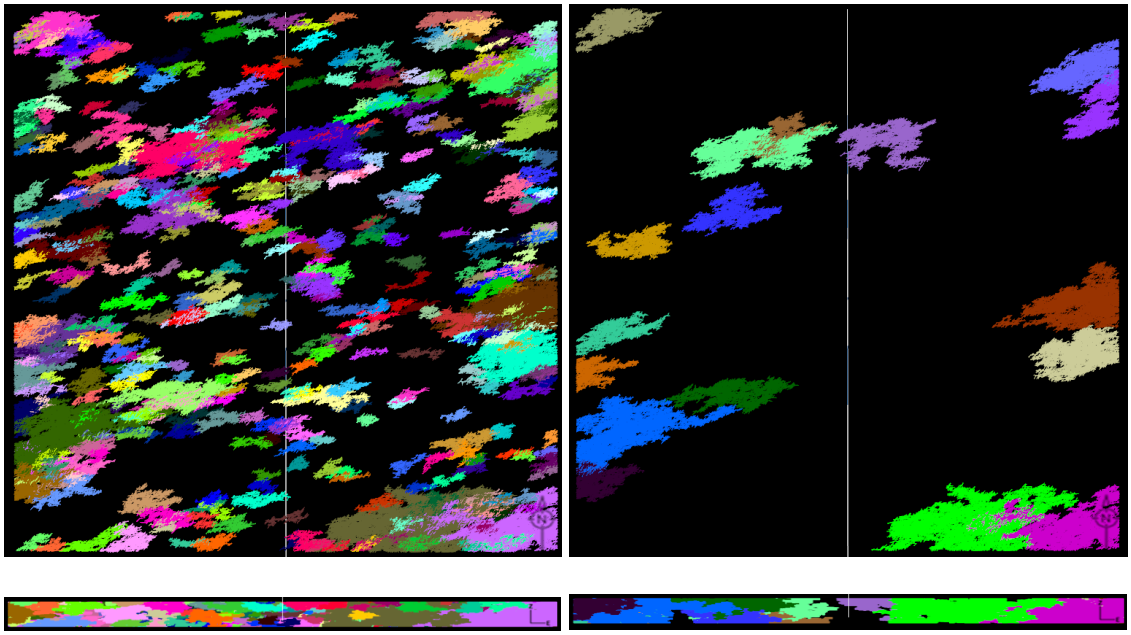

G Woodford: Half intensity (main cluster)

H Woodford: Half intensity (fractures connected to wellbore)

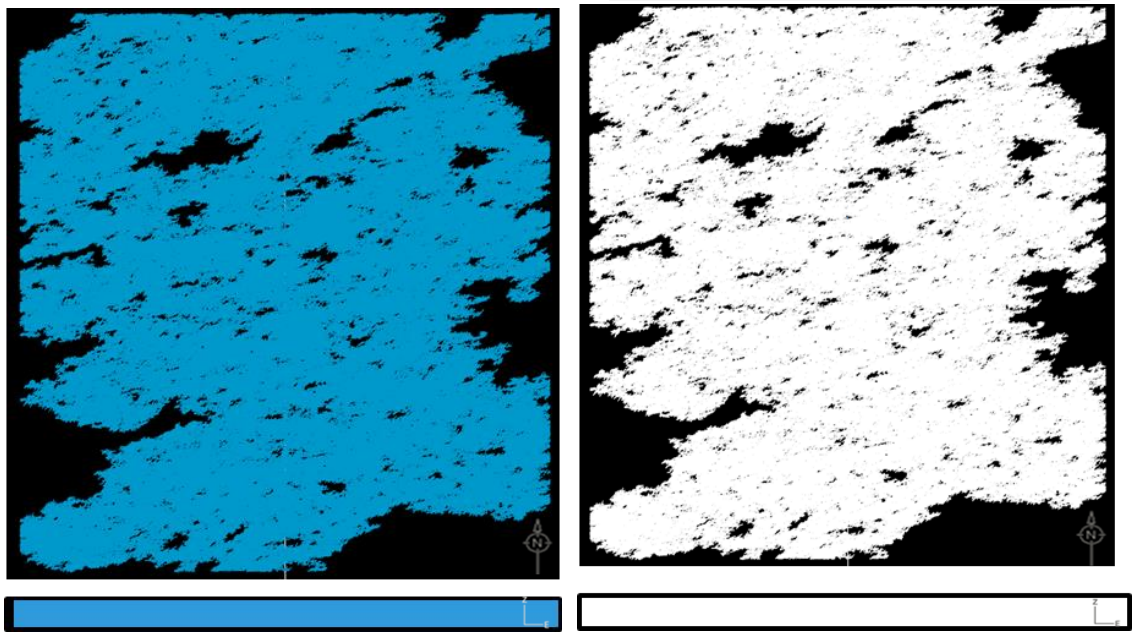

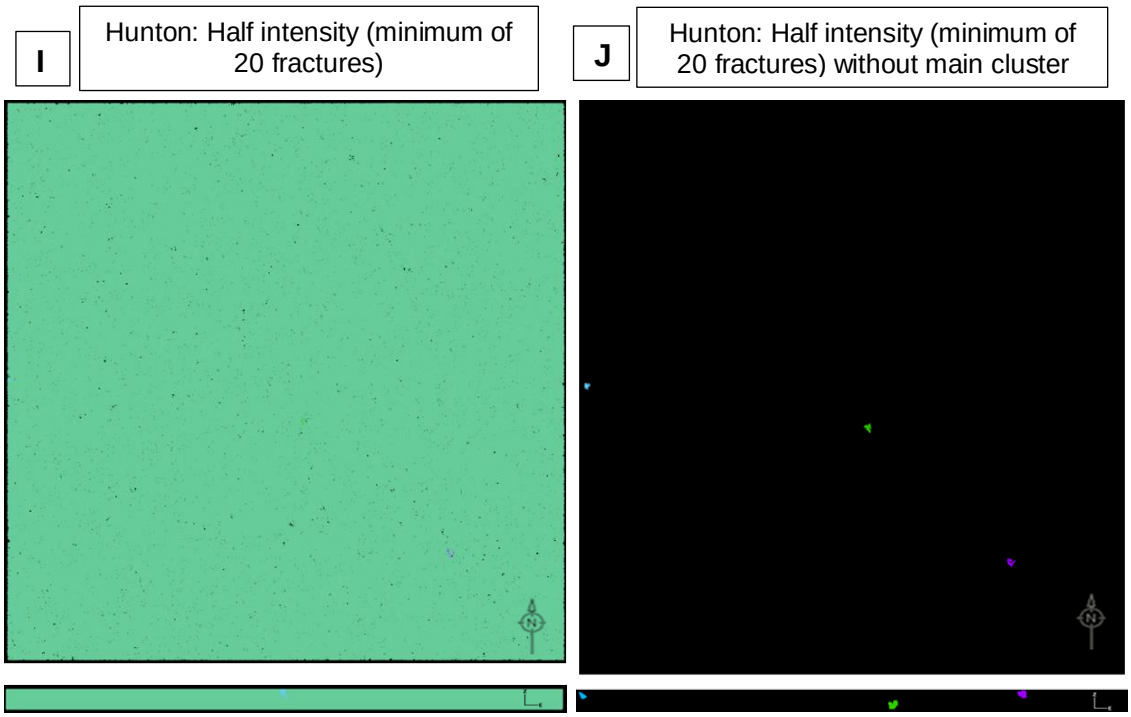

Figure 1.21: Woodford Shale and Hunton Group Limestone fracture clusters. **A-H)** Woodford shale clusters under various conditions described in the annotations. **A-B)** cluster analysis for base case intensities. **C-G)** Cluster analysis for half intensities. H) Fracture connectivity analysis to the wellbore. **I)** Fully connected DFN at half the intensity of the base case in the Hunton Group. **J)** Three fracture clusters with greater than 20 fractures in the Hunton group shown without the large cluster in Figure I.

Table 1.5: Cluster analysis results (Woodford Shale) for the base case and half intensity cases at a minimum of 20, 100, and 1000 fractures per cluster.

Woodford	Base case intensity, Min: 20 fractures	Half intensity, Min: 20 fractures	Base case intensity, Min: 100 fractures	Half intensity, Min: 100 fractures	Base case intensity, Min: 1000 fractures	Half intensity, Min: 1000 fractures
Cluster count	13	3,237	1	396	1	18
Min. frac. per cluster	20	20	1,908,961	100	1,908,961	1,021
Max. frac. per cluster	1,908,961	333,372	1,908,961	333,372	1,908,961	333,372
Average	146,867	178	1,909,819	1,184	1,909,819	21,423
Stdev	529,443	5,864	0	16,751	0	77,878

Table 1.6: Cluster analysis results (Hunton Group Limestone) for the base case and half intensity cases at a minimum of 20, 100, and 1000 fractures per cluster.

Hunton	Base case intensity, Min: 20 fractures	Half intensity, Min: 20 fractures	Base case intensity, Min: 100 fractures	Half intensity, Min: 100 fractures	Base case intensity, Min: 1000 fractures	Half intensity, Min: 1000 fractures
Cluster count	1	4	1	1	1	1
Min. frac. per cluster	1,453,576	20	1,453,576	627,423	1,453,576	627,423
Max. frac. per cluster	1,453,576	627,423	1,453,576	627,423	1,453,576	627,423
Average	1,453,576	156,871	1,453,576	627,423	1,453,576	627,423
Stdev	0	313,701	0	0	0	0

1.6 Subsurface data available

The well and hydraulic fracture/microseismic data from Hughes County, OK were obtained from a Master's thesis by Neuhaus (2011) at the Colorado School of Mines. The thesis is titled "Analysis of Surface and Downhole Microseismic Monitoring Coupled with Hydraulic Fracture Modeling in the Woodford Shale."

1.6.1 Microseismic data

All photographs of the microseismic clouds and analysis in this section were obtained from (Neuhaus, 2011). The microseismic data was recorded using surface and downhole sensors. The surface geophones were laid out radially with surface location of the treatment well being the center. One of the arms of the surface recorders was almost parallel to the treatment well. The downhole monitoring consists of nine sensors (Neuhaus, 2011) in a well located to the east of the treatment well. The hydraulic fracture job consists of five stages. Surface and downhole microseismic data are available for Stages 2-5 (Figure 1.22). The cross-section views are shown in the results section for comparison with the FracMan^{TM} simulated results. There are some

limitations to the recorded surface data. For Stage 2, the first 20 minutes were not recorded, and for Stage 4, the first 10 minutes were not recorded.

As opposed to the surface recorders, which show higher fracture growth towards the west side of the wellbore, downhole recorders show higher growth towards the east side of the wellbore. The reason is probably the location of the downhole recorders on the east side of the treatment well (Neuhaus, 2011). Also, using the downhole recorders, larger events were recorded closer to the treatment wellbore as compared to further away, i.e., towards the recording well. This might be due to higher deformation happening closer to the treatment wellbore and/or because smaller events have to cover lesser distances before being recorded at the observation well.

From Figure 1.22, Stage 2 MC has minor overlap with Stage 1 perforations. Most of Stage 3 MC grows into the already weakened Stage 2 perforations. Stage 4 has some overlap with Stage 3 MC. Similarly, Stage 5 MC has some overlap with Stage 4 MC. Importantly, both Stages 4 and 5 largely grow within the perforations of the previous stages, i.e., Stages 3 and 4 respectively, even though their microseismic overlap is not as much as that of Stages 2 and 3. Between Stages 2-5, considering all recorded events, Stage 2 shows the least scatter in the event locations and Stage 5 shows the most scatter.

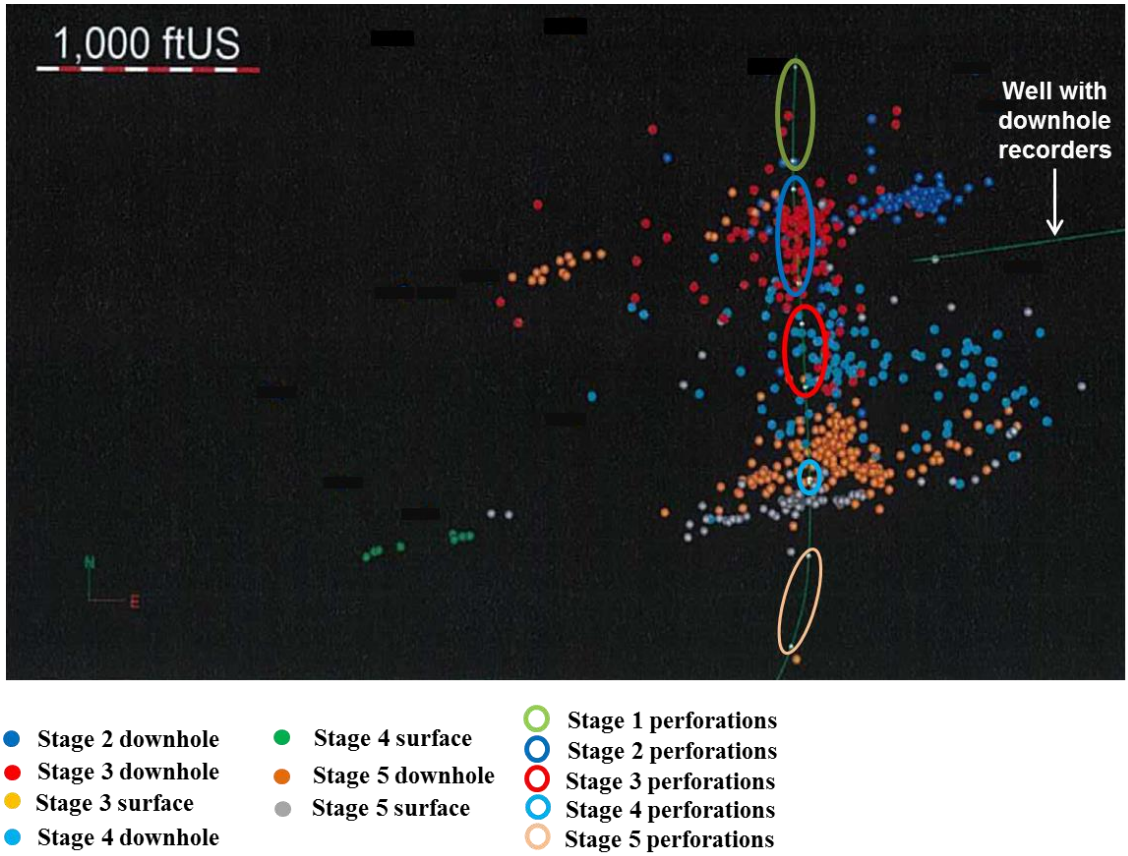

Figure 1.22: Map view of the surface and downhole recordings for Stages 2-5. Perforations for each stage are circled along the length of the well. Stage 1 only has surface recordings with a few scattered microseisms and was not modeled. Therefore, it is not shown.

On plotting the surface event magnitude vs. the cumulative number of events, (Figure 1.23A) two clear changes in slope were seen, one at M = -1.9 and another at M = -2.75. Events which with M > -2.75 (222 of 617) were retained because choosing -1.9 as cutoff would leave too few surface events for analysis. Therefore, in Figure 1.22 (above), only surface events with M > -2.75 were plotted.

Figure 1.23B shows that the furthest event recorded from the downhole sensors is 1900 ft away. At that distance, only events with M > -3.1 were detected. Only a couple of microseisms from Stage 2 have M > -3.1. Figure 1.23C shows that Stage 5 not only produced the largest events but also the highest number of events, followed by

Stages 3, 4, and 2 respectively. The event magnitudes also follow the same order. This is the reason that Stage 5 shows the highest cumulative seismic moment followed by Stages 3, 4, and 2 (Figure 1.23D). The high seismic moment in Stage 5, according to Neuhaus (2011), is not only because of interaction with previous stages but also because of interaction with faults, which provide large slip surfaces and slip distances (Gertson, 2011). Also seen in Figure 1.23D are the different trends of event occurrences. Most events for Stage 2 occur after 75 minutes into the treatment. For stage 3, most events occur at the beginning, but events keep occurring at regular intervals. For Stage 4, most events occur at the beginning and end of the treatment, with less activity in the middle. Finally, for Stage 5, most events occur during the first 50 minutes of the treatment, then the rate slows down, and finally stops at about 120 minutes, before starting again at around 180 minutes. In addition, the rate at which the events are generated is also highest for Stages 5 and 3 (Figure 1.23E). The high rate is maintained for a longer time in Stage 5 compared to that in Stage 3.

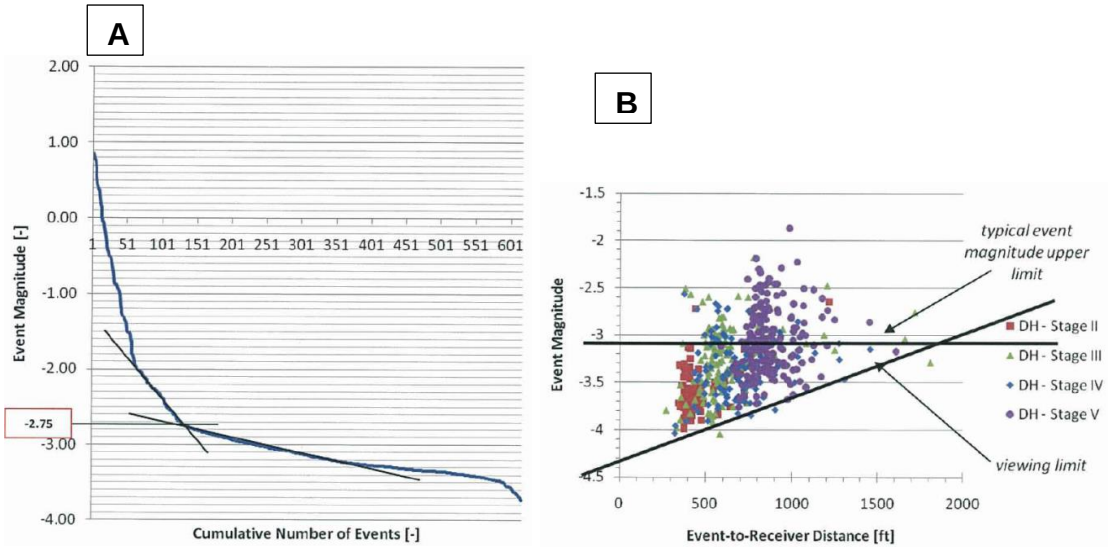

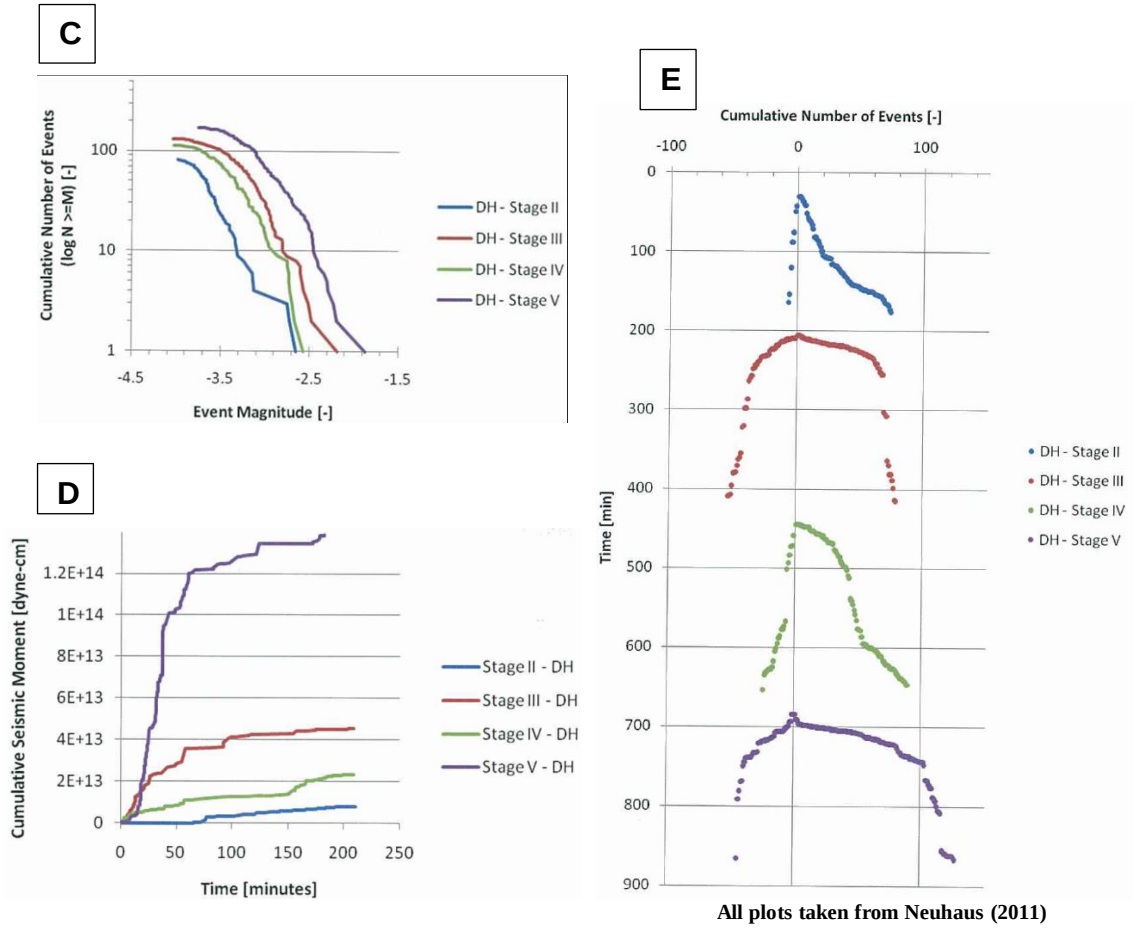

Figure 1.23: Microseismicity analysis from the treatment well. **A)** Event magnitude vs. the cumulative number of events from surface recordings. **B)** Event magnitude detection limit of ~ -3.1 at a distance of 1900 ft for downhole recorders. **C)** Cumulative distribution of event magnitudes for Stages 2-5 from downhole recordings. **D)** Cumulative seismic moment for Stages 2-5 from downhole recordings. **E)** Time vs. cumulative number of events from downhole recordings.

1.6.2 Perforation and treatment data

All data in this section was derived from Neuhaus (2011). The treatment well is located in Hughes County at the western edge of the Arkoma Basin. The hydraulic fracturing stage details are shown in Table 1.7 and Figure 1.24. The azure curve in Figure 1.24 shows two slurry rates, one at 60 bpm for a brief eight-minute period at the beginning of the treatment, and another one at nearly 95 bpm for an extended period up

to the end (blue curve in Figure 1.24). The first three proppant slugs pumped consisted of 100 mesh at 0.25, 0.50, and 0.75 lbm/gal (< 2 min each), alternately with only treatment fluid (proppant conc = 0 lbm/gal). Subsequently, 13 slugs of 30/50 proppant increasing from 0.1 lbm/gal to 1.3 lbm/gal were pumped for ~ 5 min each, with only treatment fluid (proppant conc = 0 lbm/gal) in between. A 20/40 slug of 1 lbm/gal was also pumped at the end followed by treatment fluid. Using smaller size proppant followed by larger proppant size is a common practice (Mittal, 2017).

Table 1.7: Treatment well perforation interval information obtained from Neuhaus (2011). **MD:** Measured depth, **TVD:** True vertical depth.

		Number of perforations
Total MD	10692 ft	-
Perforation depth range (TVD)	7860-7870 ft	-
Stage 1 MD range	10262-10642 ft (380 ft)	60
Stage 2 MD range	9764-10145 ft (381 ft)	96
Stage 3 MD range	9342-9598 ft (256 ft)	96
Stage 4 MD range	8951-8966 ft (15 ft)	90
Stage 5 MD range	8273-8653 ft (380 ft)	66
Casing size at perf	5.5 in.	-
Perforation diameter	0.42 in.	-
Shot density	6 shots per ft	-
Phasing	60 degrees	-

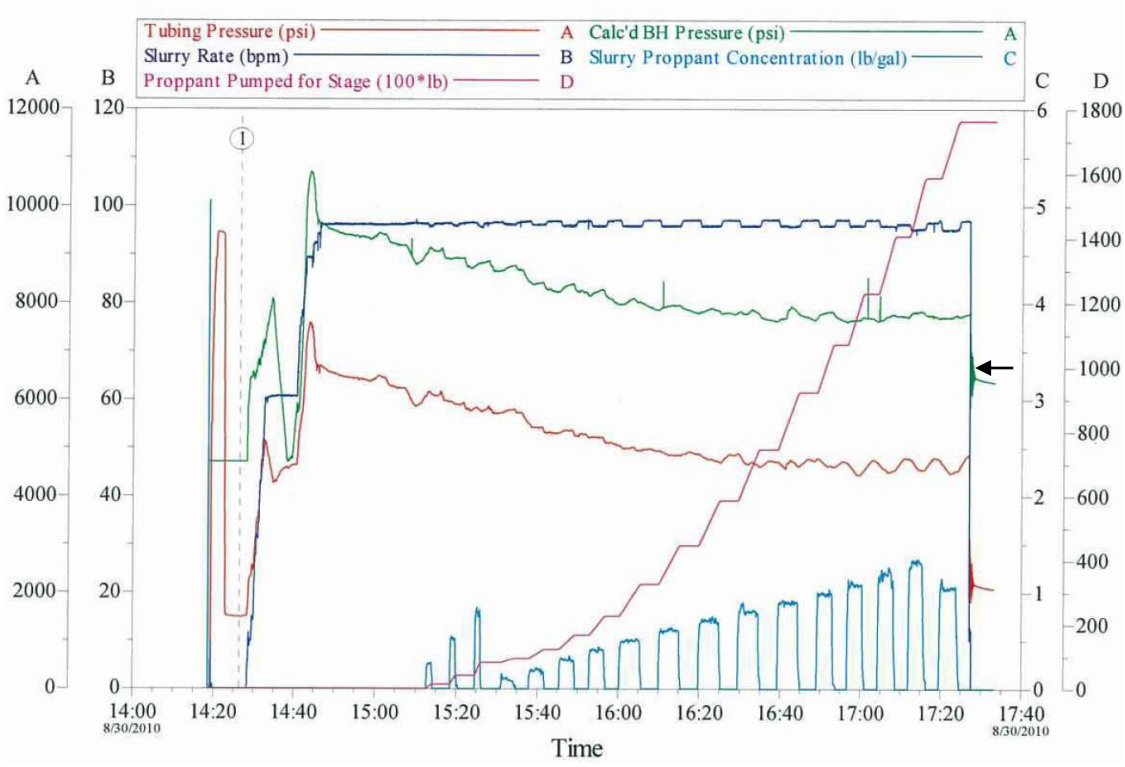

Modified from Neuhaus (2011)

Figure 1.24: Stage 2 hydraulic fracture treatment parameters. Tubing pressure at the wellhead (red), slurry rate (blue), cumulative proppant weight (magenta), calculated bottom hole pressure (green) and slurry proppant concentrations (azure) are shown. ISIP can be estimated from the green curve (arrow). However, closure pressure is not visible. Treatment parameters for all five stages are approximately identical to the one shown in this figure.

1.6.3 Well logs

The well logs used to derive the rock properties (from Caney+False Caney Shale to Hunton Group Limestone) in Neuhaus (2011) were not from the treatment well but from the monitoring well located ~ 500 ft east of the wellbore. Due to the top of the Woodford Shale being 18 ft higher in the treatment well compared to that in the offset well, the logs in the offset well were shifted up. However, Figure 1.25 shows that this did not completely match the rock properties to the lithology indicated by the GR log. In addition, the compressional wave velocity log was not available in the offset well.

Therefore, it was derived by Neuhaus (2011) in GOHFER™ software [used by Neuhaus (2011) for his models] based on the average porosity log.

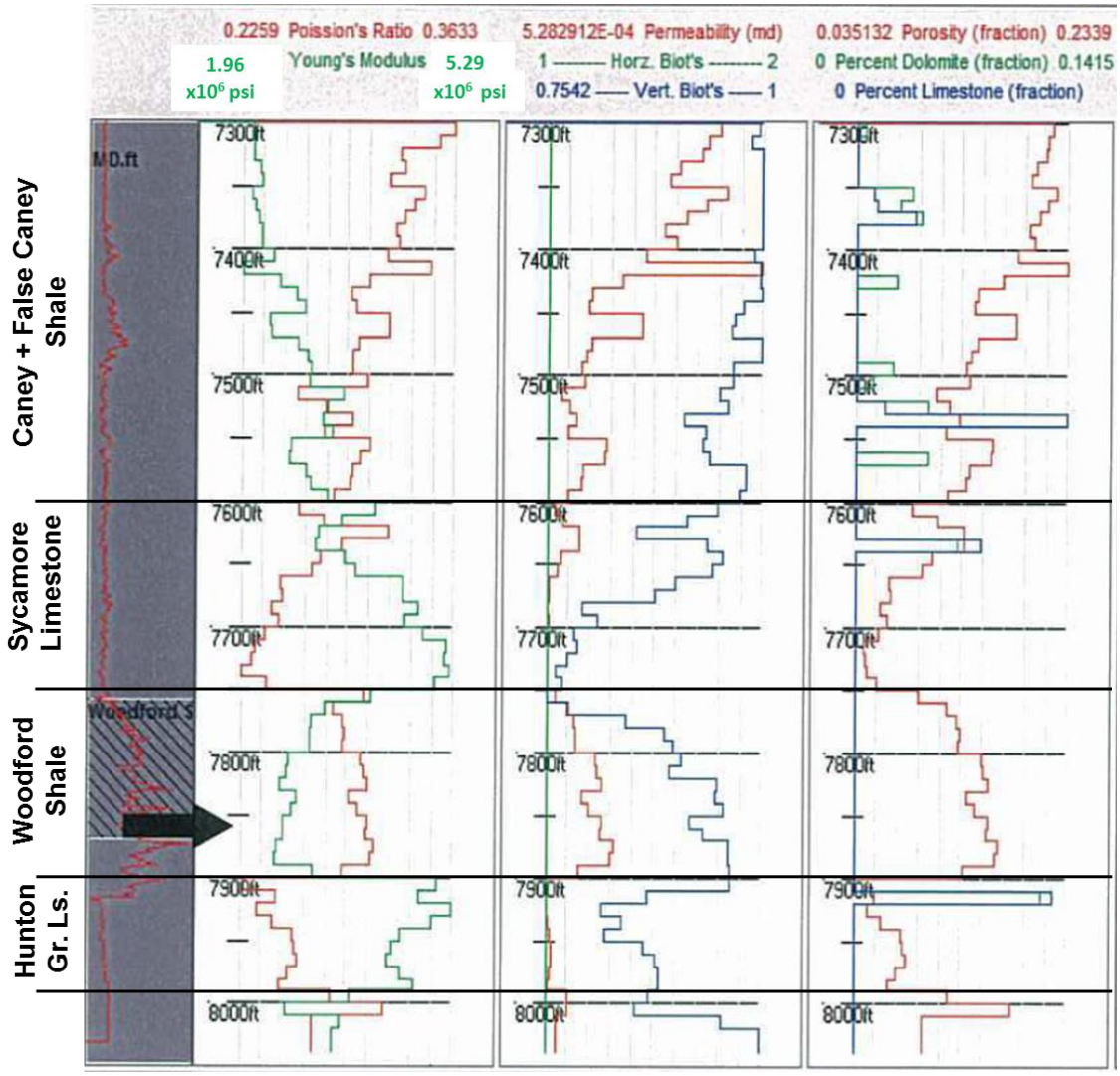

Modified from Neuhaus (2011)

Figure 1.25: Various rock properties in the treatment well calculated by Neuhaus (2011) using GOHFER™ Software. Names of various formations are mentioned on the left. The Young's Modulus and the Poisson's ratios help identify the approximate formation boundaries by the abrupt change in their values. Arrow indicates the perforation interval depth. The upper limit of the Young's Modulus scale ($5.29*10^6$ psi), which was missing in Neuhaus (2011), was estimated based on its values at the perforation interval and lower scale value of $1.96*10^6$ psi mentioned in Neuhaus (2011). There seems to be a mismatch between GR and rock properties in the lower 20 ft of the Woodford Shale in Neuhaus (2011), and therefore the base of the Woodford Shale was assigned at a TVD of 7900 ft.

1.7 Stress calculations and analysis

1.7.1 One dimensional stresses

As seen from Figure 1.25, the rock properties shown by Neuhaus (2011) span the False Caney Shale on the top and down to the Hunton Group Limestone. Although the majority of the microseisms fall below the upper limit of 7300 ft, they extend well below the Hunton Group Limestone, i.e., down to the Bromide Formation (shown in the "Dynamic Simulation" section). Therefore, the rock properties below the Hunton Group Limestone were obtained using data from another well in a nearby county.

Determination of stress as accurately as possible is important because it controls the hydraulic fracture propagation and the MC geometry. The maximum and minimum stresses were calculated using the poroelastic equations given by Blanton and Olson (1999). Zhang (2005) and Sinha et al. (2017) have used these equations for horizontal stress calculations regarding wellbore stability and optimum well spacing respectively. These equations were chosen because they have terms for the minimum (ε_{hmin}) and maximum (ε_{Hmax}) strains. These strains can be changed during the simulation to visualize their effects on the MC geometry.

$$S_{hmin} = \frac{\nu}{1-\nu}(\sigma_V - \alpha P_P) + \frac{E}{1-\nu^2}\varepsilon_{hmin} + \frac{E\nu}{1-\nu^2}\varepsilon_{Hmax} + \alpha P_P \quad \text{Eq. 1.1}$$

$$S_{Hmax} = \frac{\nu}{1-\nu}(\sigma_V - \alpha P_P) + \frac{E}{1-\nu^2}\varepsilon_{Hmax} + \frac{E\nu}{1-\nu^2}\varepsilon_{hmin} + \alpha P_P \quad \text{Eq. 1.2}$$

Where,

E = Young's Modulus
N = Poisson's ratio
A = Biot's constant
P_p = Pore pressure
Note: σ_v in Eq. 1.1 and 1.2 is actually S_v (i.e., total vertical stress).

To use Eq. 1.1 and Eq. 1.2, the initial maximum and minimum horizontal stains need to be established. Strain values were chosen in such a way that the stresses and stress ratios are limited within certain ranges that satisfy four conditions. Firstly, the Shmin value should be below the ISIP (upper limit of Shmin) at the wellbore. The second condition is to make sure that the Viola Group Limestone, whose Young's modulus (10^7 psi, i.e., ~ 70 GPa) is comparable to that of basement granites should be in the strike-slip regime, i.e., Shmin < Sv < SHmax (Figure 1.26). Earthquakes in Oklahoma due to fault slip within the basement rocks are mostly strike-slip in nature (McNamara et al., 2015). The third condition is to bring the average Woodford Shale fracture gradient (Shmin) to 0.77 psi/ft. According to Grieser (2011), the average Woodford Shale stress gradient in the Arkoma Basin is close to 0.77 psi/ft. Neuhaus (2011) also mentioned that the service company anticipated 0.78 psi/ft stress gradient. The fourth condition is that the minimum to maximum effective stress ratio ([Sv-Pp]÷ [Shmin-Pp]), in normal stress regimes, cannot exceed values of 2.46 and 3.68 for shales and carbonates respectively. These values were derived using friction angle (μ) of 25 degrees in shales and 35 degrees in carbonates. On exceeding these values, the critically stressed faults are likely to slip. Zoback (2003) shows the formula (Eq. 1.3) used is calculating the stress ratios.

$$\frac{\sigma_1}{\sigma_3} = \frac{S_1 - P_p}{S_3 - P_p} = [\,(\mu^2 + 1)^{1/2} + \mu\,]^2 \qquad \text{Eq. 1.3}$$

Hajdarwish and Shakoor (2006), on experiments conducted on several tens of mudrock samples, found an average friction angle of ~ 25 degrees. Blasio (2011) mentioned limestone friction coefficient in the range of $0.7 < \mu < 0.75$. $\mu = 0.7$ corresponds to a friction coefficient of 35 degrees.

Figure 1.26 shows the mechanical properties and calculated stresses. All the stresses were calculated at a ε_{Hmax} of 0.0005 and at variable ε_{hmin} of 0.00001, 0.000025, and 0.00003 during the simulation. However, to demonstrate the variation in stresses with changes in ε_{hmin}, an example of ε_{hmin} = 0.00009 (not used in simulation) is shown in Figure 1.26. With an increase in the minimum strain from 0.00001 to 0.00009, the gap between maximum and minimum stress closes. In addition, minimum stresses within the limestones increase faster than in shales. Therefore, stress gap between Shmin and SHmax closes faster in the carbonates compared to the shales.

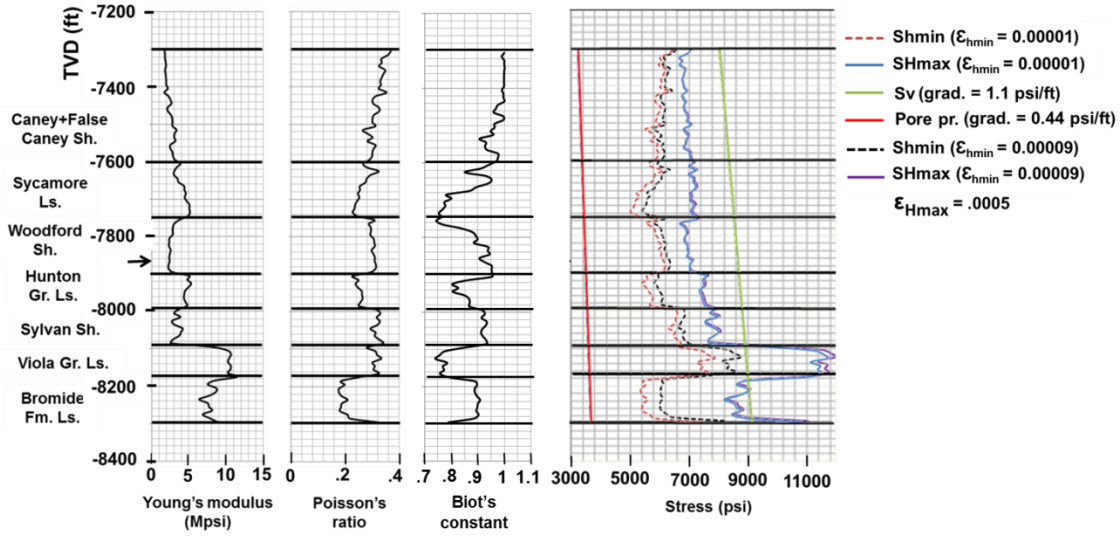

Figure 1.26: Rock properties and in situ stresses. Calculations are shown at a fixed ε_{Hmax} of 0.0005, and two ε_{hmin} values of 0.00001 and 0.00009 (for illustration). Interpretations of the formation boundaries are shown.

1.7.2 Critical stress analysis

Figures 1.27A through 1.27I are plots of the shear stress vs. effective normal stress. Points in Figures 1.27A, 1.27B, and 1.27C represent the normal and shear stresses on all fractures. Red points are critically stressed fractures, and green are not

critically stressed. The failure envelopes represent zero cohesion (assuming negligible cement cohesive strength) and friction angle of 25 degrees.

The decrease in the number of critically stressed fractures from Figure 1.27A to 1.27B, and disappearance in 1.27C shows that with increase in the minimum strain the stress state becomes more stable. Also, if a friction angle of 35 degrees is considered, none of the fractures are critically stressed (Figure 1.25D). While the Woodford Shale and other formations (Figures 1.27E through 1.27I) are largely devoid of critically stressed fractures, the Bromide Formation has a substantially high number of critically stressed fractures (Figures 1.27J through 1.27L). The reason is relatively low Shmin (broken red line in Figure 1.26), a large difference between Shmin and SHmax, and relatively high pore pressure in the Bromide Group (deepest among all formations).

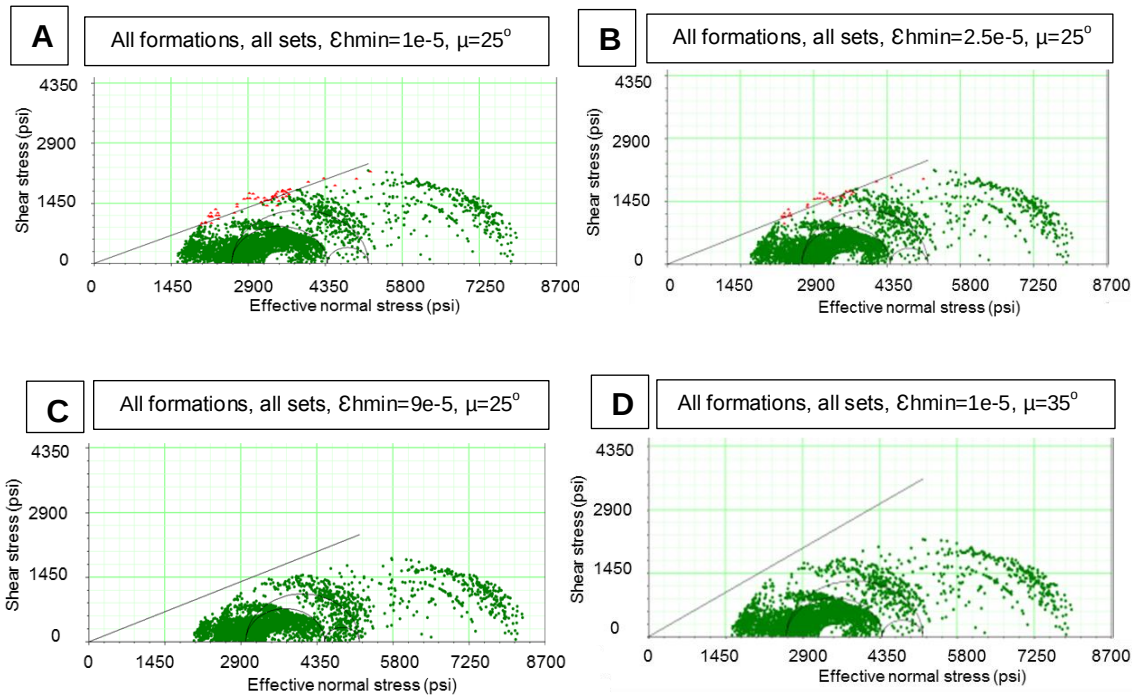

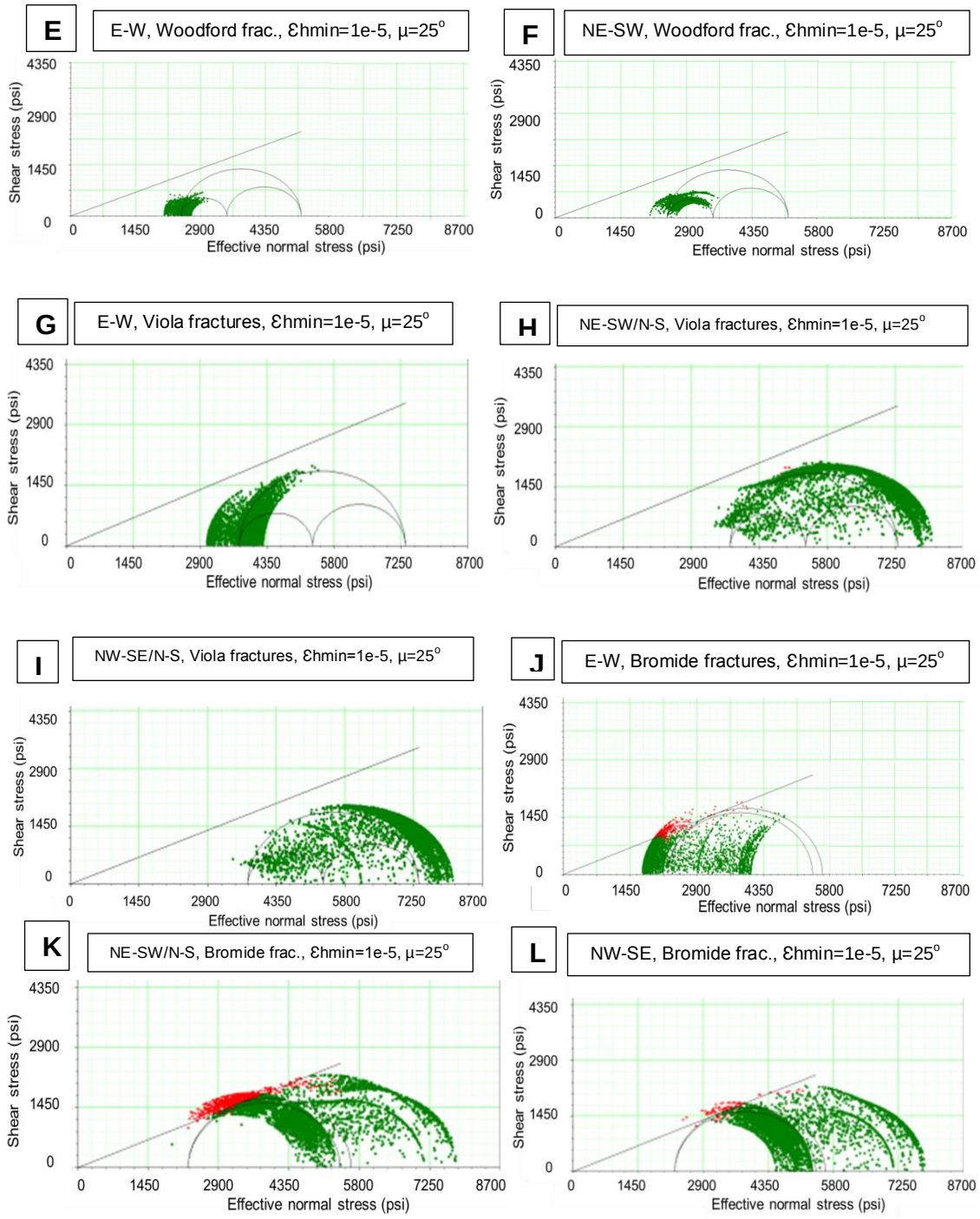

Figure 1.27: Shear and effective normal stresses (at $Ɛ_{Hmax}$ = 5e-4) on fractures along with failure envelopes with zero cohesion. Figure annotations provide more information. **A-D)** All fractures in all formations. **B)** Slightly lower number of fractures that are critically stressed at a higher $Ɛ_{hmin}$ = 2.5e-5 compared to A. **C)** No critically stressed fracture at a minimum strain of $Ɛ_{hmin}$ = 9e-5. **D)** Only plot with a friction coefficient of 35 degrees, showing that at this friction angle, none of the fractures is critically stressed. **E-F)** None of the fractures in the Woodford Shale are critically

stressed. **G-I)** Hardly any Viola group fractures are critically stressed. **J-L)** Critically stressed fractures are present only in the Bromide Group. **K)** NE-SW fractures have the highest number of critically stressed fractures.

1.8 Software

Several geomechanical modeling software packages are available today. Some well know examples are FLAC3D™ from Itasca, GOHFER™ from Barree and Associates, Elfen™ from Rockfield technology, Mangrove™ from Schlumberger and FracMan™ from Golder Associates. These software packages provide various functions which make it easy for the user to understand and visualize rock failure and fracture propagation in the subsurface. Some of these software packages such as GOHFER™ and FLAC3D™ only allow continuum modeling while the other mentioned software allow both DFN and continuum modeling. FLAC3D™ can simulate stress distribution in rock matrix during hydraulic fracturing. However, the focus is on geotechnical engineering simulations related to soil, rock, groundwater, and construction (Itasca Consulting Group Inc., 2017).

Hydraulic fracturing features of GOHFER™ include pressure history match, modeling of proppant concentration, fluid pressure distribution, leak off, non-uniform solid and liquid velocity, particle settling during pumping, and stress shadow effects (GOHFER™ brochure, 2015; GOHFER™ presentation, 2017). Critical stress analysis is not possible due to the absence of DFN capabilities. Although GOHFER™ has introduced pseudo-3D modeling now, previous versions were 2D.

Mangrove™ allows natural fracture modeling (DFN) in addition to continuum models. Mangrove™ is capable of showing the interaction of natural fractures with

hydraulic fractures (Bigdeli, 2015) in addition to the reactivation of natural fractures due to pressure perturbation.

Elfen™ is capable of both DFN and continuum modeling (Rockfield: Upside of a Downturn, 2017). It includes most features offered by Mangrove™ in addition to features such as, shearing in over and underburned (caprock integrity), aperture contours analysis, conductivity maps, proppant distribution in the fracture with time, effect of stresses distribution along the wellbore (wellbore geometry and orientation) on fracture propagation, and synthetic microseismicity generation. Elfen™ is also capable of simulating bedding interface slip (Rockfield: Upside of a Downturn, 2017).

The builders of GOHFER™, Rockfield™, and Mangrove™ claim them to be fully coupled (Bigdeli, 2015; GOHFER™ presentation, 2017; Profit et al., 2017). This also means that these software obey fracture mechanics principles and changing pumping rate affects the final geometry. In addition, all three have pressure history match functions (GOHFER brochure, 2015; GOHFER™ presentation, 2017; Profit et al., 2017; Bigdeli, 2015).

However, since these software involve equations coupling flow rate, viscosity, leak off, and stress intensity at crack tip (fracture toughness criteria), computation of process zone stresses, and realtime calculation of stress shadows (leading to change in fracture propagation path), they are computationally intensive. These features result in long run times. For example, Mangrove can demonstrate the propagation of the hydraulic fracture and its interaction with natural fractures growth of each natural fracture, in addition to features such as overall reactivation volume, but can take several hours instead of minutes, to complete the simulation.

FracMan™ software was used in the current study was provided by Golder Associates. Unlike some of the software mentioned earlier, FracMan™ allows both natural fracture (DFN) modeling, in addition to continuum modeling obtained by upscaling the DFN, or simply by assigning values to the grid cells directly. FracMan™ limitations include partial coupling, rather than fully coupled fluid flow. "Partially coupled" here means that the final geometry is based on the total volume pumped rather than the rate at which the fluid was pumped. Also, pressure history match during hydraulic fracturing is not available. Other limitations include non-availability of proppant concentration modeling. Although principles such as fracture aperture based on mechanical rock properties, pore pressure, and fluid viscosity are used, fracture mechanics concepts such as fracture toughness (or stress intensity factor at the crack tip) and the presence of process zone stresses are not taken into account.

However, regarding natural fracture modeling, FracMan™ give a realistic picture of the subsurface fracture distribution. It provides the user multiple options for generating natural fractures either from wells or directly from outcrops. Outcrop measured fracture parameters (intensity, length, height, and aperture) and interrelationships can be implemented directly in the DFN model. Also, visualization of fracture clusters and connectivity to the wellbore can be performed which is not possible through direct outcrop observations. In other words, FracMan™ natural fracture modeling is based on realistic geologic descriptions in three dimensions.

Another advantage is that each hydraulic fracturing simulation run is completed within a short time. Each run may take 5-15 minutes rather than hours or days, which is the case when all physics (related to full rock-fluid coupling and fracture mechanics

principle) are applied. Therefore, some precision is lost in favor of time. However, short run times allow the opportunity to perform several runs. For each hydraulic fracture run, changing the treatment parameters and some natural fracture parameters is permitted. After each simulation run, the user can visualize the output fracture geometry in the form of synthetic microseismic or reactivated fractures. The input parameters can be changed accordingly after each run to eventually match the generated geometry to the interpreted field geometry. Thus there exists an opportunity to test the effect of several parameters on the MC geometry in short time.

One can define regions (volumes) based on formation depths. These regions are populated with multiple fracture sets for each formation. Facture lengths, heights, and apertures measured from the outcrops are entered by defining their statistical distributions such as exponential, power-law, normal, lognormal, etc. along with their means, standard deviations, and upper and lower cutoffs. Correlations (linear, power-law, etc.) between these parameters can also be used. Fracture intensities can be defined directly, using either P32 (fracture area per unit of rock volume), or fracture total counts. For assigning fracture orientations, distributions such as the fisher, elliptical fisher, bivariate bingham, bivariate fisher, and bivariate normal distributions are available. Permeability for each fracture set in each formation can be assigned by correlating to the natural fracture aperture values, or through a user input. For simulating different scenarios, natural fracture permeability, aperture, and compressibility can be changed without having to regenerate the fracture sets again. However, natural fracture lengths, heights, and intensities cannot be changed without regenerating the fractures.

Grid cell sizes can be defined manually with variable sizes in the two horizontal and vertical directions by defining the number of cells in a given direction. The grid properties such as Vp, Vs, and density can be assigned to grids by importing a file directly. Subsequently, formulas for calculating Young's Modulus and Poisson's ratio can be assigned. On the other hand, the Young's Modulus, Poisson's ratio, Biot's constant, and friction angle values can be directly input into the grids by importing the values in a text file. Although grids are created by dividing the formation vertically and horizontally, individual fractures are also divided or "meshed". This involves assuming a 2D bounding rectangle around a natural or hydraulic fracture. The user can enter a maximum element size. The number in each direction is a function of the fracture (natural or hydraulic) bounding rectangle and the element size determined by the software, but not exceeding the user-defined size. Although smaller element size gives more accurate results, the computation time increases linearly.

Pumping of a single fluid such as slickwater or a slurry containing slickwater and proppant is permitted. Given the proppant concentration, the fluid density is adjusted accordingly. The total duration during which the total fluid volume is pumped can be divided into a number of timesteps assigned manually. Pumping parameters are the rate, duration, and net pressure. The net pressure can be assigned by either assigning an ISIP (instantaneous shut-in pressure) value or a "dp" (difference between the fluid pressure inside the fracture and stress on the fracture walls) value. Minimum injection ratio, i.e., percent of pumped fluid used in creating the new hydraulic fracture is user defined with a default value of zero. Choosing a higher minimum injection ratio than that calculated by FracMan^{TM} creates a larger hydraulic fracture (new surface area). A

convenient option used to control the fluid assignment is by controlling the exponents of transmissivity, orientation, and connection level, i.e., M, N, and L respectively. A probability of assigning fracture fluid in each time step is given by Eq. 1.4:

$$Prob = \frac{Transmissivity^{M}\ X\ Orientation^{N}}{Connection\_Level^{L}} \qquad \text{Eq. 1.4}$$

Assigning high values to M, N, and L assign priorities to the larger fractures, fractures oriented closer to SHmax, and fractures closest to the wellbore respectively. In addition, the option for pump through non-dilatable fracture is available. However, when fluid is injected in non-dilatable fractures, the storage aperture (or the change in aperture after injection) stays zero (FracMan7.5 Workshop, 2014). In other words, the non-dilatable fractures allow fluid flow or fluid pressure transmission but not for fluid storage.

The user chooses the fluid pressure drop with distance within the connected body of fractures using a pressure-drop slope "s" shown in Eq. 1.5. Fluid pressure can drop due to the resistance of fracture surface to flow or due to leak off. The pore pressure drop is calculated by the equation

$$P_{pore} = (P_{pump} - \sigma 3_{max})\left(1 - \frac{s\,d}{d_{max}}\right) + \sigma 3_{max} + \rho\ g\ dh \qquad \text{Eq. 1.5}$$

"P_{pore} = pore pressure in the injected fracture;
P_{pump} = pump pressure;
$\sigma 3_{max}$ = maximum value of the third directional principal stress;
d = flow distance from well injection point to the fracture element;
d_{max} = maximum flow distance;
ρ = fluid density;
g = gravity;
dh = vertical elevation from the well injection point to fracture element." (FracMan7.5 Workshop, 2014)

Users can enter the final maximum storage aperture values that are applicable both to the natural and hydraulic fractures. If the maximum specified value is higher than that calculated by FracMan™, it calculates the storage aperture values using the Secor and Pollard (1975) equation (Eq. 1.6). The equation is given by:

$$e = \frac{4(1-\nu^2)}{E}(P_{frac} - \sigma_N)d_{max}\sqrt{1-(\frac{d}{d_{max}})^2} \qquad \text{Eq. 1.6}$$

Pfrac = Ppore (from last equation);
σ_N = Normal stress on a given fracture face;
E = Young's Modulus;
N = Poisson's ratio;

On the other hand, if the maximum storage aperture values assigned are lower than that calculated by FracMan™, the assigned values are used for almost all dilatable injected elements. The non-dilatable elements are assigned zero apertures. Several options for performing hydraulic fracturing are available.

Hydraulic fractures can be initiated either with a new tensile fracture or an existing natural fracture that intersects the well. From the existing fractures that intersect the well, users can choose from a natural fracture that has the largest size, one that is oriented closest to the SHmax, one that has the highest shear stress, or one of these at random. Moreover, for each hydraulic fracture simulation, the option for choosing the desired natural fracture sets for simulation is available.

To summarize the above, initially, the fracture is started from the wellbore from a new tensile or a preexisting fracture. For each time step, the algorithm looks for the connected dilatable fractures that have resolved normal stresses smaller than the fluid pressure inside the fracture, calculated using Eq. 1.5. Out of the dilatable fractures, priority is given to fractures based on Eq. 1.4. Then the fluid is pumped into the fracture

element, and the pore pressure and aperture of the fracture element are updated based on Eq. 1.6, or a user-specified maximum storage aperture value. In case no connected dilatable fracture is available, and there is no predefined value of minimum fluid injection into a new hydraulic fracture, the remaining fluid is pumped into a new hydraulic fracture element. If "pump through non-dilatable fracture" option is chosen, the likelihood of creating new surfaces (hydraulic fracture elements) decreases. This process is repeated until all the fluid within a given timestep has been distributed.

Two methods are available for obtaining the volume of the reactivated fractures (microseismic cloud), and the associated new surface area due to the hydraulic fracture connected to the wellbore. In the hull volume method, the outermost points of the synthetic (simulated) microseismic volume are connected to provide a balloon shape. This shape is the maximum estimate of the microseismic volume (FracMan7.5 Workshop, 2014) due to empty spaces (unreactivated natural fractures) within the balloon shape. The slab volume, on the other hand, approximates the microseismic cloud shapes more closely, i.e., without much empty space. Therefore, it gives a lower estimate of the microseismic volume, but its values are subject to some user-defined choices. The slab volume method is the only option for the hydraulic fracture (new surface) volume measurement. Therefore, both methods (hull and slab) can be used to approximate the change in volume when comparing shapes. However, the real volume of the microseismic value lies between these two values.

1.9 Dynamic simulation

1.9.1 Geometry match

Geometry matches refer to the match between the 3D ellipsoid trace drawn on the field MC geometries and that on the simulated MC geometry. In addition to the map view of the field MC geometries, views in the directions parallel and perpendicular to the wellbore were considered. Depending on the angle at which the photographs were taken at the GOHFER^{TM} interface, there can be a slight change in the percent of microseisms in each formation, which can sometimes also result in slightly different MC height interpretations. Therefore, an average dimension from both views (along and across the well) was considered. However, the view looking north or parallel to the wellbore gives a better idea of the number of microseismic in each formation, since more microseisms are visible.

Formation permeabilities that result in a good match with the MC cloud for all three stages were used in all simulation runs. The reasonable maximum storage aperture value, or the fracture width after hydraulic fracturing, was initially 0.1 in (0.0025 m or 2.5 mm). Brady et al. (1992) found values in the range of 0.1-0.2 inch in their simulation. After that, it was modified based on the field geometry match requirements. Table 1.8 shows the permeabilities used for different formations. Table 1.9 shows the hydraulic fracture input parameters for all the field geometry matches (Stages 2, 4, and 5). Permeability values in Tables 6 were same for all simulations, including the field geometry matches for the three stages, and the forward modeling under different scenarios. Parameters in Table 1.9 were used for all runs except for two forward modeling (not geometry match) cases, where one different value of ISIP and another for

fracture pore pressure-drop slope (top two rows), were tested. All geometry matches and forward modeling results were obtained using the same volume and flow rates used in the treatment well.

Table 1.8: Natural fracture permeability input values for all simulation runs.

Caney perm (md)	Sycamore perm (md)	Woodford perm (md)	Hunton perm (md)	Sylvan perm (md)	Viola perm (md)	Bromide perm (md)
0.012	0.006	0.003	0.0045	0.011	0.025	0.005

Table 1.9: Hydraulic fracturing inputs for the three geometry matches.

ISIP (psi)	6500
Fracture pore pressure-drop slope	0.1
HF initiation from natural fracture	Largest
Sv Strike/dip	000/90
SHmax Strike/dip	078/00
Hydroshear	No
Natural fracture sets included	All
Min injection ratio	0
Cohesion	0
Friction angle Shale (degrees)	25
Frcition angle Carbonates (degrees)	35
Fluid viscosity (Pa-s)	0.00089
Fluid compressibility (1/kPa)	4.57e-7
Fluid density (kg/m^3)	1020
Fracture compressibility (1/kPa)	1.45e-6
Failure criteria	Mohr-Coulomb
Total timesteps	42

1.9.1.1 Stage 2

Table 1.10 shows the hydraulic fracture inputs used for Stage 2. Table 1.11 shows the results after the simulation. Table 1.12 shows the comparison between the field and simulated geometries. The Woodford measured volumes were manually calculated by multiplying the microseismic height, width, and length within the Woodford Shale. These are maximum estimates of the Woodford Shale volume.

Table 1.10: Specific inputs (rotating/adjustable knobs) for Stage 2.

Flow through non-dilatable fracture	Flowback (%)	Max. storage aperture (m/mm)	L	M	N	ε_{Hmax}	ε_{hmin}
No	25	0.006/6	1	0	0	0.0005	0.00001

Table 1.11: Results from the Stage 2 simulation.

No. of hydrofracture elements	57
Number of injected natural fracture elements	24,339
Vol. in induced hydraulic fractures (m^3/ft^3)	26.5/937
Vol. in reactivated natural fractures (m^3/ft^3)	1954.1/69,008
Fluid efficiency (%)	1.4%
Avg. post-hydraulic fracturing aperture (storage aperture) of inflated fractures (m/mm)	0.00589/5.89
Min. aperture of inflated fractures (m/mm)	0.000017/0.017
Woodford measured volume (m^3)	1,099,447
Inflated + hydraulic fracture hull volume (m^3)	1,886,322
Inflated + hydraulic fracture slab volume (m^3)	740,311
Hydraulic fracture (only) slab volume (m^3)	19,458
Inflated fracture (only) slab volume (m^3)	734,121

Table 1.12: Interpreted (int.) short-axis length, long-axis length, and height of the 3D ellipsoid for Stage 2. Also shown are the achieved (ach.) model dimensions and percent differences (diff.). Percentage interpreted occurrence of microseisms are using both wellbore-parallel (north) and wellbore-perpendicular (west) views.

Stage	Short-axis	Long-axis	Height	Percentages from field MC
2 int.	312 ft (95 m)	1123 ft (342 m)	335 ft (102 m)	Woodford 60 > Hunton25 > Sycamore15 > Caney = Sylvan = Viola = Bromide = 0
2 ach.	318 ft (97 m)	1050 ft (320 m)	380 ft (116 m)	-
2 diff.	1.9%	6.5%	13.4%	-

The MC geometry match for Stage 2 was achieved using L = 1, M = 0, N = 0 (Table 1.10) and Figures 1.28A through 1.28G. This means that pumping priority was given to natural fractures as close as possible to the wellbore (L = 1). The effect of permeability (M) is not very significant, i.e., changing the permeabilities between the Sycamore Limestone, Woodford, and Hunton Group Limestone did not change the simulated geometry. Moreover, a higher flowback and wider hydraulic fracture (storage) aperture (compared to that of Stages 4 and 5) was required to accommodate the fluid volume. The field microseismic grows nearly 70 feet into the overlying Sycamore Limestone, but never touches the Sycamore Limestone/Caney Shale boundary (Figure 1.28D). However, the simulated natural fracture reactivation could not be stopped before it touched the Sycamore Limestone/Caney Shale boundary (Figure 1.28E) due to the absence of stress barriers above and below the Woodford Shale. However, the density of the simulated MC is higher in the Woodford Shale compared to the over- and underlying Sycamore Limestone and Hunton Group Limestone respectively. In addition, the extent of the simulated MC is much lower in

the Sycamore Limestone. The Hunton Group Limestone has a slightly lower simulated lateral length compared to that of the field MC.

The simulation results along with field observations indicate the following scenarios. First, possibly, in the field, there are many smaller fractures (compared to the measured ones) near the wellbore that generate microseisms but are not recorded due to their low magnitudes. A lower rate (compared to Stages 3 and 5) of recorded microseisms (Figure 1.23) supports this hypothesis. Second, it is possible that fractures in the field are opening without much stress drop due to low cohesion, low shear components of dilating natural fractures (i.e., dilating natural fractures oriented sub-parallel to SHmax), or both, resulting in low magnitude events that are not recorded. It is important to remember that even though the direction was not given any weight, (i.e., N = 0) the software seems to have been programmed in such a way that overall simulation grows in the maximum horizontal stress direction. In other words, no additional weight to direction was given from the default. The third possibility is that, in the field, the fluid goes into connected fractures with low cementation and high permeability (i.e., open fractures), without reactivating significant number of natural fractures. In the simulator, a better match for Stage 2 can be obtained by reducing the fracture intensity in the Sycamore Limestone. However, the lower natural fracture intensity will not work for Stage 5 where more stimulation is required in the Sycamore Limestone and subsequently in the Caney Shale.

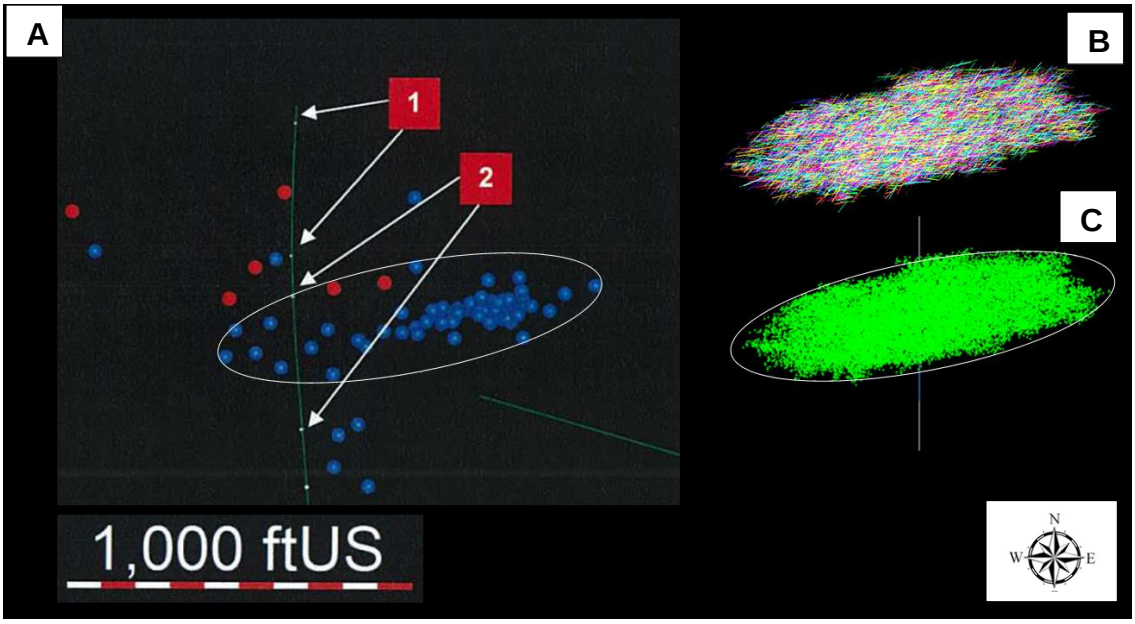
A
1
2
1,000 ftUS
B
C
N
W
E

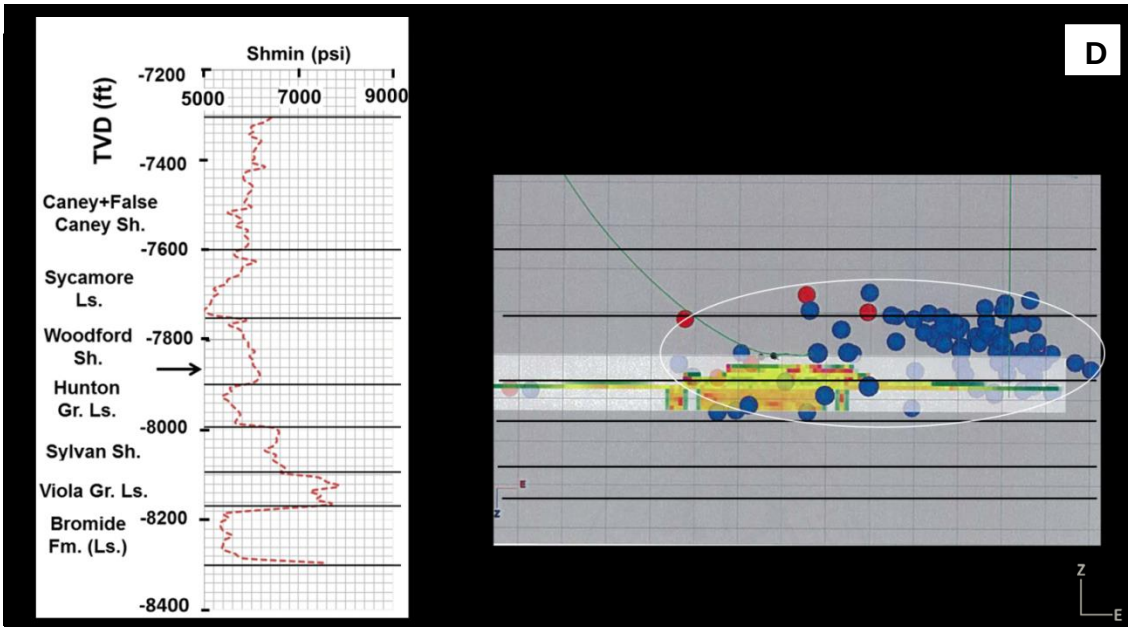
D
Shmin (psi)
TVD (ft)
-7200
5000
7000
9000
-7400
Caney+False Caney Sh.
-7600
Sycamore Ls.
Woodford Sh.
-7800
Hunton Gr. Ls.
-8000
Sylvan Sh.
Viola Gr. Ls.
Bromide Fm. (Ls.)
-8200
-8400
Z
E

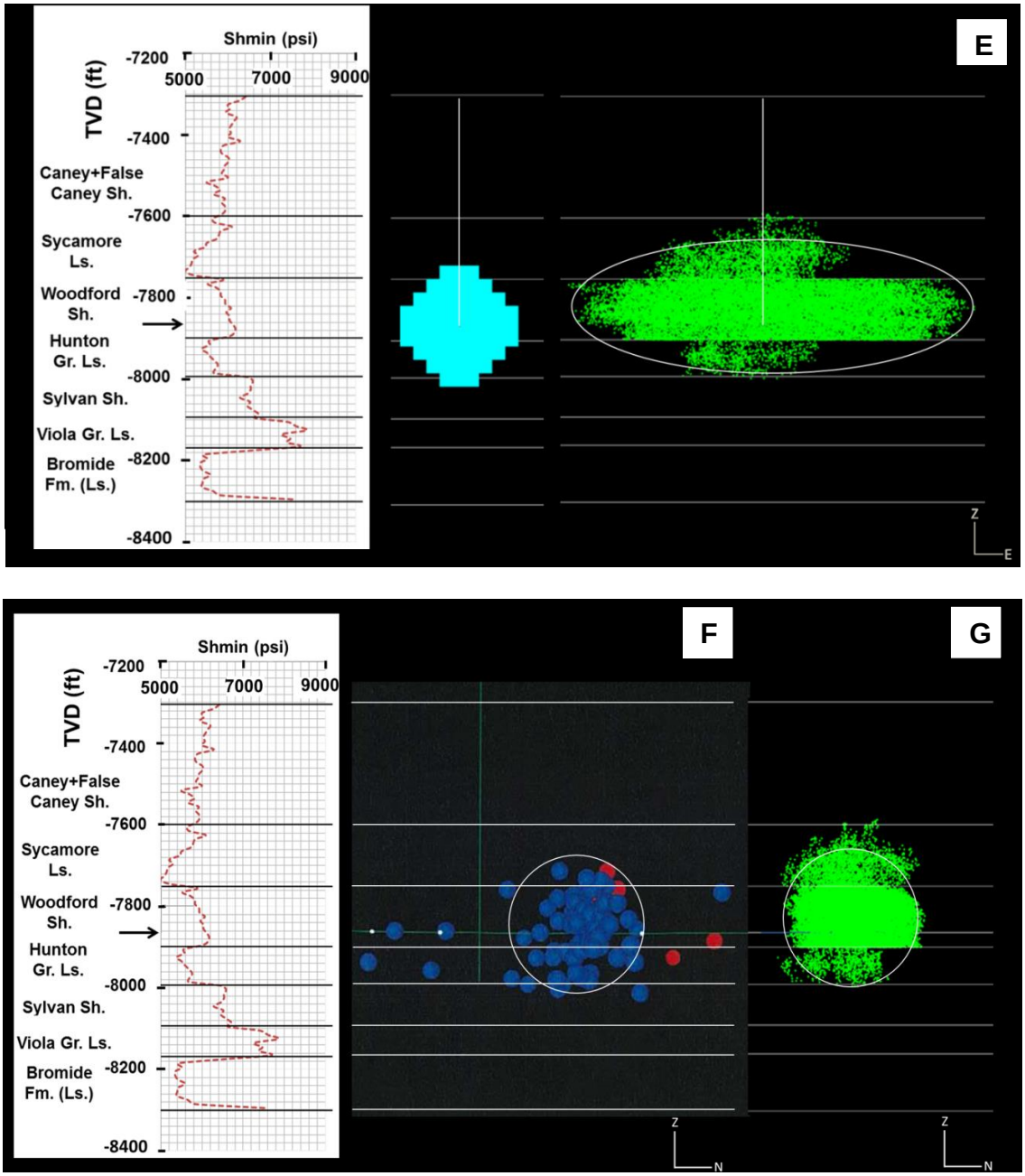

Figure 1.28: Field and modeled microseismic cloud geometries for Stage 2. **A)** Map view of the field MC obtained for Stage 2. Perforations for Stages 1 and 2 are marked. The zone containing the highest MC density is marked within the trace of a 3D ellipsoid. Red: surface recorded MC; blue: downhole recorded MC. **B)** Map view of reactivated natural fractures. **C)** Map view of the synthetic MC. Overlay of the 3D ellipsoid trace in A is shown for comparison. **D)** North (wellbore-parallel) view of the field MC along with the 3D ellipsoid trace. In yellow and orange are the proppant concentrations modeled by Neuhaus (2011) in GOHFER^{TM} Software. **E)** Synthetic MC with ellipsoid trace. The main hydraulic fracture connected to the wellbore is shown

separately on the left for clarity. **F)** West (wellbore-perpendicular) view of the field MC with an approximate trace of the 3D ellipsoid. **G)** Synthetic MC with the ellipsoid trace.

As mentioned earlier, the hull and the slab methods were used to quantify the volume of the microseismic cloud and the associated new surface area due to the hydraulic fracture connected to the wellbore. Figures 1.29A, 1.29B, and 1.29D show the hull volume in blue. The slab volumes are shown in Figures 1.29C and 1.29E. The values are reported in Table 1.11. The inflated fracture slab volume and the inflated+hydraulic fracture slab volume have nearly same values because the hydraulic fracture is contained almost entirely within the microseismic cloud of reactivated fractures. These shapes are shown for only the base case of Stage 2 (Figures 1.29A through 1.29E) for demonstration. For all other dynamic simulation results, only values are presented in the tables.

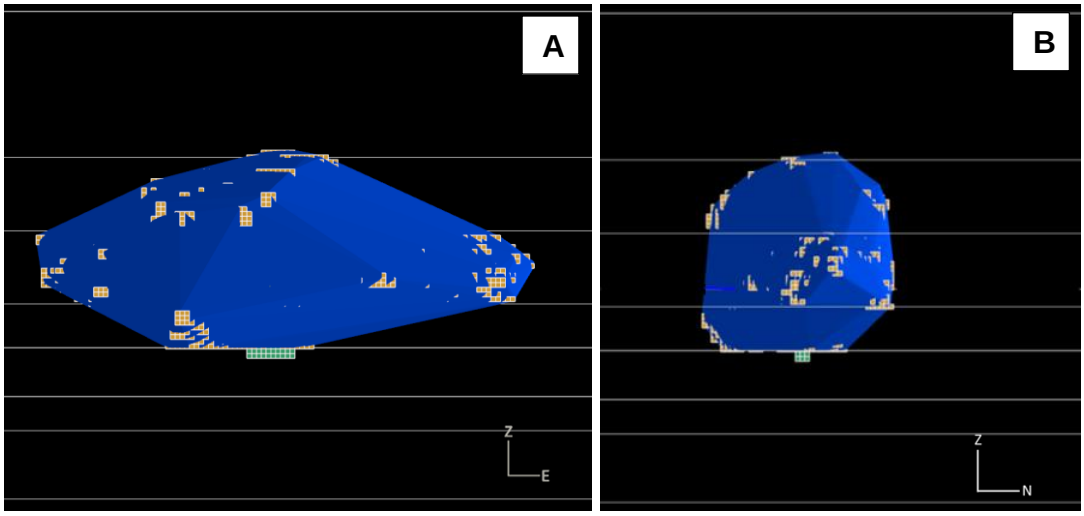

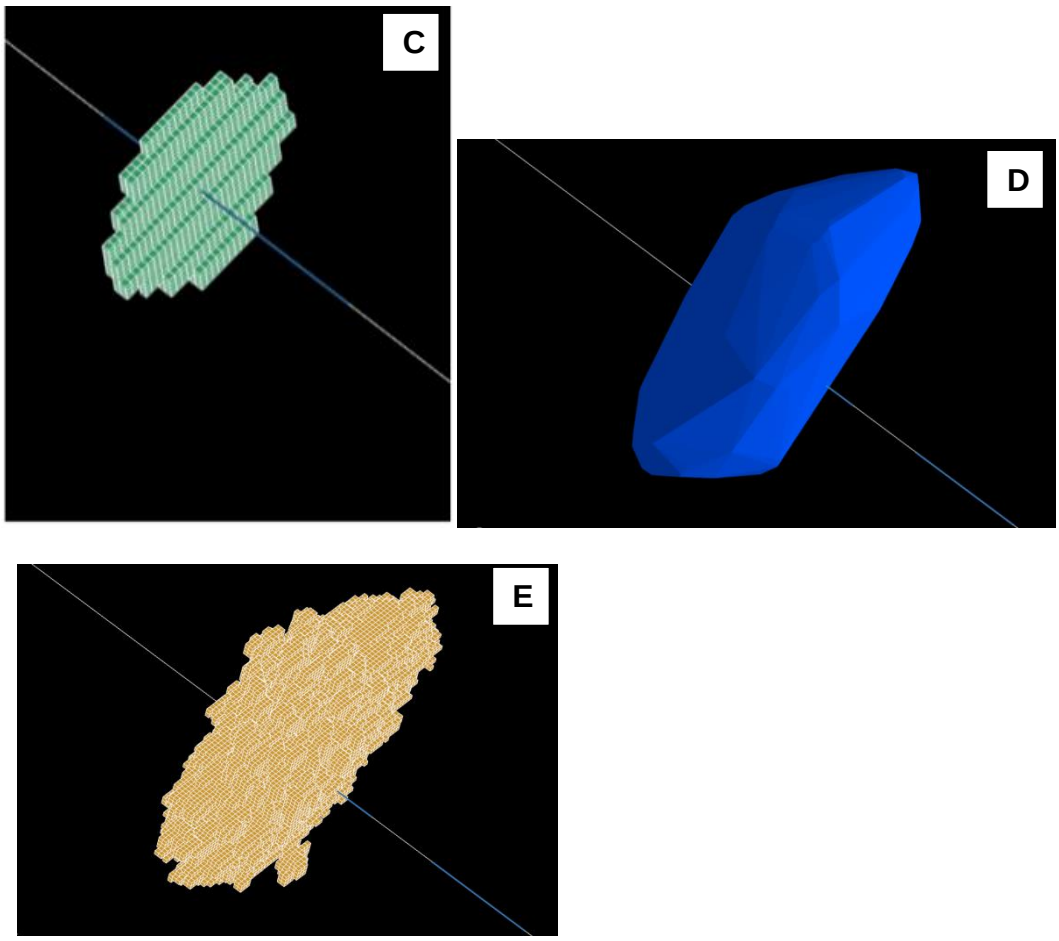

Figure 1.29: Drainage volume estimation using the Hull and Slab methods. **A)** North view of the hull (blue), slab related to natural fracture reactivation (yellow parts sticking out), and slab related to the new hydraulic fracture (green parts sticking out from the bottom). **B)** West-view of the same in A. **C)** Oblique view of the slab (only) related to the hydraulic fracture. **D)** Oblique view of the hull (only) related to the reactivated natural fractures. **E)** Oblique view of the slab (only) related to the reactivated natural fractures.

1.9.1.2 Stage 4

Table 1.13 shows the hydraulic fracture inputs used for Stage 4. Table 1.14 shows the results after the simulation. Table 1.15 shows the comparison between the field and simulated geometries.

Table 1.13: Specific inputs (rotating/adjustable knobs) for Stage 4.

Flow through non-dilatable fracture	Flowback (%)	Max storage aperture (m/mm)	L	M	N	ε_{Hmax}	ε_{hmin}
Yes	20	0.0028/2.8	0.23	0.5	0.27	0.0005	0.00001

Table 1.14: Results from the Stage 4 simulation.

No. of hydrofracture elements	129
Number of injected natural fracture elements	140,397
Vol. in induced hydraulic fractures (m^3/ft^3)	28.4/1003
Vol. in reactivated natural fractures (m^3/ft^3)	2,054.3/72,547
Fluid efficiency (%)	1.4%
Avg. post-hydraulic fracturing aperture (storage aperture) of inflated fractures (m/mm)	0.000807/0.807
Min. aperture of inflated fractures (m/mm)	0/0
Woodford measured volume (m^3)	175,374
Inflated + hydraulic fracture hull volume (m^3)	12,537,942
Inflated + hydraulic fracture slab volume (m^3)	4,788,470
Hydraulic fracture (only) slab volume (m^3)	47,475
Inflated fracture (only) slab volume (m^3)	4,775,562

Table 1.15: Interpreted (int.) short-axis length, long-axis length, and height of the 3D ellipsoid for Stage 4. Also shown are the achieved (ach.) model dimensions and percent differences (diff.). Percentage interpreted occurrence of microseisms are using both wellbore-parallel (north) and wellbore-perpendicular (west) views.

Stage	Short-axis	Long-axis	Height	Percentages from field MC
4 int.	826 ft (252 m)	1865 ft (569 m)	700 ft (213 m)	Woodford 8 > Hunton 15 > Sylvan27 > Viola 17 > Bromide 22 > Sycamore 10 > Caney 1
4 ach.	826 ft (252m)	1865 ft (569 m)	700 ft (213 m)	-
4 diff.	~ 0%	~ 0%	~ 0%	-

In Stage 4, the L = 0.23, M = 0.5, N = 0.27 were needed to get the best geometry match (Figures 1.30A through 1.30G). N = 0.27 implies that the E-W fractures are given higher preference compared to other fracture sets. L = 0.23 indicates higher fluid distribution away from the wellbore indicating higher natural fracture connectivity between formations and less natural fracture clustering near the wellbore. In addition, in the hydraulic fracture definition, the maximum hydraulic fracture aperture (storage aperture) was reduced to 2.8 mm, and the flowback was reduced to 20% (Table 1.13) to get a higher stimulated volume (compared to that in Stage 2) and to get a closer geometry match.

Stage 4 synthetic MC is largely a good match regarding the overall fracture dimension in all three directions (Table 1.15). Including both views, i.e., parallel and perpendicular to the wellbore, the synthetic microseismic cloud shows a slightly lower stimulation in the Woodford Shale and the Sycamore Limestone compared to the field MC (compare Figure 1.30D to 1.30E, and Figure 1.30F to 1.30G). However, the simulated MC agrees with the field MC in that both the Woodford Shale and the Sycamore Limestone have much lower stimulation compared to that of formations below the Woodford Shale. In other words, the stimulation happens primarily downward from the wellbore, with most growth happening in the Hunton Group Limestone, Sylvan Shale, Viola Group Limestone and the Bromide Formation regions. The field observations might be related to the presence of three fracture sets below the Woodford Shale. In the simulation, relatively high permeability values of 0.011 and 0.025 md were needed for the Sylvan Shale and Viola Group Limestone respectively, to

obtain the match. None of the downhole and only zero to two of the surface recorded microseisms are seen in the Caney Shale (Figures 1.30F and 1.30D respectively).

The Viola Group Limestone, in spite of its much higher minimum horizontal stress (Shmin ~ 7700 psi on average, compared to ~ 6650 psi of elevated pore fluid pressure at that depth due to pumping), has fracture reactivation comparable to that of the other formations with much lower horizontal stresses. This observation is remarkable, given two things. First, practically none of the fractures in the Viola Group are critically stressed (Figures 1.27G through 1.27I). Second, creation of new surface area within the Viola Group is impossible because the fluid pressure cannot exceed the normal stress on any fracture. For the simulation, the value of M (transmissivity exponent) = 0.5, and a high Viola Group Limestone permeability value of 0.025 md (used for simulation) was essential for fracture fluid to be distributed into the Viola Group Limestone. In addition, the stimulation in the Viola Group Limestone did not occur when the "pump into non-dilatable fractures" option was not chosen in the hydraulic fracture definition. The fact that the pumped fluid (in the field) passes through Viola Group Limestone fractures, all of which are non-dilatable due to high Shmin, indicates a very high natural fracture permeability due to the presence of open fractures, a high fracture density, or both. Therefore, the field MC presence in the Viola Group is likely due to shear reactivation of some natural fractures (probably with low shear strengths), even though almost none of them were initially critically stressed at a friction angle of 25 degrees (Figures 1.27G and 1.27H).

This fracture growth downward into the highly stressed Viola Group Limestone was not uniquely observed, however, during hydraulically fracturing the Woodford

Shale. This is also sometimes observed while hydraulically fracturing the Barnett Shale, (e.g., Sone and Zoback, 2014b) which is also underlain by the Viola Group Limestone with high Shmin values. The downhole time-lapse seismic shows that the fracture grows down, followed by upward growth during the latter part of the job (Neuhaus, 2011), indicating the Viola Group Limestone was breached first, followed by the Woodford Shale-Sycamore Limestone boundary.

In Table 1.14, the inflated fracture slab volume and the inflated+hydraulic fracture slab volume have nearly same values because the hydraulic fracture is contained almost entirely within the microseismic cloud of reactivated fractures.

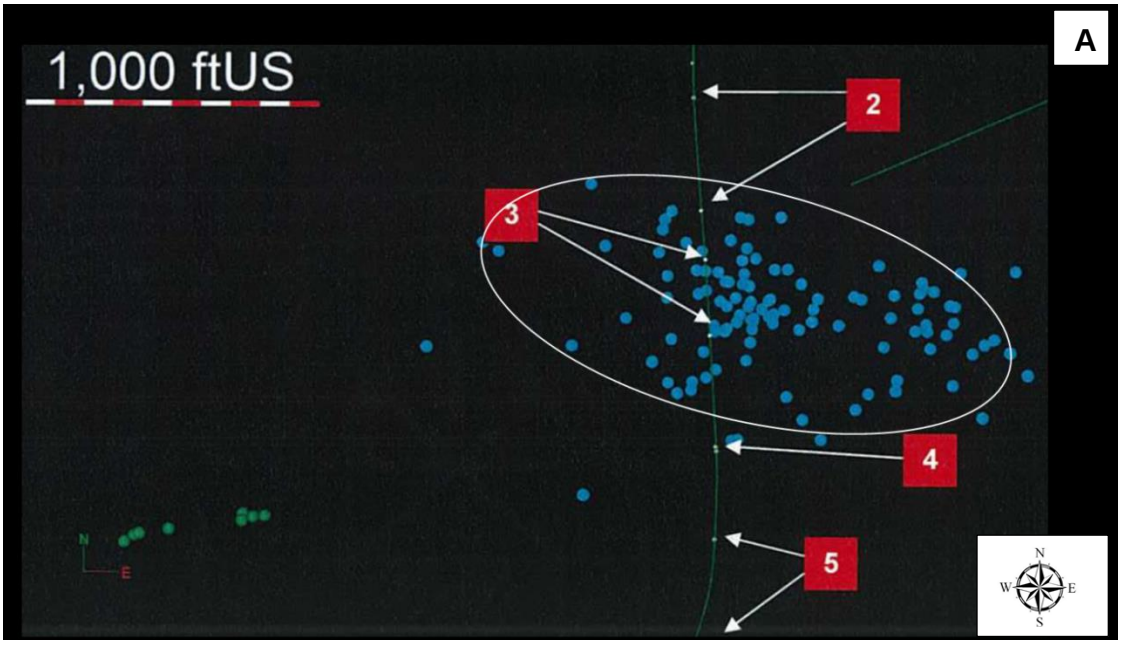

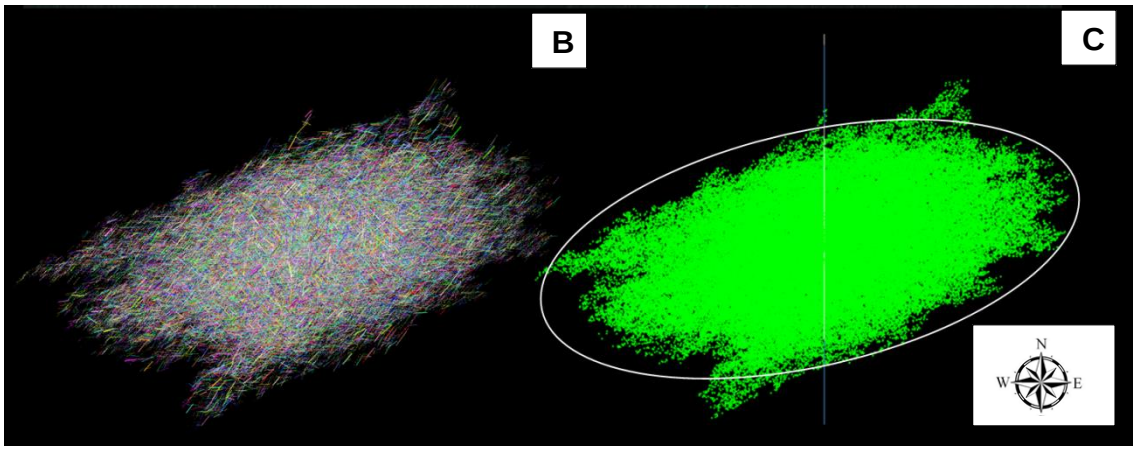
B
C
N
W
E

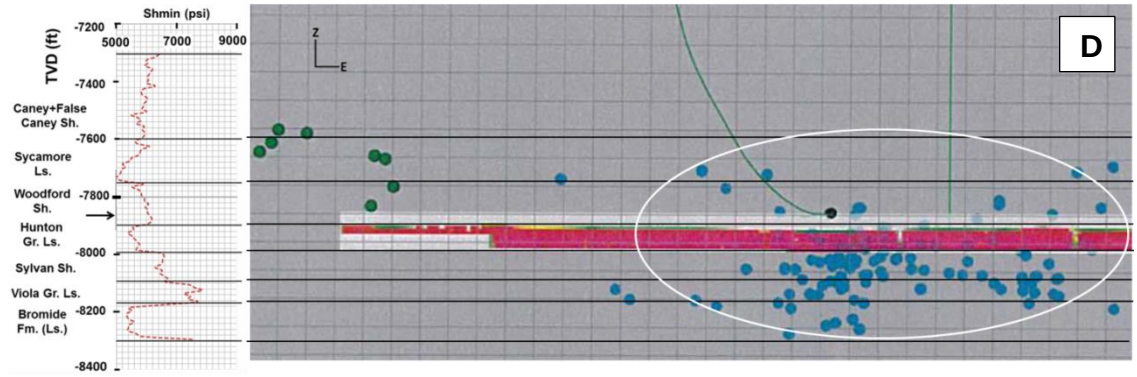
Shmin (psi)
TVD (ft)
-7200
5000
7000
9000
-7400
Caney+False Caney Sh.
-7600
Sycamore Ls.
Woodford Sh.
-7800
Hunton Gr. Ls.
-8000
Sylvan Sh.
Viola Gr. Ls.
Bromide Fm. (Ls.)
-8200
-8400
Z
E
D

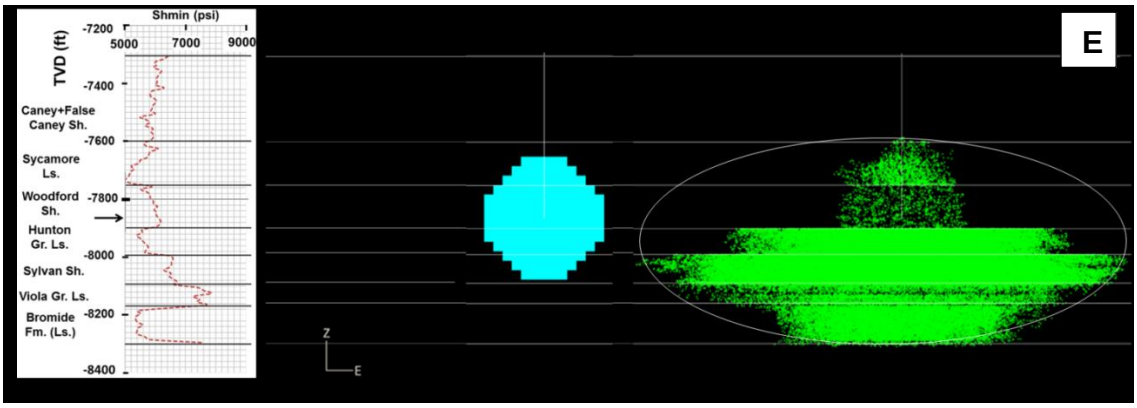
Shmin (psi)
TVD (ft)
-7200
5000
7000
9000
-7400
Caney+False Caney Sh.
-7600
Sycamore Ls.
Woodford Sh.
-7800
Hunton Gr. Ls.
-8000
Sylvan Sh.
Viola Gr. Ls.
Bromide Fm. (Ls.)
-8200
-8400
Z
E
E

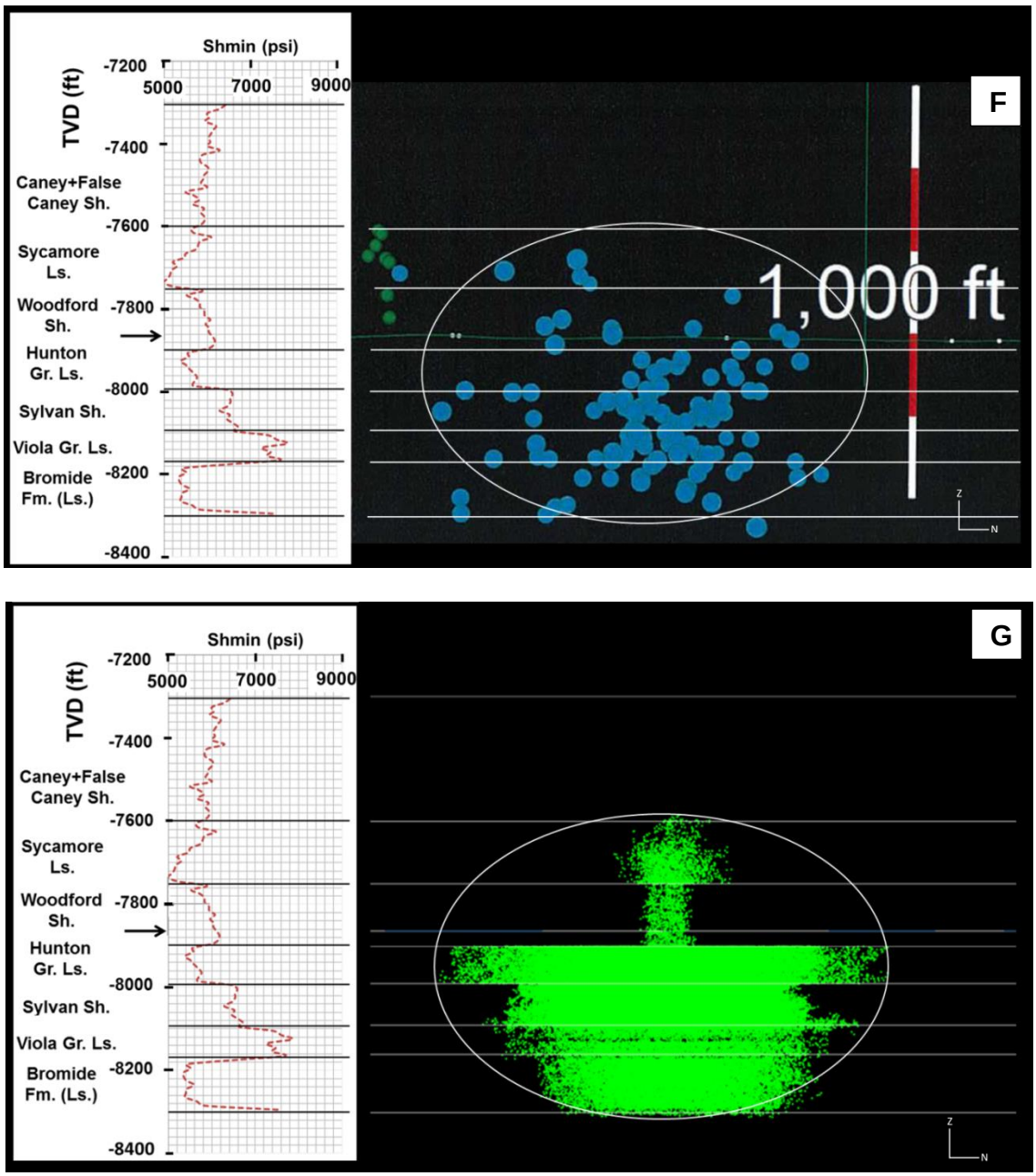

Figure 1.30: Field and modeled microseismic cloud geometries for Stage 4. **A)** Map view of the field MC obtained for Stage 4. Perforations for Stages 2, 3, 4, and 5 are marked. The zone containing the highest MC density is marked within the trace of a 3D ellipsoid. Green: surface recorded MC; blue: downhole recorded MC. **B)** Map view of reactivated natural fractures. **C)** Map view of the synthetic MC. Overlay of the 3D ellipsoid trace in A is shown for comparison. **D)** North (wellbore-parallel) view of the field MC along with the 3D ellipsoid trace. **E)** Synthetic MC with ellipsoid trace. The main hydraulic fracture connected to the wellbore is shown separately on the left. **F)** West (wellbore-perpendicular) view of the field MC with an approximate trace of the 3D ellipsoid. **G)** Synthetic MC with the ellipsoid trace.

1.9.1.3 Stage 5

Table 1.16 shows the hydraulic fracture inputs used for Stage 5. Table 1.17 shows the results after the simulation. Table 1.18 shows the comparison between the field and simulated geometries.

Table 1.16: Specific inputs (rotating/adjustable knobs) for Stage 5.

Flow through non-dilatable fracture	Flowback (%)	Max storage aperture (m/mm)	L	M	N	ε_{Hmax}	ε_{hmin}
Yes	20	0.0024/2.4	0.5	0	0.5	0.0005	0.000025

Table 1.17: Results from the Stage 5 simulation.

No. of hydrofracture elements	159
Number of injected natural fracture elements	100,694
Vol. in induced hydraulic fractures (m^3/ft^3)	28.3 /1,000
Vol. in reactivated natural fractures (m^3/ft^3)	2,054.1/72,540
Fluid efficiency (%)	1.4
Avg. post-hydraulic fracturing aperture (storage aperture) of inflated fractures (m/mm)	0.00143/1.43
Min. aperture of inflated fractures (m/mm)	0
Woodford measured volume (m^3)	2,062,259
Inflated + hydraulic fracture hull volume (m^3)	7,973,337
Inflated + hydraulic fracture slab volume (m^3)	3,120,000
Hydraulic fracture (only) slab volume (m^3)	57,501
Inflated fracture (only) slab volume (m^3)	3,108,012

Table 1.18: Interpreted (int.) short-axis length, long-axis length, and height of the 3D ellipsoid for Stage 5. Also shown are the achieved (ach.) model dimensions and percent differences (diff.). Percentage interpreted occurrence of microseisms are using both wellbore-parallel and wellbore-perpendicular views from Neuhaus (2011).

Stage	Short-axis	Long-axis	Height	Percentages from field MC
5 int.	548 ft (167m)	1580 ft (482 m)	765 (233 m)	Woodford 24 > Hunton 20 > Sylvan 20 > Sycamore 11 > Caney 10 > Viola 8 > Bromide 7
5 ach.	600 ft (183 m)	1551 ft (473 m)	730 ft (223 m)	-
5 diff.	9.4%	1.8%	4.6%	-

A discrepancy of 2-9% exists between the field and modeled MC dimensions (Table 1.18). The match between the field and the synthetic MC dimensions for Stage 5 (Figures 1.31A through 1.31G) was achieved using by L = 0.5, M = 0, N = 0.5 (Table 1.16). Again, in this case, the relative permeability of the formations is not important (M = 0). This again indicates that the E-W fractures (i.e., fractures oriented sub-parallel to the direction of maximum horizontal stress) have higher priority compared to the other fracture sets. Permeability ratios between the formations are not important for this stage (M = 0). A minimum strain of 2.5e-5 was needed to get a better match with the field microseismic shape, indicating that the minimum strain had increased from 1e-5 used in Stages 2 and 4.

The field microseismic cloud shows that the fluid was relatively evenly distributed among the six formations present above the Bromide Formation, which was matched in the model MC. Both the field and the synthetic microseismic cloud in the Woodford Shale show substantial lateral growth. Wellbore parallel view shows a well-defined fracture barrier at the Viola Group Limestone-Bromide Formation boundary due to terminations of the downhole recorded microseisms at the boundary (Figure

1.31D). However, in the view perpendicular to the wellbore, the downhole recorded microseisms seem to have breached the boundary (Figure 1.31F), which is the case with the modeled microseismic cloud. Theoretically, this boundary is easier to penetrate, given the larger number of critically stressed fractures (Figures 1.27J through 1.27L) and much lower Shmin (Figure 1.26) in the Bromide Formation, compared to that of the Viola Group Limestone. The downhole time-lapse seismic shows that the fracture grew upward and downward simultaneously (Neuhaus, 2011).

In Table 1.17, the inflated fracture slab volume and the inflated+hydraulic fracture slab volume have nearly same values, similar to that in Stages 2 and 4 because the hydraulic fracture is contained entirely within the microseismic cloud of reactivated fractures.

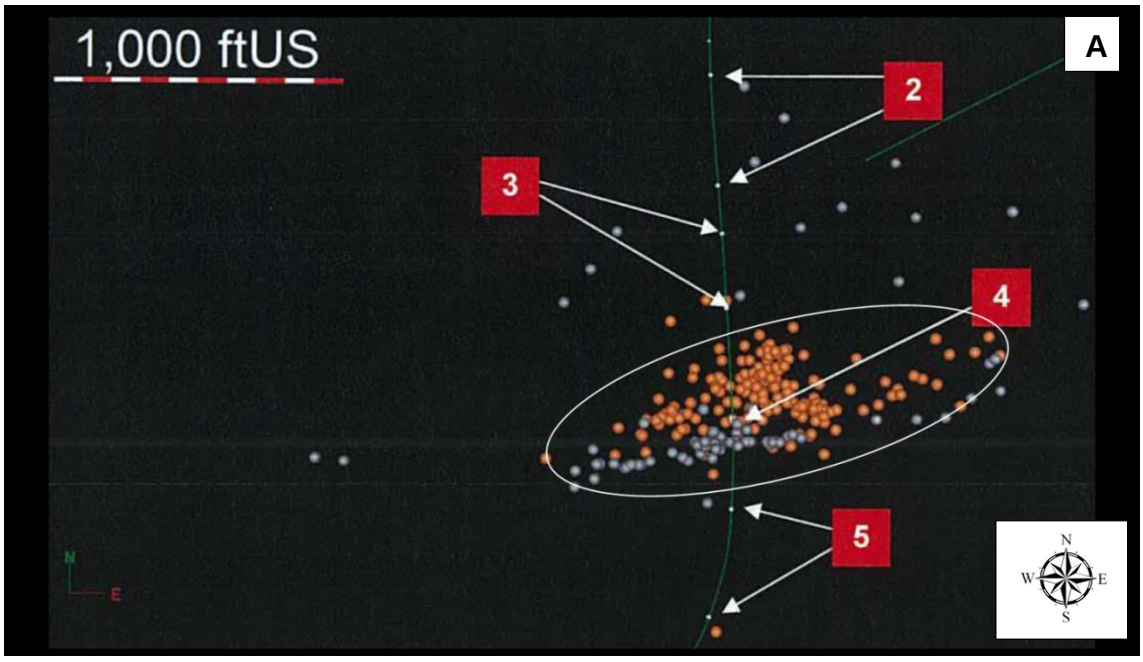

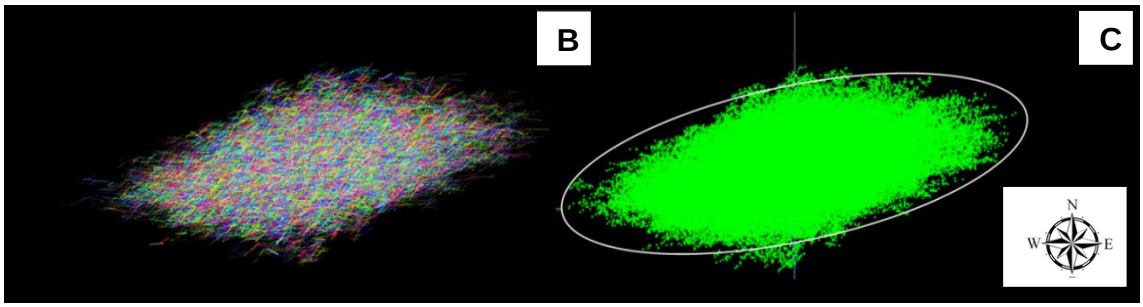
B
C
N
W
E

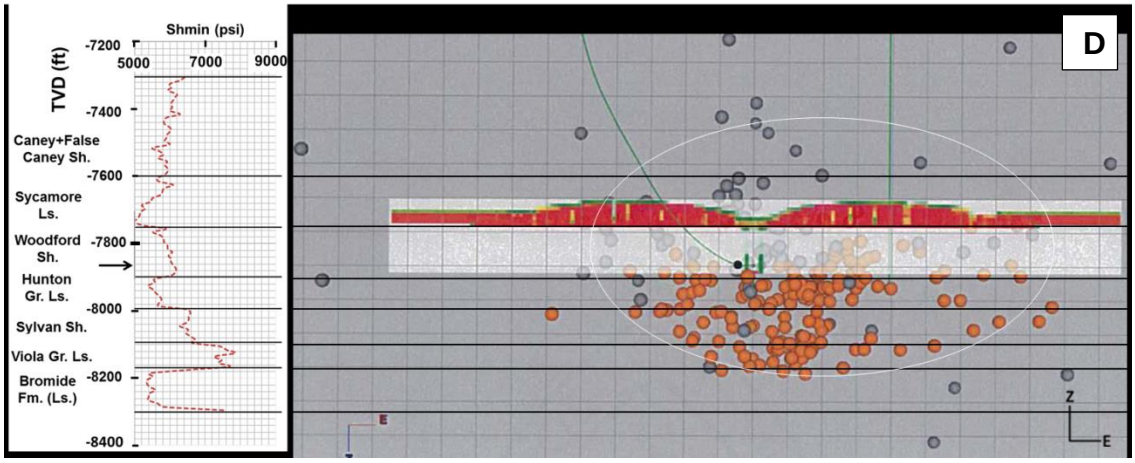
Shmin (psi)
5000
7000
9000
TVD (ft)
-7200
-7400
-7600
-7800
-8000
-8200
-8400
Caney+False Caney Sh.
Sycamore Ls.
Woodford Sh.
Hunton Gr. Ls.
Sylvan Sh.
Viola Gr. Ls.
Bromide Fm. (Ls.)
D
Z
E

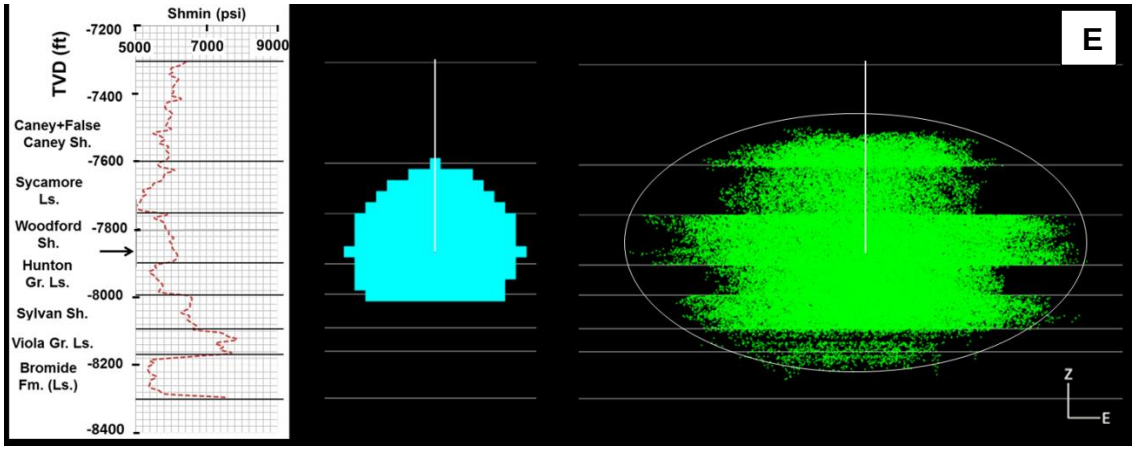
Shmin (psi)
5000
7000
9000
TVD (ft)
-7200
-7400
-7600
-7800
-8000
-8200
-8400
Caney+False Caney Sh.
Sycamore Ls.
Woodford Sh.
Hunton Gr. Ls.
Sylvan Sh.
Viola Gr. Ls.
Bromide Fm. (Ls.)
E
Z
E

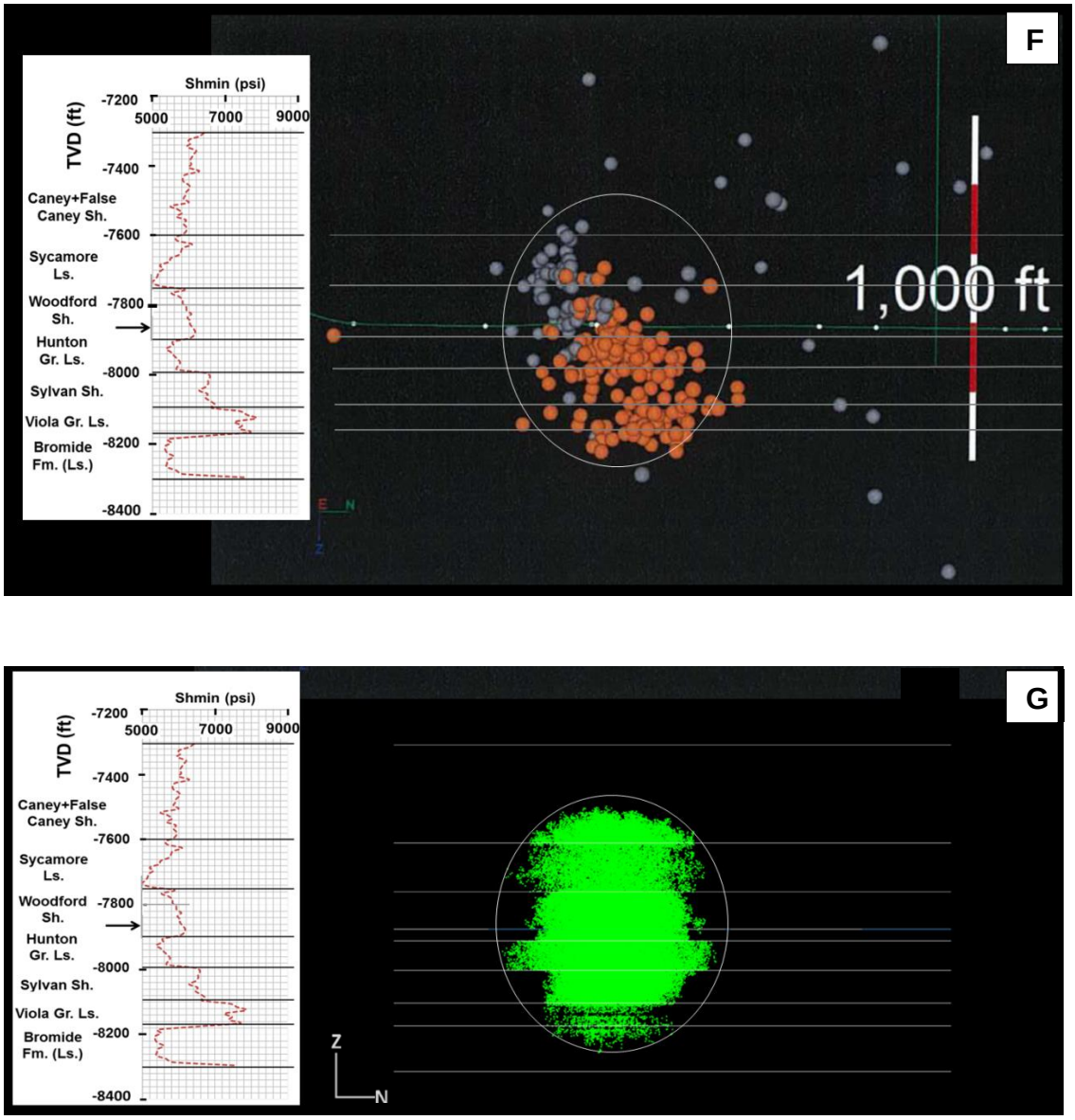

Figure 1.31: Field and modeled microseismic cloud geometries for Stage 5. **A)** Map view of the field MC obtained for Stage 5. Perforations for Stages 2, 3, 4 and 5 are marked. The zone containing the highest MC density is marked within the trace of a 3D ellipsoid. Grey: surface recorded MC; orange: downhole recorded MC. **B)** Map view of reactivated natural fractures. **C)** Map view of the synthetic MC. Overlay of the 3D ellipsoid trace in A is shown for comparison. **D)** North (wellbore-parallel) view of the field MC along with the 3D ellipsoid trace. **E)** Synthetic MC with ellipsoid trace. The main hydraulic fracture connected to the wellbore is shown separately on the left. **F)** West (wellbore-perpendicular) view of the field MC with an approximate trace of the 3D ellipsoid. **G)** Synthetic MC with the ellipsoid trace.

1.9.2 Prediction of MC geometry under different scenarios (sensitivity analyses)

The effects of well location, tectonic strain (related to Shmin and SHmax), fracture fluid efficiency, ISIP (net pressure), pressure-drop slope, and fracture intensity on the shape of the simulated microseismic cloud, and accompanying hydraulic fracture is discussed in this section. Well stages that best depict the effects of different variables are shown along with the base cases (i.e., best matches with the MC discussed earlier) for comparison.

1.9.2.1 Effect of well location

Well landing location is one of the most important issues when considering hydraulic fracturing in the Woodford Shale (Slatt et al., 2015). Stage 4 is shown as an example because it covers the highest volume among the three stages and therefore captures the MC variation in different layers. Locations of wells 2 and 3 were chosen based on the fact that the upper well (Well 3 [Figures 1.32A and 1.32B]) had a 9% lower Young's modulus and 6% higher Poisson's ratio compared to Well 2 ([Figures 1.32C and 1.32D]). Well 2 (7834 ft) and Well 3 (7824 ft) are only 10 ft apart so that height difference cannot cause a major change in MC geometry.

Table 1.19 shows that the Well 2 and Well 3 final storage apertures, hydrofracture elements, fluid efficiency, and the number of inflated fracture values are similar to that of the base case. Minor differences in the number of injected natural fractures exist because fractures in different layers are of different sizes and densities. The storage aperture progressively increases in small amounts due to a slightly lower number of non-dilatable fractures being injected, going from Well 1 to Well 3. Progressively narrower synthetic MC in the Bromide Formation and wider MC in the

Sylvan Shale and the Sycamore Limestone is seen, going from Well 1 (base case) to Well 3 (Figures 1.32G, 1.32C, and 1.32A respectively). Thinning in the Bromide Formation and widening in the Sycamore Limestone is also seen parallel to the well (Figures 1.32F, 1.32D, and 1.32B). Overall, there is an upward shift in the MC, and the hydraulic fracture due to an upward shift in the well locations. General, upward movement of the MC due to the upward shifting of the wells was also shown by the other stages. However, comparing values from Table 1.19 for the three different wells shows no significant change (< 6%) in any of the overall volumetric parameters or the number of natural fracture reactivations.

Table 1.19: Comparison of Stage 4 simulation results from Wells 2 and 3 with the base case (Well 1) Stage 4 results.

	Base case: Well 1, Stage 4 (7864 ft)	Well 2, Stage 4 (7834 ft)	Well 3, Stage 4 (7824 ft)
No. of hydrofracture elements	129	129 (0%)	129 (0%)
Number of injected natural fracture elements	140,397	136,882 (-2%)	134,194 (-4%)
Vol. in induced hydraulic fractures (m^3/ft^3)	28.4/1,003	28.4/1,003	28.4/1,003
Vol. in reactivated natural fractures (m^3/ft^3)	2,054.3/72,547	2,054.8/72,564	2054.8/72,564
Fluid efficiency (%)	1.4	1.4	1.4
Avg. post-hydraulic fracturing apertures (storage apertures) of inflated fractures (m/mm)	0.000807/0.807	0.000823/0.823 (+2%)	0.000836/0.836 (+4%)
Min. aperture of inflated fractures (m/mm)	0/0	0/0	0/0
Woodford measured volume (m^3)	175,374	175,374 (0%)	175,374 (0%)
Inflated + hydraulic fracture hull volume (m^3)	12,537,942	13,247,732 (+6%)	12,986,356 (+4%)
Inflated + hydraulic fracture slab volume (m^3)	4,788,470	4,698,676 (-2%)	4,634,090 (-3%)
Hydraulic fracture (only) slab volume (m^3)	47,475	47,050 (+0%)	48,376 (+2%)
Inflated fracture (only) slab volume (m^3)	4,775,562	4,684,882 (-2%)	4,620,147 (-3%)
Short-axis (m)	252	271	247
Long-axis (m)	569	573	568
Height (m)	213	213	213

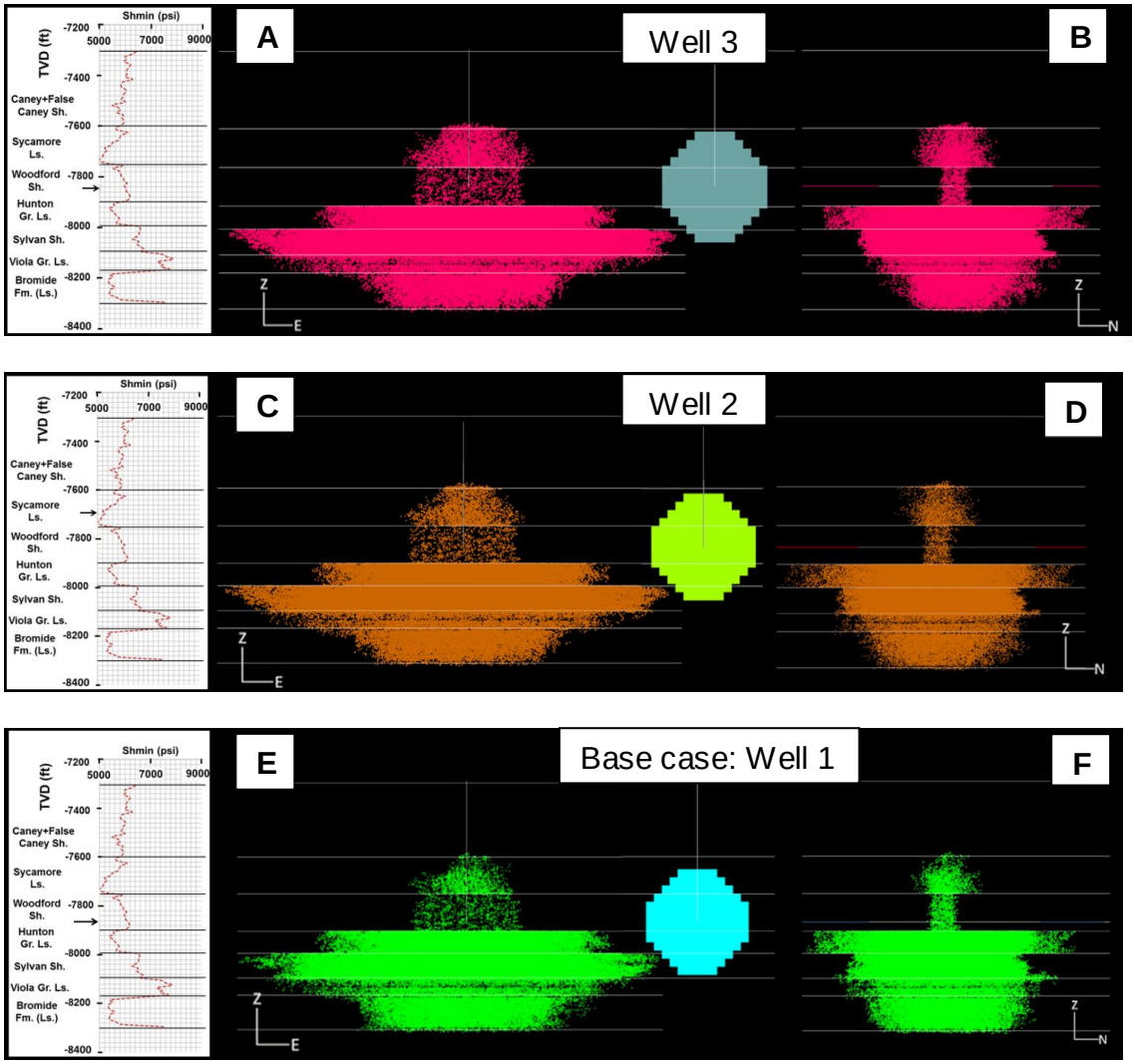

Figure 1.32: Effect of well location on Stage 4 MC geometries. **A)** North view of Well 3 (7824 ft), Stage 4 MC and hydraulic fracture. **B)** Same MC as A in west view. **C)** North view of Well 2 (7834 ft), Stage 4 MC and hydraulic fracture. **D)** Same MC as C in west view. **E)** North view of Well 1 (base case: 7864 ft), Stage 4 MC and hydraulic fracture. **F)** Same MC as E in west view.

1.9.2.2 Effect of change in horizontal stress due to change in minimum strain

It is common knowledge that with an increase in the number of hydraulic fracturing stages, there is an increase in the minimum horizontal strain. This leads to an increase in the minimum horizontal stress. Therefore, to predict the effect of strain increase with subsequent stages, a minimum strain (ε_{hmin}) of 0.00003 was chosen, which

is higher than the ε_{hmin} = 0.00001 used for Stages 2 and 4, and also slightly higher than the ε_{hmin} = 0.000025 used for Stage 5.

Figure 1.26 mentioned earlier shows that because of increase in the minimum strain, the Shmin contrast between shales and carbonates decreases. This is because Shmin buildup in shales is slower than that in carbonates. However, ε_{hmin} = 0.00003 is not enough for the carbonates (except Viola Group Limestone) to exceed the Shmin in the shales. Also, the gap between the SHmax and Shmin closes within each layer due to the previous hydraulic fracturing job. Because of the lower gap between SHmax and Shmin, more complex fractures are created closer to the wellbore. This also means that more natural fractures within the remaining layers will be injected to balance the pumped fluid volume as shown in Figures 1.33C, 1.33D and Figures 1.34C, 1.34D for Stages 4 and 5 respectively. Due to the fluid volume balance considerations, the fluid that was mainly lost by the Bromide Formation was distributed among the other formations. However, for Stage 4 and 5, the hydraulic fracture (new surface) size does not change more than a couple of percent, i.e., the extra fluid is diverted into other natural fractures rather than creating new surface area.

For Stage 4, with ε_{hmin} = 0.00003, the MC density increases in the Sycamore Limestone, Woodford Shale, and Hunton Group Limestone, with a decrease in the Sylvan Shale, Viola Group Limestone, and Bromide Formation (Figure 1.33D). For Stage 5, with ε_{hmin} = 0.00003, there is higher MC density in the Woodford with zero density in the Sylvan Shale and Viola Group Limestone (Figure 1.34D). The overall MC height decreases for both Stages 4 and 5. Because the MC shifts up, the fluid travels through fewer non-dilatable fractures, which transmit fluid (or fluid pressure)

but have zero storage apertures, reducing the total number of injected fractures (Table 1.20). With less fluid going through non-dilatable fractures, the average storage aperture increases from 0.807 mm (base case) to 0.98 mm for Stage 4, and 1.43 mm to 1.87 mm for Stage 5.

Table 1.20 shows that the Woodford Shale volume increases by 29% for Stage 4 and not much for Stage 5. There is a large discrepancy between the change in hull volumes and slab volume for Stage 4. While the hull volume increases 14%, the slab volume decreases 15% as compared to Stage 4 base case. In this case, the slab volume decrease should be considered as the real change because there is empty space in case of hull volume. For Stage 5, there is a decrease in both hull and slab volume of greater than 20%. Compared to the base case, the fracture stimulation has a slight tendency to grow upwards with increasing strain because Shmin increases faster in the layers below the Woodford compared to that above the Woodford (Figure 1.26). Therefore, minor increases in horizontal strain can cause a considerable difference in the final stimulated volume and possibly, in the number of reactivated fractures, and overall volume (> 20%). More importantly, the stimulation volume in Woodford Shale increases in all three stages with an increase in the minimum strain.

Table 1.20: Comparison of Stage 4 and 5 simulation results at ε_{hmin} = 0.00003 with base case Stage 4 and 5 results.

	Base case: Stage 4 (ε_{hmin} = 0.00001)	Stage 4 (ε_{hmin} = 0.00003)	**Base case:** Stage 5 (ε_{hmin} = 0.000025)	Stage 5 (ε_{hmin} = 0.00003)
No. of hydrofracture elements	129	129 (0%)	159	150 (-6%)
Number of injected natural fracture elements	140,397	120,066 (-14%)	100,694	78,053 (-23%)
Vol. in induced hydraulic fractures (m^3/ft^3)	28.4/1003	28.4/1003	28.3 /1000	28.3/1000
Vol. in reactivated natural fractures (m^3/ft^3)	2,054.3/72,547	2,055/72,572	2,054.1/72,540	2,054/72,536
Fluid efficiency (%)	1.4	1.4	1.4	1.4
Avg. post-hydraulic fracturing apertures (storage apertures) of inflated fractures (m/mm)	0.000807/0.807	0.000983/0.98 (+21%)	0.00143/1.43	0.00187/1.87 (+31%)
Min. aperture of inflated fractures (m/mm)	0/0	0/0	0/0	0/0
Woodford measured volume (m^3)	175,374	226,232 (+29%)	2,062,259	2,144,750 (+4%)
Inflated + hydraulic fracture hull volume (m^3)	12,537,942	14,261,715 (+14%)	7,973,337	6,121,283 (-23%)
Inflated + hydraulic fracture slab volume (m^3)	4,788,470	4,047,956 (-15%)	3,120,000	2,459,986 (-21%)
Hydraulic fracture (only) slab volume (m^3)	47,475	47,579 (+0%)	57,501	53,987 (-6%)
Inflated fracture (only) slab volume (m^3)	4,775,562	4,034,016 (-15%)	3,108,012	2,452,688 (-21%)
Short-axis (m)	252	332	183	185
Long-axis (m)	569	594	473	488
Height (m)	213	201	223	152

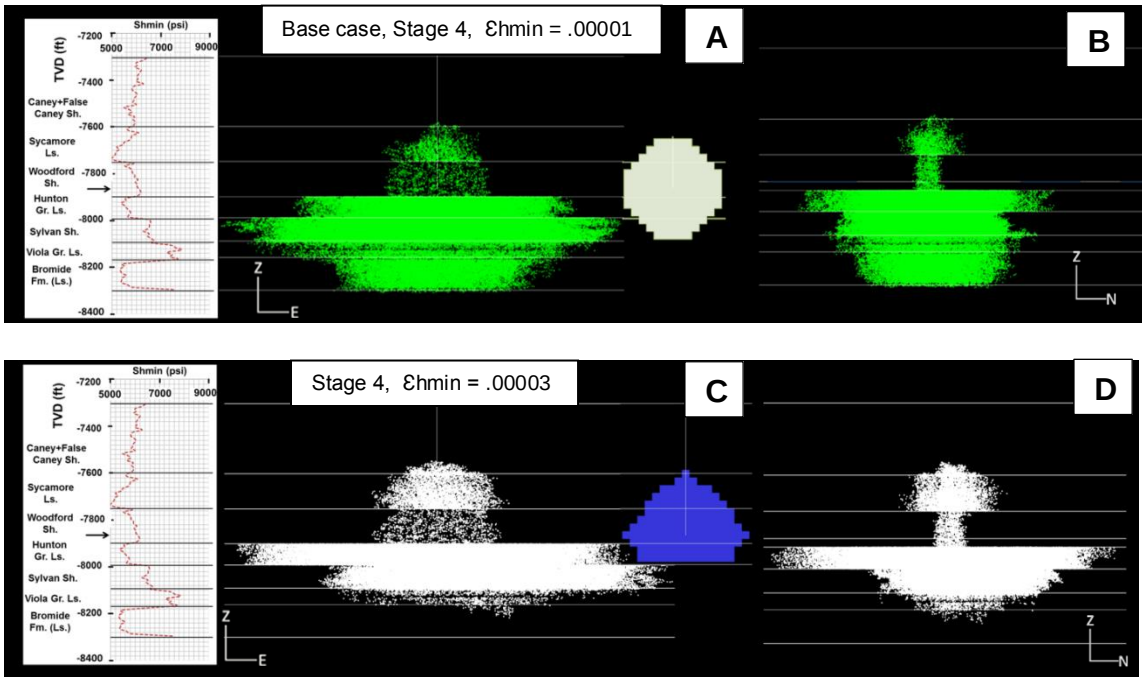

Figure 1.33: Effect of change in ε_{hmin} on Stage 4 MC geometry. **A)** Stage 4 base case MC cloud in north view along with hydraulic fracture. **B)** Stage 4 base case MC cloud in west view. **C)** MC cloud and hydraulic fracture, in north view, after an increase in the minimum and maximum stress due to increase in minimum strain from the base case of 0.00001 to 0.00003. **D)** Same MC as in C in west view.

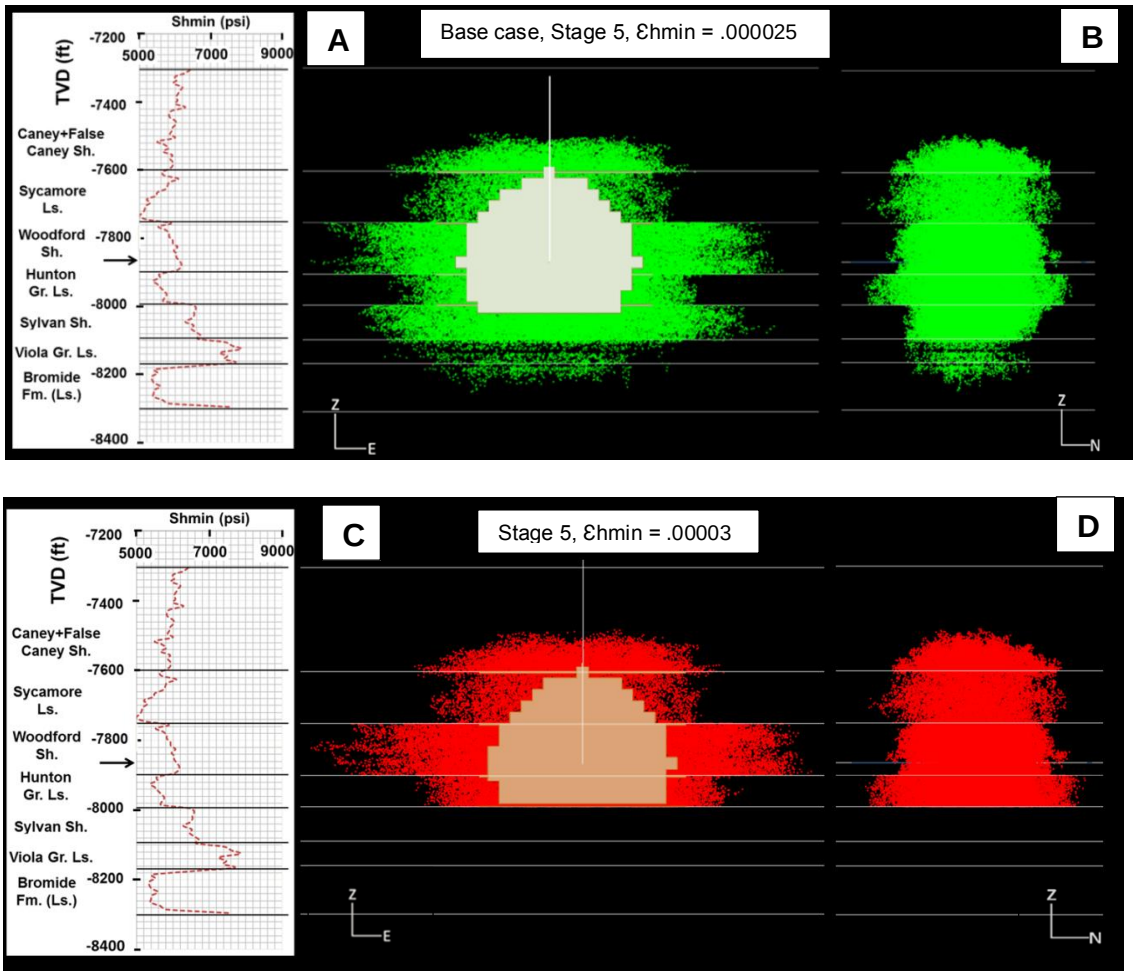

Figure 1.34: Effect of change in $Ɛ_{hmin}$ on Stage 5 MC geometry. **A)** Stage 5 base case MC cloud in north view along with the hydraulic fracture overlay. **B)** Stage 4 base case MC cloud in west view. **C)** MC cloud along with hydraulic fracture overlay, in north view, after an increase in the minimum and maximum stress due to increase in minimum strain from the base case of 0.000025 to 0.00003. **D)** Same MC as C in west view.

1.9.2.3 Effect of change in ISIP

The ISIP (instantaneous shut-in pressure) is generally known as the fracture gradient, and the difference between the ISIP and closure pressure is known as the net pressure on the fracture walls. Increasing the ISIP (fracture operational parameter in FracMan^{TM}) basically increases the fluid pressure that is applied on the fracture wall, i.e., the difference between the fluid pressure and the Shmin (grid parameter) increases.

This concept applied in FracMan^{TM} is different compared to history match concept (during the hydraulic fracturing process), in which difference between the treatment pressure and the Shmin varies during the treatment. The net pressure (ISIP-Shmin) is dependent on the pump rate among other variables. However, an equivalence of pumping rate to net pressure is difficult to obtain. To predict the shift in position and shape of the MC, a higher ISIP of 7000 psi was chosen, which exceeds the base case ISIP by 500 psi. Observing Figure 1.24, this value is within the range that might be interpreted by some as a possible ISIP value.

For Stage 2, choosing a higher ISIP showed a generally downward natural fracture reactivation into the Hunton Group Limestone and the Sylvan Shale (compare Figure 1.35C to 1.35A, and Figure 1.35D to 1.35B respectively). This stage shows 11% reduction in the number of injected natural fractures without a change in the average storage aperture (Table 1.21). Counterintuitively, there is no change in the hydraulic fracture size, i.e., according to the software, the new surface area does not increase upon increasing ISIP. This implies that the reduction in the number of reactivated fractures is related to the variation in the number and size (height and length) of fractures in different layers in which the fluid the frac fluid is pumped. Table 1.21 shows that in case of Stage 2, the Woodford stimulation volume decreases 74% and the overall stimulation volume decreases between 8% and 14% at higher ISIP value.

For Stage 4, at ISIP = 7000 psi, not just a downward growth from the Sycamore Limestone but also a substantial reduction in the volume of the synthetic microseismic cloud is seen (> 50% in the overall volume and 10% in the Woodford volume), which gives an impression that the MC is growing upward from the Bromide Formation.

(compare Figure 1.36C to 1.36 A, and Figures 1.36D to 1.36B). At ISIP = 7000 psi, a 2.5 times increase in aperture is seen along with a 50% reduction in the number of pumped natural fractures (Table 1.21). Counterintuitively, again there is a slight decrease (5%) in the hydraulic fracture size, i.e., according to the software, the new surface does not increase upon increasing ISIP. This implies that decrease in the overall stimulation volume is accommodated by an increase in average storage aperture. Due to less pumping (flow through) in non-dilatable fractures away from the wellbore (which have zero storage aperture), the average storage aperture increases. Also, at a higher pump rate, some fractures (near the wellbore) which were previously (at ISIP = 6500 psi) non-dilatable become dilated, i.e., fractures oriented at progressively higher angles to SHmax open up with higher pressure (and have non-zero apertures). A downward movement and shortening perpendicular and parallel to the well should be expected for all stages in this area. Stage 5 had results similar to that in Stage 4, i.e., a considerable reduction in MC volume accompanied by downward growth.

Therefore, considering the extent of the MC density, a higher net pressure is not desirable because in both cases, the MC density within the Woodford Shale decreases. However, in the short run, increased opening of fractures near the wellbore may provide high initial production.

Table 1.21: Comparison of Stage 2 and 4 simulation results (ISIP = 7000 psi) with base case Stage 2 and 4 (ISIP = 6500 psi) results.

	Base case: Stage 2 (ISIP = 6500 psi)	Stage 2 (ISIP = 7000 psi)	**Base case:** Stage 4 (ISIP = 6500 psi)	Stage 4 (ISIP = 7000 psi)
No. of hydrofracture elements	57	57 (0%)	129	129 (0%)
Number of injected natural fracture elements	24,339	21,470 (-12%)	140,397	68,409 (-51%)
Vol. in induced hydraulic fractures (m^3/ft^3)	26.5/937	26.9/950	28.4/1,003	28.4
Vol. in reactivated natural fractures (m^3/ft^3)	1927.5/68,051	1931.4/68,207	2054.3/ 72,547	2054.4/72,550
Fluid efficiency (%)	1.4	1.4	1.4	1.4
Avg. post-hydraulic fracturing apertures (storage apertures) of inflated fractures (m/mm)	0.00589/5.89	0.00589/5.89 (0%)	0.000807 /0.807	0.002/2 (+130%)
Min. aperture of inflated fractures (m/mm)	0.000017/.017	0.000002/0.002	0/0	0/0
Woodford measured volume (m^3)	1,099,447	395,800 (-74%)	175,374	157,837 (-10%)
Inflated + hydraulic fracture hull volume (m^3)	1,886,322	1,619,987 (-14%)	12,537,942	6,507,203 (-48%)
Inflated + hydraulic fracture slab volume (m^3)	740,311	677,513 (-8%)	4,788,470	2,310,000 (-52%)
Hydraulic fracture (only) slab volume (m^3)	19,458	19,643 (+0%)	47,475	45,070 (-5%)
Inflated fracture (only) slab volume (m^3)	734,121	673,346 (-8%)	4,775,562	2,295,779 (-52%)
Short-axis (m)	97	109	252	189
Long-axis (m)	320	203	569	375
Height (m)	116	146	213	203

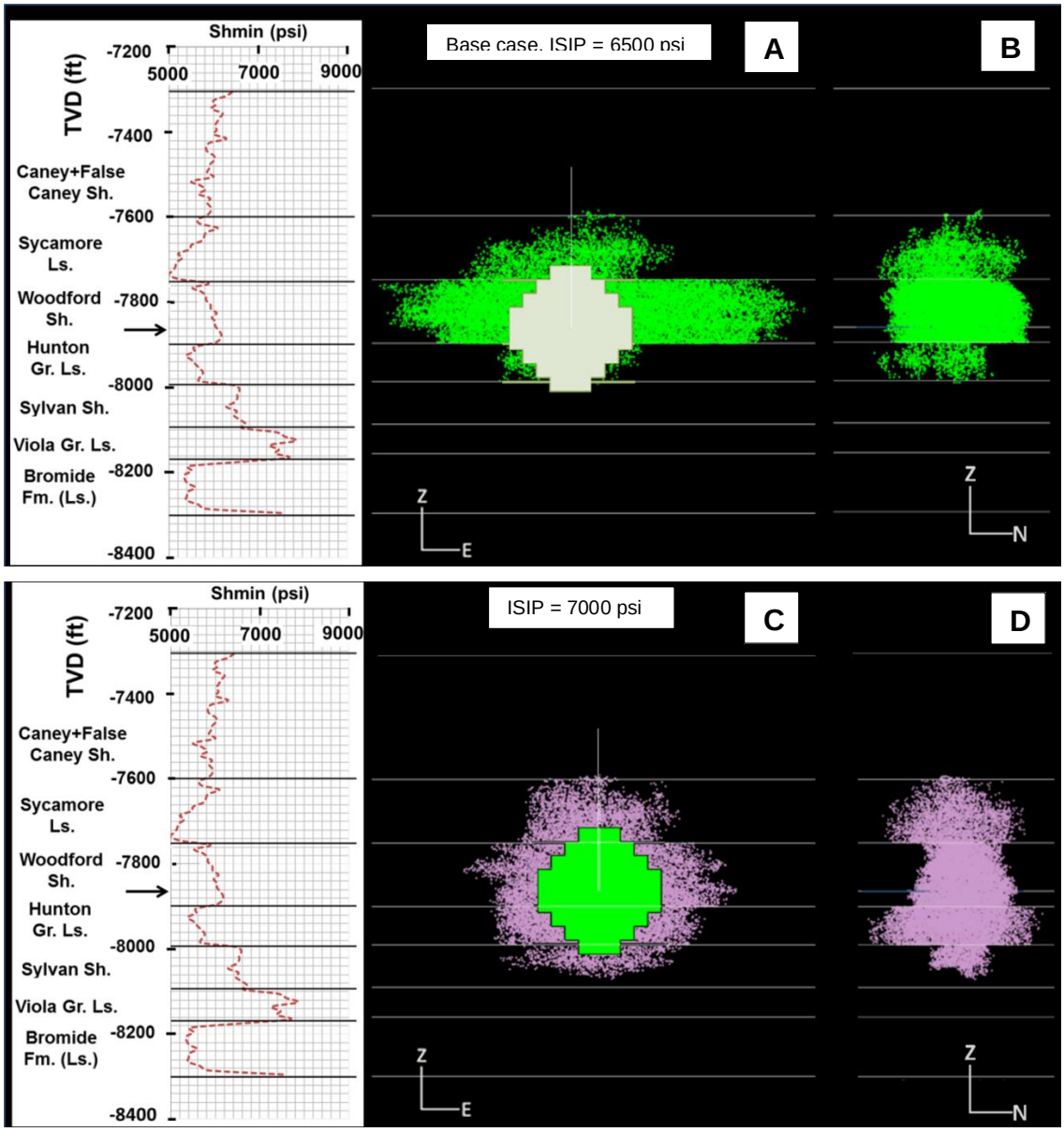

Figure 1.35: Effect of net pressure change on Stage 2 MC geometry. **A)** Stage 2 base case (ISIP = 6500 psi) MC cloud in north view along with hydraulic fracture. **B)** Stage 2 base case (ISIP = 6500 psi) MC cloud in west view. **C)** Stage 2 (ISIP = 7000 psi) MC cloud in north view along with hydraulic fracture. **D)** Same MC as C in west view. In C and D, notice the vertical growth (mainly downwards [compared to the base case]) and decrease in MC horizontal sizes in the Woodford Shale in directions both parallel and perpendicular to the wellbore (compared to the base case).

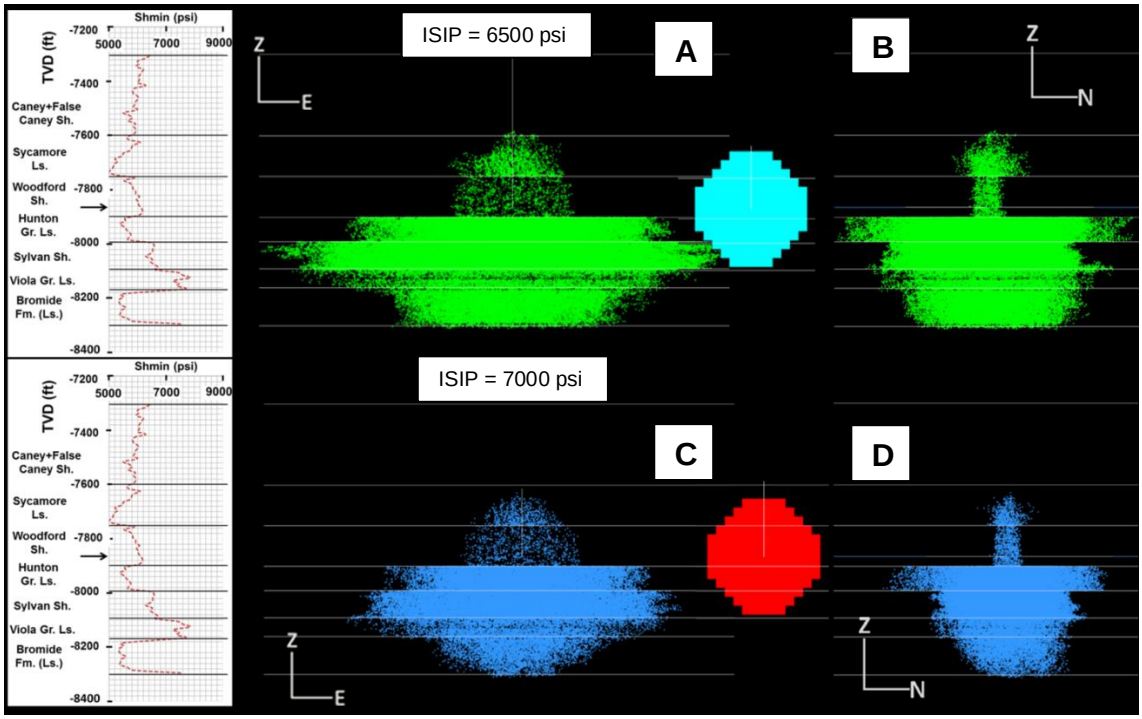

Figure 1.36: Effect of net pressure change on Stage 4 MC geometry. **A)** Stage 4 base case (ISIP = 6500 psi) MC cloud in north view along with hydraulic fracture. **B)** Stage 4 base case (ISIP = 6500 psi) MC cloud in west view. **C)** Stage 4 (ISIP = 7000 psi) MC cloud in north view along with hydraulic fracture. **D)** Same MC as C in west view. Notice the decrease in MC horizontal sizes in directions parallel and perpendicular to the well, with an increase in ISIP.

1.9.2.4 Effect of pressure-drop slope value

The pressure drop due to fluid flow in geologic fractures is not well understood. Therefore, it is worthwhile to understand its effect on the MC geometry. The pressure-drop slope in Eq. 1.5 shows the extent of fluid pressure drop with distance from the wellbore. A value of "s = 0" does not cause any pressure drop, i.e., the fluid pressure at some horizontal distance from the fracture tip is the same as the pressure at the wellbore. A value of "s = 1" leads to the pressure at the fracture tip being equal to the normal stress on the fracture walls (FracMan7.5 Workshop, 2014).

The base case simulation was performed at a low slope value of s = 0.1 which yield similar results as using s = 0. Engineers prefer using s = 0 for thin fluids (personal

communication with Golder Associates, Nov. 2016). In thin (low viscosity) fluids, the pressure drop is minor. However, with an increase in the fluid viscosity, the pressure drop can be higher. Larger pressure drops in case of single fractures can create wider (higher aperture) fractures with shorter lengths (e.g., Warpinski, 1985). Therefore, Stages 2 and 4 were simulated to observe the effects of significant pressure drop (s = 1.0) on the MC geometry as well as the main hydraulic fracture from the wellbore. Table 1.22 shows that there is 16% reduction in the number of reactivated natural fractures for Stage 4 with an increase in pressure-drop slope. The 17% increase in the average storage aperture is because less non-dilatable fracture elements are pumped. Table 1.22 shows that the fracture hull and slab volume both decrease by 15% compared to the base case, with a minor (5%) decrease in the hydraulic fracture (new surface) volume. The difference, however, is not noticeable within the Woodford Shale because it is the formation closest to the wellbore. However, under higher pressure drop, wider storage apertures, and MC shortening in all directions (especially parallel to the wellbore) should be expected in the field for all stages. To quantify the MC shortening with fluid type, a relationship between the pressure-drop slope and the fluid type needs to be developed. There was no significant difference in the geometry and number of fractures for Stage 2 geometry with a higher pressure drop. This is probably because the fluid did not travel far enough from the wellbore to experience a significant pressure drop.

Table 1.22: Comparison of Stage 4 (s = 1) simulation results with base case stage 4 (s = 0.1) results.

	Base case: Stage 4 (s = 0.1)	Stage 4 (s = 1.0)
No. of hydrofracture elements	129	129 (0%)
Number of injected natural fracture elements	140,397	118,378 (-16%)
Vol. in induced hydraulic fractures (m^3/ft^3)	28.4/1,003	28.4/1,003
Vol. in reactivated natural fractures (m^3/ft^3)	2,054.3/72,547	2,055/72,572
Fluid efficiency (%)	1.4	1.4
Avg. post-hydraulic fracturing apertures (storage apertures) of inflated fractures (m/mm)	0.000807/0.807	0.000972/0.972 (+17%)
Min. aperture of inflated fractures (m/mm)	0/0	0/0
Woodford measured volume (m^3)	175,374	175,374 (+0%)
Inflated + hydraulic fracture hull volume (m^3)	12,537,942	10,745,606 (-14%)
Inflated + hydraulic fracture slab volume (m^3)	4,788,470	4,017,845 (-15%)
Hydraulic fracture (only) slab volume (m^3)	47,475	45,168 (-5%)
Inflated fracture (only) slab volume (m^3)	4,775,562	4,004,947 (-16%)
Short-axis (m)	252	217
Long-axis (m)	569	515
Height (m)	213	210

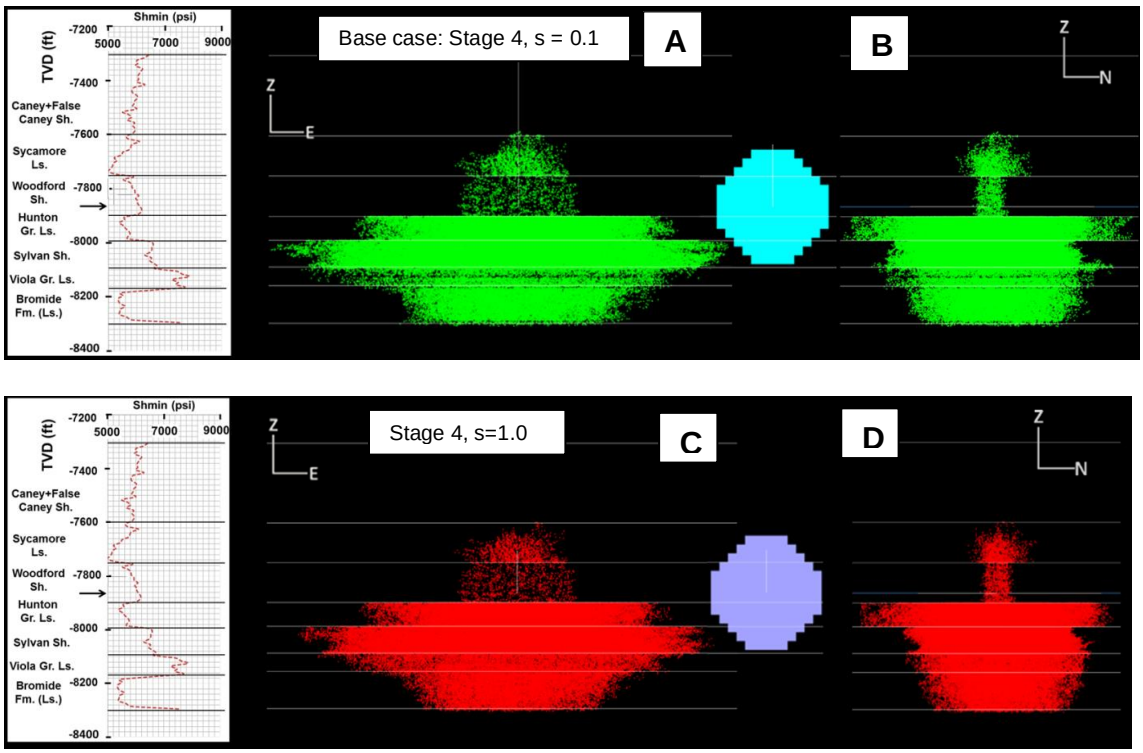

Figure 1.37: Effect of change in fluid pressure-drop slope on Stage 4 MC geometry. **A)** Stage 4 base case (s = 0.1) MC cloud in north view along with hydraulic fracture. **B)** Stage 2 base case (s = 0.1) MC cloud in west view. **C)** Stage 4 (s = 1) MC cloud in north view along with hydraulic fracture. **D)** Same as in C in west view. Notice the decrease in the MC sizes parallel and perpendicular to the wellbore, with the increase in pressure-drop slope.

1.9.2.5 Effect of higher fluid efficiency

The fluid efficiency value, or the percentage of the pumped fracture fluid going into creating new surfaces, is important in understanding the extent of leak off, i.e., amount of fluid lost into the formation. Within FracMan^{TM}, if a zero percent minimum pumping into a new hydraulic fracture is chosen, the software calculates the fluid pumped into natural or hydraulic fractures on a step by step basis. However, the user can instruct the software to pump a certain amount of fluid to create new surfaces. Since the software for all cases calculated a comparatively low fluid efficiency of 1.4%, the

effect of higher fluid efficiency on Stage 2 was simulated, which due to its smaller MC (compared to Stages 4 and 5) has room to expand in all directions. Two fluid efficiencies were tested for Stage 2, one with 10% and the other with 20%.

Comparing the base case to the 10% and 20% fluid efficiency, there is an 8 times and 15 times (respectively) increase in the number of hydraulic fracture elements and a steady decrease in the number of pumped natural fractures (Table 1.23). Table 1.23 shows that the Woodford Shale shows a +33% and a -20% volume change in the 10% and 20% efficiency cases compared to the base case. The overall volume shows an increase of 2-15% and 15-57% in the 10% and 20% fluid efficiency cases. However, there is 6% and 16% decrease respectively in the inflated fracture stimulated volume for the 10% and 20% fluid efficiency cases. Figures 1.38C through 1.38F show that a newly created hydraulic fracture cannot grow beyond the Viola Group Limestone for both the 10% and 20% cases. The increase in the HF volume was 630% and 1457% respectively compared to the base case fluid efficiency. Considering a ε_{hmin} of 0.00001, the Shmin at the top of the Viola Group Limestone is 800-1200 psi higher than the fracture fluid pressure at that depth. Therefore, a hydraulic fracture cannot expand below the Viola Group Limestone top. Once the base of the new hydraulic fracture touches the Viola Group Limestone top, it grows asymmetrically upwards into the Caney Shale until it touches the model boundary. Until the model boundary is touched, the lateral growth is only slightly higher than the upward growth of the hydraulic fracture. Figure 1.38C shows that the natural fracture reactivation keeps pace with the hydraulic fracture growth. However, at 20% efficiency (Figure 1.38E), the hydraulic fracture growth far exceeds the natural fracture reactivation. However, the creation of

new hydraulic fracture surfaces beyond the natural fracture reactivation zone is unlikely in the real world. The stimulation length along the well decreases in both the 10% and 20% efficiency cases. Looking at the mismatch between the geometries of the two cases with the base case, it is likely that the fluid efficiency is lower than 10%.

However, if a higher fluid efficiency is achieved, due to reasons such as a higher viscosity fluid or diverters (small proppant or nut-shells) an asymmetric hydraulic fracture starting from the wellbore, followed by a higher upward and lateral growth in the Sv-SHmax plane may be expected once the HF approaches the Viola Group Limestone top. The MC, in that case, is unlikely to achieve substantial growth along the wellbore. However, such a dramatic change in HF geometry is unlikely, even after using high viscosity fluids or diverters. A limitation of this simulation is that the same final storage aperture as the base case was used. With an increase in the fluid viscosity, however, wider fractures will be created (Mader, 1989, p. 432). This might cause some reduction in the length and height of the hydraulic fracture due to volume balance constraints.

Table 1.23: Comparison of Stage 2 simulation results (fluid efficiencies of 10% and 20%) with base case (fluid efficiency = 1.4%) results.

	Base case: Stage 2 (1.4% efficiency)	Stage 2 (10% efficiency)	Stage 2 (20% efficiency)
No. of hydrofracture elements	57	427 (+649%)	845 (+1382%)
Number of injected natural fracture elements	24,339	20,453 (-16%)	18,239 (-25%)
Vol. in induced hydraulic fractures (m^3/ft^3)	26.5/937	201.2/7,105	398.2/14,062
Vol. in reactivated natural fractures (m^3/ft^3)	1927.5/68,051	1752.8/61,900	1555.8/54,943
Fluid efficiency (%)	1.4	10	20
Avg. post-hydraulic fracturing apertures (storage apertures) of inflated fractures (m/mm)	0.00589/5.89	0.00585/5.85 (0%)	0.00587/5.87 (0%)
Min. aperture of inflated fractures (m/mm)	0.000017/0.017	0.000004/0.004	0.000006/0.006
Woodford measured volume (m^3)	1,099,447	736,630 (-33%)	1,257,111 (+14%)
Inflated + hydraulic fracture hull volume (m^3)	1,886,322	2,176,931 (+15%)	2,962,366 (+57%)
Inflated + hydraulic fracture slab volume (m^3)	740,311	752,002 (+2%)	848,692 (+15%)
Hydraulic fracture (only) slab volume (m^3)	19,458	142,010 (+630%)	302,927 (+1457%)
Inflated fracture (only) slab volume (m^3)	734,121	689,827 (-6%)	632,654 (-16%)
Short-axis (m)	97	82	71
Long-axis (m)	320	292	425
Height (m)	116	190	219

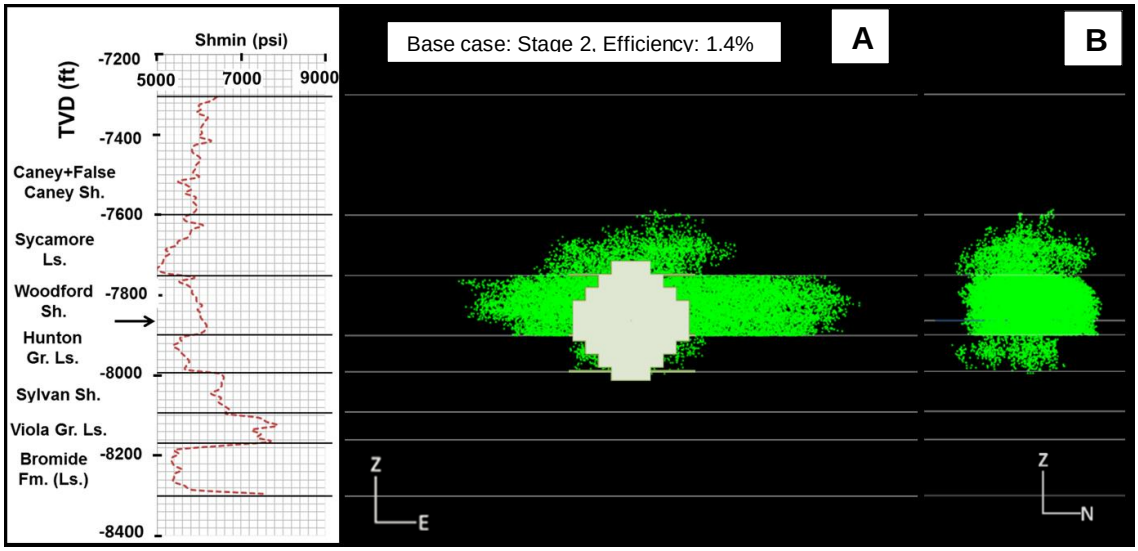
Shmin (psi)
TVD (ft)
-7200
5000
7000
9000
-7400
Caney+False Caney Sh.
-7600
Sycamore Ls.
Woodford Sh.
-7800
Hunton Gr. Ls.
-8000
Sylvan Sh.
Viola Gr. Ls.
Bromide Fm. (Ls.)
-8200
-8400
Base case: Stage 2, Efficiency: 1.4%
A
B
Z
E
Z
N

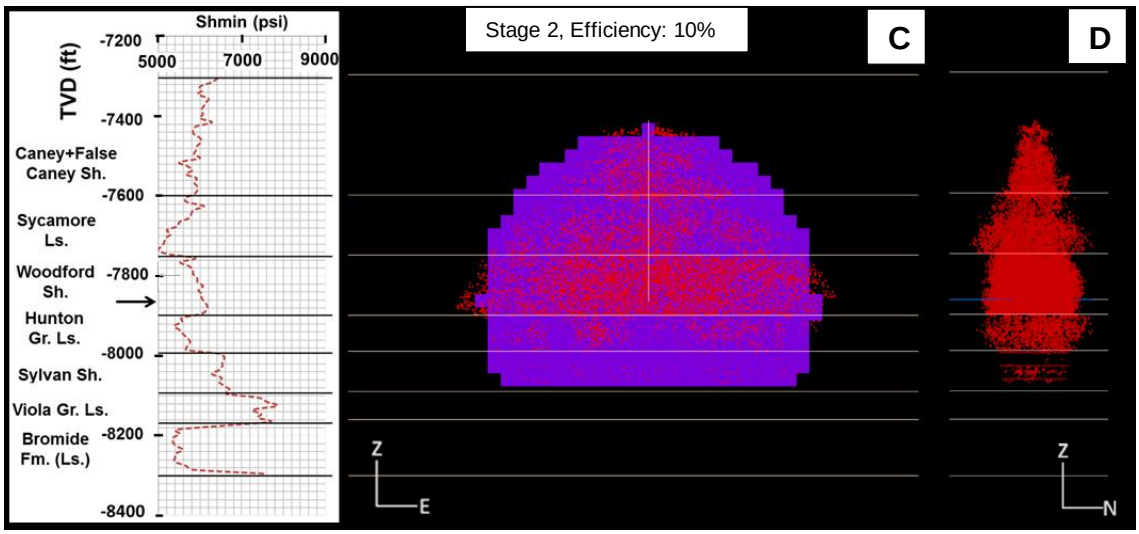
Shmin (psi)
TVD (ft)
-7200
5000
7000
9000
-7400
Caney+False Caney Sh.
-7600
Sycamore Ls.
Woodford Sh.
-7800
Hunton Gr. Ls.
-8000
Sylvan Sh.
Viola Gr. Ls.
Bromide Fm. (Ls.)
-8200
-8400
Stage 2, Efficiency: 10%
C
D
Z
E
Z
N

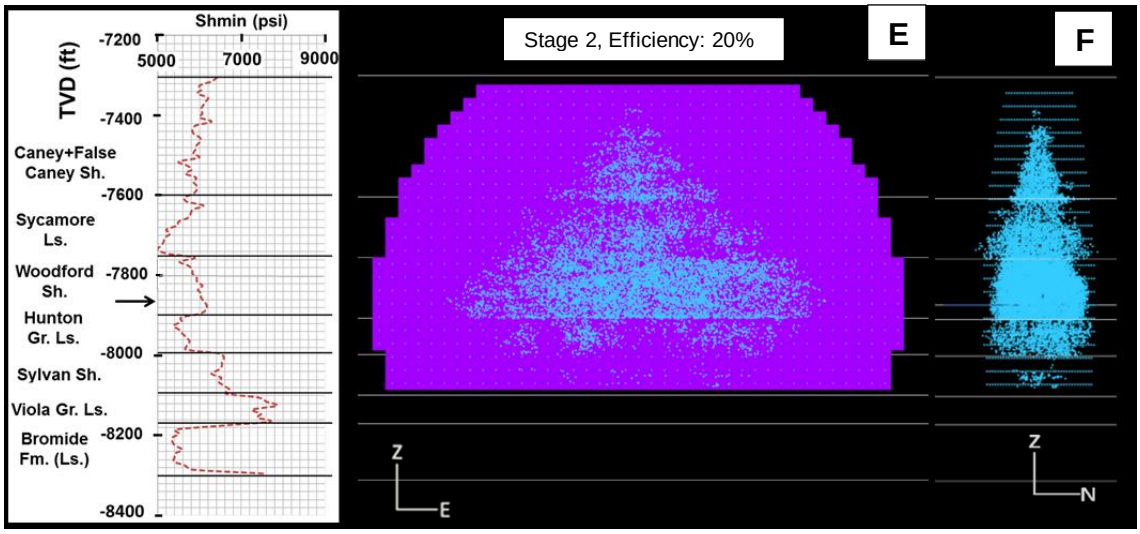

Figure 1.38: Effect of assigning higher fluid volumes to the hydraulic fracture (new surface). **A)** Stage 2 base case (1.4% fluid efficiency) MC cloud in north view along with hydraulic fracture. **B)** Stage 2 base case MC cloud in west view. **C)** Stage 2 (10% fluid efficiency) MC cloud in north view along with hydraulic fracture. **D)** West view of the same MC in C. **E)** Stage 2 (20% fluid efficiency) MC cloud in north view along with hydraulic fracture. Notice that it is unrealistic that the large hydraulic fracture develops well beyond the extent of reactivated natural fractures (synthetic microseisms). **F)** West view of the same MC in E.

1.9.2.6 Effect of halving fracture intensity and doubling fracture storage apertures

Some differences in fracture abundance may exist between the subsurface (near the treatment well) beds and the outcrop beds due to various reasons, even though both subsurface and outcrop measured beds in consideration are relatively flat (i.e., fold related fractures are unlikely). Assuming a case of only half the outcrop measured fracture intensities existing in the subsurface, the change in the stimulated geometry using the same treatment parameters was simulated. Halving the fracture intensities causes at least 3-4 times less natural fracture intersections if only a single layer, consisting of all fracture set, are considered. In addition to halving the natural fracture intensities, the maximum storage aperture was doubled to balance the volume. There is no geologic justification for doubling the maximum storage aperture. However, from

the modeling viewpoint, it is obvious that decreasing natural fracture intensity without an accompanying change in other parameters will increase the simulated MC volume as the fluid travels further to balance the pumped volume. Therefore, halving fracture intensity and doubling maximum aperture resolves the issue related to volume balance, and solely shows the effect of the reduced number of natural fractures (or intersections) in the simulated geometry. Two different behaviors were observed for Stages 2 and 4.

Table 1.24 shows that for Stage 2, the number of pumped natural fractures decreases nearly three times (-66%) and the number of hydraulic fracture elements increases ten times (~ 900%). A large hydraulic fracture is created (compare Figure 1.39C to 1.39A and Figure 1.39D to 1.39B). The fluid efficiency increases from 1.4% to 27.2%. Average final storage aperture doubles from 5.89 to 11.9 mm. Also as shown earlier, the newly created hydraulic fracture does not transect the Viola Group Limestone due to higher Shmin compared to the pumped pore pressure at that depth. The reactivated fracture MS cloud mainly grows within the Woodford Shale and the Caney Shale and has 51% lower volume compared to the base case. However, the overall volume increases by 118% using hull volume and decreases 35% using slab volume. The MC geometry mismatch with base case indicates that lower connectivity and higher aperture is not another alternative for the field MC geometry match for Stage 2. This shows that natural fracture connectivity (or natural fracture density), in addition to the final storage apertures, decides the stimulated volume. In addition, higher natural fracture density (base case) is beneficial for Stage 2 as it helps contain the stimulation within the target zone. (Woodford Shale).

For Stage 4, both the number of hydraulic fracture elements and the number of natural fractures pumped show ~ 50% reduction (Table 1.24) compared to the base case. The overall volume does not show a considerable change (20% slab volume reduction and 31% hull volume increase). The fluid efficiency stays at 1.4%. Unlike Stage 2, where a large part of the volume balance occurs by allocating fluid in the new hydraulic fracture, in Stage 4 volume balance occurs mainly by a 77% increase in the storage aperture. The main reason for this discrepancy is that in Stage 2 fluid is not allowed to flow through non-dilatable fractures. Therefore, at several time steps, any extra fluid is pumped into a new hydraulic fracture element when a dilatable natural fracture is not available. For Stage 4, however, the extra fluid is made to flow through a non-dilatable fracture, instead of creating a new surface area, until the next dilatable fracture becomes available. In the field as well, if fluid can flow through a non-dilatable (Sn > Pp) fracture due to reasons such as intrinsic permeability (e.g., surface roughness due to minor displacement), the fluid flow capacity of the reservoir will increase, as these unfavorably oriented fractures don't need to be opened. This will reduce the likelihood of creating new hydraulic fractures during pumping as in Stage 4. Also, because L = 0.23, M= 0.5, and N = 0.27 were used, the fluid tends to move away from the Woodford Shale, which has a lower permeability (0.003 md) compared to all other formations. Therefore, a large MC is created above and below the Woodford Shale (Figures 1.40C and 1.40D). The hydraulic fracture (new surface) length and width decrease due to its higher aperture (compare Figures 1.40C and 1.40A). The similarity in the MC geometry in this case with the base case and field MC geometry shows that a higher aperture and

lower connectivity (due to lower fracture intensity) could have existed in the field case.

Stage 5 results were similar to those of Stage 4.

Table 1.24: Comparison of Stage 2 (half intensities, max aperture = 12 mm) and Stage 4 (half intensities, max aperture = 5.6 mm) simulation results with base case Stages 2 (original intensities, max aperture = 6 mm) and Stage 4 (original intensities, max aperture = 2.8 mm) results.

	Base case: Stage 2 (original intensity, aperture = 6 mm)	Stage 2 (half intensity, aperture = 12 mm)	**Base case:** Stage 4 (original intensity, aperture = 2.8 mm)	Stage 4 (half intensity, aperture = 5.6 mm)
No. of hydrofracture elements	57	569 (+898%)	129	66 (-49%)
Number of injected natural fracture elements	24,339	8,371 (-66%)	140,397	70,388 (-50%)
Vol. in induced hydraulic fractures (m^3/ft^3)	26.5/937	533.1	28.4/1003	28.6
Vol. in reactivated natural fractures (m^3/ft^3)	1,927.5/68,051	1,427.3	2,054.3/72,547	2,056.4
Fluid efficiency (%)	1.4	27.2	1.4	1.4
Avg. post-hydraulic fracturing apertures (storage apertures) of inflated fractures (m/mm)	0.00589/5.89	0.0119/11.9 (+102%)	0.000807/0.807	0.00142/1.42 (+77%)
Min. aperture of inflated fractures (m/mm)	0.000017/0.017	0.00022/0.22	0/0	0/0
Woodford measured volume (m^3)	1,099,447	1,253,370 (+14%)	175,374	98,210 (-44%)
Inflated + hydraulic fracture hull volume (m^3)	1,886,322	4,127,073 (+118%)	12,537,942	16,497,292 (+31%)
Inflated + hydraulic fracture slab volume (m^3)	740,311	485,016 (-35%)	4,788,470	3,872,046 (-20%)
Hydraulic fracture (only) slab volume (m^3)	19,458	193,357 (+893%)	47,475	25,560 (-46%)
Inflated fracture (only) slab volume (m^3)	734,121	358,828 (-51%)	4,775,562	2,387,246 (-50%)
Short-axis (m)	97	97	252	265
Long-axis (m)	320	403	569	593
Height (m)	116	214	213	214

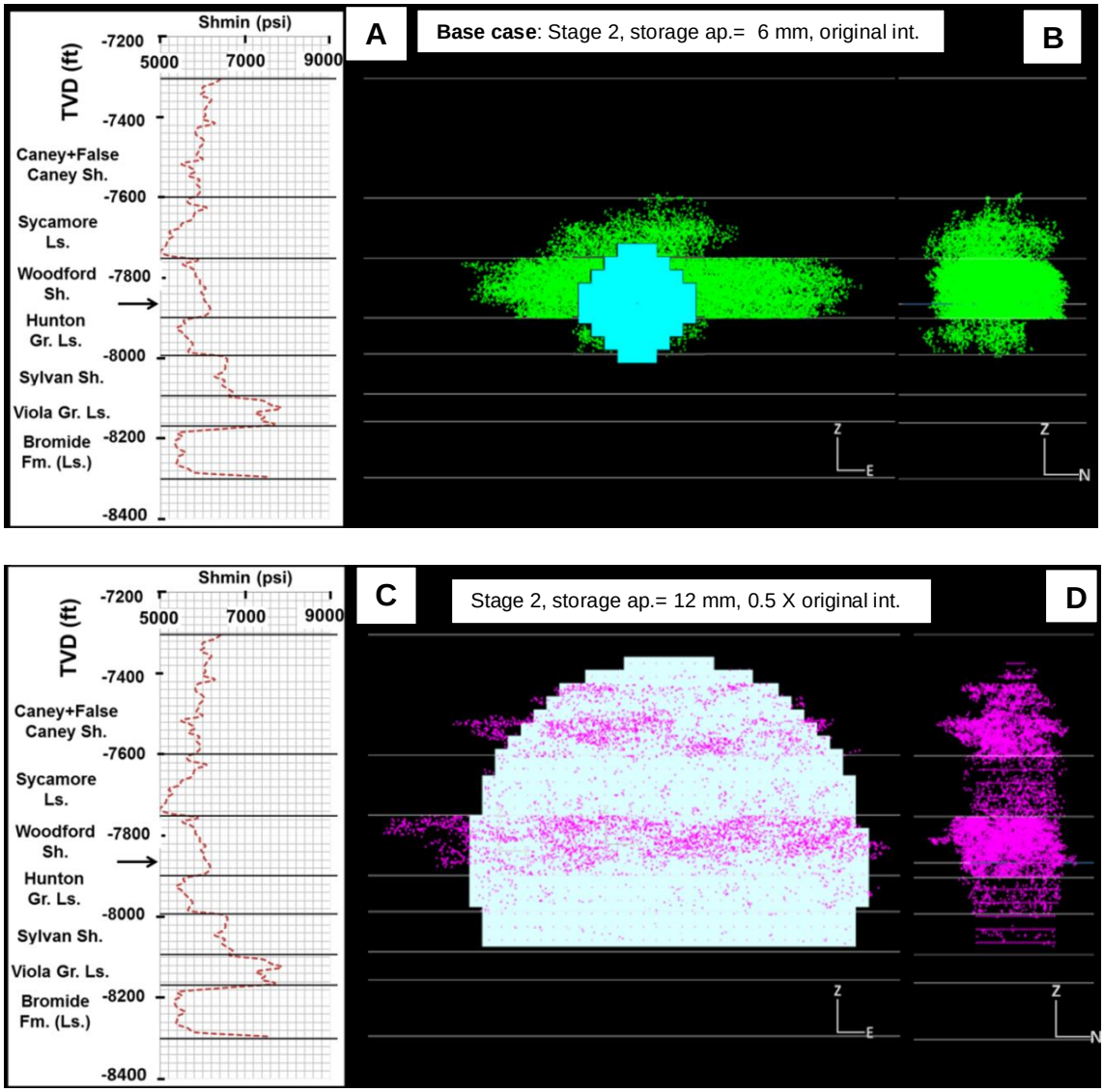

Figure 1.39: Effect of change in natural fracture intensities and final storage apertures on Stage 2. **A)** Stage 2 base case (original intensities, maximum assigned hydraulic fracture aperture = 6 mm) MC cloud in north view along with hydraulic fracture. **B)** Stage 2 base case MC cloud in west view. **C)** Same as in A, with twice the original max. assigned hydraulic fracture aperture (12 mm) and half the intensities. **D)** Same MC as C in west view.

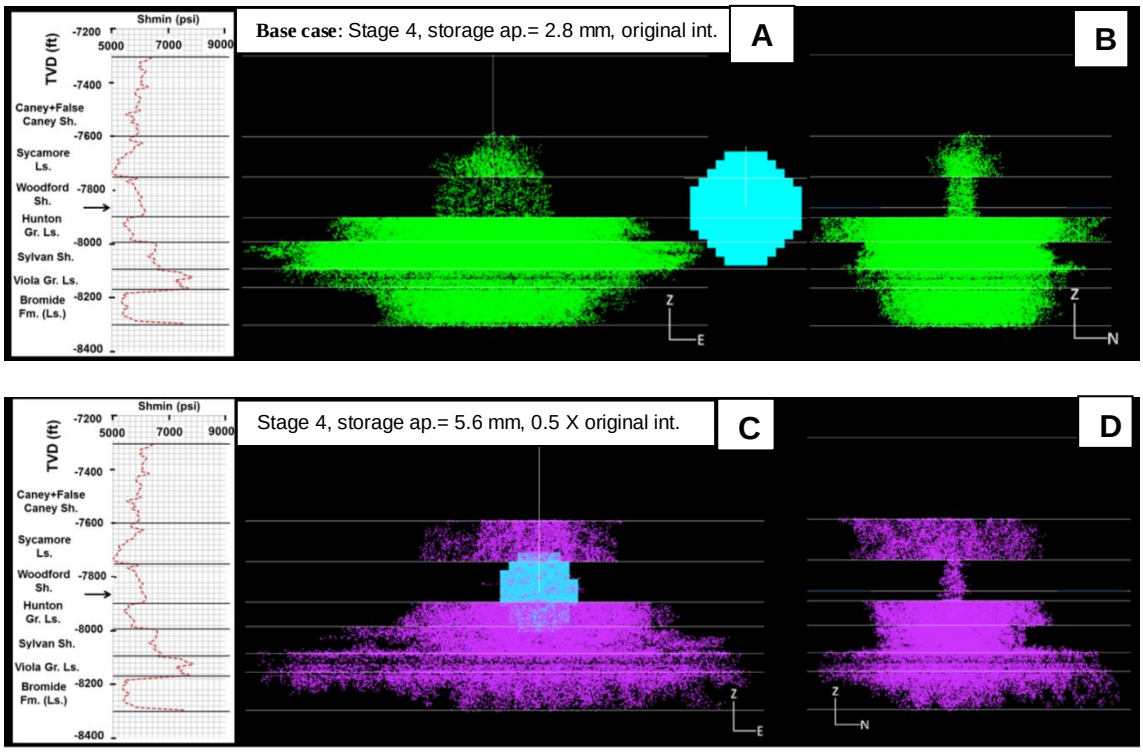

Figure 1.40: Effect of change in natural fracture intensities and final storage apertures on Stage 4. **A)** Stage 4 base case (original intensities, max. assigned hydraulic fracture aperture = 2.8 mm) MC cloud in north view along with hydraulic fracture. **B)** Stage 4 base case MC cloud in west view. **C)** Same as in A, with twice the original max. assigned hydraulic fracture aperture (5.6 mm) and half the intensities. **D)** Same MC as C in west view.

1.10 Discussion

Seismic data or image logs were not available near the treatment well. Therefore, the DFN model stands entirely on the outcrop observations. Neither the Woodford Shale nor the Hunton Group Limestone were totally exposed at the studied outcrop/quarry locations. Additionally, outcrops were not available for measuring fracture parameters of formations other than the Woodford Shale and Hunton Group Limestone. Therefore, fracture intensities, apertures, heights, and length-height relations in the Woodford Shale and the Hunton Group Limestone were assigned to all shale and carbonate formations respectively.

Secondly, even though the log derived rock properties introduce layer-wise variability every ten feet, the intraformational fracture intensities do not vary layer-wise, as only sufficiently large (long) fractures were considered which often crosscut different layers. Computational capabilities, along with non-visibility of the entire strata were reasons for not considering fractures with height < 1 m (3.28 ft). However, using only large fractures may not be an unrealistic assumption. Zhang and Jeffery (2013) mentioned that longer fractures are more compliant and therefore, open wider. Therefore, longer fractures are more important for fluid flow. Also, the larger fractures can impact flow more than smaller fractures due to less natural cementation (Laubach, 2003). Germanovich and Astakhov (2004) through physical and numerical modeling observed that mechanical interaction between adjacent joints has a considerable effect on the opening displacements (joint apertures). Therefore, the opening of longer fracture also minimizes the opening of the shorter fractures (which are more likely to be bedbound) due to stress shadow effects from the longer ones. Agar et al. (2010), upon simulation of waterflooding in carbonate rocks, found strong fingering or bypassing of the matrix in the presence of hierarchical fractures. In addition, longer fractures contribute more to the reservoir connectivity compared to the shorter fractures. Therefore, the longer fractures were prioritized over the shorter ones in the model. However, a limitation of measuring large fractures is that some of the fracture ends are not visible. Therefore, some of the long fracture heights are underestimated. However, the software maintains the fracture intensities (assigned P32 [areal intensity]) values, given the maximum and minimum cutoffs, and statistical distributions of lengths and

heights. Therefore, minor underestimation due to truncation will not affect the results significantly.

Given the two potential sources of error discussed above the inherent assumption for the DFN model/simulations is that the fracture observations made at the outcrops are not radically different from those in the subsurface location of the treatment well. The L, M, and N input values, along with other adjustable parameters (final storage aperture, maximum strain, minimum strain, flowback percentage and permeability values) values come handy overcoming these uncertainties in data for the final geometry match. If all fracture sets from each formation were available for measurements, variation in the current adjustable parameters (rotating knobs) could be expected for matching the same MC geometries.

The strength of the three geometry matches is that the dense part of the field MC (marked within ellipses) for the three stages are relatively well matched in 3D. In addition, an attempt was made to match the field and the simulated percentage microseismic cloud in each formation. Also, the lowest possible time steps and vertical grid sizes were used. Therefore, the model is as robust as possible. The utility of the geometry match lies in understanding the relative permeabilities between the formations that lie above and below the Woodford Shale. The permeability values, however, are not absolute. For example, if Kfrac (average) (Formation A) = 0.010 md and Kfrac (average) (Formation B) = 0.005 md, Formation A fracture permeability is twice that of Formation B on average, under the given in situ conditions. Under the given fracture dimensions and in situ stresses, the average formation fracture permeabilities (md) in decreasing order are: Viola Group Limestone (0.025) > Caney Shale (0.012) > Sylvan

Shale (0.011) > Sycamore Limestone (0.006) > Hunton Group Limestone (0.0045) > Bromide Formation (0.005) > Woodford Shale (0.003). Neuhaus (2011, p. 190) mentions the presence of karst in the Viola Group Limestone at a location towards the west of the wellbore. Karsting may be one of the reasons for a higher fracture abundance (e.g., Milad and Slatt, 2017), leading to a higher average permeability value.

Maximum and minimum tectonic strain values were obtained for the area based on the rock mechanical properties, known fracture gradient within the Woodford Shale, fault shear strengths based on friction coefficient values, and the geometry matches. Moreover, change in tectonic strain from Stage 4 to Stage 5 was also estimated, which gives us a relatively closer Stage 5 MC geometry match, compared to using tectonic strain values for Stages 2 and 4. This gives an estimate of the change in tectonic strain values that can happen for from one stage to the next (~ 1.5e-5). Minimum tectonic strain values of 0.00001 (Stages 2 and 4), 0.000025 (Stage 5) used in this study are lower than the lowest tectonic strain value (0.000045) reported by Neuhaus (2011). While the maximum tectonic strain = 0.0005 used in this study is higher than the highest value (0.00014) used by Neuhaus (2011). However, Neuhaus did not use both the strain values at the same time for calculating the SHmax and Shmin. Instead, the values were used to match geometries parallel or perpendicular to the wellbore one at a time.

The simulated fluid efficiency was determined to be low, i.e., 1.4%. However, the field efficiencies can be a few percent higher or lower than 1.4%. At larger time steps, under the same conditions, this number can be as high as 4%, though without a proper geometry match. A 4% efficiency value can also be considered as low

efficiency. However, the green curve has a stable slope in Figure 1.24, indicating that a critical treating pressure was achieved, which may be a result of excessive leak off into natural fractures (Nolte and Smith, 1979). Moreover, all the observed fractures have not been considered for the simulation, i.e., only large fractures were considered. Though smaller fractures have low permeability values, they possibly can act as conduits for fluid flow if reactivated. Therefore, under the given conditions, it is unlikely that significantly large new fracture surfaces will be created and mostly natural fracture reactivation will take place, i.e., fluid efficiency will stay low.

Shifting the wells upward showed a corresponding upward shift of the MC. Almost no volume change within the MC in the Woodford Shale (~ 0%) was observed with the change in well location. This, however, does not indicate that changing well location will not cause a difference in the stimulation within the Woodford Shale. It is important to remember that fractures with height < 1 m were not considered in the model. Therefore, the results only suggest that there is not much effect on the overall geometry without suggesting details about stimulation within each formation.

Minor change in horizontal stresses (due to a minor change in the minimum strain) results in a dramatic change in the MC geometry. MC shifts towards the layers closer to the wellbore with longer and wider stimulated zones within these layers, even though volume change within the Woodford Shale may or may not be significant (+29 and +4% for Stages 4 and 5 respectively). This was observed for both stages even though a high percentage of fractures in the Bromide Group (away from wellbore) are critically stressed. On the contrary, pumping at a higher rate (higher ISIP in the software) results in a downward growth of the MC, and a decrease in the number of

dilated fractures for all stages. The MC volume decreases in all stages due to more fractures dilating closer to the wellbore. In addition, within the Woodford Shale, the volume decreases by 74% and 10% in Stages 2 and 4 respectively. Therefore, to increase the stimulated volume within the target Woodford Shale, very high slurry rates should be avoided in the study area. However, if a higher slurry rate is chosen, considering that the stimulation tends to grow downwards, wells should be landed higher up in the Woodford Shale for obtaining larger stimulation volume in the Woodford Shale.

On the other hand, halving the fracture intensity and doubling the maximum aperture results in two different behaviors. In the first case, if flow is not allowed through non-dilatable fractures (e.g., 50% intensity case of Stage 2), fluid efficiency increases manyfold. For Stage 2, the extent of the new fracture running out of zone far outruns its extent within the Woodford Shale. The size of the hydraulic fracture (new surface) and associated fluid efficiency is also affected by the amount of clustering. As the number of natural fracture clusters disconnected from the wellbore, and each other, increases, the fluid efficiency will likely increase (e.g., 50% intensity case of Stage 2) as fluid travels through disconnected areas (intact matrix). On the other hand, if fluid flow can take place without fracture dilation, fluid efficiency stays low (e.g., 50% intensity case of Stage 4) regardless of whether the DFN is fully connected or is clustered. For Stage 2 and 4, the Woodford Stimulation volume changes by +14% and -44% respectively for the half intensity DFNs.

Similarly, large hydraulic fractures (new surface), sometimes exceeding the reactivated fracture volume were observed by deliberately pumping 10% and 20%

fracture fluid into creating new fracture surfaces. The large hydraulic fracture geometry is unrealistic because as the fracture fluid travels away from the wellbore, it is less likely to create new surfaced due to energy loss. It is certainly easier to stimulate preexisting fractures than to create new surfaces at large distances away from the wellbore. The unrealistic geometry, rather than being a software limitation, shows that it is geologically unreasonable to expect 10-20% fluid efficiencies in the studied area due to high natural fracture abundance. For Stages 4 and 5, the fluid efficiency cannot increase theoretically due to the fluid being pumped into non-dilatable fractures.

The higher pressure-drop slope, which can be caused by pumping a higher viscosity fluid does not make a difference if the stimulation takes place primarily close to the wellbore (Stage 2 in this case). There is almost no change (~ 0%) change in stimulated volume in the Woodford Shale with a higher pressure-drop slope value of 1.0. However, the MC volume can significantly decrease when the stimulation takes place away from the wellbore (Stages 4 and 5), both in the target and non-target formation.

From the above observations, the utility of the simulations under different scenarios have two distinct advantages. First, and the most obvious, is the prediction (forward modeling) of the MC geometry under different scenarios of reservoir conditions and pump rates. Second, the simulations tell if the field MC geometries can be obtained in a non-unique way (e.g., half intensity/twice aperture case).

1.11 Conclusions

In this study, an analogue modeling approach with field measured inputs was to understand the propagation of hydraulic fractures and reactivation of natural fractures

within the Woodford Shale and under/overlying shales and carbonates. The outcrop fracture parameters were used as input into FracMan^{TM} discrete fracture network simulator to match the microseismic geometry for three stages from an Arkoma Basin well. Mostly characteristic size distributions were obtained for the fracture heights and apertures. According to the simulations, due to high fracture density, reactivated natural fractures receive almost all the fracture fluid. Consequently, fluid efficiency is not high. The natural fracture stimulation in the highly stressed Viola Group Limestone indicates the presence of fractures with substantially higher permeability compared to the other formations. Natural fracture connectivity (abundance), in addition to final storage apertures, affected the fluid efficiency and final storage volume in some but not all stages. However, in the studied area, increased fluid efficiency promotes growth out of the target zone (Woodford Shale). High slurry rate (resulting in higher net pressure) lowers the stimulation volume in the Woodford Shale. However, a downward growth of natural fracture reactivation provides an incentive in placing the wellbore high up in the Woodford Shale. While changing well position does not change the MC geometry considerably, increasing minimum strain after each successive stage creates considerable change in the MC geometry and more lateral reactivation in the layers closer to the wellbore.

Abbreviations

CSP: Clarita Shale Pit, **DFN**: discrete fracture network, **Gr.**: group, **JQ**: Jennings Quarry, **MC**: microseismic cloud, **WSP**: Wyche Shale Pit, **Ls.**: limestone, **Sh.**: shale, **Sn**: normal stress on fracture, **Pp**: pore pressure within fracture.

References

Agar, S.M., S. Geiger, S.K. Matthai, S. Thomas, A. Immenhauser, R. Shekhar, J. Paul, G. Benson, Z. Karcz, L. Kabiri, 2010. The impact of hierarchical fracture networks on flow partitioning in carbonate reservoirs: Examples based on a Jurassic carbonate ramp analog from the High Atlas, Morocco. Paper SPE 135135, presented at the SPE Annual Technical Conference and Exhibition, Florence, Italy, 19–22 September.

Ahmadhadi, F., J.M., Daniel, M., Azzizadeh, and O., Lacombe, 2008. Evidence for pre-folding vein development in the Oligo-Miocene Asmari Formation in the Central Zagros Fold Belt, Iran. Tectonics 27, TC1016.

Allison, M.D., W.H. II Willis, and N.H. Suneson, 2012. The geology and deep structure of the Oklahoma Ouachita Mountains – the SOPC 1-22 Weyerhaeuser well: Shale Shaker, v. 62, p. 362-376.

Amsden, T.W., 1980-1. Isopach and Structure Map of Sylvan Shale in Eastern Oklahoma. OGS Bulletin 129-1. http://www.ogs.ou.edu/pubsscanned/BULLETINS/bulletin-ill/B129P-1.pdf

Amsden, T.W., 1980-2. Isopach and Structure Map of Hunton Group in Eastern Oklahoma. OGS Bulletin 129-2. http://www.ogs.ou.edu/pubsscanned/BULLETINS/bulletin-ill/B129P-2.pdf

Amsden, T.W., 1980-3. Isopach and Structure Map of Woodford Shale in Eastern Oklahoma. OGS Bulletin 129-3. http://www.ogs.ou.edu/pubsscanned/BULLETINS/bulletin-ill/B129P-3.pdf

Andrews, R.D., 2003-2. Cromwell Play in Southern Oklahoma. Oklahoma Geological Survey. Special Publication 2003-2.

Andrews, R.D., 2008. Panola field: multiple Atoka sandstone gas reservoirs in T. 5 N., Rs. 19 – 20 E., Latimer County, Oklahoma, in Suneson, N.H.; Çemen, Ibrahim; and Slatt, R.M., eds., Stratigraphic and structural evolution of the Ouachita Mountains and Arkoma Basin, southeastern Oklahoma and west-central Arkansas: applications to petroleum exploration: 2004 field symposium technical papers: Oklahoma Geological Survey Circular 112B, p. 31-50.

Arbenz, J.K., 1984. A structural cross-section through the Ouachita Mountains of western Arkansas, in Stone, C.G.; and Haley, B.R., eds., A guidebook to the geology of the central and southern Ouachita Mountains: Arkansas Geological Commission Guidebook 84-2, p. 76-82.

Arbenz, J.K., 2008. Structural framework of the Ouachita Mountains, in Suneson, N.H., ed., Stratigraphic and structural evolution of the Ouachita Mountains and Arkoma Basin, southeastern Oklahoma and west-central Arkansas: applications

to petroleum exploration: 2004 field symposium. The Arbenz–Misch/Oles volume: Oklahoma Geological Survey Circular 112A, p. 1-40.

Ataman, O. 2008. Natural Fracture Systems in the Woodford Shale, Arbuckle Mountains, OK. Master's thesis, University of Oklahoma, Norman, OK.

Barbier, M., Y., Hamon, J.P., Callot, M., Floquet, and J.M., Daniel, 2012a. Sedimentary and diagenetic controls on the multiscale fracturing pattern of a carbonate reservoir: the Madison Formation (Sheep Mountain, Wyoming, USA). Mar. Pet. Geol.29, p. 50–67.

Barker, J. C., 1951. Geology of a Portion of the Lawrence Uplift, Pontotoc County, Oklahoma. Tulsa Geol. Soc. Digest. vol. 19, p. 169-191.

Beaudoin, N., R. Leprètre, N. Bellahsen, O. Lacombe, K. Amrouch, J.P. Callot, L. Emmanuel, and J.M. Daniel, 2012. Structural and microstructural evolution of the Rattlesnake Mountain Anticline (Wyoming, USA): new insights into the Sevier and Laramide orogenic stress build-ups in the Bighorn Basin. Tectonophysics, p. 576–577.

Bertotti, G., N. Hardebol, J.K. Taal-van Koppen, and S.M. Luthi, 2007. Toward a quantitative definition of mechanical units: New techniques and results from an outcropping deep-water turbidite succession (Tanqua-Karoo Basin, South Africa), Am. Assoc. Pet. Geol. Bull. 91(8), p. 1085-1098.

Bigdeli, 2015. Introduction to Mangrove, A Hydraulic Fracturing Simulator. https://www.researchgate.net/publication/305994120_Introduction_to_Mangrove_A_Hydraulic_Fracturing_SimulatorIntroduction to Mangrove, A Hydraulic Fracturing Simulator, doi: 10.13140/RG.2.1.4285.7209

Blanton, T.L. and J.E. Olson, 1999. Stress Magnitudes from Logs: Effects of Tectonic Strains and Temperature, SPE Paper 54653.

Blasio D., 2011. Introduction to the Physics of Landslides: Lecture Notes on the Dynamics of Mass Wasting, doi: 10.1007/978-94-007-1122-8_2

Boardman, D. R., J. Puckette, and I. Cemen, 2008. Middle and Late Paleozoic Organic-Rich Gas Shales of the North American Midcontinent. Paper SPE 110069, presented at the 2008 AAPG Annual Convention, San Antonio, TX, 20-23 April.

Brady, B., J. Elbel, M. Mack, H. Morales, K. Nolte, and B. Poe, 1992. Cracking Rock: Progress in Fracture Treatment Design," Schlumberger Oilfield Review 4, No 4, October, 4-17.

Byrnes, A.P. and G. Lawyer, 1999. Burial, Maturation, and Petroleum Generation History of the Arkoma Basin and Ouachita Foldbelt, Oklahoma and Arkansas. Natural Resources Research, 8(1).

Champlin, S. C., 1958. The problem of the Welden, Sycamore and Lower Caney in the eastern Arbuckle Mountains. Okla. Acad. Sci., Proc., Vol. 38.

Cipolla, C.L., N.R. Warpinski, and M.J., Mayhoffer, 2008b. Hydraulic fracture complexity: Diagnosis, remediation, and exploitation: Asia Pacific Oil and Gas Conference and Exhibition, SPE 115771.

Cooke, M.L., J.A. Simo, C.A. Underwood, and P. Rijken, 2006. Mechanical stratigraphic controls on fracture patterns within carbonates and implications for groundwater flow. Sedimentary Geology 184(3-4), p. 225-239.

Cooper., J.C., 1995. Geologic Evolution of the Criner Hills Trend, Ardmore Basin, Oklahoma. In Johnson, K.S., 1992. Structural Styles in the Southern Midcontinent, 1992 Symposium. Oklahoma Geological Survey Circular 97, p. 146.

Dershowitz, W.S., 2006. Hybrid Discrete Fracture Network and Equivalent Continuum Model for Shaft Sinking. Paper presented at the 41st US Symposium on Rock Mechanics (Golden Rocks), Golden, Colorado, USA, 19-21 June.

Dershowitz, W.S., M.G. Cottrell, D.H. Lim, T.W. Doe, 2010. A Discrete fracture network approach for evaluation of hydraulic fracture stimulation of naturally fractured reservoirs. ARMA10-475. In: Presented at 44th US Rock Mechanics symposium, Salt Lake City, UT, 27–30 June.

Eppheimer, J., 2016. Spatio-Temporal Microseismic Analysis of the Woodford Shale, Canadian County, OK. Master's thesis, Colorado School of Mines, Golden, CO.

Fairhurst, C., 2013. Fractures and Fracturing: Hydraulic Fracturing in Jointed Rock. Intech open access journal, doi: 10.5772/56366.

Fischer, M.P., I.C. Higuera-Díaz, M.A. Evans, E.C. Perry, L. Lefticariu, 2009. Fracture controlled paleohydrology in a map-scale detachment fold: insights from the analysis of fluid inclusions in calcite and quartz veins. J. Struct. Geol. 31, p. 1490–1510.

FracMan7.5 Workshop, 2014. Golder Associates Inc.

Germanovich, L.N., and D.K. Astakhov, 2004. Fracture closure in extension and mechanical interaction of parallel joints. J. Geophys. Res. 109: B02208.

Gertson, R., Personal communication, 2011. Taken from Neuhaus, C.W., 2011. Analysis of Surface and Downhole Microseismic Monitoring Coupled with

Hydraulic Fracture Modeling in the Woodford Shale. Master's Thesis, Colorado School of Mines, Golden, CO

Gillespie, P.A., J.D. Johnston, M.A. Loriga, K.J.W. McCaffrey, J.J. Walsh, and J. Watterson, 1999. Influence of layering on vein systematics in line samples, in Mc-Caffrey, K.J.W., Longeran, L., and J.J., Wilkinson, eds. Fractures, Fluid Flow and Mineralization: Geological Society [London] Special Publication 155, p. 35–56.

GOHFER™ Brochure. http://barree.net/images/documents/GOHFER_Brochure_2015.pdf

GOHFER™ Presentation. Retrieved on June 3, 2017. http://barree.net/images/documents/GOHFER%20Presentation.pdf

Grieser, W.V., 2011. Oklahoma Woodford Shale: Completion Trends and Production Outcomes from Three Basins. Society of Petroleum Engineers, doi:10.2118/139813-MS.

Gross, M.R., 1993. The origin and spacing of cross joints: examples from the Monterrey Formation, Santa Barbara coastline, California. J. Struct. Geol. 15(6), p. 737–751.

Hajdarwish, A., and A. Shakoor, 2006. Predicting the shear strength parameters of mudrocks. The Geological Society of London. IAEG Paper number 607.

Ham, W.E., and M.E. McKinley, 1954; revised by Johnson K.S. (1990). Geologic Map and Sections of the Arbuckle Mountains, Oklahoma. Oklahoma Geological Survey, Norman, OK.

Hanks, C.L., J. Lorenz, L. Teufel, and A.P. Krumhardt, 1997. Lithologic and structural controls on natural fracture distribution and behavior within the Lisburne Group, northeastern Brooks Range and North Slope subsurface, Alaska. AAPG Bull. 81, p. 1700–1720.

Hardie, W.E., 1988. Structural style of the frontal thrust belt of the Ouachita Mountains, southern Pittsburg County, Oklahoma: Oklahoma Geology Notes, 48, p. 232-246.

Hooker, J.N., S.E. Laubach, and R. Marrett, 2013. Fracture-aperture size—Frequency, spatial distribution, and growth processes in strata-bounded and nonstrata-bounded fractures, Cambrian Mesón Group, NW Argentina.

Hooker, J.N., S.E. Laubach, and R. Marrett, 2014. A universal power-law scaling exponent for fracture 924 apertures in sandstones. Geological Society of America Bulletin published online 22 May 2014, doi: 925 10.1130/B30945.1

Itasca Consulting Group. Inc. Retrieved on June 2, 2017. http://www.itascacg.com/software/flac3d.

Kamann, P.J., 2006. Surface to surface correlation and lithostratigraphic framework of the Caney Shale (Including the "Mayes" Formation) in Atoka, Coal, Hughes, Johnston, Pittsburg, and Pontotoc Counties, Oklahoma. Master's Thesis, Oklahoma State University, Stillwater, OK.

Keller, G.R., 2010. Woodford Production History and Future Analysis. http://groundwork.iogcc.ok.gov/sites/default/files/Woodford_Keller_v2.pdf

Laubach, S. E., 2003. Practical approaches to identifying sealed and open fractures: AAPG Bulletin, 87(4), p. 561–579.

Li, Q., H. Xing, J. Liu, and X. Liu, 2015. A review on hydraulic fracturing of unconventional reservoir Petroleum, 1(1), p. 8–15.

Mader, D., 1989. Hydraulic proppant fracturing and gravel packing. Developments in Petroleum Sceince 26. Elsevier Science Publishing Company Inc. New York, NY.

Mauldon, M., W.M. Dunne, and M.B. Rohrbaugh Jr., 2001. Circular scanlines and circular windows: new tools for characterizing the geometry of fracture traces: Journal of Structural Geology, 23, p. 247–258, doi:10.1016/S0191-8141(00)00094-8.

McNamara, D. E., H. M. Benz, R. B. Herrmann, E. A. Bergman, P. Earle, A. Holland, R. Baldwin, and A. Gassner, 2015. Earthquake hypocenters and focal mechanisms in central Oklahoma reveal a complex system of reactivated subsurface strike-slip faulting, Geophys. Res. Lett. 42, p. 2742–2749, doi: 10.1002/2014GL062730.

Milad, B., 2013. Modeling and simulation of production from commingled multilayer zone and hydraulically fractured horizontal wells in unconventional gas reservoirs. M.S. thesis, University of Oklahoma, Norman, OK.

Milad, B. and R.M. Slatt, 2017. 3-D Seismic, Outcrop, and Core Data for Characterization of Natural Fractures of the Hunton Limestone and the Woodford Shale in Central Oklahoma. Search and Discovery Article #51382.

Mittal, A., C.S. Rai, and C.H. Sondergeld, 2017. A Study of Propped-Fracture Conductivity: Impairment Mechanisms Under Laboratory Conditions. SPWLA 58th Annual Logging Symposium, June 17-21.

Mytopo, 2016. http://www.mytopo.com/oklahoma

Neuhaus, C.W., 2011. Analysis of Surface and Downhole Microseismic Monitoring Coupled with Hydraulic Fracture Modeling in the Woodford Shale. Master's Thesis, Colorado School of Mines, Golden, CO. https://dspace.library.colostate.edu/bitstream/handle/11124/170559/T6836.pdf?...1

Nolte, K.G. and M.B. Smith, 1979. Interpretation of Fracturing Pressures. Paper SPE 8297 presented at the 54th Annual. Technical Conference and Exhibition, Las Vegas, NV.

Pahl, P.J., 1981. Estimating the mean length of discontinuity traces: International Journal of Rock Mechanics and Mining Sciences and Geomechanics Abstracts, 18, p. 221–228.

Pirayehgar, A., and M.B. Dusseault, 2014. The stress ratio effect on hydraulic fracturing in the presence of natural fractures. ARMA 14-7138, prepared for presentation at the 48th US Rock Mechanics/Geomechanics Symposium held in Minneapolis, MN, USA, 1-4 June.

Portas, R.M. 2009. Characterization and Origin of Fracture Patterns in the Woodford Shale in Southeastern Oklahoma for Application to Woodford Shale in Southeastern Oklahoma for Application to Exploration and Development. Master's Thesis, University of Oklahoma, Norman OK.

Priest, S.D., 1993. Discontinuity analysis for rock engineering: London, United Kingdom, Chapman & Hall, p. 473.

Profit, M., M. Dutko, and A. Bere. Tight Gas Reservoir (TGR) Fracture Model. Retrieved on June 3, 2017. http://www.rockfieldglobal.com/files/7614/6834/4838/Fracture_Model_tgr_by_Rockfield.pdf

Puckette, J.O., B. Darwin, and W.W. Lynn, 2010. Mississippian Stratigraphy of South-Central Oklahoma. North-Central Section (44th Annual) and South-Central Section (44th Annual) Joint Meeting.

Riahi, A., and B. Damjanac, 2013. Numerical Study of Interaction Between Hydraulic Fracture and Discrete Network. Intech open access journal, doi: 10.5772/56416.

Rockfield: Upside of a downturn-Part 1: Breakthrough Geo-Modeling Technologies for Cost Effective Fracture Design and Optimization. Retrieved on June 3, 2017. http://www.rockfieldglobal.com/files/5714/6842/3959/RockfieldLinkedin-Editorial-Elfentgr-01.pdf.

Rogers, S., P. McLellan, and G. Webb, 2014. Investigation of the Effects of Natural Fractures and Faults on Hydraulic Fracturing in the Montney Formation, Farrell Creek Gas Field, British Columbia. DFNE 2014 – 224.

Rohrbaugh, M.B. Jr., W.M. Dunne, and M. Mauldon, 2002. Estimating fracture trace intensity, density and mean length using circular scanlines and windows: AAPG Bulletin, 86, p. 2089–2104.

Sayers, C.M., and J. Le Calvez, 2010. Characterization of microseismic data in gas shales using the radius of gyration tensor. SEG Technical Program Extended Abstracts, p. 2080–2084.

Secor, D.T., and D.D. Pollard, 1975. On the stability of open hydraulic fractures in the Earth's crust. Geophysical Research Letters 2.11, p. 510-513.

Shapiro, S.A., 2008. Microseismicity a tool for reservoir characterization. European Association of Geoscientists & Engineers (EAGE Publications bv)

Shuttle, D.A., W. Dershowitz, E. Glynn, S. Burch, and T. Novak, 2000. Discrete Fracture Network Analysis of Foundation Grouting. in Girard, Liebman, Breeds and Doe (eds) Proceedings of the Fourth North American Rock Mechanics Symposium, Pacific Rocks 2000. 31 July-3 August. Balkema, Rotterdam, p. 1369-1376.

Sinha, S., D. Devegowda, and B. Deka, 2017. Quantification of Recovery Factors in Downspaced Shale Wells: Application of a Fully Coupled Geomechanical EOS compositional Simulator. URTEC-2697500-MS.

Slatt, R. M., B. McCullough, C. Molinares, E. Baruch, F. Cardona, and B. Turner, 2015. Paleotopographic and Depositional Environment Control on "Sweet Spot" Locations in Unconventional Resource Shales: Woodford and Barnett Shale Examples. American Association of Petroleum Geologists, Search and Discovery Article #10713.

Sone, H., and M. D. Zoback, 2014b. Viscous relaxation model for predicting least principal stress magnitudes in sedimentary rocks: Journal of Petroleum Science and Engineering, 124, p. 416–431.

Suneson, N. H., 1997.The geology of the eastern Arbuckle Mountains in Pontotoc and Johnston counties, Oklahoma – An introduction and field-trip guide: Oklahoma Geological Survey Open File Report 4-97.

Suneson, N.H., 2012. Arkoma basin petroleum-past, present, and future, a geologic journey through the Wichitas, Black Mesa basalt, and much more: Shale Shaker, 63(1), p. 38-70.

Vulgamore, T., T. Clawson, C. Pope, S. Wolhart, M. Mayerhofer, S. Machovoe, and C. Waltman, 2007. Applying Hydraulic Fracture Diagnostics to Optimize

Stimulations in the Woodford Shale. SPE 110029. SPE annual Technical Conference and Exhibition, Anaheim, CA, November 11-14.

Warpinski, N.R., 1985. Measurement of Width and Pressure in a Propagating Hydraulic Fracture SPEJ., p. 46-54.

Zahm, C.K. and P.H. Hennings, 2009. Complex fracture development related to stratigraphic architecture: Challenges for structural deformation prediction, Tensleep Sandstone at the Alcova anticline, Wyoming. Am. Assoc. Pet. Geol. Bull., 93(11), p. 1427-1446.

Zeeb, C., E. Gomez-Rivas, P. D. Bons, and P. Blum, 2013. Evaluation of sampling methods for fracture network characterization using outcrops: AAPG Bulletin, 97(9), p. 1545–1566, doi: 10.1306/02131312042.

Zhang, J. 2005. The impact of shale properties on wellbore stability. Ph.D. Dissertation, University of Texas, Austin.

Zhang, X., and R. Jeffrey, 2013. Development of Fracture Networks Through Hydraulic Fracture Growth in Naturally Fractured Reservoirs. Intech open access journal, doi: 10.5772/56405.

Zoback, M.D., C.A. Barton, M. Brudy, D.A. Castillo, T. Finkbeiner, B.R. Grollimund, D.B. Moos, P. Peska, C.D. Ward, D.J. Wiprut, 2003. Determination of stress orientation and magnitude in deep wells, Int. J. Rock Mech. Min. Sci., 40, p. 1049–1076.

CHAPTER 2: AN OUTCROP BASED APPROACH TO UNDERSTANDING THE ORIGIN, SIZE, AND ABUNDANCE OF NATURAL FRACTURES IN THE WOODFORD SHALE

Abstract

Subsurface natural fractures in shales are vital for fluid transport pre- and post-hydraulic fracturing. However, the dominant fracture sets that control the fluid flow in the subsurface are mostly unseen, and their intensity and size variation are largely unknown. This study presents an assessment of the possibility that two main natural fracture sets in the Woodford Shale are present in the subsurface by understanding their generation timings from outcrop studies. Additionally, the relationships between fracture intensity, bed thickness, bed mineral composition, and fracture aperture have been discussed.

The fracture timing investigation includes observations regarding crosscutting, termination, and fracture fill. In addition, knowledge from previous studies regarding burial depth, thermal maturity, bitumen signature, tectonic events, reported subsurface fractures, and fractures from other outcrops were used as clues for fracture timing. Fracture intensities (P10) were quantified by counting fractures (mainly joints) along scanlines. Fracture aperture and spacing were also determined along scanlines.

Out of the several fracture sets identified in the Woodford Shale in the McAlister Cemetery Quarry, two joint sets (E-W and NE-SW) were interpreted as the oldest sets based on crosscutting relationships and fill. These fracture sets also indicate the regional paleostress directions during their genesis. These sets date back to before the Mid-Virgilian Arbuckle Orogeny and likely have different generation timings. Relatively quartz and carbonate-rich beds primarily contain the E-W fractures and the

relatively clay-rich beds mainly contain the NE-SW fractures. The E-W and NE-SW sets are likely ubiquitous in the subsurface due to a higher influence of pore pressure (overpressure) in their generation compared to structural bending. These two fracture sets probably also control the fluid flow in the subsurface. Younger fracture sets show more influence of local folding and are overrepresented in the outcrops with tilted beds. In the observed thin sections, bitumen and quartz cement is prevalent in early bed-perpendicular fractures. Carbonate cement is more prevalent in late bed-perpendicular and late bed-parallel fractures.

Also, a negative correlation between fracture intensity and bed thickness, and a positive relationship between fracture intensity and quartz/carbonate content exist in the studied location. Fracture opening displacements show characteristic best-fit trends and lack crack-seal texture. Fracture spacing coefficient of variation ($\sigma_{spacing} \div \mu_{spacing}$) < 1, i.e., uniform fracture spacing was seen in all outcrop measured beds.

2.1 Introduction

The standard and necessary stimulation method in shales is hydraulic fracturing which improves oil and gas recovery. Natural fractures are critical in controlling the fluid flow in the subsurface and connectivity to an artificial hydraulic fracture because these are planes of weaknesses (Ferrill et al., 2014; Busetti et al., 2014; Smart et al., 2014). Outcrops are useful in measuring some of the basic natural fracture parameters such as relative fracture intensities among facies, fracture cementation, and fracture timing through crosscutting relations over laterally extensive areas.

Studies related to the natural fracture generation timings have been conducted by Cosgrove (2001), Tan et al. (2014), and Pireh et al. (2015) using outcrop

observations. They have attributed diverse mechanisms such as folding and overpressure to the natural fracture generation. Also, Einstein and Dershowitz (1990) mentioned that a single stress regime is capable of producing multiple fracture sets. On the other hand, multiple stress regimes are also capable of producing multiple fracture sets. Therefore, one of the main aims of this study is interpreting the mechanism (cause) of several joint sets, their origin timings, and related paleostress regimes using outcrop observations. A related goal is to predict the major subsurface fracture sets in the Woodford Shale using the outcrop fracture interpretations. The non-unique mode or timing of genesis of the E-W and the NE-SW fracture sets has been addressed by suggesting alternative scenarios of their genesis.

Besides, understanding the relative natural fracture abundance among different beds is important because it indicates the relative fluid flow capacity. Preexisting fractures can control the hydraulic fracture geometry (Cipolla et al., 2008b; Li et al., 2015). Wennberg et al. (2006) found a weak correlation between the bed thickness and fracture intensities. Ladeira and Price (1981) found a negative relationship between fracture intensity and bed thickness with considerable scatter in the datapoints. Lamarche et al. (2012) did not find a relationship between bed thickness and fracture intensity. Laubach et al. (2009) mentioned that mechanical and fracture stratigraphy may or may not coincide. These observations were tested in the studied outcrops by studying the dependence of fracture intensity on bed mineralogy and mechanical bed thickness.

In addition to the intensities, fracture opening displacements (kinematic aperture) distributions and spacing have not been systematically studied in the

Woodford Shale. Aperture distribution is important because this can significantly affect the flow characteristics of the reservoir (Renshaw, 1997; Keller, 1998). Non-bed-bounded fractures exhibit a broad range of apertures and show power-law scaling and crack-seal texture (Hooker et al., 2013). On the other hand, bed-bounded fractures exhibit narrow aperture-size ranges and do not show crack-seal textures (e.g., Weiss et al., 2006; Odonne et al., 2007). However, wide ranges in aperture size have also been documented in stratabound fracture sets (Ortega et al., 2010).

The McAlister Cemetery Quarry (MCQ) located in the Criner Hills of Southern Oklahoma (USA) is the primary focus of this study. However, examples from other outcrops and subsurface studies as are used as supporting evidence. In summary, a multiscale (outcrop and derived thin section) approach to understanding the fractures in the Woodford Shale is presented to address the following major questions: a) What are the most relevant fracture sets in the Woodford Shale, i.e., the ones that exist in the flat subsurface beds (fractures not related to folding) and control fluid flow; b) when and under what stress regime did they originate?; c) how do fracture intensities vary with bed mineralogy and thickness?; d) what is the best-fit opening displacement (kinematic aperture) distributions in the studied area?

2.2 Geology

The Woodford Shale was deposited during a 29 million year time interval (388 mya to 359 mya), which makes it a 2nd order depositional sequence (Slatt, 2013). The Woodford Shale has three informal divisions- upper Woodford Shale (UW), middle Woodford Shale (MW), and lower Woodford Shale (LW) (Slatt, 2013). As mentioned by (Serna-Bernal, 2013) from her study in the MCQ, an increasing gamma ray trend

from the base of the LW to the base of the MW indicates that the LW was deposited as a 2nd order transgressive systems tract (TST). A decreasing gamma ray (GR) trend from the base of the MW and again increasing toward the to the base of the UW indicates that the MW was deposited during a transition between a 2nd order highstand systems tract (HST) and TST. The MW consists of a condensed section, a maximum flooding surface, and has the highest organic content among the three members in the studied area. A relatively stable GR trend, commonly observed for the UW, indicates that the UW was deposited as an HST (Serna-Bernal, 2013). The UW is organic-poor; MW followed by LW are organic-rich (Serna-Bernal, 2013).

Figure 2.1 shows the NW-SE fold and fault trends in the Criner Hills area and the MCQ. Figure 2.2 shows the general stratigraphy of the Criner Hills and the bed deposition times. According to Cooper (1995), the Ardmore Basin (north) and the Criner Hills trend went through several stages of deformation. Figure 2.2 shows that the Woodford Shale was deposited on an unconformity above the Hunton Group during the Devonian Period. After the Woodford Shale had been deposited, there was an accumulation of more than 5000 ft (~ 1500 m) of sediments during which, the Sycamore Limestone, Caney Shale, Goddard Formation, and the Springer Formation were deposited (Lang III, 1957). Subsequently, during the Late Mississippian to Early Pennsylvanian Period, there was an Orogeny associated to the Criner Hills. This orogeny coincides in time with that of the well-known Ouachita Orogeny in Oklahoma and Arkansas. The Criner Hills were moderately folded, and formations as high as the Caney Shale were exposed due to the erosion of the overlying sediments near the anticline crests (Lang III, 1957). The Woodford Shale was also possibly exposed at a

few places (Tomlinson, 1936). Progressively away from the crests, formation such as the Springer Formation was partially eroded. Subsequently, the Dornick Hills Group was deposited away from the anticlinal crests. Not much deposition took place near the crests (where the Woodford Shale is exposed today) because of its higher elevation. This period was followed by an epeirogeny removing some of the Dornick Hill Group sediments. Subsequently, in the second half of the Pennsylvanian Period, the Deese Group, Hoxbar Group, and Cisco Formation were deposited with the total thicknesses being 3500-4500 ft (~ 1070-1370 m) near the crests and thicker, moving away (interpreted from Stage I, II, and III schematics in Lang III [1957, between p. 24-25]). During the Mid-Virgilian Arbuckle Orogeny, there was an extensive uplift along the Overbrook Fault and hundreds of feet of displacement along the Criner, Kirby, and Rock Crossing faults (Lang III, 1957). With subsequent erosion, the Deese Group, Hoxbar Group, and the Cisco Formation were eroded, exposing the Woodford Shale and the Sycamore Formation near the crests. Since Mid-Virgilian, there has not been a substantial structural change in the area except for a broad uplift of Oklahoma related to the uplift of the rocky mountains in the Late Cretaceous and Early Tertiary (Johnson, 2008). Currently, the beds in the MCQ dip approximately 30-60 degrees towards the east and strike NW-SE to NS (Figure 2.3).

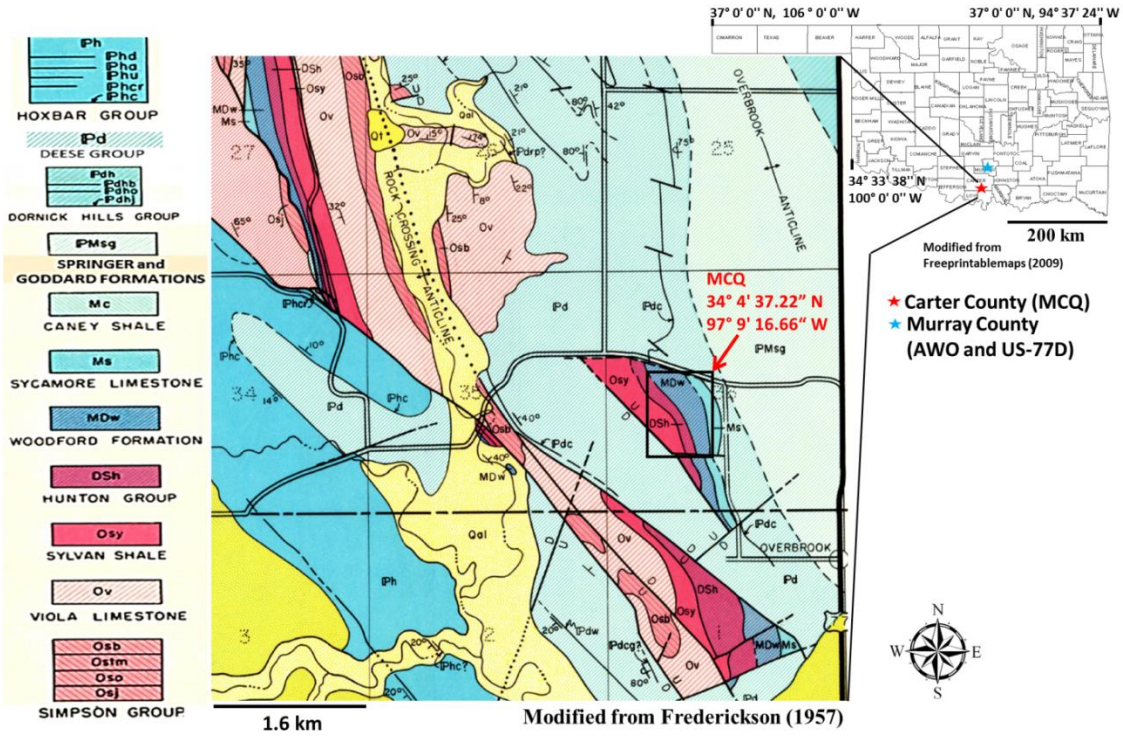

Figure 2.1: Geologic map of the Criner Hills area in which the MCQ is located. The MCQ is marked using a rectangle (center-right of the geologic map) and is the primary focus of this study. Top right: Oklahoma map shows the location of the Criner Hills (red star) in Carter County. In addition, the locations of the Arbuckle Wilderness Outcrop (AWO) and the US-77D Outcrop (Murray County) are shown in the azure star and will be mentioned during the discussion.

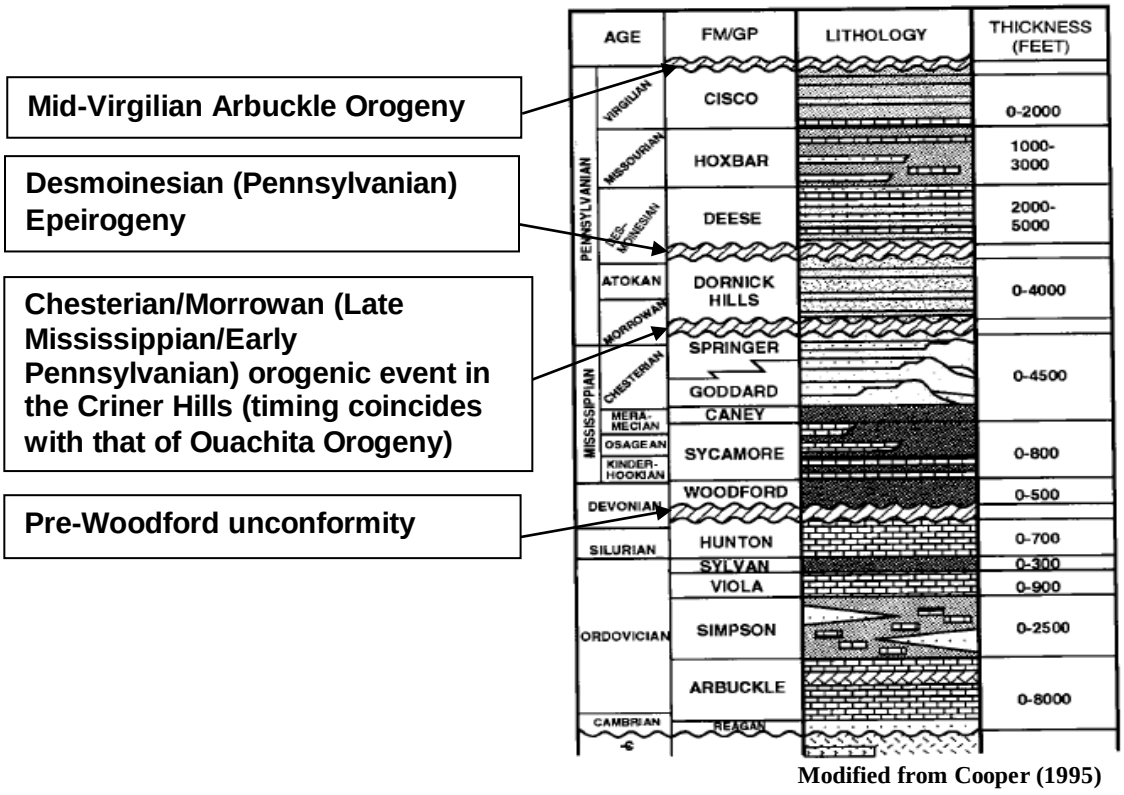

Modified from Cooper (1995)

Figure 2.2: General stratigraphy of the Criner Hills. Some of the significant unconformities and orogenic events are depicted. In the MCQ, the Sycamore Limestone, located stratigraphically above the Woodford Shale, is the topmost formation exposed.

2.3 Methods

2.3.1 Mineralogy

The mineral percentages were measured using X-ray diffraction (XRD) analysis, which assisted in defining the lithofacies based on the rock compositions. Rigaku Ultima IV XRD analyzer and Jade™ Software were used for quantifying mineralogies. Turner et al. (2015) describe the XRD methodology in more detail. Since TOC (total organic carbon) values are not available for most beds, the fraction weight of quartz and carbonates was used as a measure of brittleness. Therefore, these are pseudo brittleness index (Pseudo-BI) values. In a complete BI equation, the TOC fractional weight is

present along with the mineral fractions (e.g., Jin et al., 2015). Pseudo-BI values were assigned to each lithofacies and plotted against the average fracture intensities. Spots in the MCQ from where samples were collected for XRD and intensity measurement are shown in Figure 2.3. The differentiation between brittle and ductile lithologies also forms a part of the discussion on fracture strikes.

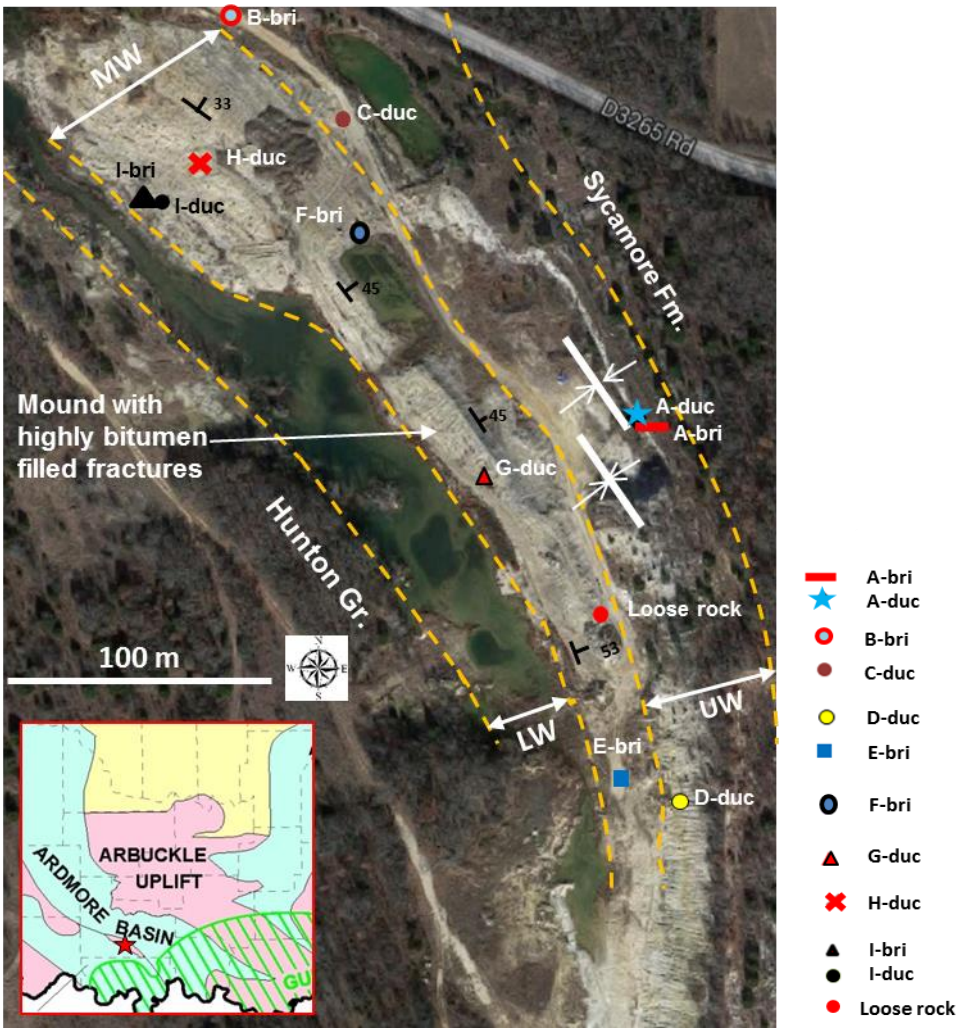

Figure 2.3: Plan view of the MCQ (34°04'42.5"N, 97°09'22.3"W). The rightmost dashed line is the top of the upper Woodford Shale (UW). The leftmost dashed line is the base of the lower Woodford Shale (LW). The middle Woodford Shale (MW) is also shown. Locations where fracture intensities were measured and samples were collected for XRD and thin sections are marked by different symbols with designations A, B, C, D and so on. Here "bri" and "duc" signify brittle and ductile beds respectively. Folds located on the east side of the quarry are marked. An out of place rock piece (probably

came from UW) was named “Loose rock.” A mound (higher profile area in the pit left unmined) is shown in the middle of the pit.

2.3.2 Fracture intensity, aperture, and spacing

Many researchers have used the scanline method, in which fracture intensities are measured along scanlines oriented sub-perpendicular to the fracture traces (e.g., Ladeira and Price, 1981; Engelder et al., 2009). In this study, the scanline lengths ranged between 0.6-2 m (~ 2ft-7ft) at places with well-exposed fractures (filled or open) on the bedding cross section. The number of macrofractures, i.e., the fractures that are visible to the naked eye (apertures usually > 0.05 mm) were counted along each bed. In addition to scalines for macrofractures, a microscanline was used on a thin section for measurement of microfracture parameters as several microfractures were visible on the thin section. This number of fractures is divided by the scanline length to find the linear fracture intensity [P10] for the particular bed (unit: fractures/m). Individual bed thicknesses (unit: cm) were also measured. Intensities vs. bed thickness were plotted for individual beds.

Fracture opening displacement (kinematic aperture) sizes were measured along a few competent bed cross sections using a hand lens and a comparator along scanlines (e.g., Ortega et al., 2006; Hooker et al., 2013). Comparator width markings range 0.05 - 5 mm (0.000164-0.0164 ft). Aperture cumulative frequencies were calculated, and goodness of fit (χ^2) analyses were performed to quantify the discrepancy between the measured and the calculated cumulative-frequency values.

During this process, the spacing between each adjacent fracture was recorded to understand the degree of clustering. A parameter $C_v = \sigma_{spacing} \div \mu_{spacing}$ was calculated. $C_v = 1$ indicates random positioning for fractures, $C_v < 1$ indicates more evenly spaced

fractures than random spacing, and $C_v > 1$ indicates more clustering than random spacing (Gillespie et al., 1999).

2.3.3 Fracture timing determination

The fracture timing investigation began with observations regarding the crosscutting and termination relationships between several fracture sets in the Woodford Shale in the MCQ. These observations are followed by studying the type of fracture fill, both at the bed scale and thin-section scale. Presence or absence of dead bitumen, along with the knowledge from previous studies regarding burial depth, thermal maturity, and bitumen signature from the adjacent rocks were used as clues for the timing of the fracture fill. Additionally, the mode of fracture origin (tensile and shear) was interpreted using the difference in strikes between two fracture sets. This was followed by looking for evidence of similar fractures at other outcrops and reported subsurface observations in both the Woodford Shale and under/overlying formations. All of these observations were combined with the knowledge of the major documented tectonic events in an attempt to pinpoint the generation timings.

2.4 Results

2.4.1 Mineralogy and facies description

For assigning siliceous, dolomitic, and argillaceous names to the facies, XRD mineral percentages were used. Lazar et al. (2015) provide a scheme for assigning facies names. Using this naming scheme, most of the Woodford Shale would carry the name "siliceous mudstone" since most brittle and ductile beds have > 50% quartz component. Therefore, this scheme was slightly modified to attach higher importance to non-quartz, i.e., the calcareous (mainly dolomite) and argillaceous minerals.

Figure 2.4 shows the ternary plot of the minerals. To give higher resolution, for the purpose of assigning names to the Woodford Shale facies, the baseline (carbonate-clay) was lifted to the position of Carbonate'-Clay' effectively discounting quartz by 60%. Therefore, the new triangle is now defined by the three points: quartz, carbonate', and clay.' Wang and Gale (2009) defined a brittleness index equation in which they described quartz and dolomite as brittle minerals. Calcite, clay, and TOC were defined as ductile. Therefore, the words "brittle" and "ductile" do not indicate the mode of failure (Herwanger et al., 2015) but only mineralogy.

To the left of the dashed line are the brittle, and to the right are the ductile facies. For the ductile facies, points on or very close to the quartz-clay'-clay line are classified as argillaceous mudstones. The "bri" and "duc" are suffixes at the end of the spot names meaning brittle and ductile facies respectively, collected from these spots. The beds classified as "brittle" usually have > 80-85% quarz+carbonate (mainly dolomite) content and have blockier textures, compared to the ductile beds. A-bri, B-bri, E-bri, I-bri, F-bri are considered brittle. The brittle beds have < 15-20% argillaceous components and contain organic matter between 3-6.5% with most below 5% (Fishman et al., 2013). These beds can range from laminated to massive in texture. The majority of the brittle beds seen directly appear massive. However, under microscope smaller scale laminations are visible. Therefore, if laminations are prominent under the microscope in the collected samples, the brittle beds are considered laminated.

On the other hand, beds with < 80-85% non-siliceous, non-dolomitic components are classified as "ductile." Laminations increase with clay content and are visible in both bed scale and under the microscope as opposed to the brittle rocks.

Because some of the relatively silica or dolomite-rich ductile beds are not as highly laminated as the ones with higher clay content, it was necessary to differentiate between these two ductile facies types. Therefore, the rocks classified as argillaceous-siliceous (or siliceous-argillaceous), and argillaceous-dolomitic (dolomitic-argillaceous) are classified as "less ductile" compared to the highly laminated argillaceous beds, which are classified as "more ductile." The less ductile beds would lie on either side, but not far from dashed line in the ternary diagram (Figure 2.4). Therefore, some beds classified as "argillaceous," such as C-duc, A-duc, can be considered as "less ductile," since they are located relatively close to the dashed line. The argillaceous-dolomitic bed, located outside the quartz-carbonate'-clay' triangle can also be considered as less ductile because the presence of 15-20% dolomite makes the beds relatively resistant (shown later). However, beds such as G-duc and D-duc are clearly more ductile. In the text, the use of only "ductile" means both "less ductile" and "more ductile" beds unless specified.

Serna-Bernal (2013) reported TOC values ranging 0.1-15.5% in the MCQ. In the ductile (or non-brittle beds) beds, TOC values ranging 8-22% were reported by Fishman et al. (2013) in the AWO (Arbuckle Wilderness Outcrop) and US-77D area (azure star in Map of Oklahoma in Figure 2.1). Since the Woodford Shale has varying degrees of organic material, it is worthwhile to differentiate between beds with high organic content from beds with lower organic content. Therefore, beds containing > 10% organics, as visualized from thin sections, were assigned a "carbonaceous" prefix. This naming scheme automatically excludes all brittle beds and some ductile beds from having the "carbonaceous" prefix.

Becerra (2017), using uniaxial tests performed perpendicular to the bedding, reported Young's modulus and Poisson's ratio values of chert: E = 31 GPa and υ = 0.14; dolomitic mudstone: E = 19 GPa, υ = 0.17; argillaceous mudstone: E = 9 GPa, υ = 0.2. However, these values can vary with changes in sample mineralogy and preexisting microfracture density.

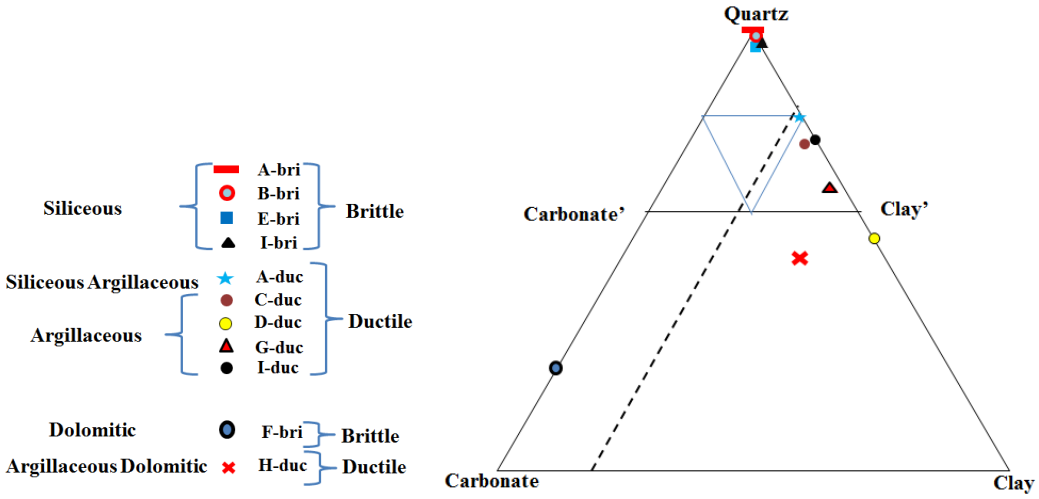

Figure 2.4: Ternary diagram of the compositions of collected samples in the McAlister Cemetery Quarry. Left of the dashed line are the brittle facies, and right are ductile facies. Brittle facies are either rich in quartz or dolomite (carbonate). Locations of spots A-I are shown in Figure 2.3.

2.4.2 Fracture set identification and orientation from outcrop

The fractures discussed here are mainly "joints," as no visible offsets along the faces are visible at bed scale. Also, there is no evidence of slickenlines on the faces of any of these fractures. However, the term "fractures" is used in this study because it implies both tensile joints and joints with minor shear (pre- or post-genesis) that may not be visible to the naked eyes.

Five bed-perpendicular fracture sets were identified: Sets 1, 2, 3S, 3P, and 4, based on crosscutting, orientation, and fill. Here 3S and 3P mean Set 3 "sinuous" and Set 3 "planar" fractures respectively. Fracture sets 1, 2, 3P and 4 are mostly planar.

These fractures are identified on the outcrop with arrows (drawn perpendicular to their strikes) in Figures 2.5A through 2.5C. Also, Figure 2.5A defines these fractures with lines drawn directly above some for the fractures. Their orientations, as measured on the outcrop, are shown in Figure 2.6A, 2.6B and Table 2.1. Set 1 (ENE-WSW to E-W striking) fractures are long (up to several feet visible), planar, systematic, and contain mm thick bitumen. Sometimes, hackles are seen on Set 1 faces (top right inset in Figure 2.5A). Set 1 fractures are more developed in the brittle beds and less ductile beds, and relatively underdeveloped in the more ductile beds, i.e., present in 5-10% of the more ductile (especially thin ones) beds. Set 2 (NE-SW striking) fractures are also long (up to several feet visible), planar, systematic, contain mostly bitumen and sometimes thick cement (Figure 2.5C). Set 2 fractures are well developed in the more ductile beds (Figures 2.5A and 2.5B) and sometimes cut the less ductile ones. However, they are generally absent from the brittle beds.

Set 3S fractures are sinuous (mm scale wavelengths), unevenly spaced (non-systematic), bitumen-filled, and have 20-30 degrees variation in the strike. Most of them terminate at Set 2 fractures, and some of them crosscut the Set 2 fractures. Set 3P fractures (ESE-WNW striking) also terminate at Set 1 fractures and are mostly open, with occasional bitumen and cement fill, as seen on the outcrop. Set 3P fractures are relatively well developed in the brittle and less ductile beds (Figure 2.5A). These are generally absent from more ductile beds. Set 4 fractures (NW-SE striking) are even to unevenly spaced with no clear evidence of cementing as seen on the outcrop. They mostly strike parallel to the fold direction and terminate at, or crosscut Set 1 fractures.

No clear evidence of slickensides is present on any of the fracture faces. Set 4 fractures are present in both brittle and ductile beds.

Some of the Set 2 and Set 3S fractures in the MCQ have low heights, i.e., a fraction of a mm to a few mm, because they are contained within very thin beds. These thin beds are richer in clay and probably organics compared to the over and underlying brittle beds and may be connected to the over- and underlying brittle beds. Figure 2.5A gives an example of a thin clay-rich bed and underlying, thick dolomitic bed. The thin clay-rich beds also have higher intensities of Set 2 fractures compared to Set 1. At some places, however, Set 2 fractures are a couple of centimeters high allowing orientation measurements. Due to their presence in the ductile beds, which are fissile and prone to weathering and erosion, fracture-face features are rarely preserved. However, occasionally, hackles are visible on the faces (top left inset in Figure 2.5B). Figure 2.6A shows the poles to the fracture planes as measured near the mound (higher profile area in the pit left unmined) shown in Figure 2.3. Figure 2.6B shows the rose diagram for the fracture orientations.

The rose diagram in Figure 2.6C shows considerable variation in the bed orientations in the MCQ. The fracture orientations presented in Table 2.1 were measured where the beds have an orientation of 326/46 (using right-hand rule) near the mound (Figure 2.3). Comparing Figures 2.6A and 2.6D show that upon restoring the beds to horizontal, orientations remain roughly the same for Set 1 and Set 2 fractures (5-10 degrees of variation in the strikes and 7-8 degrees variation in the dips). Set 1 fractures, after bed restoration, strike almost E-W, and will be referred to as either “Set 1” or “E-W” fractures without calling them as “ENE-WSW” fractures hereafter (even

though some of them strike ENE-WSW). For Set 4 and Set 3P fractures, strikes remain roughly the same, and dips change 40-50 degrees post-bed-restoration to horizontal.

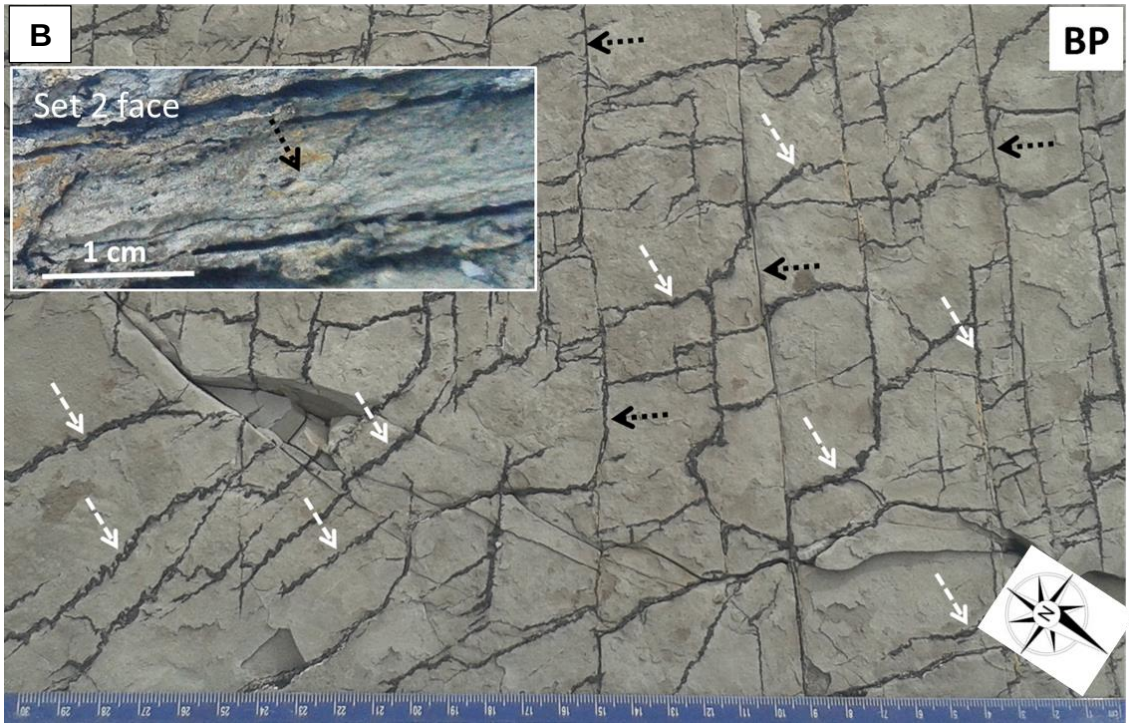

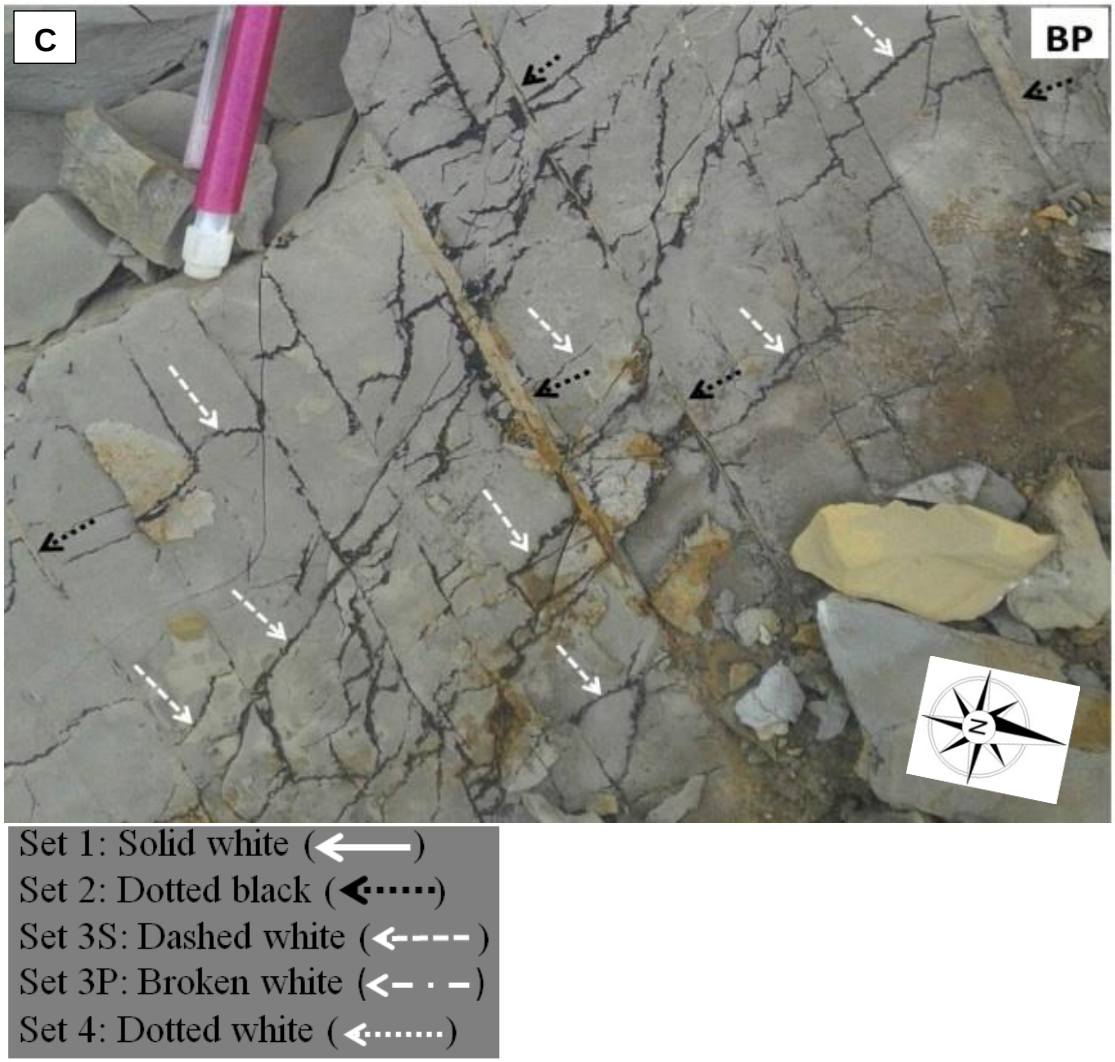

Figure 2.5: Joint sets in the McAlister Cemetery Quarry. **A)** 13 cm (5 in) thick dolomitic mudstone bed (top marked by a black triangle shape) with mm scale argillaceous mudstone bed on top (marked by a black star shape). The location is the mound (higher profile) located in the middle of the quarry (Figure 2.3). Notice the abundance of Set 2 and 3S fractures in the thin mudstone bed and their absence in the underlying thick dolomitic bed. Sets 1, 3P, and 4 fractures crosscut both the thin argillaceous mudstone (ductile) and the underlying dolomitic mudstone (brittle) bed. The double-headed arrow shows nearly 0.5 mm thick dead bitumen sheet cement (held in hand) that is pervasive within the Set 1 fractures in the MW. The double-headed arrow also shows hackles on the Set 1 fracture face (top right inset). **B)** Closer view of the mildly wiggly/sinuous, systematic, and bitumen-filled Set 2 fractures, and very sinuous, non-systematic, bitumen-filled Set 3S fractures in the thin mudstone bed. Set 2 face is shown in the top left inset. **C)** Cemented Set 2 fractures. Notice that the sinuous Set 3S fractures not only terminate at the Set 2 fractures but also crosscut the thick cement of Set 2 fractures at a few places. **Abbreviation- BP**: looking at the top, as opposed to a cross section of a bedding plane.

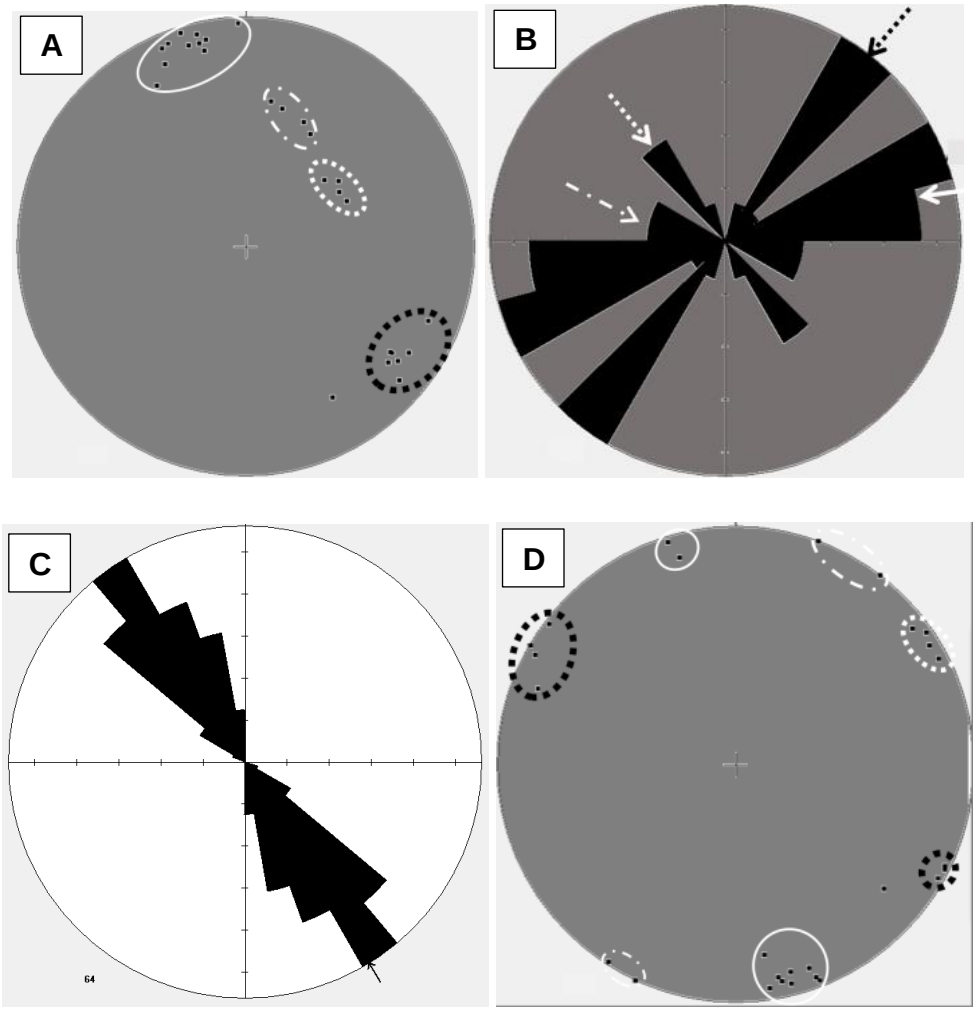

Figure 2.6: Joint and bed orientations in the McAlister Cemetery Quarry. **A)** Poles to the planes of four fracture sets (1, 2, 3P and 4) as measured on the outcrop using the same line styles as in Figure 2.5. Measurements were made on a bed oriented close to 146/046 near the mound. **B)** Rose diagram showing strikes of Sets 1, 2, 3P and 4. The diagram does not reflect the relative fracture abundance. **C)** Rose diagram showing bed strikes. **D)** Fracture orientations after bed rotation of 46 degrees about 146 degrees azimuth (i.e., bed restoration to horizontal). Notice that most are high angle bed-perpendicular fractures (joints).

Table 2.1: Pre- and post-bed-restoration fracture orientations in the McAlister Cemetery Quarry using right-hand rule.

Set	Average fracture orientations as measured on the outcrop on beds oriented close to 146/046	Average fracture orientations after bed restoration to horizontal
1	073/81	256/88
2	215/72	030/90
3S	Sub-perpendicular to Set 2	Sub-perpendicular to Set 2
3P	109/51	118/90
4	149/38	147/86

The Set 1 and 2 fractures were also seen at several other outcrops, i.e., Figure 1.4D and 1.4F (Woodford: Wyche Shale Pit), Figure 1.6J through 1.6M (Hunton: Jennings Quarry), and Figures 1.8A and 1.8B (Woodford: Clarita Shale Pit) shown earlier and Figure 3.5A through 3.5J (US-77D and AWO) shown later. The locations in Figure 3.5 is depicted in azure star in Figure 2.1 on the map of Oklahoma (AWO and US-77D Outcrops).

2.4.3 Lithofacies and fracture fill

The upper part of the UW is mainly marked by the presence of phosphate nodules, and low GR values (Table 2.2). Thin sections of massive to laminated siliceous-argillaceous mudstone (white arrow in Figure 2.7A) and brittle massive siliceous mudstone (chert) beds (black arrow in Figure 2.7A) are shown in Figure 2.7C through 7H. This area has one of the highest overall fracture intensities of the entire Woodford exposed in the MCQ. A stylolite with bitumen spread into the matrix is shown in Figure 2.7C in the ductile siliceous-argillaceous mudstone (A-duc) but not commonly seen in the other thin sections or the same thin section. Figures 2.7E and 2.7H show subhedral quartz crystal growth into voids in both directions from the wall

and from one direction of the wall to the other respectively. Two growth stages, where there is growth of quartz cement at the wall and calcite cement at the void is shown in Figure 2.7F. The crystal sizes progressively increase from wall to the fracture center going from quartz to calcite and also quartz and calcite considered individually. Generally, the younger crystals are the large subhedral/blocky quartz crystals towards the center of the fracture, and the older ones are smaller (more elongate) quartz crystals near the fracture edges (Bons et al., 2012). In Figure 2.7F, the probable growth direction of calcite crystals is indicated by an arrow. Quartz cement bridges (Figure 2.7G) and blocky and elongate blocky crystals are shown in Figures 2.7E (2.7D), 2.7F and 2.7H. Bons et al. (2012) discuss crystal cement growth in greater detail. Sometimes bitumen is also seen in both fracture sets in the UW but is much rarer compared to quartz and calcite. Porosity in the central and right fractures in Figure 2.7D are probably artifacts of thin-section making. Voids in Figures 2.7F and 2.7H seem to be related to deposition (probable burrows) rather than fracturing.

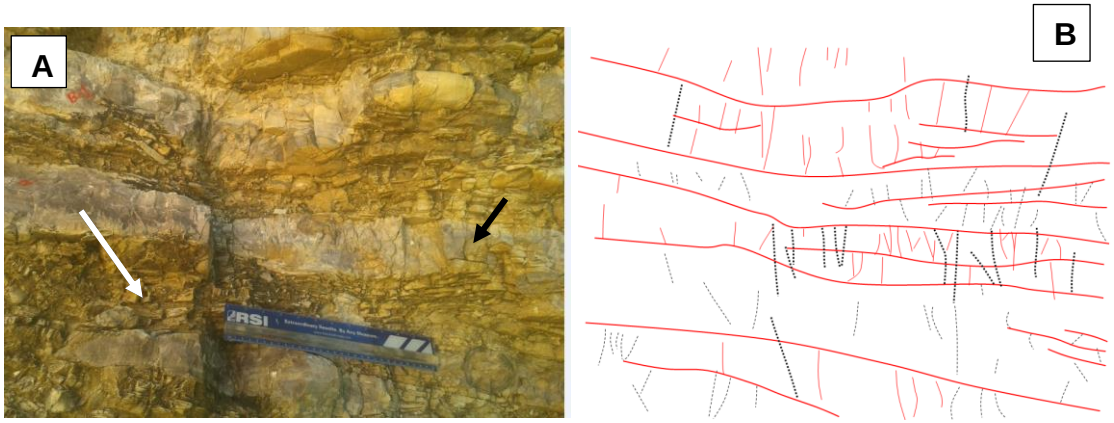

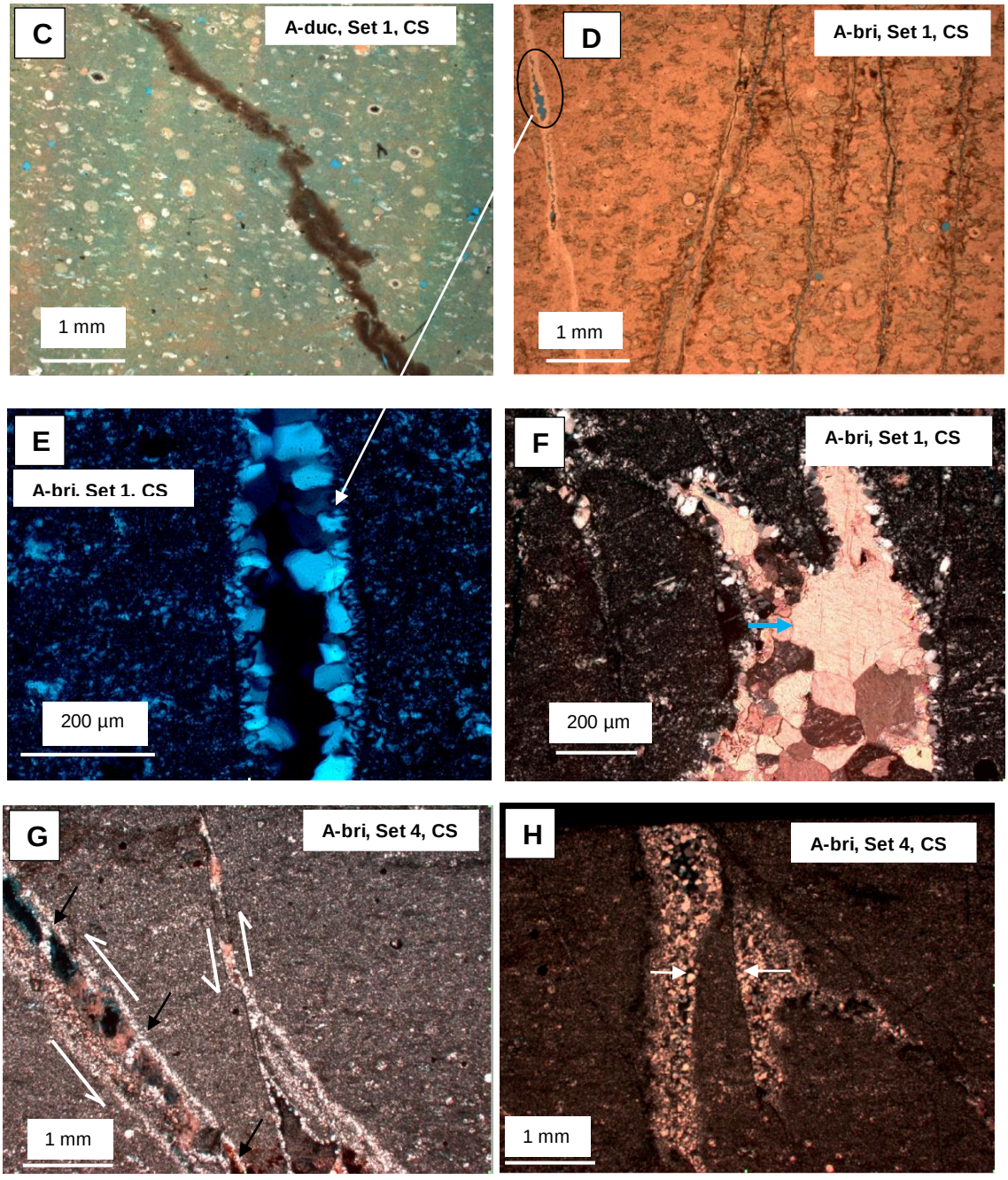

Figure 2.7: A-duc and A-bri outcrop and thin-section expressions. **A)** Photograph of the UW wall showing alternating facies of siliceous-argillaceous mudstone (white arrow: A-duc) and massive siliceous mudstone [Chert] (black arrow: A-bri) **B)** Bed and fracture traces. Fractures in brittle beds are marked in solid red and ductile beds are marked in thin dashed black lines. The thick dotted black lines represent bed boundary crossing fractures. Bed boundaries are in red. Note that, based on fracture terminations, sometimes bed boundaries can change within the same thick chert bed. The lines drawn are not the only macrofractures but only the ones seen in the photograph in A. Closer look at the bed directly reveals more macrofractures (scale same as in A). **C)** Thin-section (PPL) photograph of the siliceous-argillaceous mudstone (A-duc) is mainly

composed of radiolaria (round) and microcrystalline (probably authigenic) silica and detrital (irregular shape) silica. This facies is not very well cemented. **D)** Thin-section (PPL) view of UW massive siliceous mudstone [Chert] (A-bri) dominated by microcrystalline (authigenic) quartz and radiolaria. It has many more quartz-filled fractures compared to C. Some of the fractures are partially to completely healed. The fracture on the left (in circle) is almost completely healed with subhedral quartz cement with some remaining space/porosity for crystal growth. Some porosity is also present in the fractures to the right, but it is doubtful if those are artifacts or really empty pores. **E)** Magnified view (CPL) of the circled area in C. Elongate blocky crystals suggest growth from the wall towards the center. **F)** Thin-section (CPL) view of elongate blocky quartz crystal cement at fracture walls and blocky calcite crystal cement in the middle. **G)** Thin-section (PPL) view of quartz bridges (arrows), calcite-fill in pores (pink) and porosity. **H)** Thin-section (CPL) view of voids filled with blocky/subhedral quartz crystals. Arrows indicate growth directions within individual voids. **Abbreviations-BP**: thin section showing the top of a bedding plane; **CS**: thin section showing bed cross section.

Figure 2.8A shows the most highly jointed (Figure 2.8B) facies laminated siliceous mudstone (with intermittent chert and radiolarian-rich laminae) in the MCQ. Figure 2.8B also shows bed boundary crosscutting fractures (microfaults) that are oriented oblique to the beds and contain mm scale displacements. This facies is located in the lower part of the UW (B-bri). These siliceous mudstones/siltstones have 99.5% quartz content. They appear distinct from the UW chert-rich facies. The fractures, as observed in the thin sections, are mainly bitumen-filled (Figure 2.8D). This facies has only slightly higher organic content (based on thin-section observations) compared to the upper section silica-rich facies but generally has a low concentration of organic material compared to the MW and LW. Probable burrows that resemble bed-parallel fractures are common in areas with microcrystalline (authigenic) silica (Figure 2.8C).

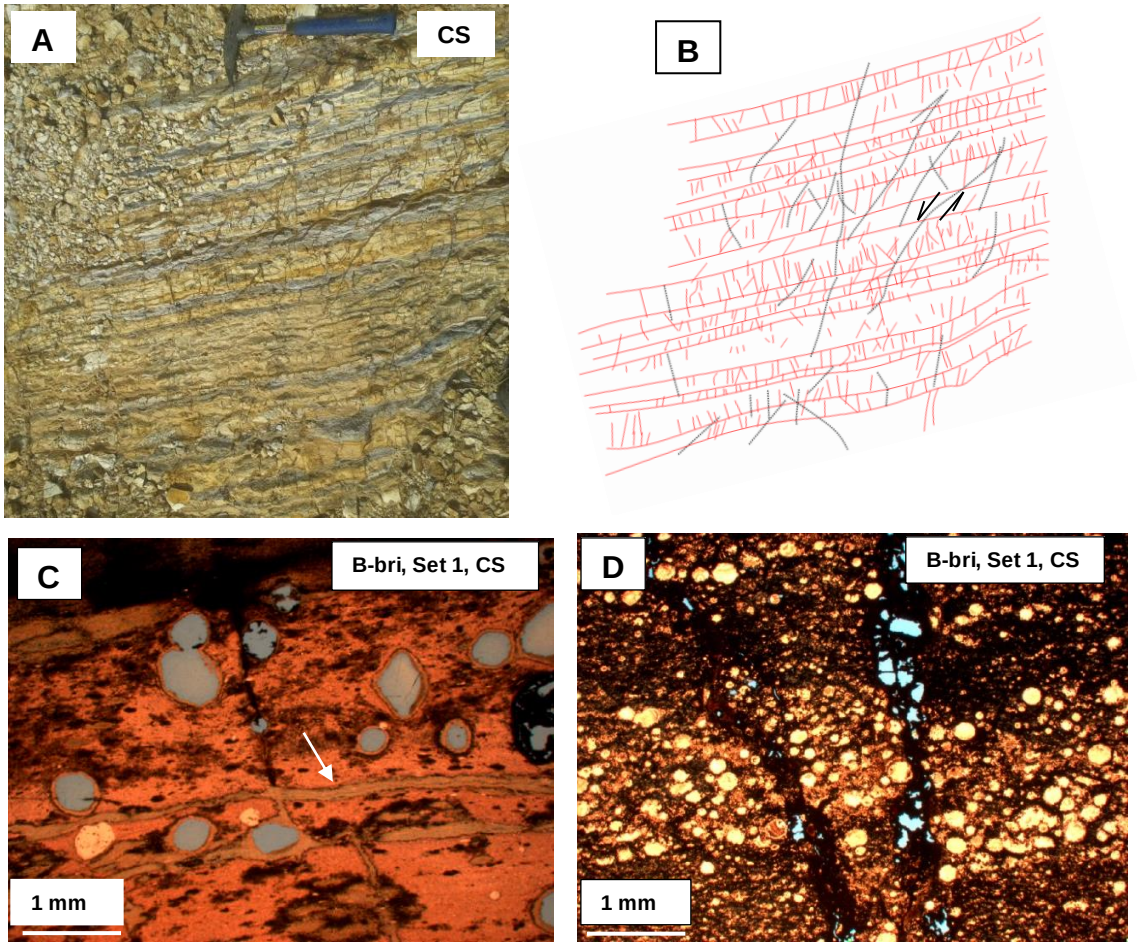

Figure 2.8: B-bri outcrop and thin-section expressions. **A)** Photograph of the laminated siliceous mudstone (with intermittent chert and radiolarian-rich laminae) visible in the lower part of the UW (B-bri). **B)** Bed and fracture traces (Scale same as in A). **C)** The matrix is cherty (microcrystalline quartz) and less organic-rich compared to D. Large empty holes are probably burrows that were bitumen-filled before the thin section was created. The white arrow indicates structures that resemble fractures but are probably borrows identified by their morphology and lack of continuity. **D)** Laminated siliceous mudstone with intermittent radiolarian rich laminae. It is also richer in organics compared to C. The holes in C and D probably lost the filling material during thin-section making. Both C and D photographs (PPL) were obtained from the same thin section.

A massive to laminated carbonaceous, argillaceous mudstone (~ 75% quartz, ~ 25% clay) whose photograph was taken from the lower part of the UW (C-duc), but exists at several places in the MW and LW is shown in Figure 2.9A. Fracture and bed traces are shown in Figure 2.9B. In a thin section, this facies appears mostly massive

with a few continuous, planar, parallel laminations. Due to their high quartz content compared to other ductile facies these beds can be considered less ductile. Figure 2.9C shows a probable bitumen-filled fracture broken at several points due to slip along clay-rich laminations.

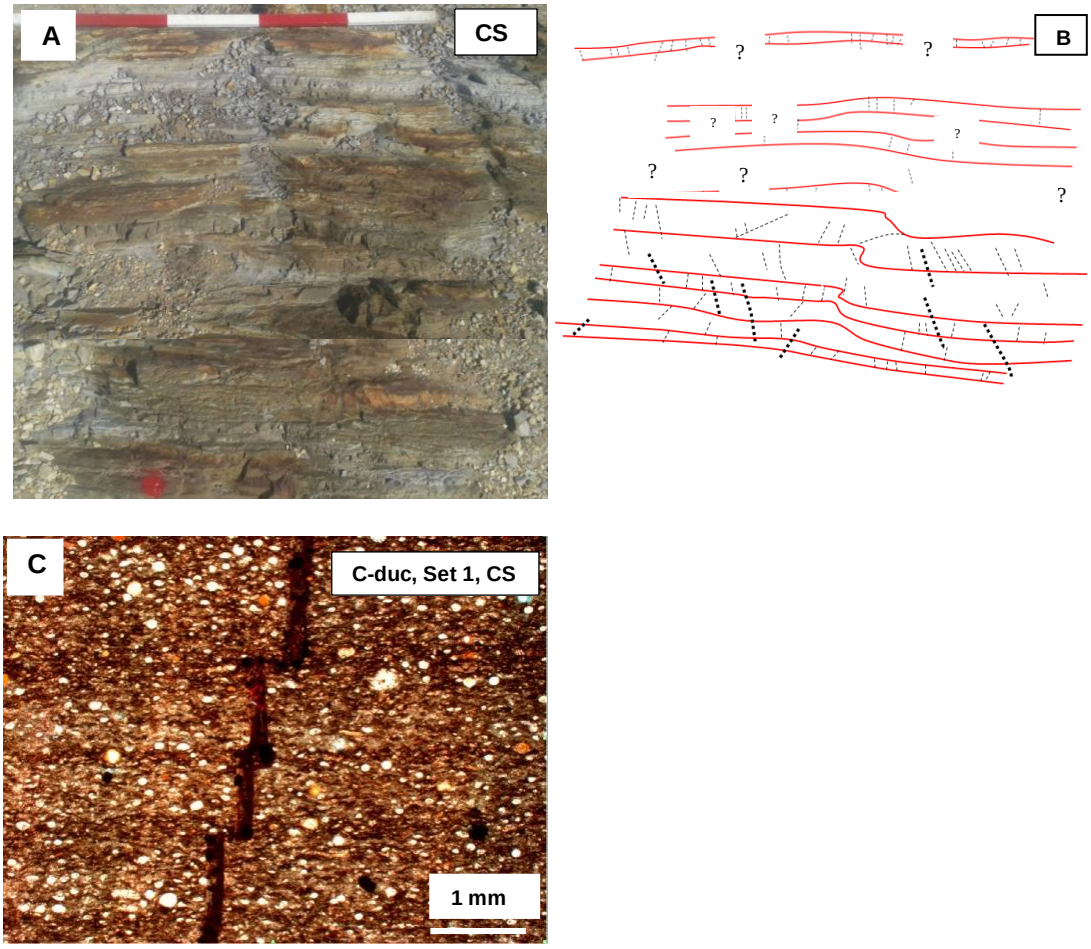

Figure 2.9: C-duc outcrop and thin-section expressions. **A)** Photograph of the massive to slightly laminated carbonaceous, argillaceous mudstone beds visible in the lower part of the UW (C-duc). **B)** Bed boundary and fracture traces. Fracture traces are not very well exposed (Scale same as in A). **C)** Thin-section (PPL) view showing bed-parallel slip perpendicular to Set 1 fractures, i.e., parallel to Set 4 fractures. Notice that Set 1 bitumen-filled fracture is offset along several darker clay-rich thin laminations and has blunt tips.

An argillaceous mudstone zone (D-duc), is located in the lower part of the UW (Figure 2.10A). Fracture and bed traces are shown in Figure 2.10B. It is devoid of

organics. The main mineral constituents are quartz (~ 53%), and clays (~ 47%). The thin section is shown in Figure 2.10C. Several bed-parallel dolomite and calcite cement fractures are found in this zone and upper horizons near this zone (arrows in Figure 2.10D). Sometimes the bed-parallel fractures are wide enough to resemble beds (middle arrow in Figure 2.10D). The cement is mainly calcite (Figure 10E) and dolomite (Figure 2.10F).

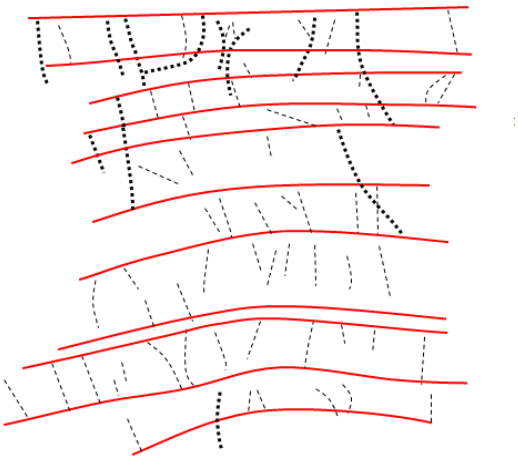

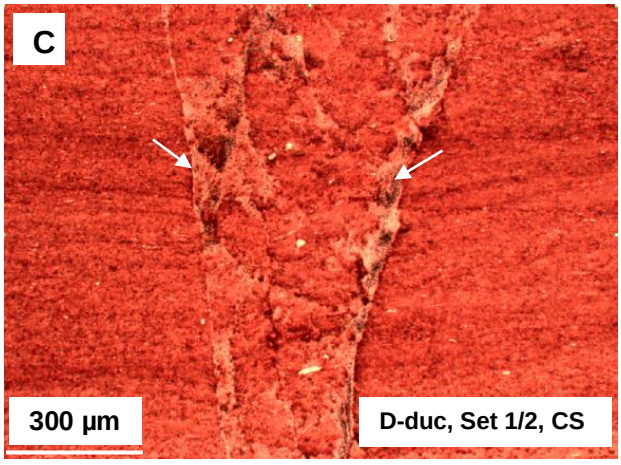

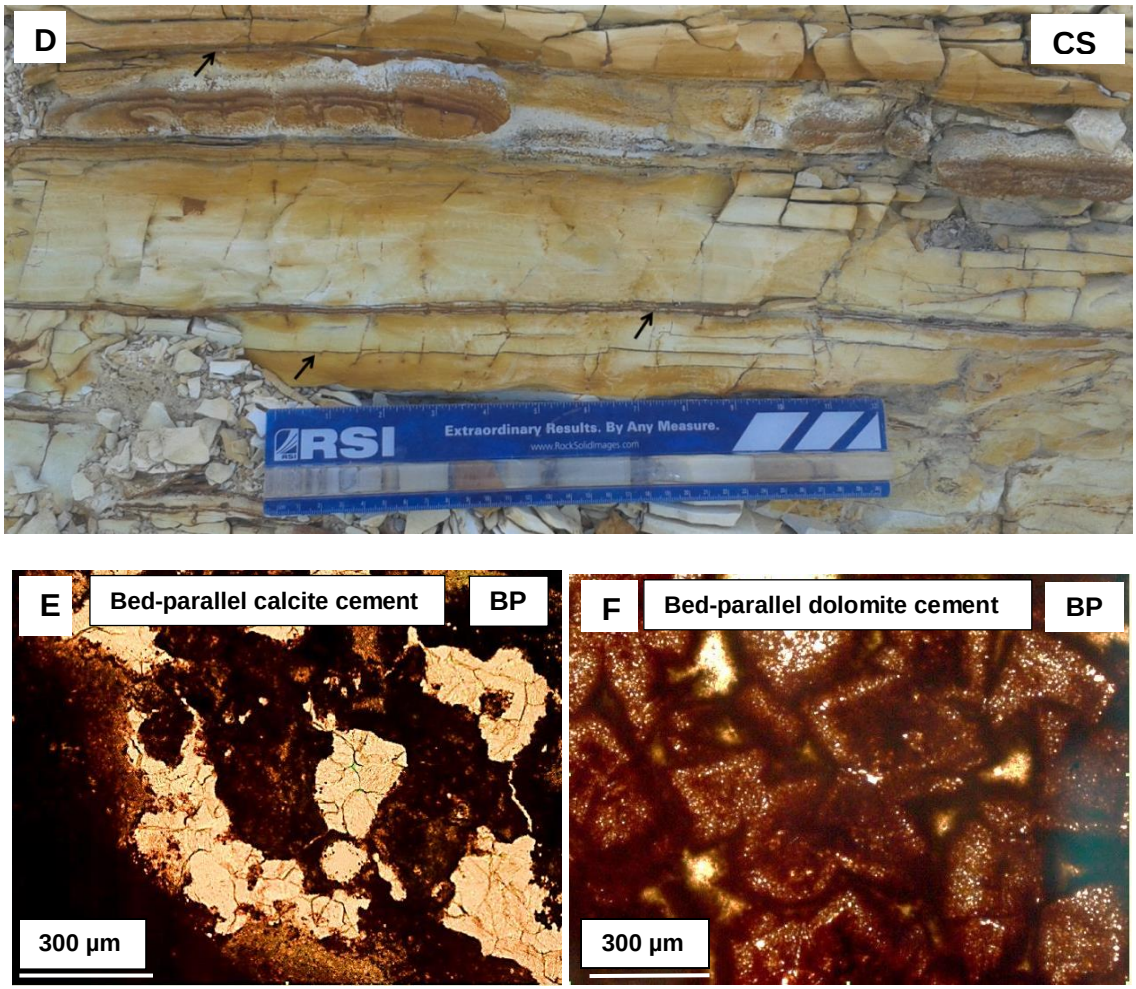

Figure 2.10: D-duc outcrop and thin-section expressions. **A)** Outcrop photograph of the argillaceous mudstone (D-duc) and bed-parallel cement. Beds appear yellowish when weathered and white to light gray in a fresh sample. **B)** Bed and fracture traces (Scale same as in A). **C)** Thin-section (PPL) expression of the clay-rich beds (D-duc). Interpreted shear zone is indicated by white arrows. **D)** Same argillaceous beds at another laterally offset spot containing bed-parallel carbonate cement. Bed-parallel fractures are marked in black arrows and look brownish black in the outcrop. Notice bed-parallel cement terminating at bed-perpendicular cement (lower arrow). **E)** White blobs in the thin section (PPL) are well-developed calcite crystals in bed-parallel fractures in D. **F)** Thin section (PPL) shows well-developed dolomite rhombs in bed-parallel fractures in D.

Highly fractured laminated carbonaceous, siliceous mudstones (Figure 2.11A) were seen in the MW (E-bri); fracture and bed traces are shown in Figure 2.11B. XRD analysis reveals that these beds are quartz-rich (~ 97% quartz) and the morphology and

mineralogy are similar to those in B-bri (Figure 2.8). Unlike B-bri, however, these beds are also very organic-rich, which is rather unusual for highly quartz-rich beds. Alternately, the collected sample could have been had locally high silica concentration. High angle small normal faults are shown in Figure 2.11C. Bitumen-filled fractures are common (Figure 2.11D).

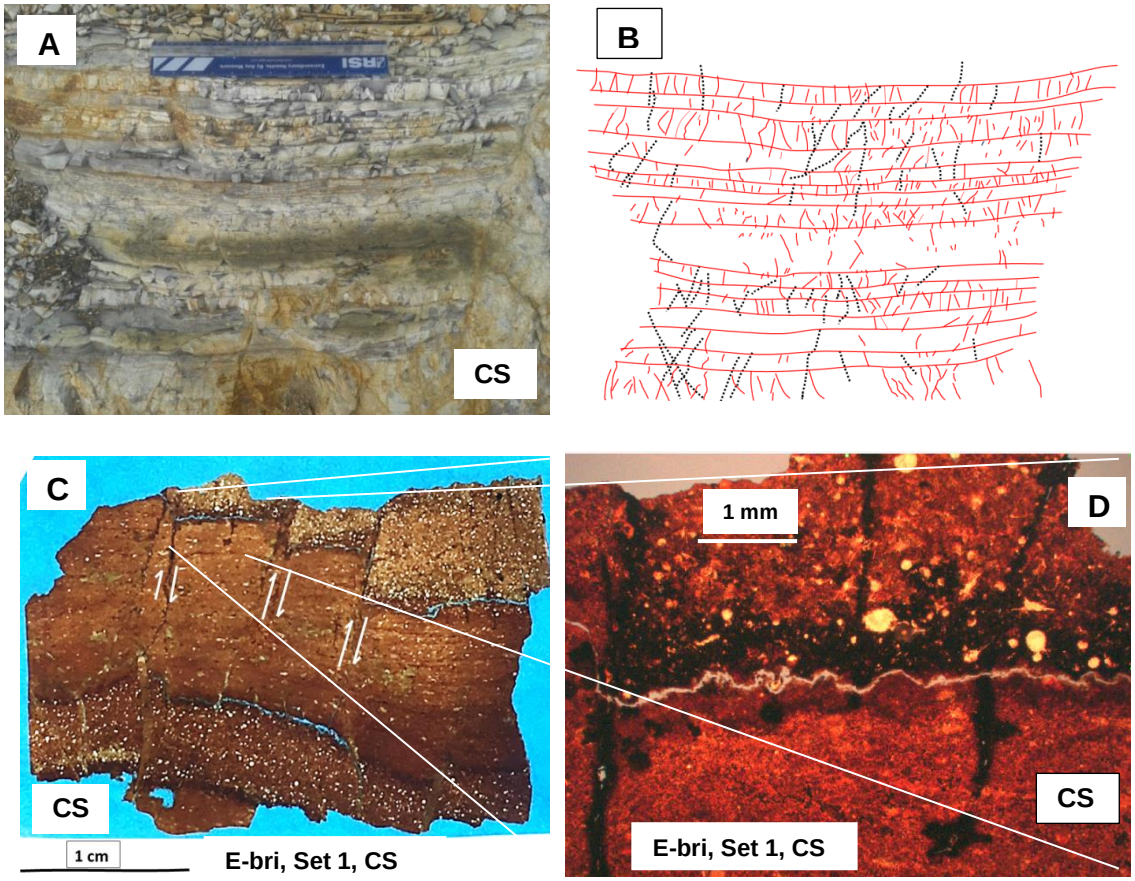

Figure 2.11: E-bri outcrop and thin-section expressions. **A)** Outcrop photograph of laminated carbonaceous, siliceous beds in the MW (E-bri). **B)** Bed and fracture traces (scale same as in A). **C)** Whole thin-section photograph of E-bri. Differential compaction microfaults are bitumen-filled and have porous gouge lining. Top and bottom beds of the thin sections are richer in radiolarians compared to the middle part. **D)** Thin section (PPL) shows orange phosphate-filled radiolarians and silica-rich matrix with organic matter. A bed-parallel plane of weakness is present at the boundary between the radiolarian-rich (top) and clay-rich (bottom) bed.

Figure 2.12A shows an example of laminated carbonaceous, argillaceous mudstone beds composed of ~ 66% quartz, ~ 27% clay, ~ 7% sulfates and phosphate (G-duc) found in the MW; bed and fracture traces are shown in Figure 2.12B. Thin-section bed texture in a cross-section view is not available because the section could not be obtained in cross section due to bedding plane fissility. The outcrop bed texture is continuous, planar, and parallel-laminated. At around the aforementioned percentage of brittle and ductile components, and the presence of considerable organic matter, the parallel laminations become more prominent in the outcrop and many laminations act as one thick bed (based on fracture termination) (Figures 2.12A and 2.12B). In this case, the bed boundaries were defined based on fracture terminations at a certain height. If several fractures terminated at a particular height, that height is defined as a mechanically significant bed-boundary within the same lithologic unit.

This facies has the highest mechanical bed thickness of all facies seen in the quarry. All Set 1 (few exist at this spot) and Set 2 fractures are overwhelmingly bitumen-filled, one of which is shown in Figure 2.12C.

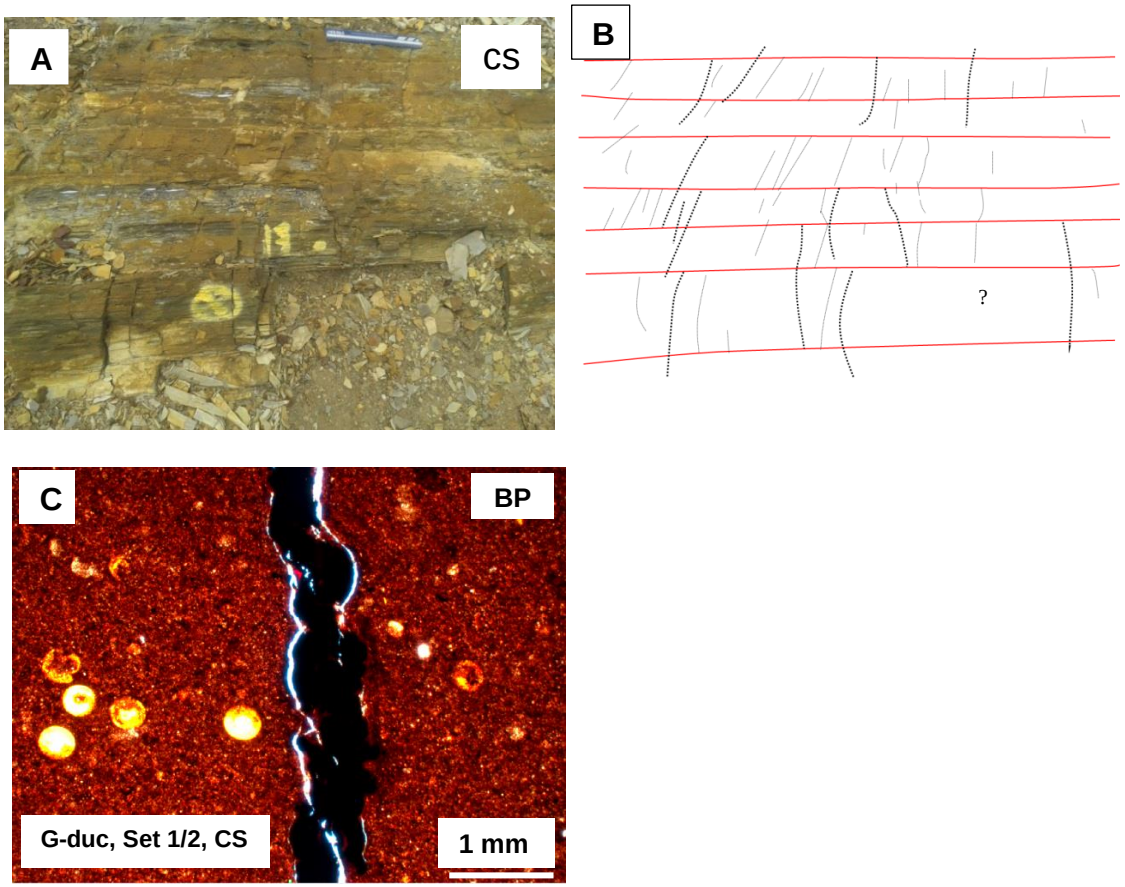

Figure 2.12: G-duc outcrop and thin-section expressions. **A)** Outcrop photograph of carbonaceous, argillaceous mudstone bed (G-duc) with several laminae acting as thick beds. **B)** Bed boundaries are depicted based on fracture terminations (scale same as in A). **C)** A bed top thin-section photograph (PPL) of radiolarians being replaced by phosphates (yellow). A wide bitumen-filled, fracture is visible. The white regions on fracture periphery are the glass slide.

Around 15-20 dolomite-containing beds were observed in the MW and LW. One of them (F-bri: Massive dolomitic mudstone) is shown in Figure 2.13A (with arrow) where most of the other beds are of G-duc type shown in Figure 2.12A. Fracture and bed outline especially show the Set 4 fractures G-duc type in addition to the single massive dolomitic mudstone bed (Figure 2.13B). The other bed (H-duc: dolomitic-argillaceous mudstone) is not shown. These two beds show variability in the amounts of dolomite (15-70%), quartz (25-50%) and clay (0-33%). Two episodes of fracture fill/growth are visible in Figure 2.13C. Elongate chalcedony with elongation

perpendicular to the fracture wall, followed by blocky, well-developed calcite crystals (center) are visible.

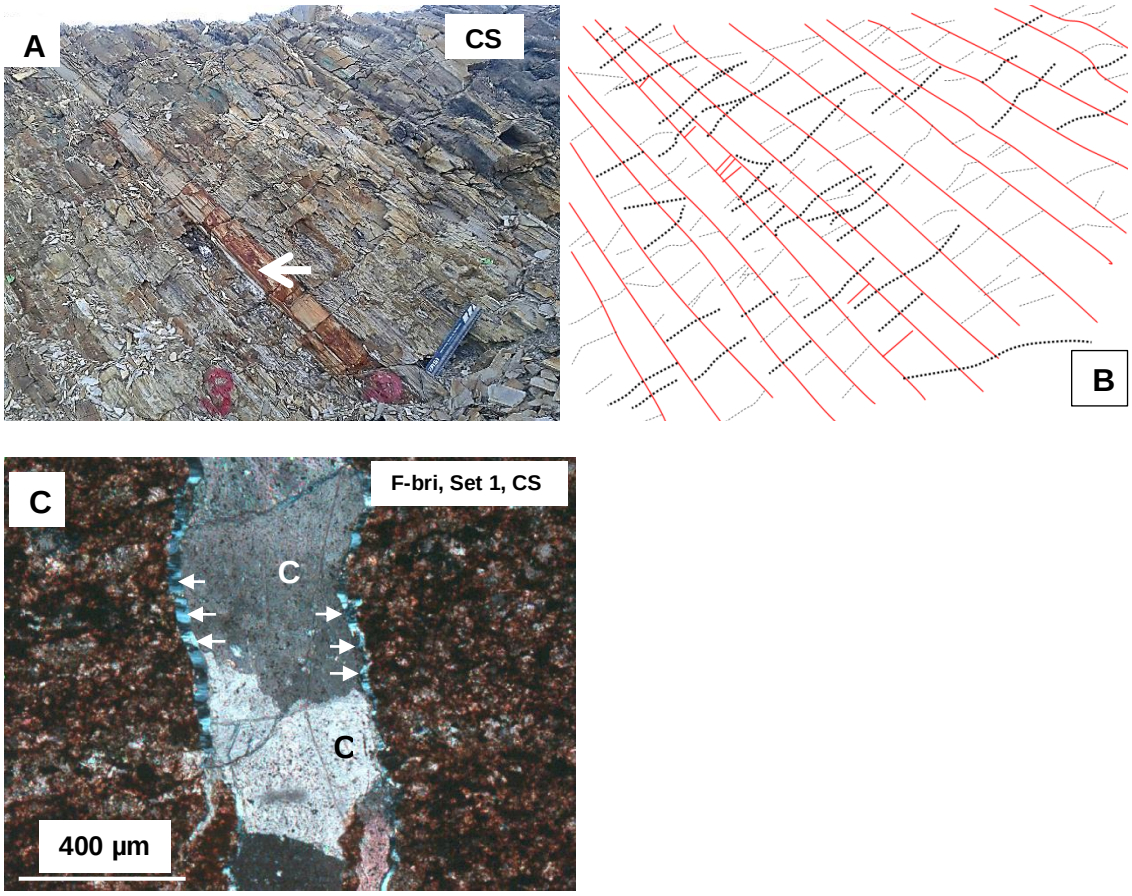

Figure 2.13: Outcrop and thin-section expressions of a dolomitic mudstone. **A)** Outcrop photograph of a dolomitic mudstone (arrow). Rest of the beds are laminated carbonaceous, argillaceous mudstones. Set 4 and some Set 3 fracture traces are seen. **B)** Bed and fracture traces (scale same as in A). **C)** Thin-section (CPL) photograph (F-bri) showing the microdolomite crystals in the matrix; chalcedony (arrows at fracture edge pointing at the black and white stripes) and calcite (C) at the center indicates two stages of fracture fill.

In the LW, beds with three different mineralogies were identified. All except one have been observed in the UW and MW. Overall, the LW has few scattered brittle (I-bri) siliceous mudstone beds of 1-3 cm thickness (arrows in Figure 2.14A). Beds and fracture outlines are shown in Figure 2.14B. I-bri siliceous mudstones are similar in

mineralogy and organics as in B-bri (Figure 2.4). I-duc argillaceous mudstones (organic-poor in this case but can have variable amounts of organic matter) are beds not marked in arrows in Figure 2.14A. These beds are abundant in the lower part of the MW and upper 70% of the LW, and are similar in mineralogy to C-duc (Figure 2.4).

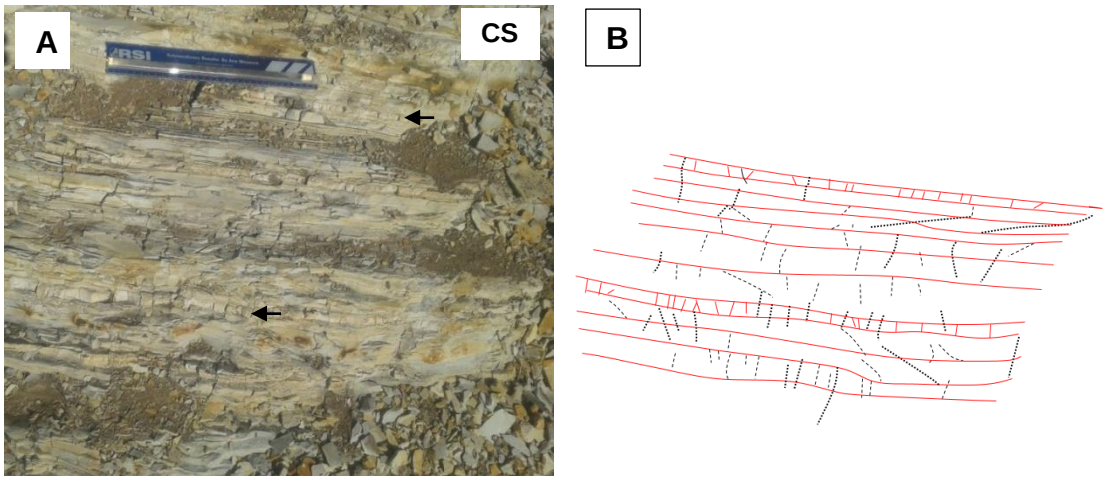

Figure 2.14: Outcrop expressions of I-bri and I-duc. **A)** Laminated siliceous mudstone I-bri (arrows). However, these beds are few and far apart. I-duc: laminated argillaceous mudstone (remaining beds with no arrows). These are more commonly observed compared to the I-bri type beds (scale same as A). **B)** Bed and fracture traces (scale same as in A).

Figure 2.15A shows a loose chunk of rock (hereby referred to as "loose rock") in the middle of the quarry which likely came from the lower part of the UW. It shows the morphology of a normal fault with about 25 cm throw. Most of the fractures are bed bounded, where the beds are indicated by change in bed color. Some of the bed bound fractures are wide (~ 1 mm) and still bed bounded (dotted white and dotted black arrows). The red beds in Figure 2.15A have ~ 46% quartz, ~ 49% carbonates and ~ 5% clay. Thin sections in Figures 2.15B (CPL) and 2.15C (PPL) show a wide bitumen-filled zone and a calcite-filled fractures within.

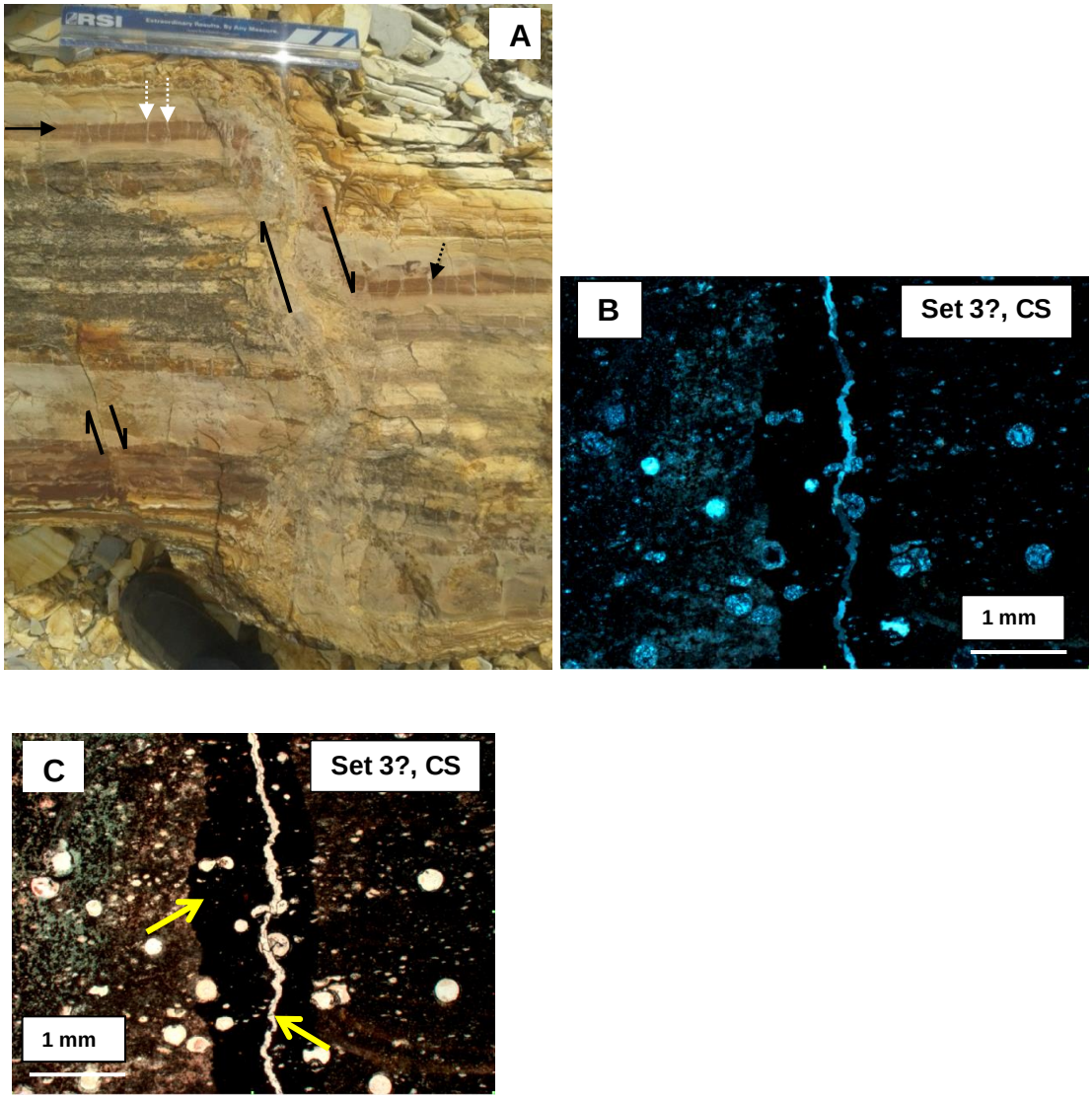

Figure 2.15: Outcrop and thin-section expressions of the loose rock. **A)** Normal faults within the loose chunk of rock. Notice that in the red layer marked by the solid arrow the fractures seem to derive their cement from the white layers above and below. **B)** This is probably a Set 3 fracture indicated by the presence of both bitumen and calcite cement. Thin section (CPL) showing bitumen (dark linear area in the middle) going through the matrix without disturbing the matrix (intact radiolarians) indicating either a permeable matrix or a weakness plane that allows the bitumen to go through. A fracture, with well-developed calcite crystal cement, is seen within the bitumen-filled zone. This fracture traverses a radiolarian. **C)** Thin section in plain-polarized light (PPL) of the same area in B. Black bitumen in better visible in this figure (upper arrow); lower arrow shows calcite-filled fracture.

Table 2.2 summarizes the above observations. It shows that except B-bri, where some microfractures terminate at layer boundaries, at most places the microfractures

terminate abruptly (without significant thinning at tips) or thin out away from any layer boundary. Mostly, only macrofractures are seen terminating at some type of layer boundary. Bed-perpendicular fractures terminating at a bed-parallel fracture is rare (in the thin sections) while the opposite is more common. Also, most microfractures are planar with only a few showing slightly sinusoidal shape. Fractures filled with only quartz are only seen in the UW (Table 2.2). In addition, in the UW, some Set 1 fractures contain a bitumen-quartz mix or bitumen-clay mix. None of the Set 4 fractures in the UW seen in the thin sections contain bitumen. Dolomitic beds in LW and MW also have calcite cement. The vertical fractures in the D-duc layer are also primarily quartz-filled. Almost all of the Set 1 and 2 MW fractures seen in the thin section and directly on the outcrop contain only dead bitumen. As observed from the outcrop directly, most of the LW fractures do not contain bitumen.

Table 2.2: Fracture termination, porosity, fill, and shape characteristics in the MCQ. Gamma ray values near the measured spots are also shown. Except for G-duc and bed-parallel cements, all thin sections show bed cross sections, therefore both bed ⊥ and bed ‖ fractures are visible. **Abbreviations**: "-": not applicable or not seen; **WL:** fractures terminate within a layer; **LB:** fractures terminate at layer boundary; **Cal.C-Sil.E:** calcite in center and silica or chalcedony at the fracture edges; **Cal.:** calcite; **Bit.:** bitumen; **Sil**.: silica. Percent occurrence of each characteristic is also shown if possible. Otherwise, terminologies such as rare, few, some, and most are used. **Rare:** at least 1-2 cases were seen but very difficult to find; **Few:** more than a couple cases visible but not common; **Some:** fairly common but not a majority; **Most:** > 60% cases. In the thin-section observations, **narrow** means narrower sizes of microfractures and **wide** means wider microfractures and narrow macrofractures. **LBNC:** layer boundaries not clear (mostly massive to gradational in thin sections); **TSNA:** thin section not available.

Beds	Fracture type	Fracture termination			Fracture fill					Fracture shape		
		At bed ⊥ frac.	WL	LB	Bit. only	Sil. only	Sil-bit mix?	Cal.C-Sil.E	Cal. only	Sinusoidal	Planar	GR
A-duc Set 1	**Bed** ⊥ (only oblique fracs, prob. Burrows)	-	All	- (LBNC)	-	-	All	-	-	-	All semi planar	301
	Bed ‖	-	-	-	-		All		-	none	All	-
A-bri Set 1	**Bed** ⊥	-	All	- (LBNC)	Few	Most	Few	In voids/burrows	~20%	Rare semi-sinusoidal ones	All	274
	Bed ‖	-	-	-	-	-	-		-	-	-	-
A-bri Set 4	**Bed** ⊥	-	Not clear (many terminate outside thin section	- (LBNC)	-	Most	-	In voids/burrows	~10%	-	All	274
	Bed ‖ (only 1)	Yes	-	-	-	-	All	-	-	-	Yes	-
B-bri Set 1	**Bed** ⊥	-	Some	Some	**All** : in ogranic- rich zone. **Few**: silica-rich zone	**Most**: in silica-rich zone. **Not seen**: in organic- rich zone	-	-	-	-	All	318
	Bed ‖	-	-	-	-	-	-	-	-	-	-	-

Beds	Fracture type	Fracture termination			Fracture fill					Fracture shape		
		At bed ⊥ frac.	WL	LB	Bit. only	Sil. only	Sil-bit mix?	Cal.C-Sil.E	Cal. only	Sinusoidal	Planar	GR
C-duc, Set 1/2	**Bed ⊥**	-	All	- (LBNC)	All	-	-	-	-	-	All	560
	Bed ‖ streaks	Rare	All	-	All	-	-	-	-	-	All	-
D-duc, Set 1/2	**Bed ⊥**	-	Not clear	Rare (LBNC)	-	All	-	-	-	-	All	346
	Bed ‖	-	-	-	-	Only 1 visible fracture	-	-	-	-	Yes	-
G-duc, Set 1/2	**Bed ⊥** Only 1 fracture)	-	-	-	All	-	-	-	-	Semi-sinusoidal	-	990, 1479
G-duc, Set 4	**Bed ⊥**	-	-	-	-	-	-	-	-	-	-	-
E-bri, Set 1	**Bed ⊥**	-	Most	Rare	Most	-	Few	-	-	Rare semi-sinusoidal ones	All	617
	Bed ‖	-	-	-	-	-	-	-	-	-	-	-
Dolomitic beds, Set 1	**Bed ⊥**	-	-	-	-	-	-	-	-	-	-	566
	Bed ‖	-	-	-	-	-	-	-	-	-	-	-
Dolomitic beds, Set 4	**Bed ⊥**	-	All narrow ones	- (LBNC)	-		-	1 wide macrofracture	Most	-	All	-
	Bed ‖	-	-	-	-	-	-		-	-	-	-
I-duc	**Bed ⊥**	TSNA	-	-	-	-	-	-	-	-	-	404
J-duc	**Bed ‖**	TSNA	-	-	-	-	-	-	-	-	-	-
	Bed ⊥	TSNA	-	-	-	-	-	-	-	-	-	-
Loose rock, Set 3?	**Bed ‖**	-	-	-	-	-	-	-	-	-	-	353
	Bed ⊥	-	-	-	Two thick (1-2 mm wide) bitumen filled zones with calcite in center	-	-	-	-	Few semi Sinusoidal	Most	-

2.4.4 Lithology, bed-thickness, and fracture intensity

A decreasing trend of fracture intensity with bed thickness exists, along with scattering in the datapoints. Figure 2.16A shows the fracture intensity vs. bed thickness of all the measured beds. Part of the scatter is due to all lithologies being plotted on the same plot. Figure 2.16B, explains this spread in terms of the quartz and carbonate content of each facies. A plot of the average fracture intensity of each of the facies, i.e., A-duc, A-bri, and so on, from plot A against the corresponding fraction of quartz and carbonates (pseudo-BI) value of each facies is shown. Average bed thickness (cm) corresponding to the facies are shown against the names. The downward pointing arrow on the left shows decreasing fracture intensity with increasing bed thickness (bed thickness increases in the direction pointed by the arrow) for the two points on the left which have pseudo-BI in the range of 0.55-0.65. The center arrow shows the decreasing fracture intensity with increasing bed thickness for points in the BI value range of 0.75-0.83. For dolomitic beds, averaging of F-bri and H-bri minerals were performed and named "dolomitic ave. (averaged)" for the pseudo-BI value, and the average intensities are from the seven isolated dolomitic beds in the quarry, probably with variable compositions. That is probably why they do not fit into the bed thickness vs. pseudo-BI trend. The rightmost arrow shows this for facies with pseudo-BI close to one. Within the circled area, both the points (B-bri and E-bri) have 98-99% quartz, i.e., nearly equal pseudo-BI; they also have the same average bed thicknesses. However, there is a considerable difference in the average fracture intensities. B-bri beds, on average, have higher grain size and are poorer in TOC content compared to E-bri mudstones.

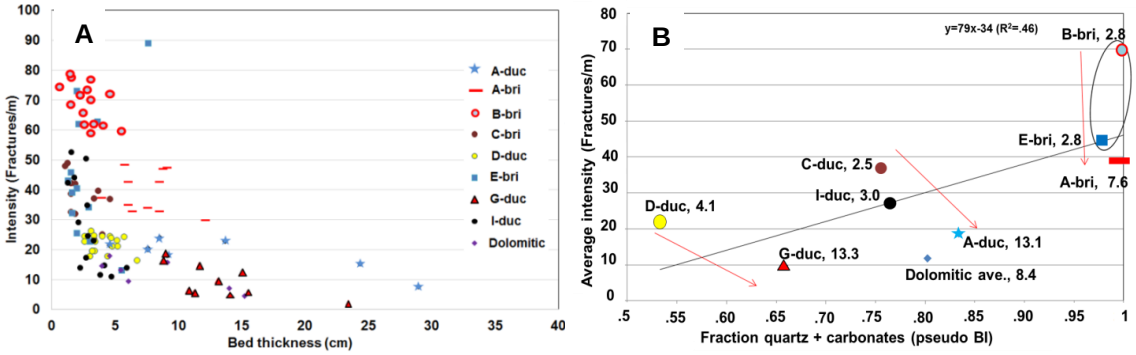

Figure 2.16: Effect of bed thickness and mineralogy on fracture intensity. **A)** Decreasing trend of fracture intensity vs. thickness of individual beds for Set 1 and Set 2 fractures. **B)** Set 1 and Set 2 average fracture intensity vs. BI plot. Arrows belong to groups with similar BI. Notice increasing overall average fracture intensity vs. pseudo-BI and decreasing average fracture intensity vs. average bed thickness (three arrows). Dolomitic beds have variability because variable degree of dolomitization exists in different beds.

2.4.5 Fracture aperture size and spacing

Most of the macrofracture cumulative frequencies show a non-power-law aperture-frequency distribution (Figures 2.17A and 2.17D) based on the goodness of fit (χ^2 error) calculations (Table 2.3). Even though the macrofractures in Figure 2.17C follow an overall power-law distribution, except the last 3 points all other points fall on a lognormal distribution line. In the absence of a substantial number of microfractures in most thin sections (Table 2.3), statistical analysis from only one microfracture set was available (Figure 2.17B), showing an exponential distribution. Hooker et al. (2013) discuss cumulative aperture-frequency distribution in detail.

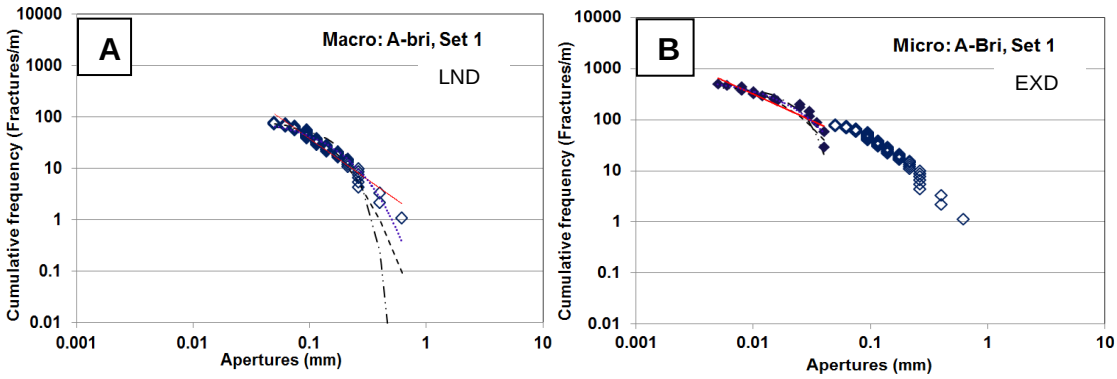

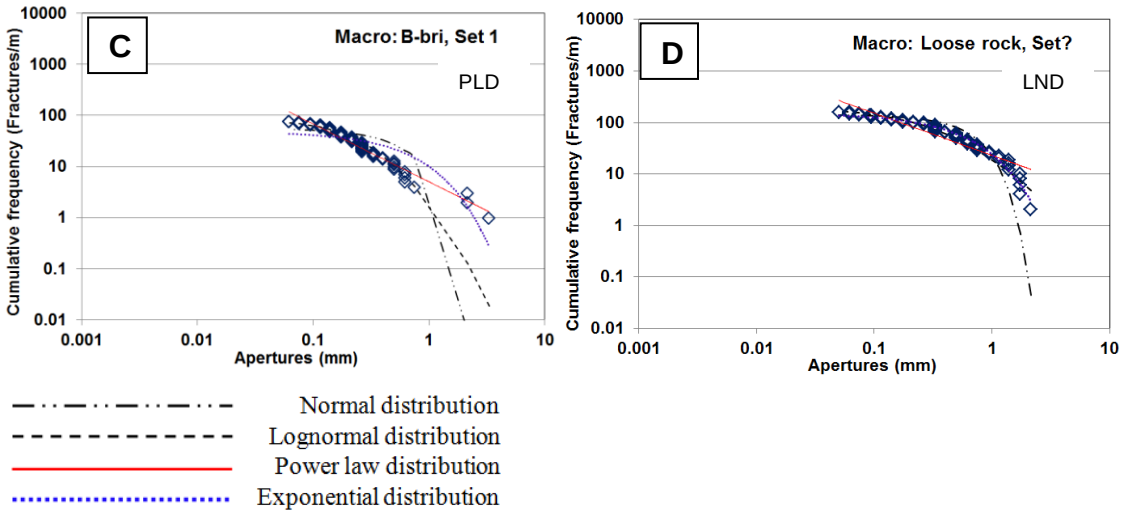

Figure 2.17: Cumulative-frequency plots of kinematic apertures. **A**, **C**, **D** are log-log plots of the cumulative-frequency distribution of macrofractures (> 0.05 mm; open diamond shapes) measured directly at the outcrop and fitted with different distributions. **B)** Microfracture cumulative-frequency distribution fit shown along with the points in A since thin sections were obtained from the same bed in A. Best fit cumulative distributions (**EXD**: exponential; **LND**: lognormal, **PLD**: power-law) are mentioned in the figures.

Table 2.3 shows that in the brittle beds, the spacing coefficient of variation (C_v) is higher for the microfractures compared to that in the macrofractures (> 0.05 mm aperture-size up to ~ 1 mm), i.e., more clustering was observed in microfractures. One exception, however, is C-duc Set 1 (Table 2.3), which shows higher clustering in macrofractures (C_v = 0.82) compared to microfractures (C_v = 0.68) and could be a local anomaly. However, if only macrofractures are considered, the C_v values for brittle and ductile bed macrofractures are indistinguishable as they are usually < 1 and do not show specific values in that range. Average fracture spacing is 2-6 times higher in the macrofractures (aperture > 0.05 mm) compared to the microfactures (aperture < 0.05). Bed-parallel fractures were mostly absent in thin section except near D-duc where wide bed-parallel (fraction of a millimeter to a few millimeters) fractures were observed.

Table 2.3: Natural fracture parameters obtained from the McAlister Cemetery Quarry. All values belong to direct observations in particular beds or thin sections obtained from these beds observed under an optical microscope. The number of fractures (**NF**) used to calculate the parameters for both macro and microfractures are given individually. Macrofracture apertures were not measured on all beds mentioned due to lack of suitable fractures for that purpose. However, for some beds, thin section showed macrofracture apertures, which could not be measured from the outcrops directly. Therefore, some **AA** (average fracture aperture, mm) slots have a thin-section fracture count in brackets showing the number of fractures used for only aperture measurements. **Abbreviations- FS**: fracture aperture-size classification, **ND:** normal distribution χ^2 error, **LND:** lognormal distribution χ^2 error, **PLD:** power-law distribution χ^2 error, **EXD:** exponential distribution χ^2 error (distribution showing the lowest χ^2 error is in bold), **PLD exp**: Exponent of the power-law distribution. **EXD exp**: exponent of the exponential distribution. **NF**: number of fractures used for aperture, intensity, and spacing measurements. **C_v**: coefficient of variation, **AS**: average fracture spacing (cm), **GR:** gamma ray (cps), **BT**: bed thickness of the specific bed on which the macrofracture linear intensities were measured (cm). **Dashes (-)**: not applicable or not available.

Bed-perpendicular fractures													Bed-parallel fractures			
Bed	**FS**	**ND**	**LND**	**PLD**	**EXD**	**PLD exp**	**EXD exp**	**NF**	**AA**	**C_v**	**AS**	**BT**	**NF**	**AA**	**C_v**	**AS**
A-duc, Set 1	**Mac.**	-	-	-	-	-	-	-	-	-	-	-	-	-	-	-
	Mic.	-	-	-	-	-	-	1	0.01	-	-	-	3	0.02	-	0.06
A-bri, Set 1	**Mac.**	$6*10^4$	**59**	125	63	-1.6	-9.2	71	0.137	0.83	1.09	10	-	-	-	-
	Mic.	211	184	388	**77**	-1	-62	17	0.019	1.2	0.19	-	-	-	-	-
A-bri, Set 4	**Mac.**	-	-	-	-	-	-	23	-	0.43	2.1	3.5	-	-	-	-
B-bri, Set 1	**Mac.**	$3*10^7$	169	**118**	487	-1.13	-1.58	78	0.32	0.58	1.34	3	-	-	-	-
	Mic.	-	-	-	-	-	-	5	0.028	-	-	-	-	-	-	-
C-duc, Set 1	**Mac.**	-	-	-	-	-	-	35	-	0.82	2.49	3.5	3	0.11	-	-
	Mic.	-	-	-	-	-	-	8	0.025	0.68	0.4	-	-	-	-	-

Bed-perpendicular fractures													Bed-parallel fractures			
Bed	**FS**	**ND**	**LND**	**PLD**	**EXD**	**PLD exp**	**EXD exp**	**NF**	**AA**	**C_v**	**AS**	**BT**	**NF**	**AA**	**C_v**	**AS**
D-duc, Set 1	**Mac.**	-	-	-	-	-	-	29	0.11	0.52	2.94	2	12	0.35	0.55	5.1
	Mic.	-	-	-	-	-	-	-	-	-	-	-	-	-	-	-
G-duc, Set 1	**Mac.**	-	-	-	-	-	-	50	0.16 (3)	0.77	6.4	18	-	-	-	-
	Mic.	-	-	-	-	-	-	2	0.035	-	-	-	-	-	-	-
E-bri, Set 1	**Mic.**	-	-	-	-	-	-	9	0.027	0.78	0.3	-	-	-	-	-
Dolomitic, Set 1	**Mac.**	-	-	-	-	-	-	9	-	0.48	11.7	9.5	-	-	-	-
Dolomitic, Set 4	**Mac.**	-	-	-	-	-	-	14	0.2 (2)	0.62	12.4	12.5	-	-	-	-
	Mic.	-	-	-	-	-	-	2	0.024	-	0.1	-	2	0.04	-	-
I-duc	**Mac.**	-	-	-	-	-	-	7	NA	0.79	20	3.5	-	-	-	-
	Mic.	-	-	-	-	-	-	-	-	-	-	-	-	-	-	-
J-duc	**Mac.**	-	-	-	-	-	-	-	-	-	-	-	-	-	-	-
	Mic.	-	-	-	-	-	-	-	-	-	-	-	-	-	-	-
Loose rock	**Mac.**	817	**79**	826	138	-0.82	-1.82	87	0.45	0.6	0.74	2.8	-	-	-	-
	Mic.	-	-	-	-	-	-	4	0.04	-	-	-	-	-	-	-

2.5 Discussion

2.5.1 Fracture origin timing

2.5.1.1 Set 1, Set 2, and Set 3S fractures

In the MCQ, all Set 1, Set 2, Set 3S fractures in the MW mound contain bitumen. On the other hand, barely any of the Set 3P fractures and none of the Set 4 fractures in the MW include bitumen. The absence of bitumen indicates that by the time of generation of Set 3P and 4 fractures, Set 1, Set 2, and Set 3S fractures already existed and the bitumen generation phase was essentially over. According to Paxton and Cardott (2008), a vitrinite reflectance value of 0.54% was obtained based on 41 measurements from the MCQ, which indicates marginal or early thermal maturity. Also, Cardott (2014) showed a similar bitumen signature in the organic content of the matrix and the fractures in the MW mound indicating bitumen in the fractures is locally derived even though oil generation was low. Higley (2014) showed that the early maturity of around 0.54% in the nearby Anadarko Basin reached when the Woodford Shale was buried under 4000 ft of sediments. This observation is in agreement with Lang III's (1957) observations, where he mentions that around 5000 ft of sediments were deposited above the Woodford Shale before the Chesterian/Morrowan Orogeny happened in the Criner Hills. This orogeny brought the Woodford Shale above the oil window in the study area due to the erosion of the overlying sediments. After that, the Woodford Shale was likely not buried more than 3500-4500 ft in the study area before the occurrence of the Arbuckle Orogeny, which uplifted it to near-surface elevation. Therefore, the dead bitumen in the MW mound in the three fracture sets likely existed in these fractures before or during the early stage of the Chesterian/Morrowan Orogeny

(timing coincides with that of the Ouachita Orogeny). This also implies the existence of the Set 1, Set 2, and Set 3S fractures during this time. It is likely that this orogeny altered the preexisting maximum horizontal stress direction in the study area, and possibly, away from the area, i.e., the regional stress orientation was altered from approximately E-W to approximately NE-SW.

The presence of plumose structures on several Set 1 fracture (striking E-W) faces indicates their tensile origin. The maximum bed-parallel stress (SHmax) direction during this time, i.e., before the Chesterian/Morrowan Orogeny was probably ENE-WSW to E-W as seen in today's map view (Figure 2.18A). Tan et al. (2014) and Pireh et al. (2015) mentioned the possibility of natural fracture formation under substantial overpressure without considerable structural bending. Berryman (2013), using fluid inclusion analysis and without naming a fracture set, mentioned that the earliest fracturing within the Woodford Shale occurred between 345-362 mya. This period ranges from the end of the Woodford Shale deposition to the Middle Mississippian Period, i.e., before the Chesterian/Morrowan Orogeny. Three hundred and forty five Mya is nearly 20 million years before the Chesterian/Morrowan Orogeny. This observation implies Set 1 origin before the Chesterian/Morrowan Orogeny if the early fractures discussed by Berryman (2013) happen to be Set 1 Fractures.

Therefore, it is suggested here that the Set 1 fractures in organic-rich beds originated due to overpressure generated due to the bitumen cracking under nearly 5000 ft of overlying sediments before the Chesterian/Morrowan Orogeny. In organic-poor beds (e.g., UW chert beds), the cause of overpressure could have been some other type of fluid, as well as some early oil migration into the fracture in organic-poor beds. Post

kinematic (syntaxial) quartz crystal fill (Figures 2.7D and 2.7E), and bitumen-fill in some fractures in Figure 2.7D, and blocky to elongate blocky, burrow-filling, quartz crystal (syntaxial) cement (Figures 2.7F and 2.7H) in the UW supports this assumption. Micro-normal faults parallel to the Set 1 fractures (Figure 2.11C) may be local, i.e., related to early soft sediment deformation or could have originated under the influence of a similar regional stress regime that caused the fractures in Figure 2.7D.

At the beginning of the Chesterian/Morrowan Orogeny, high horizontal compressive stresses would have started to develop in the NNE-SSW to NE-SW direction, i.e., in a direction parallel to Set 2 fractures/joints and perpendicular to the average orientation of the Set 3S fractures. Cooper (1995, p. 144) documented tectonic shortening in the area from southwest to northeast from the late Mississippian to early Atokan. The high stresses, accompanied by a rise in pore pressure, likely caused generation of the Set 2 fractures (Figure 2.18B). The high horizontal stresses also explain the selective presence of the Set 2 joints in the more ductile (clay-rich) beds. The high horizontal stress (strain) due to horizontal compression (although lower that leading to reverse faulting stress regime), is mainly supported by the high stiffness (defined as "brittle" beds in the current study) layers (e.g., Gudmundsson and Brenner, 2001; Herwanger et al., 2015). This resulted in higher Shmin values in the brittle beds compared to the ductile beds. Therefore, tensile fractures during this period developed in the ductile (low stiffness) beds, which had lower Shmin compared to the brittle beds.

However, if shear origin of Set 2 fractures is to be assumed, there can be alternative interpretations for Set 1 and Set 2 fracture generation. In one interpretation, a crosscutting relation between Sets 1 and 2 could suggest an overlapping or simultaneous

timing of Set 1 and 2 origins before or during the early stage of the Chesterian/Morrowan Orogeny. In this case, Set 2 fractures are shear joints, with a fraction of mm displacement, leading to a near joint-like appearance. In other words, thin, clay-rich (ductile) beds responded differently to the same stress (ENE-WSW to E-W maximum horizontal stress) that led to Set 1 origin. However, this interpretation is less likely to be correct, given the high (40-45 degree) average strike difference between Sets 1 and 2 fractures. To satisfy a 40 and 45 degree difference between these sets (i.e., assuming a tensile and a shear origin for Set 1 and 2 respectively) using Mohr-Coulomb failure criterion, the friction angle should be 10 and 0 degrees respectively, which is not true for any rock type.

On the other hand, let us consider the possibility that both Set 1 and Set 2 fractures originated as shear joints, with SHmax = S1 (Sv = S2, Shmin = S3, i.e., strike-slip regime) that bisects the Set 1 and 2 fracture orientations. In this case, the 40-45 degree difference is low. To obtain a 40 and 45 degree difference between two shear joints the friction angle (during fracture formation) should be 50 and 45 degrees respectively, which is unlikely in shales. In addition, there is clear evidence of hackles on Set 1 faces (indicating tensile origin). These observations suggest that shear origin of both Set 1 and 2 fractures is not likely. Therefore, separate origin of the E-W (Set 1) and NE-SW (Set 2) sets is most probable.

Set 3S fractures are sinuous and non-systematic. Their shapes are very similar to that of stylolites. These bitumen-filled Set 3S fractures, possibly stylolites, terminating (mostly) at Set 2, and crosscutting (sometimes) the cement in Set 2 fractures is observed. After the development of Set 2 fractures, and with more compression, Set 3S

stylolites (intermediate stage of the Chesterian/Morrowan Orogeny) (Figure 2.18B) developed. Possibly, part of the remaining organic matter (after bitumen filling of Sets 1 and 2) in the clay-rich thin beds was deposited in the stylolite seams during their generation. Additionally, because of higher pressure in stylolites than the rest of the rock (Bons et al., 2012), some bitumen from the stylolite could have been injected into the Set 2 fractures. There is a possibility that Set 3S stylolites are connected to the brittle layers over- and underlying the ductile layers (rich in clays) even though it is not clear from outcrop observations. In other words, there is a possibility that some Set 3S could have originated in the brittle layers during due to bed-parallel compression and then cut into to the thin clay-rich layers. Some of the Set 2 fractures are also sinuous but not as much as Set 3S fractures (Figure 2.5B and 2.5C). It is likely that under the same stress regime (NNE-SSW to NE-SW max bed-parallel stress) seen in Figure 2.18B, some of the Set 2 fractures (along with the rock matrix) would have buckled, making them look slightly sinusoidal.

There may be another, less likely, reason for the sinuosity of the Set 3S fractures. It is possible that they originated as extensional or hybrid cracks due to dextral microshear along the Set 2 fractures because of SHmax direction being slightly oblique to Set 2. The Set 3S fractures could have later compacted (in a direction sub-parallel to Set 3S strikes and sub-perpendicular to Set 2), along with the rock matrix, giving them (Set 3S) the sinuous shape, along with minor sinuosity of Set 2 fractures. The generation of extensional and hybrid cracks was shown by Kim et al. (2004) in fault damage zones, and Ishii (2016) in core experiments. However, it is important to note that there is no clear evidence of slickenlines on Set 2 fracture faces. Therefore, it

is less likely that Set 3S originated as extensional cracks, i.e., they probably originated as stylolites. The end of Set 3S generation phase was probably also the end of the bitumen maturation phase, as the beds would have moved above the oil window.

Regardless of the shear or tensile origins of Set 1, Set 2, and Set 3S fractures, at least two stress regimes are needed to explain all three bitumen-filled sets in the MCQ. In other words, a single stress regime cannot account for the presence of all three sets, i.e., Set1, Set 2, and Set 3S. Also, these are the only fractures that have any significant presence in flat-lying beds (Clarita and Wyche Shale Pits mentioned in Chapter 1) and are the earliest fractures in the respective lithologies (brittle and ductile) in the overturned beds of US-77D and AWO. Fractures from these outcrops are discussed in detail in Chapter 3 (see stereonets [Figures 3.6D and 3.6H] for fracture orientations after bed restoration from US-77D and AWO]. In addition, Waters et al. (2009), and Portas (2010) have reported the E-W and NE-SW fractures as the major fractures using image logs (in unfolded subhorizontal beds) of the Woodford Shale in areas 60 miles (~ 100 km) and 45 miles (~ 75 km) NE of the MCQ respectively. Portas' (2010) well location is adjacent to the Wyche Shale Pit.

There are reports of the fractures in the over and underlying formations (of the Woodford Shale) in the available literature. Johnson (2009) reported E-W fractures in the underlying Hunton Group Limestone using core obtained from nearly 100 miles (~ 160 km) north of the MCQ. Staples (2011), studied image logs from eight horizontal wells in the underlying Hunton Group Limestone in an area located 60 miles (~ 100 km) northeast of the MCQ. He reported additional N-S and NW-SE sets in addition to the E-W, and NE-SW sets in relatively flat beds of the Hunton Group Limestone with no

significant folding. These additional sets could be pre-Woodford Shale deposition because they are absent in the Woodford Shale flat (unfolded) beds. Stearns III (2015), using image logs on relatively flat beds (no significant folding) reported only two major sets, i.e., the E-W and NE-SW sets on the overlying Sycamore Limestone (Mississippian Lime) in an area located 150 miles (~ 250 km) north of the study area. The Sycamore Limestone (Mississippian Lime) was deposited before the Cehsterian/Morrowan Orogeny. Therefore, the presence of additional sets in the underlying Hunton Group and only the E-W and NE-SW sets in the overlying Sycamore limestone, along with observations regarding the bitumen fill (MCQ), indicates that the E-W and NE-SW set originated most likely before or during the early stage of the Mississippian Ouachita Orogeny (or Chesterian/Morrowan Orogeny). In other words, these fractures originated before the Mid-Virgilian Arbuckle Orogeny.

The Set 1 and Set 2 fracture sets have a high influence of overpressure compared to structural bending. Consequently, their (either one or both) presence is expected in the flat and unfolded subsurface strata in all formations that were deposited during the Mississippian Period and earlier, wherever the local pore pressure was high enough to generate these two sets. The Hunton Group (located directly below the Woodford Shale) and the formations below may have additional sets in non-folded areas related to the pre-Woodford stress regimes. Waters et al. (2009) mentioned an approximately E-W present SHmax from wellbore breakouts nearly 75 miles (100 km) from the MCQ. Dart (1990), based on wellbore breakouts and drilling-induced hydraulic fractures, mentioned that the present SHmax direction in the eastern Anadarko Basin, located north of the MCQ, is N78^{o}E. On the other hand, the same for the Marietta Basin,

located just south of the MCQ, is N41^{o}E (NE-SW). Therefore, it is a matter of coincidence that today's stress field is locally parallel to one of the major subsurface fracture sets, i.e., the E-W and the NE-SW sets.

2.5.1.2 Set 3P, Set 4, and bed-parallel fractures (MCQ)

In the MCQ, Set 3P fractures, which are sub-parallel to the Set 3S fractures, probably originated during the end of the Chesterian/Morrowan Orogeny or later, when the maximum local bed-parallel stress direction had a 90-degree rotation due to outer arc extension (i.e., oriented in the WNW-ESE direction) (Figure 2.18C compared to Figure 2.18B). The fact that these fractures (broken white arrows in Figure 2.5A) are sub-parallel to the Set 3S stylolites supports this hypothesis. The parallelism also suggests that some of the Set 3S and Set 3P fractures could have had overlapping timing. A relatively wide scatter in Set 3S strike directions also suggests that the stress field could have been changing during Set 3S generation, i.e., from that in Figure 2.18B to that in 2.18C, leading to greater stress homogeneity. However, the Set 3P fractures could have been reactivated during the much-later Arbuckle Orogeny. Figures 2.15B and 2.15C show a wide, bitumen-filled fracture (or plane of weakness) with blocky, semi-planar calcite-cemented fracture inside. In the previous discussion, bitumen filling was interpreted to be early (before or during the early stage of Chestrian/Morrowan Orogeny), which is probably the case here. Also, as seen in Figures 2.15B and 2.15C, the blocky calcite-fill is relatively younger and could have originated after the Chesterian/Morrowan Orogeny to during the Mid-Virgilian Arbuckle Orogeny. These observations indicated that relatively folded/deformed regions in the subsurface might have Set 3P fractures in variable amounts, in addition to, Set 1 and 2 fractures.

Finally, Set 4 fractures are sub-parallel to the fold trend in the MCQ. They crosscut or terminate at Set 1 fractures, and do not show clear evidence of bitumen content. These observations suggest their late origin. Therefore, these probably are type 2 extension fractures defined by Stearns (1968), i.e., related to outer fold extension and created under a local fold strike-parallel (bed-parallel) maximum stress (Figure 2.18D). Bed-parallel slip (Figure 2.9C) perpendicular to Set 1 direction also indicates that the local maximum bed-parallel stress direction was NW-SE during this time. In Set 4 fractures in the UW, which is organic poor, sometimes silica is the only cement. Sometimes, silica cement bridges, indicating synkinematic cement growth, followed by calcite cement (post-kinematic) in the pores is also seen (Figure 2.7G). In a Set 4 fracture of a dolomitic bed (in the MW), antitaxial elongate chalcedony growth (indicating synkinematic cement), followed by, post-kinematic, blocky calcite crystals growth (in open space) is seen (Figure 2.13C). The calcite crystal cement is probably not derived from the same bed as this cement was also seen in non-dolomitic beds.

Finally, the presence of well-developed carbonate cement crystals in the bed-parallel fractures (Figures 2.10E and 2.10F), likely occurring in a reverse faulting stress regime is present. This observation, along with secondary, well-developed/blocky pore-filling calcite in burrows and Set 4 bed-perpendicular fractures indicate late stage carbonate cement-fill.

The above observations indicate that majority of the older fractures have bitumen and quartz cement, and the majority of younger fractures have calcite, and sometimes dolomite, cement. Bons et al. (2012) mentioned that silica, which exists as H_4SiO_4 in solution, is more soluble in basic conditions, i.e., it is deposited in more

acidic conditions. Calcite, on the other hand, is soluble in acidic conditions, i.e., deposited in more basic conditions. Therefore, if just the non-bitumen cement, i.e., quartz and calcite are considered, their presence may be explained by the area becoming progressively basic, i.e., losing it acidic character, with uplift and exhumation due to escape of gasses such as CO_2. Another way that the observation can be explained is a decrease in solubility of calcite with the decrease in temperature and pressure. Peng et al. (2015) have shown an increase in calcite dissolution in a CO_2+H_2O system between 50-100 degrees Celsius. They also mention an increase in calcite dissolution with pressure. In this case, the carbonate cement probably came by advection from the underlying Hunton Group Carbonates due to a fluid pressure difference. In other words, at high temperature, fluid dissolved calcite and other materials from the underlying Hunton Group carbonates. As pressure decreased during uplift, these upward-traveling fluids deposited the dissolved materials in the Woodford Shale fractures. Table 2.4 summarizes the interpretation on the origins of fracture Sets 1, 2, 3S, 3P, and 4.

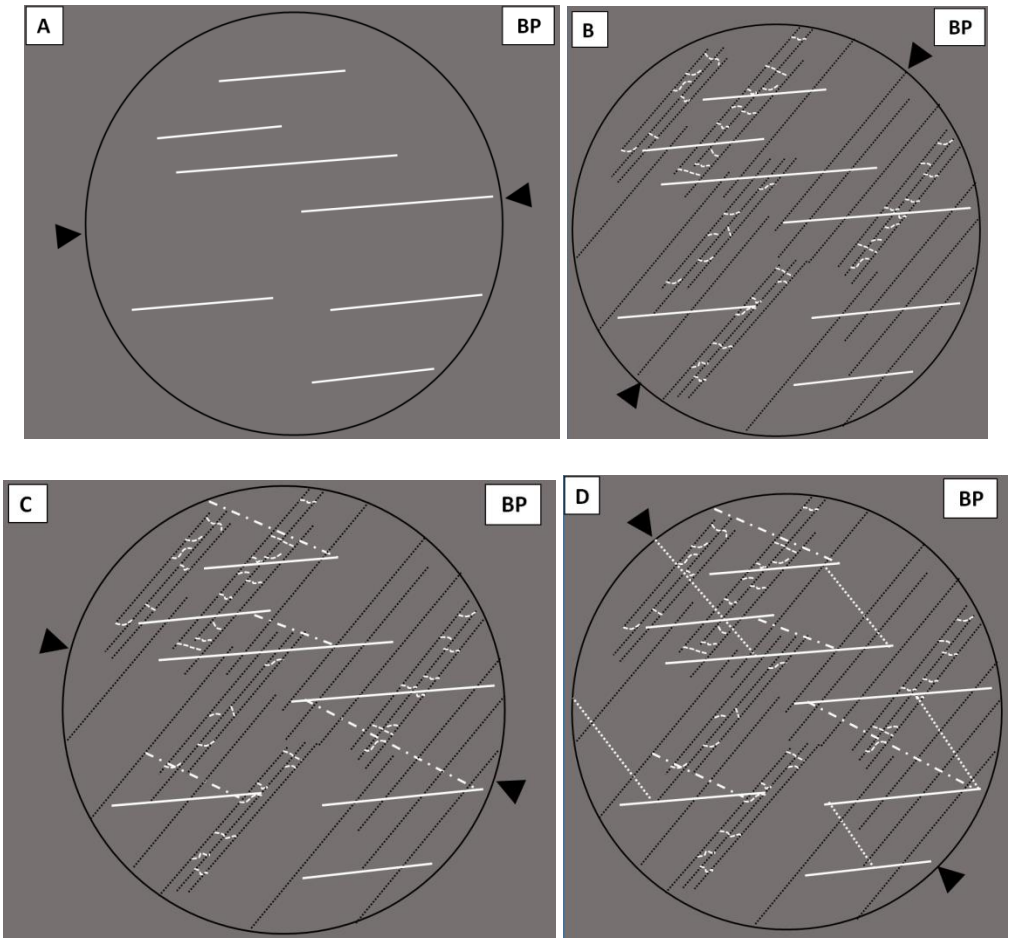

Figure 2.18: Bed restored versions of fractures and paleo maximum bed-parallel stress directions (circumferential arrows) showing the probable sequence of fracturing from outcrop observations for the original (non-alternative) interpretation. **A)** Development of Set 1 fractures with maximum bed-parallel stress (regional and local) direction of ENE-WSW to E-W. **B)** Development of Set 2 and 3S fractures with maximum bed-parallel stress (regional and local) direction of NE-SW to NNE-SSW, based on the average orientations of both Set 2 and 3S (interpreted as stylolites) fractures. **C)** Development of Set 3P fractures. Notice that the maximum bed-parallel stress direction is sub-perpendicular to one shown in B due to the outer arc extension, i.e., circumferential arrows indicated the direction of minimum stretching or direction of local fold related SHmax. **D)** Development of Set 4 fractures (NW-SE strikes), also due to the outer arc extension during Arbuckle Orogeny. Circumferential arrows indicated the direction of minimum stretching.

Table 2.4: Summary of the most likely scenario (separate timing of Set 1 and Set 2) of fracture origin sequence as observed from the thin sections and outcrops.

Seq	Stress orientation and timing	Fracture origin
1	**Regional**: S1 = Sv, S2 = SHmax: ENE-WSW to E-W (Figure 2.18A) (i.e., normal faulting stress regime) **Time**: Pre-Chesterian/Morrowan Orogeny	Set 1 generation due to bitumen cracking and filling in organic-rich areas (MW and LW), and to a lesser extent in organic-poor areas. Burrows and Set 1 fracture quartz filling in organic-poor areas (UW).
2	**a) Regional**: S1 = SHmax: NE-SW to NNE-SSW, S2 = Sv (Figure 2.18B) (i.e., strike slip faulting regime) **Time**: early stage of Chesterian/Morrowan Orogeny Or **b) Regional**: S1 = Sv, S2 = SHmax: NE-SW to NNE-SSW (Figure 2.18B), (i.e., normal faulting regime) **Time**: same as **a**	Set 2 generation with bitumen filling, followed by non-bitumen cement filling in organic-rich areas (MW) in Set 2; only quartz filling in organic-poor areas (UW and LW) in Sets 1 and 2.
3	**a) Regional**: S1 = SHmax: NE-SW to NNE-SSW (Figure 2.18B), S2 = Sv (i.e., strike slip faulting regime) **Time**: early to mid stage of Chesterian/Morrowan Orogeny Or **b) Regional**: S1 = SHmax: NE-SW to NNE-SSW (Figure	Set 3S generation and simultaneous squeezing of bitumen into Set 2 fractures. Stylolites (Set 3S) crosscut a few Set 2 cemented fractures. Some Set 2 buckle along with rock matrix.

	2.18B), S3 = Sv (i.e., reverse faulting regime) **Time**: same as **a**	
4	**Local fold:** S1 ~ SHmax (but not exactly equal to SHmax as beds are not horizontal) ~ bed-parallel maximum stress: WNW-ESE to NW-SE (Figure 2.18C); S2 ~ Sv (i.e., proably a near strike-slip regime due to high stresses related to orogeny but not reverse fault as Set 3P not bed-parallel) **Regional** SHmax: NE-SW **Time**: late stage of Chesterian/Morrowan Orogeny - Desmoinesian epeirogeny	Set 3P generation due to outer arc extension and possibly oil deposited in rare occasions. A few Set 4 fractures generated and filled with quartz/chalcedony.
5	**Local fold** S1 ~ SHmax (but not exactly to SHmax as beds are not horizontal) ~ bed-parallel maximum stress: NW-SE (Figure 2.18D); S2 ~ Sv (i.e., probably strike-slip regime due to high stresses related to orogeny but not reverse faulting as Set 4 not bed-parallel) **Regional** SHmax: NE-SW **Time**: early to late stage of Mid-Virgilian Arbuckle Orogeny	Generation of more Set 4 fractures. Carbonate cement deposition in unfilled burrows, Set 3P, Set 4 fractures.
6	**Regional**: S3 ~ Sv, S1 ~ SHmax: NE-SW (i.e., reverse faulting stress regime) **Time**: late stage of Mid-Virgilian Arbuckle Orogeny	Bed-parallel fracture generation; carbonate filling in bed-parallel fractures. Regional scale NW-SE trending reverse fault generation.

2.5.2 Bed composition, thickness, and intensity

Regardless of the fracture genesis timing, increase in the bed thickness shows a decrease in the fracture intensity in both brittle and ductile beds, consistent with the observations made by Ladeira and Price (1981). For the individual beds (Figure 2.16A), there is considerable scatter. However, when average intensity values are plotted against the pseudo-BI, the effects of bed thickness and bed composition are clearly seen (Figure 2.16B). Intensities decrease downward, i.e., the direction of increasing bed thickness for each pseudo-BI group. The Woodford Shale pseudo-BI values in the range of 0.55-1 are similar to log calculated BI values of 0.4-0.8 reported by Milad (2017) from a different area. Moreover, the fracture intensity correlates with the bed composition, i.e., on average, the fracture intensity shows a gradual increase as the amount of silica and dolomite increases, i.e., moving from the left to right in Figure 2.16B. In other words, as the facies classification changes from argillaceous to siliceous-argillaceous to siliceous according to the modified Lazar et al. (2015) methodology, fracture intensity shows an apparent increase. Therefore, a correlation between mechanical and fracture stratigraphy is present. However, even though this relationship exists, there is scatter in the intensity if individual beds are considered (Figure 2.16A).

A pitfall of the scanline method is that if the area exposed is not large enough, the scanline might be too short. Therefore, the obtained intensity may not be a true representation of the average fracture intensity in a particular bed or facies. The second pitfall is that the bed boundaries can sometimes be subjective, e.g., in Figures 2.12A and 3.9C, unlike Figures 2.8A, 3.8A, and 3.10A, where bed boundaries are clearer. Therefore, fracture intensity vs. bed thickness plots can appear slightly different depending on the interpreter's judgment of bed boundary locations. These factors

explain part of the scatter in the intensity-bed thickness plot.

Given the ultra-low permeability of shale matrix, fractures are the main fluid carriers upon stimulation. Therefore, due to lower fracture intensities in the low pseudo-BI beds, their effective permeabilities are expected to be lower compared to that in the high pseudo-BI (brittle) beds. However, the low pseudo-BI beds have progressively higher intensities of NE-SW fractures compared to that in high pseudo-BI beds. Therefore, in the Woodford Shale, progressively higher NE-SW effective permeabilities should be expected going from brittle to ductile zones. Alternately, progressively higher E-W effective permeabilities should be expected moving from ductile to brittle zones.

2.5.3 Fracture size, spacing, and termination

In addition, mostly characteristic aperture cumulative-frequency distribution is consistent with the observation that the majority of the macrofractures in the brittle beds are bed bounded (Gillespie et al., 2001; Hooker et al., 2013). Regardless of the type of fracture fill, most fractures show a characteristic distribution, showing that bed boundedness can control the aperture distribution. This was also observed by Hooker et al. (2013). Timing and causes of fracture origin are probably less important. Moreover, even fracture spacing exists, i.e., $C_v < 1$ was seen in most cases. $C_v > 1$ was seen in only one case of microfractures.

2.6 Conclusions

This study helped understand the relative timings of origin of different fracture sets. The relevant subsurface fracture sets (E-W and NE-SW sets) in the Woodford Shale likely developed before the Mid-Virgilian Arbuckle Orogeny. These fractures most likely originated at different times as Mode I joints. These fracture sets also

indicate the regional paleostress directions during their genesis as they have been reported at places several tens of miles away from the study areas. Information regarding the bitumen signature, thermal maturity, and burial depth indicate that these fractures originated before or during the Chesterian-Morrowan Orogeny. The fold related fractures that originated later, terminated against these fractures and lack bitumen fill in the McAlister Cemetery Quarry. In addition, a negative correlation between fracture intensity and bed thickness, and a positive relationship between fracture intensity and quartz/carbonate content were observed. Therefore, higher effective permeability is expected in the brittle beds compared to the ductile beds. However, given the fact that the NE-SW fractures are selectively located in the ductile (relatively rich in clays) beds, these beds likely have higher flow capacity in the NE-SW direction. On the other hand, since the E-W fractures are located in the brittle (relatively quartz and carbonate-rich) beds, these beds likely have higher flow capacity in the E-W directions. Also, largely uniform fracture spacing and characteristic aperture size distribution were observed.

Abbreviations

Pseudo-BI: brittleness index without TOC fraction; **BP**: looking at the top of the bedding plane (in thin section or outcrop); **Bri**: brittle; **CS**: looking at the cross section of the beds (in thin section or outcrop); $\mathbf{C_v}$: coefficient of variation; **Duc**- ductile; **GR**: gamma ray; **LW**: lower Woodford Shale; **MCQ**: McAlister Cemetery Quarry; **MW**: middle Woodford Shale; **PPL**: plain-polarized light; **CPL**: cross-polarized light; **TOC**: total organic carbon; **UW**: upper Woodford Shale; **XRD**: x-ray diffraction.

References

Becerra, D., 2017. Integrated geological characterization at the bed scale of the Woodford Shale at the I-35 Outcrop, Southern Oklahoma. M.S. thesis, University of Oklahoma, Norman.

Berryman, J.R., 2013. Timing and Paragenesis of the Calcite Fracture in the Woodford Shale. Shale Shaker, p. 40-54.

Bons, P.D., M.A. Elburg, E. Gomez-Rivas, 2012. A review of the formation of tectonic veins and their microstructures: Journal of Structural Geology, 43, p. 33–62.

Busetti, S., W. Jiao, and Z. Reches, 2014. Geomechanics of hydraulic fracturing microseismicity: Part 1. Shear, hybrid, and tensile events: AAPG Bulletin, 98(11), p. 2439–2457, doi: 10.1306/05141413123.

Cardott, B.J., 2014. Woodford Shale Play Update: Expanded Extent in the Oil Window. Woodford Shale Forum 2014. Oklahoma Geological Survey.

Cipolla, C.L., N.R. Warpinski, and M.J. Mayhoffer, 2008b. Hydraulic fracture complexity: Diagnosis, remediation, and exploitation: Asia Pacific Oil and Gas Conference and Exhibition, SPE 115771.

Cooper, J.C., 1995. Geologic Evolution of the Criner Hills Trend, Ardmore Basin, Oklahoma. In Johnson, K.S., 1992. Structural Styles in the Southern Midcontinent, 1992 Symposium. Oklahoma Geological Survey Circular 97.

Cosgrove, J.W., 2001. Hydraulic fracturing during the formation and deformation of a basin: a factor in the dewatering of low permeability sediments: AAPG Bulletin, 85, p. 737–748.

Dart, R.L., 1990. In Situ Stress Analysis of Wellbore Breakouts from Oklahoma and the Texas Panhandle. US Geological Survey Bulletin.

Einstein, H.H., and W.S. Dershowitz, 1990. Tensile and shear fracturing in predominantly compressive stress fields-a review. Engng. Geol., 29, p. 149-172.

Engelder, T., G.G. Lash, and R.S. Uzcátegui, 2009. Joint sets that enhance production from Middle and Upper Devonian gas shales of the Appalachian Basin: AAPG Bulletin, 93(7), p. 857–889, doi:10.1306/03230908032.

Ferrill, D.A., A.P. Morris, P.H. Hennings, and D.E. Haddad, 2014. Faulting and fracturing in shale and self-sourced reservoirs: introduction. AAPG Bull., 98, p. 2161–2164.

Fishman, N.S., G.S. Ellis, A.R. Boehlke, S.T. Paxton, and S.O. Egenhoff, 2013. Gas Storage in the Upper Devonian–Lower Mississippian Woodford Shale, Arbuckle Mountains, Oklahoma: How Much of a Role do Chert Beds Play? In J.

Chatellier and D. Jarvie, eds., Critical assessment of shale resource plays: AAPG Memoir, 103, p. 81–107.

Frederickson, E.A., 1957. Geologic map of the Criner Hills area, Oklahoma, Oklahoma Geological Survey. http://ogs.ou.edu/docs/geologicmaps/GM4.pdf

Freeprintablemaps, posted on February 19, 2009. Retrieved from http://freeprintablemaps.w3ec.com/maps/map-of-cities-and-counties-in-oklahoma-state-map.

Gillespie, P.A., J.D. Johnston, M.A. Loriga, K.J.W. McCaffrey, J.J. Walsh, and J. Watterson,1999. Influence of layering on vein systematics in line samples, in Mc-Caffrey, K.J.W., Longeran, L., and Wilkinson, J.J., eds., Fractures, Fluid Flow and Mineralization. Geological Society [London] Special Publication, 155, p. 35–56.

Gillespie, P.A., J.J. Walsh, J. Watterson, C.G. Bonson, and T. Manzocchi, 2001. Scaling relationships of joint and vein arrays from The Burren, Co. Clare, Ireland: Journal of Structural Geology, 23, p. 183–201, doi: 10 .1016 /S0191-8141 (00)00090-0: SPE 171604-MS. http://dx.doi.org/10.2118/171604-MS.

Gudmundsson, A., and S.L. Brenner, 2001. How hydrofractures become arrested. Terra Nova, 13, p. 456-462.

Herwanger, J.V., A.D. Bottrill, and S.D. Mildren, 2015. Uses and Abuses of the Brittleness Index With Applications to Hydraulic Stimulation. Unconventional Resources Technology Conference (URTeC), doi:10.15530/urtec-2015-2172545.

Higley, D.K., 2014. Thermal Maturation of Petroleum Source Rocks in the Anadarko Basin Province, Colorado, Kansas, Oklahoma, and Texas, Ch.3, USGS Province 58: U.S. Geological Survey Digital Data Series DDS–69–EE, p. 53. http://dx.doi.org/10.3133/ds69EE.

Hooker, J.N., S.E. Laubach, and R. Marrett, 2013. Fracture-aperture size-Frequency, spatial distribution, and growth processes in strata-bounded and nonstrata-bounded fractures, Cambrian Mesón Group, NW Argentina.

Ishii, E., 2016. Far-field stress dependency of the failure mode of damage-zone fractures in fault zones: Results from laboratory tests and field observations of siliceous mudstone, J. Geophys. Res. Solid Earth, 121, 70–91, doi:10.1002/2015JB012238.

Jin, X., S.N. Shah, J. Roegiers, and B. Zhang, 2015. An Integrated Petrophysics and Geomechanics Approach for Fracability Evaluation in Shale Reservoirs. SPE Journal, 20 (3). http://dx.doi.org/10.2118/168589-PA

Johnson, K.S., 2008. Geologic History of Oklahoma. Educational publication 9.

Johnson, B., 2009. Petrophysical Study of the West Edmond Field, in parts of Oklahoma, Canadian, Kingfisher, and Logan Counties, Oklahoma. Master's Thesis, Oklahoma State University, Stillwater, OK.

Keller, A., 1998. High resolution, non-destructive measurement and characterization of fracture apertures. International Journal of Rock Mechanics and Mining Sciences, 35(8), p. 1037–1050.

Kim, Y.S., D.C.P. Peacock, and D.J. Sanderson, 2004. Fault damage zone, J. Struct. Geol., 26, p. 503-517.

Ladeira, F.L., and N.J. Price, 1981. Relationship between fracture spacing and bed thickness. J. Struct. Geol., p. 179–183.

Lamarche, J., A. P. C. Lavenu, B. D. M. Gauthier, Y. Guglielmi, and O. Jayet, 2012. Relationships between fracture patterns, geodynamics and mechanical stratigraphy in Carbonates (South-East Basin, France) (Crustal stresses, fractures, and fault zones: The legacy of Jacques Angelier): Tectonophysics, 581, p. 231–245, doi:10.1016/j.tecto.2012.06.042.

Lang III, R.C., 1957. The Criner Hills: a key to the geologic history of southern Oklahoma, in Kempf, J. H., ed., Criner Hills field conference, Lake Murray Area, Southern Oklahoma Guidebook: Ardmore Geological Society, p. 18–25.

Laubach, S.E., J.E. Olson, and M.R. Gross, 2009. Mechanical and fracture stratigraphy. AAPG Bulletin, 93 (11), p. 1413-1426. http://dx.doi.org/10.1306/07270909094.

Lazar, O.M., K.M. Bohacs, J.H.S. Macquaker, J. Schieber, and T. Demko, 2015. Capturing key attributes of fine-grained sedimentary rocks in outcrops, cores, and thin sections: nomenclature and description guidelines. Journal of Sedimentary Research, 85, p. 230-246.

Li, Q., H. Xing, J. Liu, and X. Liu, 2015. A review on hydraulic fracturing of unconventional reservoir Petroleum, 1(1), p. 8–15.

Milad, B., 2017. The Effect of Karsting on Natural Fracture, Hardness, and Brittleness of the Hunton Limestone and Paleo-Deposition of the Woodford Shale: A Study Using 3-D Seismic, Outcrop, Well Log, and Core Data. Search and Discovery Article #51417.

Odonne, F., C. Lézin, G. Massonat, and G. Escadeillas, 2007. The relationship between joint aperture, spacing distribution, vertical dimension and carbonate stratification: an example from the Kimmeridgian limestones of Pointe-du-Chay (France). Journal of Structural Geology, 29, p. 746-758.

Ortega, O.J., R. Marrett, and S.E. Laubach, 2006. A scale-independent approach to fracture intensity and average fracture spacing: AAPG Bulletin, 90, 193–208, doi:10.1306/08250505059.

Ortega, O.J., J.F.W. Gale, and R., Marrett, 2010. Quantifying diagenetic and stratigraphic controls on fracture intensity in platform carbonates: An example from the Sierra Madre Oriental, northeast Mexico, Journal of Structural Geology, 32(12), p. 1943-1959, doi:10.1016/j.jsg.2010.07.004.

Paxton, S.T., and B.J. Cardott, 2008. Oklahoma gas shales field trip, October 21 & 23, Oklahoma Geological Survey Open File Report 2-2008, p. 110.

Peng, C., J.P. Crawshaw, G.C. Maitland, and J.P.M. Trusler, 2015. Kinetics of Calcite dissolution in CO_2 –Saturated water at temperatures between 323 K and 373 K and pressure up to 13.8 MPa. Chemical Geology, 403, p. 74-85.

Pireh, A., S.A. Alavi, M.R. Ghassemi, and A. Shaban, 2015. Analysis of natural fractures and effect of deformation intensity on fracture density in Garau formation for shale gas development within two anticlines of Zagros fold and thrust belt, Iran. Journal of Petroleum Science and Engineering, 125, p. 162-180.

Portas, R.M., and R.M. Slatt, 2010. Characterization and Origin of Fracture Patterns in a Woodford Shale Quarry in Southeastern Oklahoma for Application to Exploration and Development. Search and Discovery Article #50352.

Renshaw, C. E., and Park, J. C., 1997. Effect of mechanical interactions on the scaling of fracture length and aperture, Nature, 386, p. 482–484.

Serna-Bernal, A., 2013. Geological Characterization of the Woodford Shale McAlister Cemetery Quarry, Criner Hills, Ardmore Basin, Oklahoma: M.S. thesis, University of Oklahoma, Norman, OK.

Slatt, R.M., 2013. Sequence Stratigraphy of the Woodford Shale and Application to Drilling and Production. Search and Discovery Article #50792.

Smart, K.J., G.I. Ofoegbu, A.P. Morris, R.N. McGinnis, and D.A. Ferrill, 2014. Geomechanical modeling of hydraulic fracturing: Why mechanical stratigraphy, stress state, and pre-existing structure matter: AAPG Bulletin, 98(11), p. 2237–2261, doi:10.1306/07071413118.

Staples, E.R., 2011. Subsurface and Experimental Analyses of Fractures and Curvature. Master's Thesis, University of Oklahoma, Norman, OK.

Stearns, D.W., 1968. Certain Aspects of Fractures in Naturally Deformed Rocks. In: Riecker, R. E., ed., Rock Mechanics Seminar. Terrestrial Sciences Laboratory, Bedford., p. 97–118.

Stearns III, V.G., 2015. Fracture Characterization of the Mississippi Lime Utilizing Whole Core, Horizontal Borehole Images, and 3D Seismic Data from a Mature Field in Noble County Oklahoma. Master's Thesis, University of Oklahoma, Norman, OK.

Tan, Y., T. J. Johnston, and T. Engelder, 2014. The concept of joint saturation and its application: AAPG Bulletin, 98(11), p. 2347–2364, doi: 10.1306/06231413113.

Tomlinson, C.W., 1936. Structural History of the Criner Hills. Tulsa Geological Society Digest Vol. 5 (1936), p. 11.

Turner, B.W., C.E. Molinares-Blanco, and R.M. Slatt. 2015. Chemostratigraphic, palynostratigraphic, and sequence stratigraphic analysis of the Woodford Shale, Wyche Farm Quarry, Pontotoc County, Oklahoma: Interpretation, 3(1), p. 1-9, doi: 10.1190/INT-2014-0089.1.

Wang, F.P., and J. F. W. Gale, 2009. Screening criteria for shale-gas systems: Gulf Coast Association of Geological Societies Transactions, 59, p. 779-793.

Waters, G., B. Dean, R. Downie, K. Kerrihard, L. Austbo , B. McPherson, 2009. Simultaneous Hydraulic Fracturing of Adjacent Horizontal Wells in the Woodford Shale. Paper SPE 119635, presented at the SPE Hydraulic Fracturing Technology Conference, The Woodlands, TX, 19-21 January.

Wennberg, O.P., T. Svånå, M. Azizzadeh, A.M.M. Aqrawi, P. Brockbank, K.B. Lyslo, and S. Ogilvie, 2006. Fracture intensity vs. mechanical stratigraphy in platform top carbonates: the Aquitanian of the Asmari Formation, Khavizantic line, Zagros, southwest Iran. Pet.Geosci., 12, p. 235–246.

Weiss, M., Y. Rubin, E. Adar, and R. Nativ, 2006. Fracture and bedding plane control on groundwater flow in a chalk aquitard. Hydrogeology Journal, 14, p. 1081-1093.

CHAPTER 3: HIGH-RESOLUTION CHARACTERIZATION OF NATURAL FRACTURE STRATIGRAPHIC DENSITY VARIATION AND SIZE-DISTRIBUTION IN THE WOODFORD SHALE, ARBUCKLE WILDERNESS AND US-77D OUTCROPS, MURRAY COUNTY, OKLAHOMA

Abstract

Understanding the aperture-size distribution and stratigraphic variation in natural fracture density is important in determining the fluid flow capacity of low permeability formations. In this study, several facies were identified in a Woodford Shale whole section. The section was divided into four broad stratigraphic zones based on the interbedding of similar facies. The average bed thicknesses of brittle and ductile beds in the entire section were recorded. Also, five fracture sets were identified. These sets were split into two groups based on their trace exposures. Fracture linear intensities (P10: fractures/ft or fractures/m) were quantified for both brittle and ductile beds. Individual fracture intensity-bed thickness linear equations (negative slope) were derived for both brittle and ductile lithologies. These equations, along with average bed thickness and percentage of brittle and ductile lithologies in each stratigraphic foot, were used to construct an areal fracture density (P20: fractures/ft^2 or fractures/m^2) profile of the whole section. Macrofracture (opening displacements > 0.05 mm) and microfracture (opening displacements < 0.05 mm) kinematic apertures were measured along scanlines oriented sub-perpendicular to the fracture traces on outcrops and under microscopes using thin sections respectively. The cumulative frequencies of the apertures were plotted (separately) to find the best-fit distributions for each. Apertures vs. lengths measured along scanlines for some fractures were also plotted. In addition, macrofracture and microfracture spacings were recorded along scanlines.

Zone 1 (top of the upper Woodford) is cherty with few argillaceous mudstone beds. Zone 2, comprising the lower three-quarters of the upper Woodford and the top half of the middle Woodford has interbedding of chert and carbonaceous, argillaceous mudstones. Zone 3 (lower half of the middle Woodford) has interbedding of chert, argillaceous-siliceous mudstones, and argillaceous mudstones. Zone 4 (entire lower Woodford) has siliceous mudstones and carbonaceous, argillaceous mudstones, most dolomitized to variable degrees. The linear equations predict ~ 1.5-3 times higher fracture intensities in the brittle beds compared to the ductile beds at any given bed thickness. Parts of Zone 2 and the entire Zone 3 have high fracture densities and are located in relatively organic-rich areas, and may be suitable well landing targets.

Measured microfractures kinematic apertures range 0.001-0.05 mm, and macrofracture apertures range 0.05-1 mm. Both primarily exhibit exponential, followed by lognormal distributions. Crack-seal textures are not evident in thin sections. Fracture aperture (mm) vs. length (m) plots exhibit power-law (exponent range: 0.53-0.59) relationships. Microfractures show higher clustering ($\sigma_{spacing}$ /$\mu_{spacing}$ > 1) compared to the macrofractures ($\sigma_{spacing}$/$\mu_{spacing}$ < 1).

3.1 Introduction

Refer to Chapter 2.1, paragraphs 1-4 for first part of the introduction.

The Arbuckle Wilderness Outcrop (AWO) and the US-77D Outcrop located in the Arbuckle Mountains of Southern Oklahoma are the primary focus of this study. Using these two outcrops, the following questions regarding the Woodford Shale have been addressed: a) how do fracture intensities and spacing vary with bed mineralogy and thickness in the Woodford Shale?; b) how does the overall fracture density vary in

an entire section of the Woodford Shale and what are the good horizontal well landing spots?; c) what is the best fit aperture distribution in the studied areas?

3.2 Geology of Arbuckle Mountains

Refer to Chapter 2.2, paragraph 1 for Woodford Shale deposition.

Post Woodford deposition structural uplift in the Arbuckle Mountains began in the Late Mississippian (Sanchez, 2012) and continued into the late Pennsylvanian as a series of orogenic pulses (Ham, 1973). Desmoinesian orogenic activity resulted in the uplift of early Arbuckle structures such as the Arbuckle and Hunton Anticlines; however, structural deformation during this time was broad in scale and occurred relatively slowly (epiorogenic uplift). Subsequent mid-Virgilian deformation occurred over a much shorter time span and in greater magnitude, resulting in reactivation and thrusting along Precambrian normal faults, folding of the basement and Paleozoic strata, and overturning of Arbuckle Mountain folds. This event is largely referred to as the Arbuckle Orogeny (Ham, 1973). The product of Pennsylvanian deformation was a series of NW-SE trending anticlines and synclines, separated by parallel high-angle thrust faults (Badra, 2011).

The Arbuckle Wilderness Outcrop (AWO) lies on the southern, overturned limb of the Washita Valley Syncline in Sec. 29, T1S, R2E. A series of crosscutting streams and roads expose Ordovician Sylvan Shale through Mississippian Sycamore Limestone. Bontempi (2015) describes the structure of the AWO area in detail. The US-77D outcrop is located nearly a mile northwest of the AWO. Figure 3.1 shows the ground locations of the AWO and the US-77D outcrops. Figure 3.2 shows the outcrop position in a cross section.

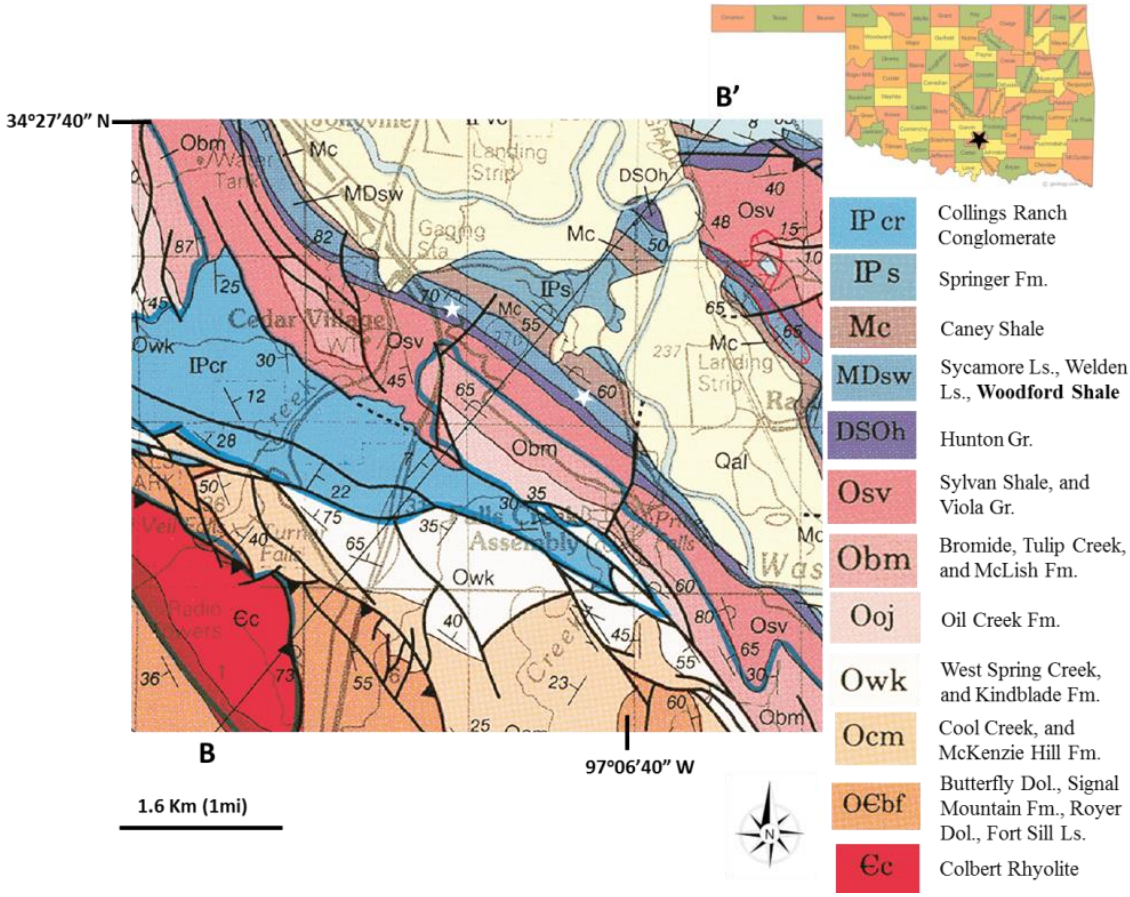

Figure 3.1: AWO and US-77D Outcrop locations. AWO (right white star) and US-77D outcrops (left white star) located in the northern overturned limb of the Arbuckle Mountains (modified from Ham and McKinley [1954]; revised by Johnson [1990]). In the AWO, the average strike and dip of exposed beds is approximately 130/60 (Right-hand rule) in areas devoid of minor folds and 113/72 (Right-hand rule) in the US-77D Outcrop.

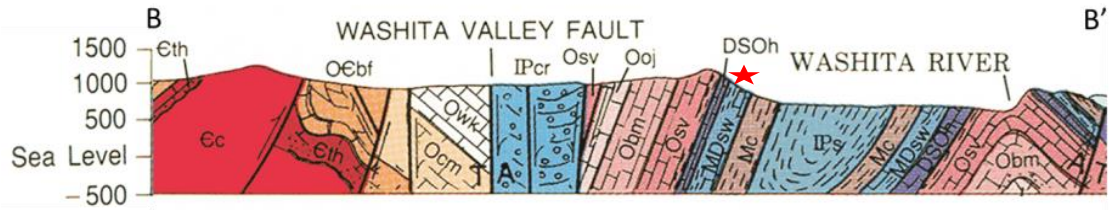

Figure 3.2: Regional cross section from southwest to northeast (modified from Ham and McKinley [1954]; revised by Johnson [1990]). Star shows the approximate cross section of the measurement areas.

3.3 Methods

3.3.1 Measured section

Bontempi (2015) performed a measured section along the entire AWO Woodford section (Figure 3.1). Field descriptions were made every one stratigraphic foot, which includes rock texture, the percentage of brittle and ductile beds in a stratigraphic foot, and average thicknesses of brittle and ductile beds in a stratigraphic foot. Also, gamma ray (GR) measurements were taken at each stratigraphic foot using a Centrex GRS-500^{TM} differential GR-scintillometer. In the US-77D Outcrop, a measured section was not attempted because only a few laterally extensive, nearly vertical (overturned), bedding surfaces are available.

3.3.2 Mineralogy and rock texture

Sixteen samples were collected for both thin section and mineralogy from both the brittle and ductile beds. X-ray diffraction (XRD) was performed to determine the mineralogy. Turner et al. (2015) describe the XRD methodology. In addition, Bontempi (2015) collected nearly 40 samples for thin sections along the entire stratigraphic section solely for rock description (texture, composition). Sample collection spots for the thin section and XRD, denoted by stars, are shown in Figure 3.3. Several types of lithofacies and lithofacies groups based on texture, organic content (observed from thin sections), and mineralogy were identified during construction of the lithologic column. These lithofacies and lithofacies groups were lumped into four broad zones based on XRD mineralogy (Figure 3.4), direct outcrop observations and thin-section observations.

3.3.3 Fracture intensity, aperture size, and spacing measurement

Refer to Chapter 2.3.2 for the scanline method for measurement of intensity, aperture size, and spacing. In addition to scalines for macrofractures, microscanlines were also used on several thin sections for measurement of microfracture parameters.

3.3.4 Fracture density (P20) measurement for each stratigraphic foot

Same scanline method described in Chapter 2.3.2 was used for measuring fracture intensities in the AWO. In the US-77D, the scanlines were placed on bed faces instead of cross sections because bed faces are more accessible compared to bed cross sections. In the AWO, fracture intensities and bed thicknesses were plotted for brittle and ductile beds separately for Zones 1-4 resulting in eight intensity vs. bed thickness plots. Equations used to calculate the areal fracture density, i.e., P20 (fractures/ft^2 [fractures/0.093 m^2]) for each 0.305 m (1 ft) stratigraphic interval is shown in Appendix A. The P20 values for each stratigraphic foot were then plotted to obtain the P20 profile for the entire Woodford Shale section. Fracture areal density (P20) is defined as the number of fracture traces observed in a given area (FracMan7.5 Workshop, 2014). For example, an areal density can be obtained by dividing the number of observed fracture traces in Figure 1.4D by the area in which they are exposed [(P20: fractures/m^2]. In the missing GR sections, bed thicknesses were noted by making observations at a distance of 3-6 m (~ 10-20 ft) in a stratigraphically equivalent position. Also, at several spots, due to soil and debris covering the joints, only bed thickness could be observed. Therefore, P20 values were calculated, rather than counted directly for each 0.305 (1 ft) interval.

3.4 Results

3.4.1 Mineralogy and facies naming

Refer to Chapter 2.4.1 for facies naming conventions.

The modified ternary diagram is defined by quartz, carbonate', and clay' points. Values falling within and below the bottom-right sub-triangle in the quartz-carbonate'-clay' triangle are classified as "argillaceous." Values at the top of the quartz-carbonate'-clay' triangle are classified as "siliceous." The lowermost red star and the rightmost orange star falling outside the quartz-carbonate'-clay' triangle can be considered "dolomitic" and "argillaceous" respectively. Two red stars falling within the central sub triangle of the quartz-carbonate'-clay' triangle can be considered in the siliceous-argillaceous-slightly dolomitic to a siliceous-dolomitic range. The orange star in the central triangle (touching the dashed line) can be considered as siliceous-argillaceous or argillaceous-siliceous. The dashed line, along with an uncertainty of a few percent, represents the boundary between the brittle and the ductile facies.

The siliceous mudstones (cherts), siliceous-dolomitic mudstones, and dolomitic mudstones fall under the "brittle" category. Rocks classified as argillaceous-siliceous (or siliceous-argillaceous), and dolomitic-argillaceous (or argillaceous-dolomitic) are classified as "less ductile" compared to the highly laminated argillaceous beds, which are classified as "more ductile."

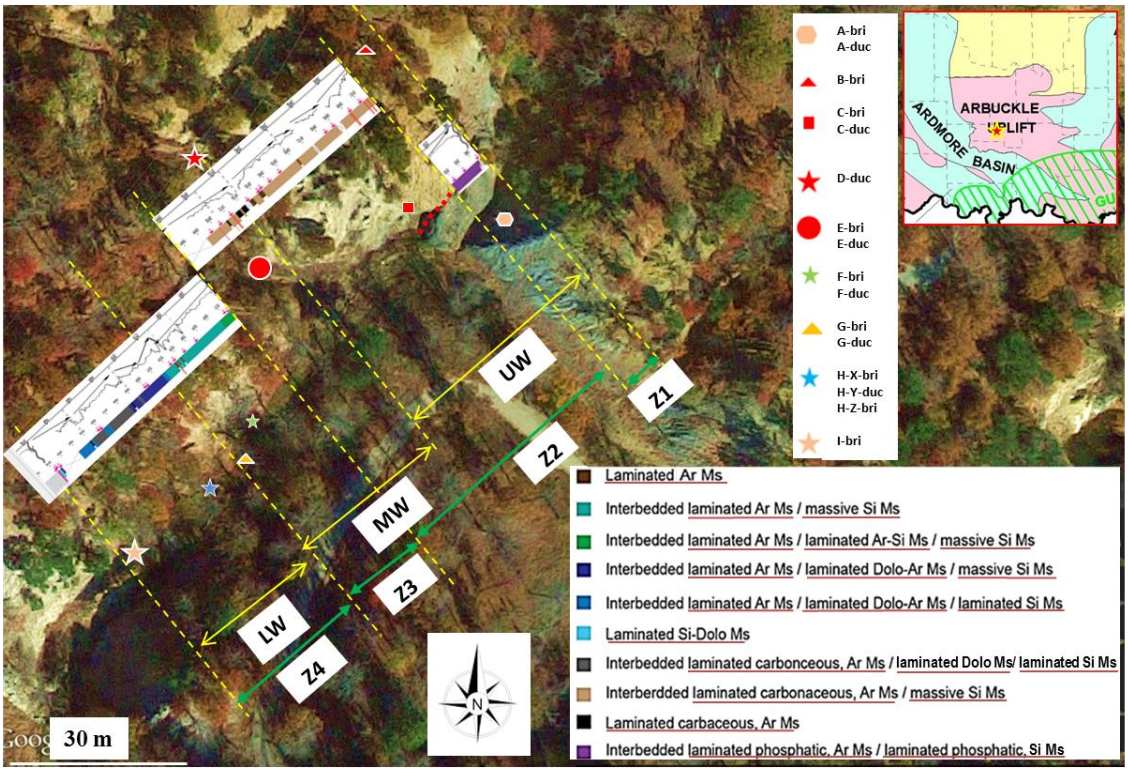

Figure 3.3: Aerial view of the AWO (34°26'14.8"N, 97°07'00.3"W) and sampling locations. The top dashed line is the top of the Woodford Shale, and the bottom dashed line is the contact between the Woodford Shale and the Hunton Limestone. Trace of a fault between Zone 1 and Zone 2 is shown in dotted red line. Facies names (underscored in red) in the measured section are presented on the bottom right. Interbeds of different facies have been assigned separate colors. Sample collection spots are on top right near the map inset. The measured GR log, along with interpretations of increasing and decreasing upward trends is shown with the lithologic column (taken from Bontempi [2015]). **Abbreviations:** **Ar**=argillaceous; **Dolo**=dolomitic; **Ms**=mudstone; **Si**=siliceous; **Si Ms**=chert.

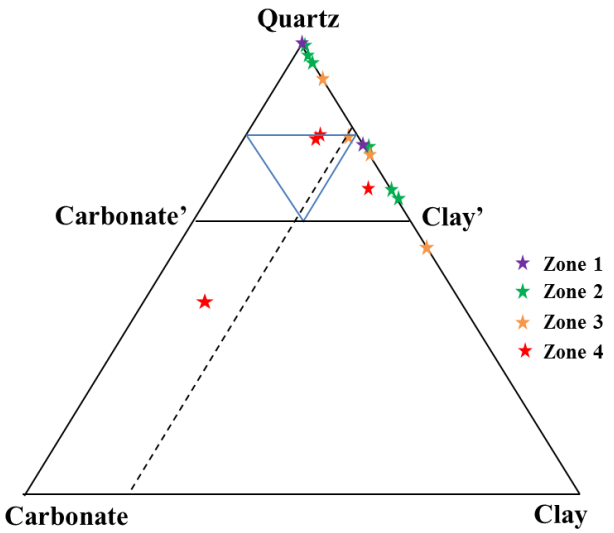

Figure 3.4: Ternary diagram showing XRD mineralogies of the brittle and ductile samples collected from Zones 1-4. Note that all Zone 4 compositions have higher carbonate (dolomite) compared to other zones. Illite is the dominant mineral in the clay portion of the both cherts and mudstones. Star colors are not related to those in Figure 3.3.

3.4.2 Fracture set identification and orientation from outcrop

Five main fracture sets were identified in both the AWO and the US-77D Outcrops. The five main fracture sets are marked in Figures 3.5A through 3.5H. The orientations of the five sets (3.6A, 3.6B, 3.6E, and 3.6F) along with the bedding (3.6C and 3.6G) are shown. Poles to the fracture planes after bed restoration are shown in Figures 3.6D and 3.6H for US-77D and AWO respectively. Set 1 is more developed in the brittle beds (Figures 3.5A, 3.5C, 3.5F, and 3.5I) and less ductile beds, and relatively underdeveloped in the more ductile beds (present in 5-10% of the more ductile beds). Set 1 fractures are the longest ones seen at the US-77D Outcrop and do not terminate at any other fracture set. Set 2 fractures are well developed in the more ductile beds (Figure 3.5B, 3.5D, and 3.5E) and sometimes cut the less ductile ones. However, they are generally absent from the brittle beds. Set 3 is relatively well developed in the brittle (Figure 3.5A) and less ductile beds. These are generally absent from more ductile beds.

Set 4 fractures are non-systematic, run sub-parallel to the fold axis, and found in all beds (Figure 3.5B, 3.5G, and 3.5H). These are sub-parallel to Set 1 fractures and may be difficult to differentiate from small (usually < 2 m [6.6 ft] long) Set 1 fractures. The Set 4 fractures, however, are non-systematic, shorter, and more numerous compared to the Set 1 fractures and mostly abut and sometimes crosscut other sets (Figure 3.5B). Set 5, running perpendicular to the fold axis is well developed in the brittle beds (Figures 3.5A, through 3.5D, 3.5G, and 3.5H), slightly less developed in the less ductile beds, and are present in 5-10% of the more ductile beds. There are some randomly occurring fractures in various directions intermittently due to stress heterogeneity caused by the overturning of the outcrops, which have not been assigned set designations.

Seen directly on the beds, fractures from all sets have a variable degree of cementation (i.e., empty to fully cemented). However, fractures in dolomite-rich beds show the highest degree of cementation (mainly calcite cement). In the chert beds, some wide fractures (~ 1 mm [0.003 ft] aperture) have cement. However, cement (mostly silica) is seen more frequently, though not always, in narrower fracture (< 0.2 mm [0.00066 ft] aperture) compared to the wider ones. Cement is not clearly visible in fractures within the argillaceous beds as observed directly at the outcrops. However, thin sections show clear presence of cement. Bitumen filled fractures were seen in all zones in thin sections.

As exposed at the bed cross sections, Sets 2 3, 5 and Sets 1, 4 can be considered as two separate groups due to high angles (45-90 degrees) between the two groups for intensity measurement purposes. In most bed cross-section exposures, one group can

usually be differentiated from the other. Table 3.1 shows the average orientations before and after bed restoration.

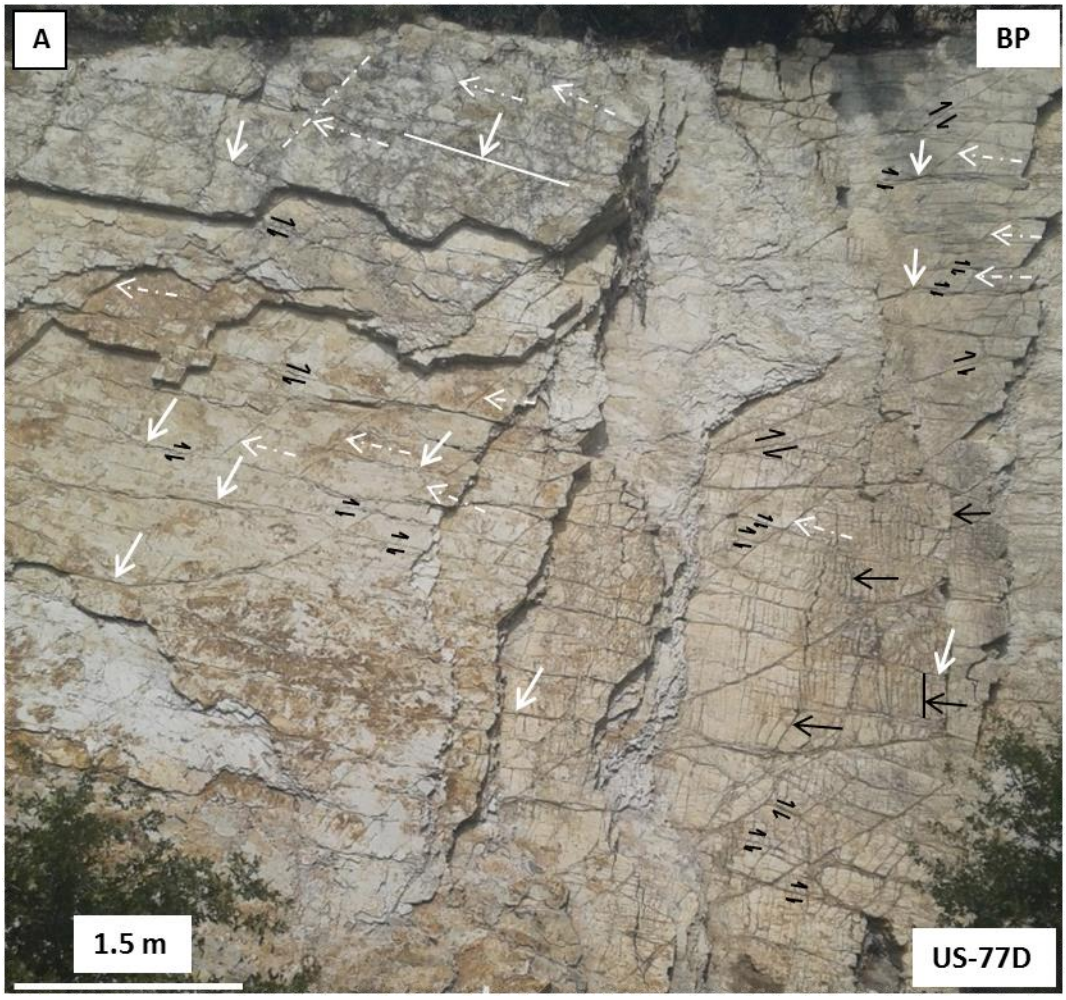

Set 1: Solid white (←)
Set 2: Dotted black (←)
Set 3: Broken white (←)
Set 4: Dotted white (←)
Set 5: Solid black (←)

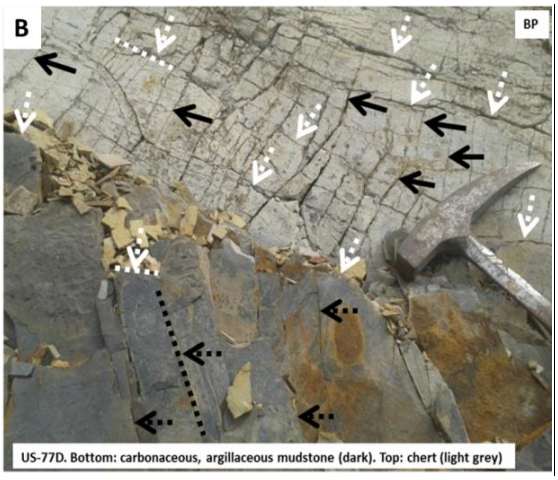

US-77D. Bottom: carbonaceous, argillaceous mudstone (dark). Top: chert (light grey)

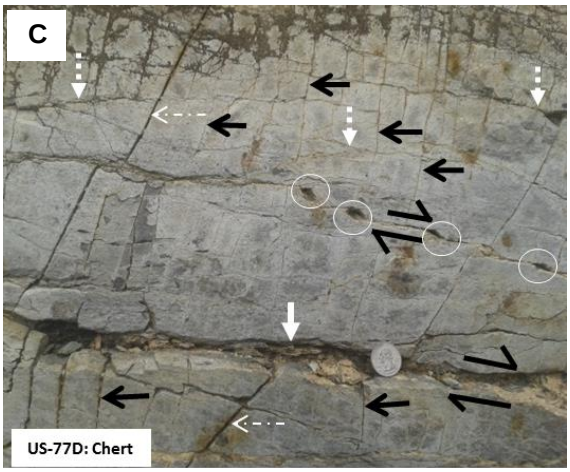

US-77D: Chert

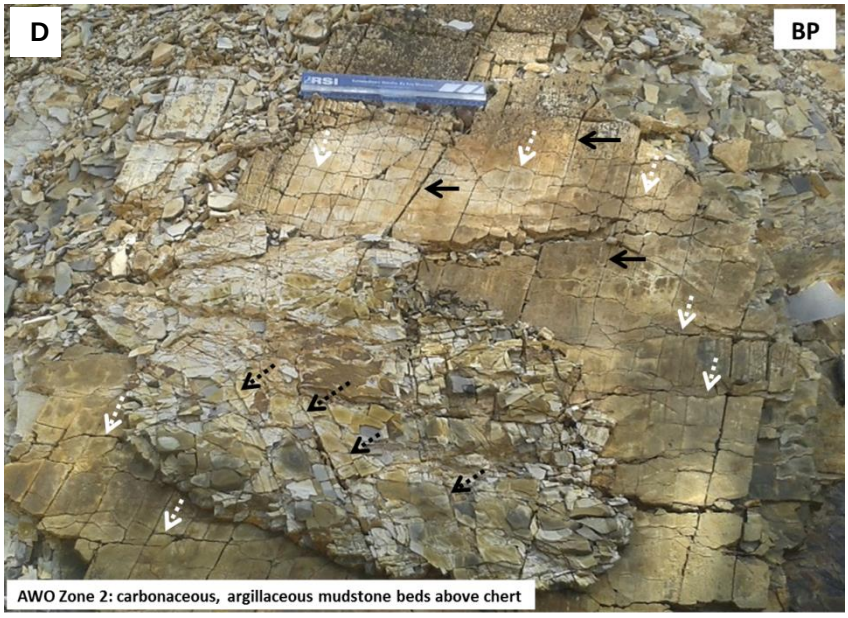

AWO Zone 2: carbonaceous, argillaceous mudstone beds above chert


E
BP
AWO Zone 2: argillaceous mudstones


F
BP
AWO Zone 2: dolomitic beds

Figure 3.5: Fracture (joint) sets in the US-77D and AWO. Fractures are identified on the outcrop with arrows drawn sub-perpendicular to their traces. Some fractures are indicated by both arrows and lines drawn directly above the fractures for easier identification. **A)** US-77D wall (34°26'38.6"N, 97°07'40.6"W) from the lower Woodford Shale showing the different fracture sets. Set 4 fractures are not shown in this photograph due to their small sizes. **B)** Carbonaceous, argillaceous mudstones (more ductile) with Set 2 fractures that are generally absent in the brittle beds. Notice that Set 4 fractures are non-systematic and shorter compared to the other sets. **C)** Set 2 fractures with substantial right-lateral displacement and gouge. Opening bends are circled. **D)** Remnant cake of a ductile mudstone bed on a chert bed. Note that Set 2 fractures present on the mudstone are oriented about 35-40 degrees counterclockwise (as seen in the photograph of the overturned beds) to the Set 5 fractures in the chert beds. **E)** Massive ductile mudstone beds dominated by Set 2 and Set 4 fractures. **F)** Dolomitic beds showing crosscutting between Set 1 and Set 5 fractures. **G)** Heavily quartz cemented Set 5 fractures and non-systematic Set 4 fractures. **H)** Narrow, systematic,

quartz cemented Set 1 and Set 5 fractures, and empty Set 4 fractures. **I)** Dolomite containing bed at Zone 3/Zone 4 boundary showing a high degree of calcite cementation in Set 1 and Set 5 fractures. **J)** Plumose structure and calcite cement on a 12 cm thick dolomite bed in Zone 3 indicating brittle fracturing.

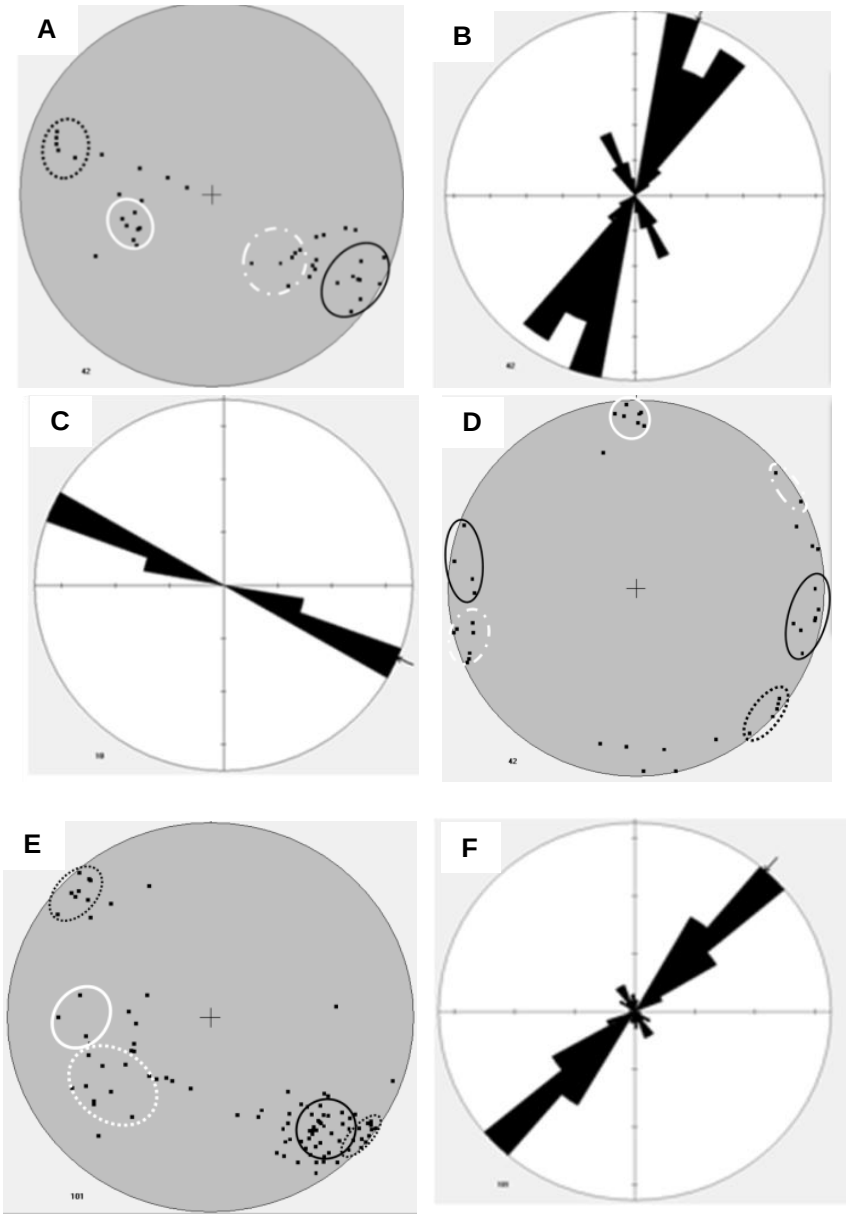

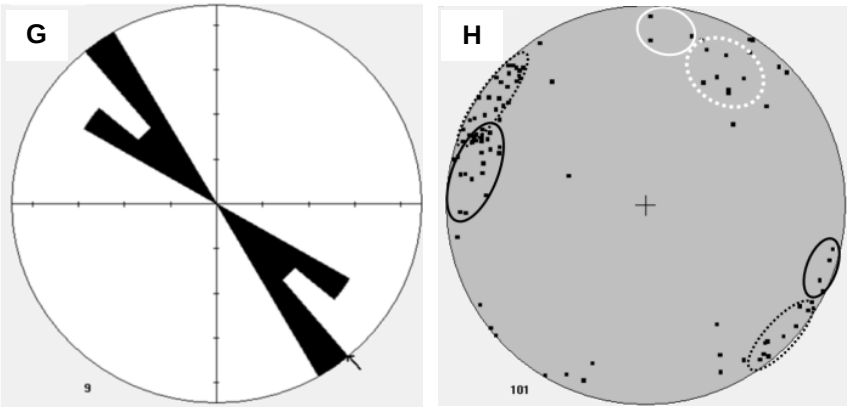

Figure 3.6: Bed and fracture orientations in the US-77D and AWO. **A)** Poles to Sets 1, 2, 3 and 5 fractures in the US-77D Outcrop. **B)** Rose diagram representation of fracture orientations in the US-77D Outcrop. **C)** Rose diagram representation of the bed strikes in the US-77D Outcrop (Average orientation: 113/72 using RHR). **D)** Data from A, after bed restoration to horizontal after rotation of 108 (i.e., 180-72 = 108) degrees (beds are overturned) around 113 degrees azimuth. **E)** Poles to Sets 1, 2, 4 and 5 fractures in the AWO. **F)** Rose diagram representation of all measured fracture strikes. **G)** Rose diagram representation of the bed strikes (also fold strikes) in the AWO (Average orientation: 134/59 using right-hand rule). **H)** Data from G after bed restoration to horizontal after rotation of 121 (i.e., 180 - 59 = 121) degrees around 134 degrees azimuth.

Table 3.1: Pre- and post-restoration average fracture orientations of measured sets using right-hand rule.

Fracture Sets	Average fracture orientations as measured on the outcrops	Average post-restoration fracture orientations
1 (US-77D)	333/35	091/81
1 (AWO)	04/53	97/84
2 (US-77D)	018/69	224/87
2 (AWO)	046/86	226/86
3 (US-77D)	238/40	142/85
3 (AWO)	-	-
4 (US-77D)	-	-
4 (AWO)	322/56	127/76
5 (US-77D)	210/78	189/87
5 (AWO)	227/70	026/83

3.4.3 Lithology and fracture fill from thin sections (Four zones of AWO)

Zone 1 (Figures 3.3 and 3.7A) consists of mainly organic-poor chert (siliceous mudstone) beds with few intermittent argillaceous mudstone beds. Phosphate nodules are commonly seen in this zone. This zone has the lowest average GR values out of the four zones. Most of the bed-perpendicular fractures are planar, not sinusoidal, unlike in some of the other beds in stratigraphically lower areas (refer to Figures. 3.8G, 3.9E, 3.9F, and 3.9H). In Set 1, most narrow fractures are completely bitumen (some clay) filled with the thicker ones completely chalcedony-filled. A few chalcedony-filled oblique fractures also are present (Figure 3.7D). No presence of bed-parallel fractures was found in the thin section taken in this Zone (which are possibly present but not seen here). Microfractures are rare in the ductile beds. However, a couple of bifurcating macrofractures with calcite fill (Figure 3.7E) were seen.

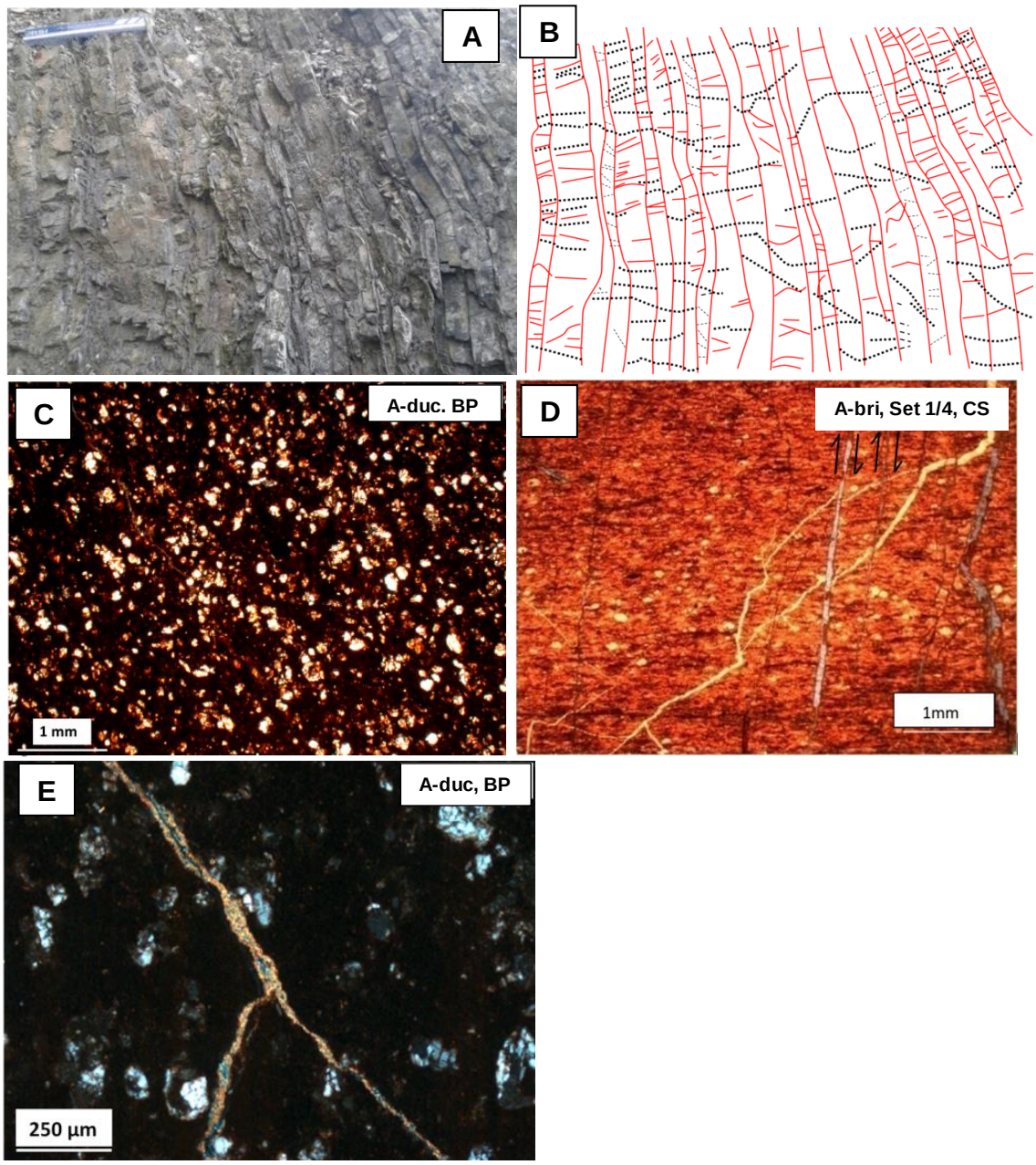

Figure 3.7: Outcrop and thin-section expressions of Zone 1. **A)** Outcrop expression of beds in Zone 1. Footlong ruler is shown for scale. **B)** Bedding and fracture traces interpreted from A. Thick dotted lines (black) show bed-boundary crosscutting fractures. Thin dashed lines (black) show fractures in mudstones. Solid lines (red) depict bedding as well as fractures in chert beds. Line styles are not related to arrow styles denoting fracture sets in Figure 3.5. **C** (PPL) and **D** (PPL) are the thin sections of the ductile (laminated carbonaceous, argillaceous mudstone) and the brittle (laminated siliceous mudstone (chert) facies respectively. In **D** the white, non-systematic fractures, pointing up and right are chalcedony-filled and offset (half arrows) along some of the bed-perpendicular fractures. Thin planar fractures are bitumen and clay-filled and crosscut chalcedony-filled fractures. **E)** Thin section (CPL) of carbonaceous,

argillaceous mudstone with an oblique calcite (nonauthigenic cement) filled fracture. **Abbreviations**: **BP**-looking at bedding planes, **CS**-looking at bed cross sections.

Zone 2 (Figure 3.8A) is rich in organic matter, indicated by the high GR (Figure 3.3). It has a more even distribution of chert and carbonaceous argillaceous beds (Figures 3.8A and 3.8B). However, in this zone, four distinct areas of laminated argillaceous and laminated carbonaceous, argillaceous mudstones are present without interbedding with chert beds.

For the Set 5 bed-perpendicular microfractures, ~ 85% fractures terminate within a layer at different elevations away from any significant mechanical boundary, i.e., they are unbound. Around 15% terminate at bed/mechanical boundaries, mostly near slightly clay/organic-rich layers, i.e., they are bedbound (e.g., Figure 3.8D). Therefore, the majority of the microfractures can be considered unbound based on imaging the fracture tips in the optical microscope.

In two thin sections, a majority of fractures are bitumen-filled. Some of the wider microfractures have bitumen as the main component with intermittent quartz (not chalcedony) in the middle. Many fracture tips (< 5 microns wide) that thin out are entirely quartz-filled. Ignoring these very thin ones, there is a tendency that the ones with cement lining in the middle and bitumen lining at walls are wider.

Sinusoidal traces, all bitumen-filled, are present in only five out of ~ 35 bed-perpendicular Set 1/4 fractures examined. Many fractures crosscut thin alternating brittle-ductile laminations and terminate at different thin lamination boundaries leading to an approximately hierarchical pattern at the microscopic scale. Hooker et al. (2013, p. 58) describe hierarchical fracture pattern along with other patterns of fracture termination. A majority of bitumen-filled, bed-parallel fractures terminate against

bitumen-filled, bed-perpendicular fractures (Figures 3.8E and 3.8 F). Younger wider clay or bitumen-filled fracture crosscutting older bitumen-filled sinuous fractures are also seen (Figure 3.8G). A few bitumen-filled bed-perpendicular fractures also terminate or dogleg at bed-parallel fractures indicating that some of the bed-parallel fractures are older than the Set 4 (most probably) bed-perpendicular fractures (Figure 3.8H).

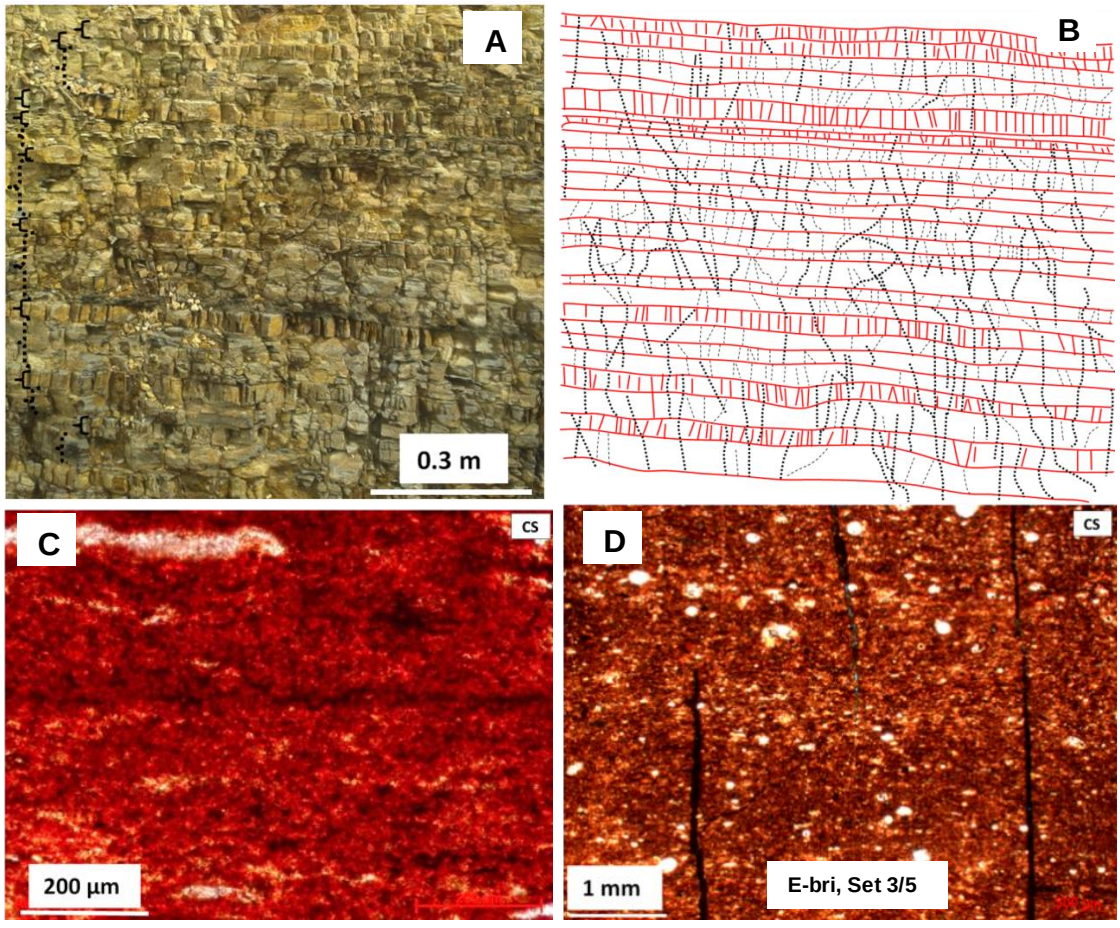

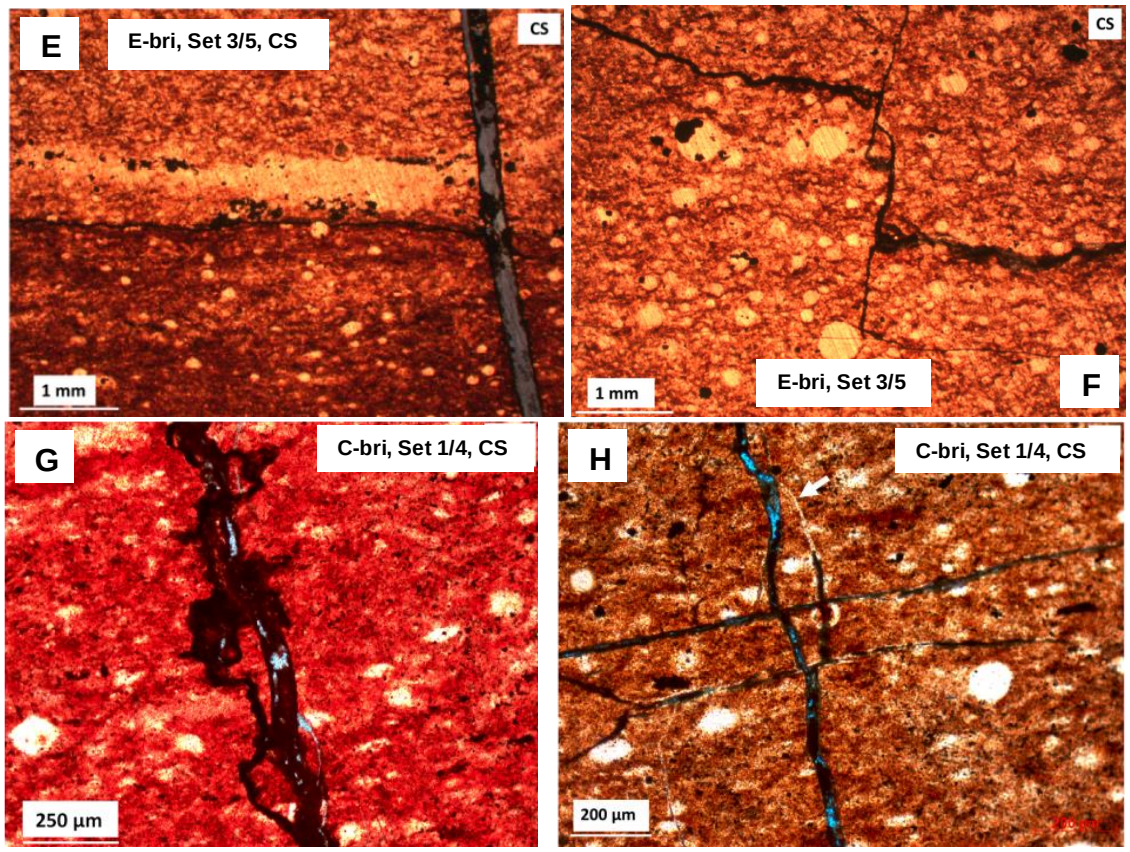

Figure 3.8: Outcrop and thin-section expressions of Zone 2. **A)** Outcrop expression of Zone 2. Within dotted curly bracket are laminated carbonaceous, argillaceous mudstones. Within the solid brackets are massive siliceous mudstones (or chert). **B)** Bedding and fracture traces interpreted from A follow the same marking convention as Figure 3.7B. **C)** Thin section (PPL) showing laminated argillaceous mudstone (Bontempi, 2015). **D)** Thin section (PPL) of the brittle facies (E-BRI: massive siliceous mudstone [chert]) with bitumen-filled fractures terminating in areas slightly richer in clays. Radiolarians are common to both the brittle and the ductile facies. Note that on the left, a completely bitumen-filled fracture abruptly terminated without thinning out and without any considerable change in lithology, while the bitumen-filled fracture at the center has slight porosity and gradually thins out. The rightmost fracture terminates at the tip of another fracture. **E)** Thin section (PPL) showing younger bed-parallel, bitumen-filled fracture at a significant bed boundary terminating at an older bed-perpendicular bitumen-filled fracture. **F)** Thin section (PPL) showing younger bed-parallel, bitumen-filled fractures, away from a significant bed boundary terminating at older bed-perpendicular bitumen-filled fracture. **G)** Thin section (PPL) showing older bitumen-filled sinusoidal fracture crosscut and intersected by younger bitumen/clay-filled planar fracture. **H)** Thin section (PPL) showing bed-perpendicular, partially bitumen-filled fractures doglegging and crosscutting bed-parallel bitumen-filled fractures. Notice that the tip is quartz cement-filled (arrow). **Note**: Arrow style is not related to those in Figure 3.5. **Abbreviations**: **BP**-looking at bedding planes, **CS**-looking at bed cross sections.

Zone 3 (Figures 3.3 and 3.9A) is poorer in organic content compared to Zones 2 and 4, as organic matter was not observed as frequently in the Zone 3 ductile-bed thin sections compared to those in Zones 2 and 4. However, in addition to the argillaceous mudstones and chert, there are beds that have mineralogy in the argillaceous-siliceous, or siliceous-argillaceous ranges (Bontempi, 2015) (Figures 3.9A and 3.9C). XRD analysis shows higher clay content in both the brittle and ductile beds compared to the corresponding beds in other zones (Figure 3.4). Figures 3.9B and 3.9D show bed fracture and bed boundary interpretations. Nearly 90% of the bed-perpendicular Set 5 fractures are sinusoidal and bitumen-filled (Figures 3.9E and 3.9F) as observed in thin sections. Generally, the narrower ones terminate by thinning out within a bed and are not affected by the bed boundaries. Only a couple of wide, planar bed-normal fracture with bitumen lining at the walls and dolomite/calcite in the middle were present (Figure 3.9G). A calcite-filled bed-parallel fracture terminating at bed-perpendicular bitumen-filled fracture (arrow in Figure 3.9F) is shown. Bed-parallel fractures are planar, unlike their perpendicular counterparts.

Most bed-perpendicular Set 1/4 fractures appear unbound because, in the thin section, bed boundaries are not visible due to matrix homogeneity like Set 5 fractures. A majority (~ 90%) of fractures contain only bitumen. The remaining ~ 10% are multiple anastomoses and crosscutting between younger calcite/dolomite-filled planar fractures and older bitumen-filled sinusoidal fractures (Figure 3.9H). Generally, anastomosis of bitumen-filled and cement-filled fractures occurs when they meet at low angles and crosscut at higher angles. In a Set 1/4 or Set 3/5 thin section in Zone 3, while measuring bed-perpendicular fracture aperture along a scanline, there is only a slight chance that a

solely non-bitumen cement-filled fracture will occur.

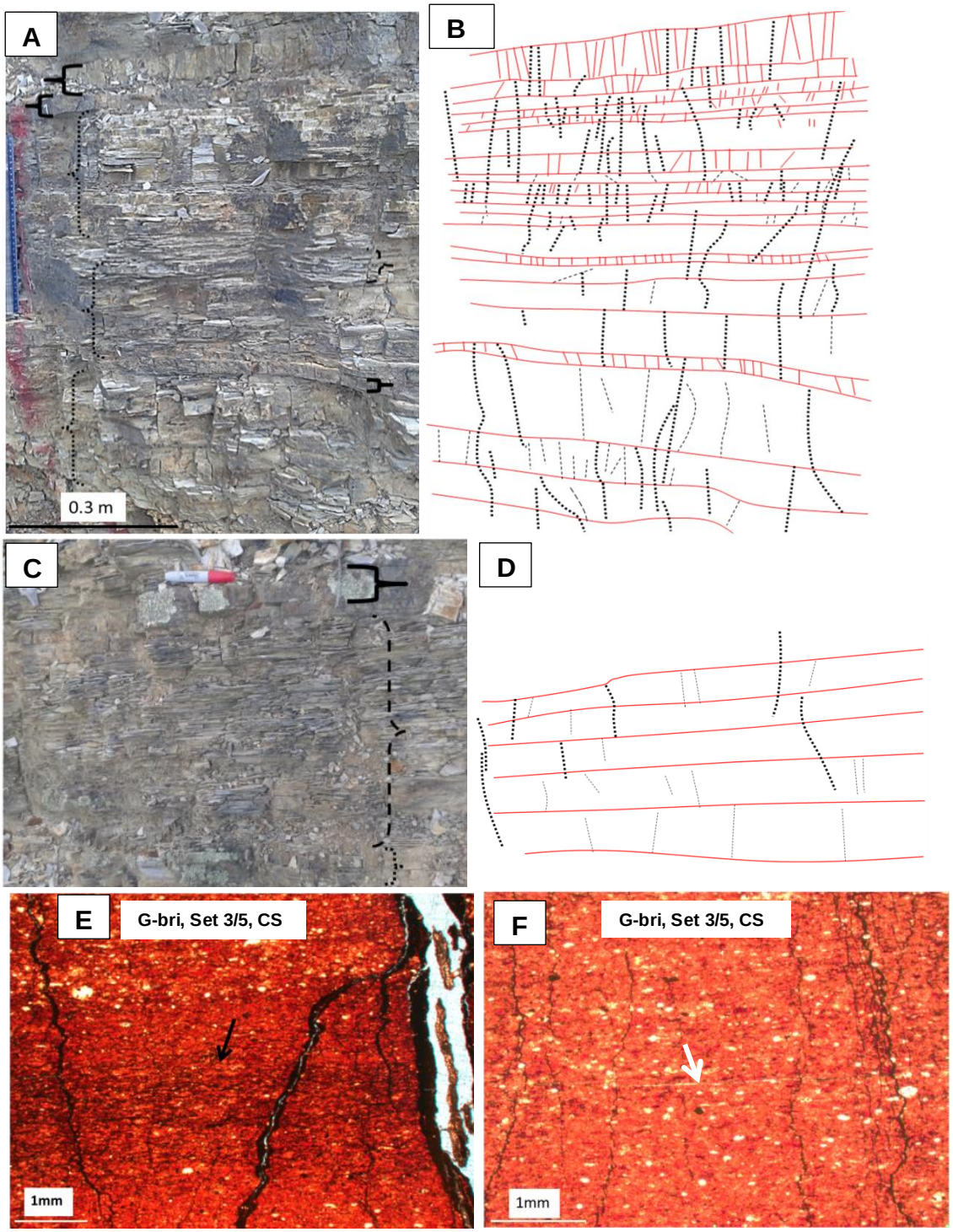

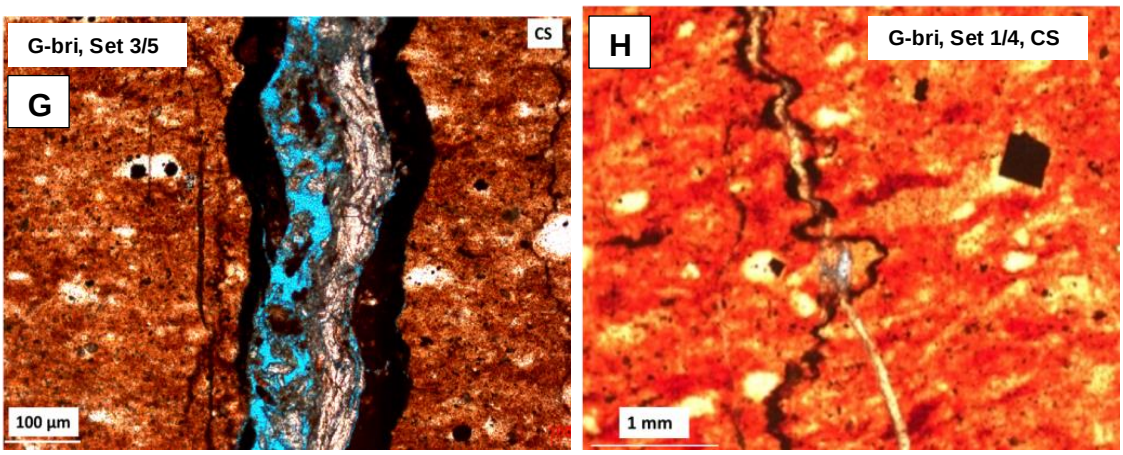

Figure 3.9: Outcrop and thin-section expressions of Zone 3. **A)** In dotted curly brackets are laminated siliceous-argillaceous, or argillaceous-siliceous mudstones. In solid curly brackets are cherts. In dashed curly brackets are laminated argillaceous mudstones. Foot long ruler is shown for scale. **B)** Bedding and fracture traces interpreted from A follow the same marking convention mentioned earlier. **C)** Thick continuous section of laminated argillaceous mudstones marked by dashed curly bracket. **D)** Demonstration of determining mechanical boundaries within the thick laminated mudstone section shown in Figure C. Within dashed curly brackets several fractures terminating at a similar elevation within the same thick section of laminated argillaceous mudstone beds define mechanical bed boundaries within the section. **E)** Thin section (PPL) showing a brittle bed with laminated texture of bed-parallel bitumen. Notice that the middle portion of the thin section is low in radiolarians and higher in organics (arrow). **F)** Thin section (PPL) of massive siliceous mudstone in the same thin section (G-bri). **G)** Thin section showing (PPL) fracture with sparry calcite cement in the middle precipitating in a previously bitumen-filled fracture. **H)** Thin section (PPL) of a calcite-filled planar fracture following a sinusoidal bitumen-filled fracture in ~ 50% of its length. **Note:** Arrow style is not related to those in Figure 3.5. **Abbreviations**: **BP**-looking at bedding planes, **CS**-looking at bed cross sections.

Zone 4 (Figures 3.3 and 3.10A) has variable degrees of dolomite in most beds, whether brittle or ductile when observed under thin sections. Figure 3.10B shows fracture traces. Figure 3.10C shows a thin section of a dolomitic bed. Figure 3.10D shows interlamination of two types of facies, one brittle and other ductile, both containing variable amounts of dolomite. In the quartz-rich, slightly dolomitic brittle beds of Zone 4 approximately 90% of the bed-perpendicular microfractures extending through brittle layers thin out in one or the other clay-rich thin bed but not exactly at the brittle-ductile boundary (Figure 3.10D). Thin section of a brittle bed is shown in Figure

3.10E. Micro to pseudosparry calcite-filled compacted fractures are also seen (Figures 3.10C and 3.10E). Bed-perpendicular fractures are all fully calcite-filled with one stage of growth. It is surprising that rarely any bed-perpendicular fracture in thin sections taken from brittle beds is partially or fully bitumen-filled, even though this zone is more organic rich compared to Zone 3. One reason could be that, by chance, only rock samples devoid of bitumen-filled bed-perpendicular fractures were picked for thin section analysis. However, the ductile bed thin-section fracture (if seen) could possibly have shown bitumen filled fractures. All the bed-parallel fractures in this zone, however, are filled with bitumen (similar to that in Figure 3.8H), and most terminate against or go through calcite-filled bed-perpendicular fractures and thin out later. In the dolomite-rich bed thin section (Figure 3.10C), neither sinusoidal nor bitumen-filled fractures were present. Fractures are mainly calcite-filled, which is probably due to proximity to the Hunton Limestone or the presence of carbonates in the matrix itself. In clay/organic-rich beds, no microfractures are visible (Figure 3.10F).

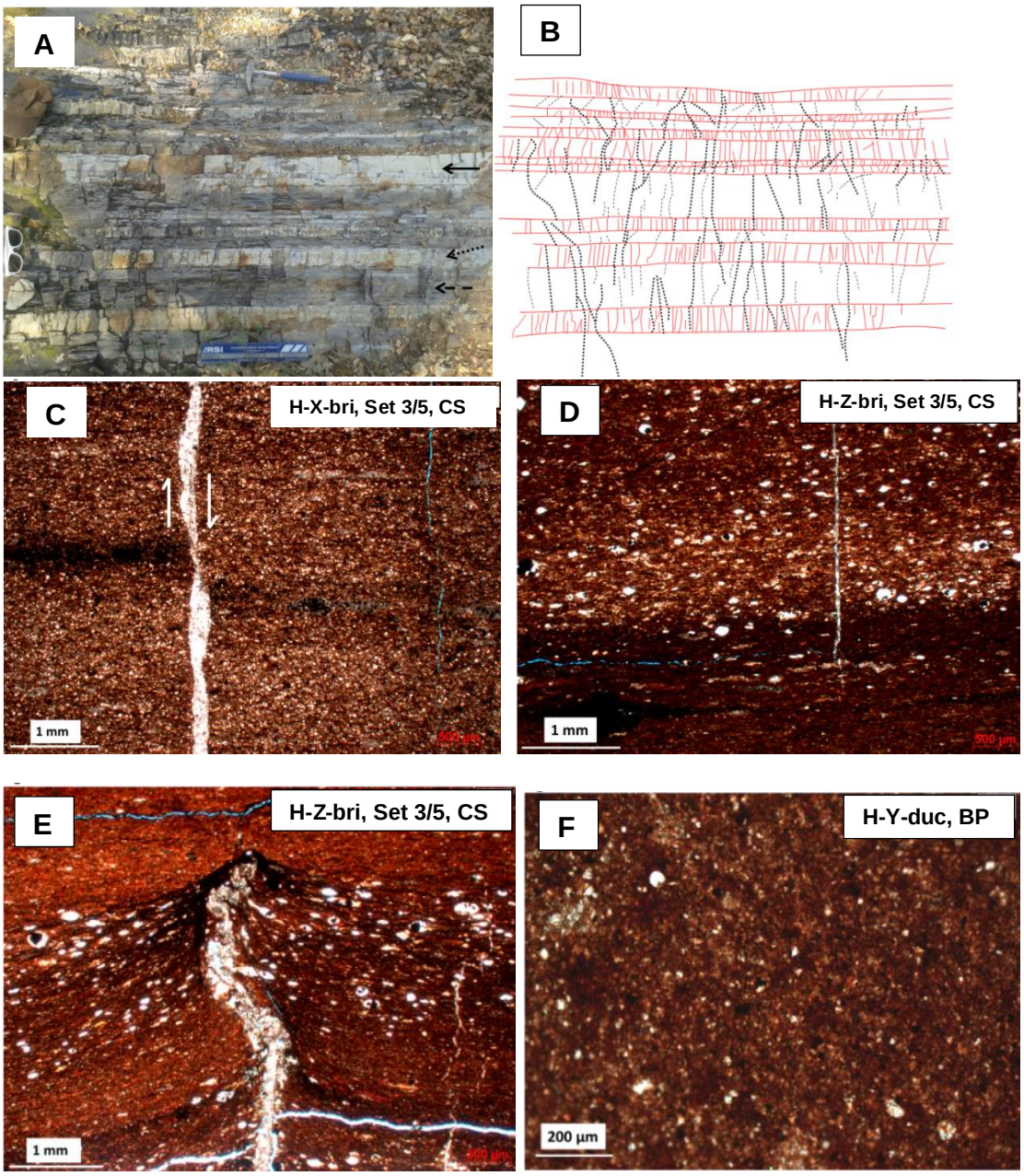

Figure 3.10: Outcrop and thin-section expressions of Zone 4. **A)** Solid, dotted and dashed arrows show the three beds in Zone 4 whose thin sections are shown in C, D, E, and F respectively. Arrow styles are not related to those in Figure 3.5, i.e., they do not depict fracture sets. **B)** Bedding and fracture traces interpreted from A. **C)** Thin-section expression (PPL) of the massive dolomitic mudstone (chert) facies. Fracture is calcite-filled. **D)** Thin-section expression (PPL) of interbeds of laminated carbonaceous, argillaceous mudstone and siliceous-dolomitic mudstone facies. The round objects are mostly quartz-filled radiolarians. Fracture is calcite-filled and terminates in an organic-rich area. **E)** Thin-section expression (PPL) of early calcite fill in a fracture (or probably a burrow) leading to differential compaction. **F)** Thin-section expression (PPL) of the laminated argillaceous, slightly dolomitic mudstone facies. Shiny crystals are a mix of

quartz and dolomite. **Abbreviations**- **BP**: looking at bedding planes, **CS**: looking at bed cross sections.

Table 3.2 summarizes the observations in different zones. In Zone 3, and to some extent Zone 4, bitumen-filled fractures are largely sinusoidal while in the other zones this is not the case. In the beds with large quantities of dolomite (mainly Zone 4), the cement is only calcite in bed-perpendicular fractures in both set groups.

Overall, fractures with non-bitumen cement are largely planar. Bed-parallel fractures can have either bitumen or non-bitumen cement with no particular spatial trends. Fractures with only bitumen outnumber the fractures with only silica fill. However, bitumen fill with later silica fill is sometimes seen. Bed-parallel fracture terminations at bed-perpendicular ones are common. However, bed-perpendicular fractures terminating at bed-parallel ones are rarely seen. Fracture terminations at layer boundaries are less common compared to the fractures terminating within a thin bed because, in most cases of collected thin sections, the layer boundaries are gradational or not clear.

Table 3.2: Fracture termination, porosity, fill, and shape characteristics in the Arbuckle Wilderness Outcrop. **Abbreviations**: "-": not applicable or not seen; **WL:** fractures terminate within a layer; **LB:** fractures terminate at a layer boundary; **CC-BE:** cement (non-bitumen, i.e., quartz or calcite) in center and bitumen at the edges. Percent occurrence of each characteristic is also shown if possible. Otherwise, terminologies such as rare, few, some, and most are used. **Rare:** at least 1-2 cases seen but very difficult to find; **Few:** more than a couple of cases visible but not common; **Some:** fairly common but not a majority; **Most:** > 60% cases. In the thin-section observations, **narrow** means narrower size of microfractures and **wide** fractures mean wider size of microfractures and narrower macrofractures.

Beds	Frac.	Frac fill								Frac shape	
		At bed ∥ frac.	At bed ⊥ frac.	WL	LB	Bitumen only	Silica only	CC-BE	Calcite/dolomite only	Sinusoidal	Planar/straight
Zone 1, Set 1/4, A- bri	Bed ⊥ frac	-	-	Most	Few	Most (narrow fr.)	Some (wide fr.: chalcedonly fill)	-	-	0-5%	95-100%
	Bed ∥ frac	-	-	-	-	-	-	-	-	-	-
Zone 2, Set 1/4, C-bri	Bed ⊥ frac	Few	-	Few	Most	All	-	-	-	~15%	~85%
	Bed ∥ frac	-	Most	-	-	All	-	-	-	Few	Most
Zone 2, Set 3/5, E-bri	Bed ⊥ frac	-	-	85%	15%	Most	Few	Few (quartz at center)	-	~10%	~90%
Zone 3, Set 1/4, G-bri	Bed ⊥ frac	Rare	Few planar fr. terminate at sinusoidal ones	90-100%	Boundaries not common	~90%	-	Few (wide fr. only, calcite at center)	Few (wide fr. only)	>90%	Few
	Bed ∥ frac	-	Most	-	-	Some	-	-	Some	-	All
Zone 3, Set 3/5, G-bri	Bed ⊥ frac	Few	-	80%	10%	~90%	-	Some wide fr. (calcite at cemter)	Rare	~90%	Few
	Bed ∥ frac	-	Most	-	-	Rare	-	-	Most	-	All
Zone 4, Set 3/5, H-X-bri	Bed ⊥ frac	-	-	Not clear	Not clear	-	-	-	All	-	All
Zone 4, Set 3/5, H-Z-bri	Bed ⊥ frac	-	-	~90%	~10%	-	-	Rare (calcite at center)	>95%	Rare	>95%
	Bed ∥ frac	-	~25%	~75%	-	All	-	-	-	All moderately sinusoidal	Rare

3.4.4 US-77D fracture fills from thin sections

In the thin sections, fractures partially or fully filled with clay and/or quartz are a common occurrence. Heavily gypsum-filled fractures and bedding planes were observed at one spot on the western side of the exposed wall. Set 5 (likey) or Set 3 clay-filled fractures invading a Set 1 bitumen-filled fracture is shown in (Figure 3.11A). Figure 3.11B shows an organic devoid area near a Set 1 fracture wall suggesting organic-rich matrix near the fracture wall as a source of the escaped oil. Figures 3.11C and 3.11D shows a fault zone and corresponding thin section respectively with four distinct colors indicating fault gouge, quartz, organic-rich matrix, and migrated oil. Overall, the majority of the observed microfractures (< 0.05 mm) in the US-77D are bitumen-filled.

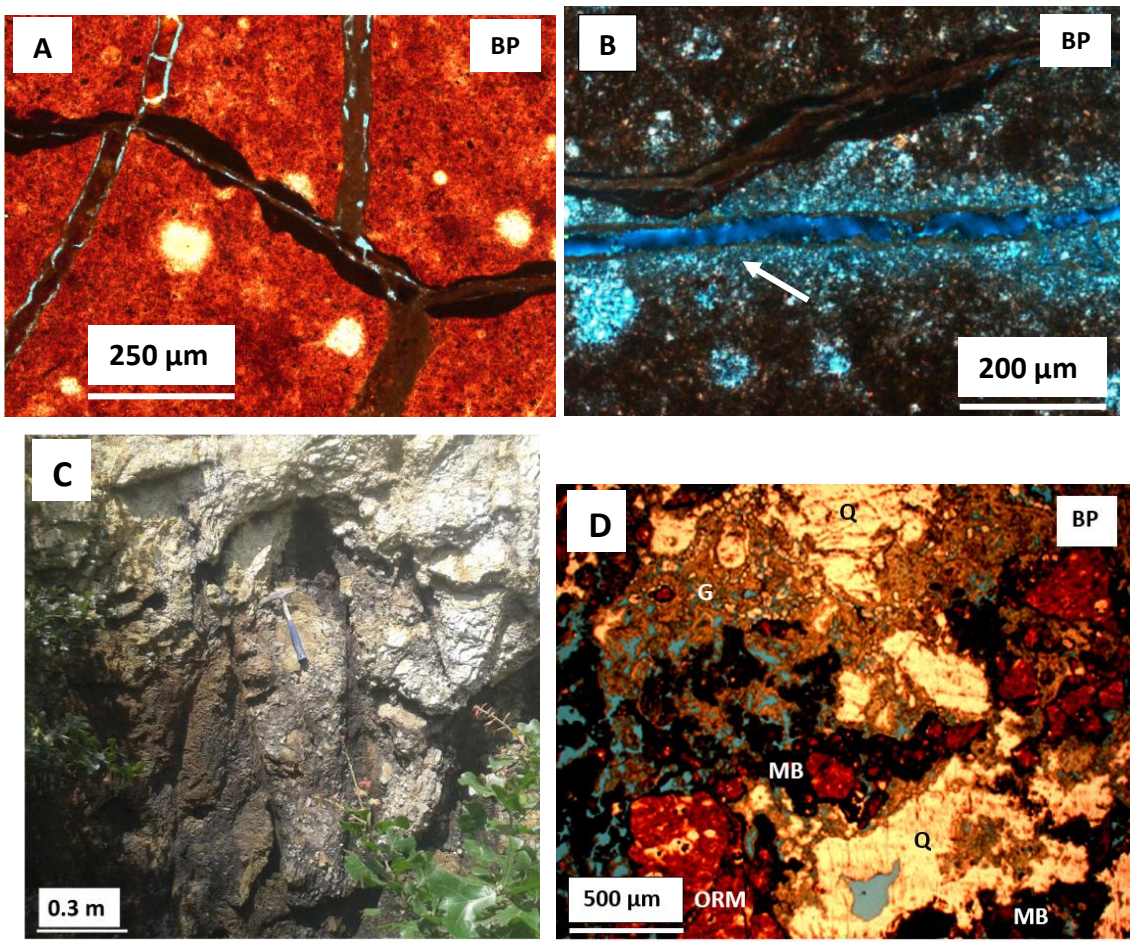

Figure 3.11: Thin section and outcrop photographs from the lower Woodford wall at the US-77D Outcrop. **A)** Thin section (PPL) showing older bitumen-filled bed-perpendicular Set 1 fracture invaded by younger clay-filled Set 5 (likely) or 3 bed-perpendicular fractures in the US-77D Outcrop. **B)** Thin-section (CPL) expression of an organic devoid area near fracture wall. Above this fracture is another fracture with clay (center of fracture) and bitumen (near the walls). **C)** Bitumen-rich areas within a shear zone. **D)** Thin-section (PPL) expression of the shear zone. **Abbreviations**- **G**: gouge, **MB**: matured bitumen, **ORM**: organic-rich matrix, **Q**: quartz. **CS**: thin sections showing bed cross section, **BP**: thin section showing the top of a bedding plane.

3.4.5 Outcrop fracture intensity and stratigraphic fracture density

Increasing macrofracture densities with decreasing bed thickness were seen in all zones and both brittle and ductile beds. As mentioned earlier, eight fracture density-bed thickness trends were developed (Figures 3.12A through 3.12H). Availability of thicker beds for intensity measurements increases confidence in the intensity-bed

thickness relationship (Figures 3.12A, 3.12C, 3.12E, 3.12F, and 3.12H). In the majority of cases, there is higher scatter and higher slope for brittle bed data. In Zone 1 (Figures 3.12A and 3.12B), the mudstone beds measurements are clustered between 2-5 cm bed thicknesses because most beds fall within this thickness range. The slopes of the curve fits show the sensitivity of fracture intensity to bed thickness. In Zone 2 Set 1/4 fractures, there is a greater change in the fracture intensity values with bed thickness represented by a high angle slope (Figure 3.12D). The slopes range between -0.69 to -4.18 for ductile and -1.01 to -9.04 for brittle beds. The regression lines reveal that at any given bed thickness, the fracture intensity values in the brittle beds are ~ 1.5-3 times that in the ductile beds.

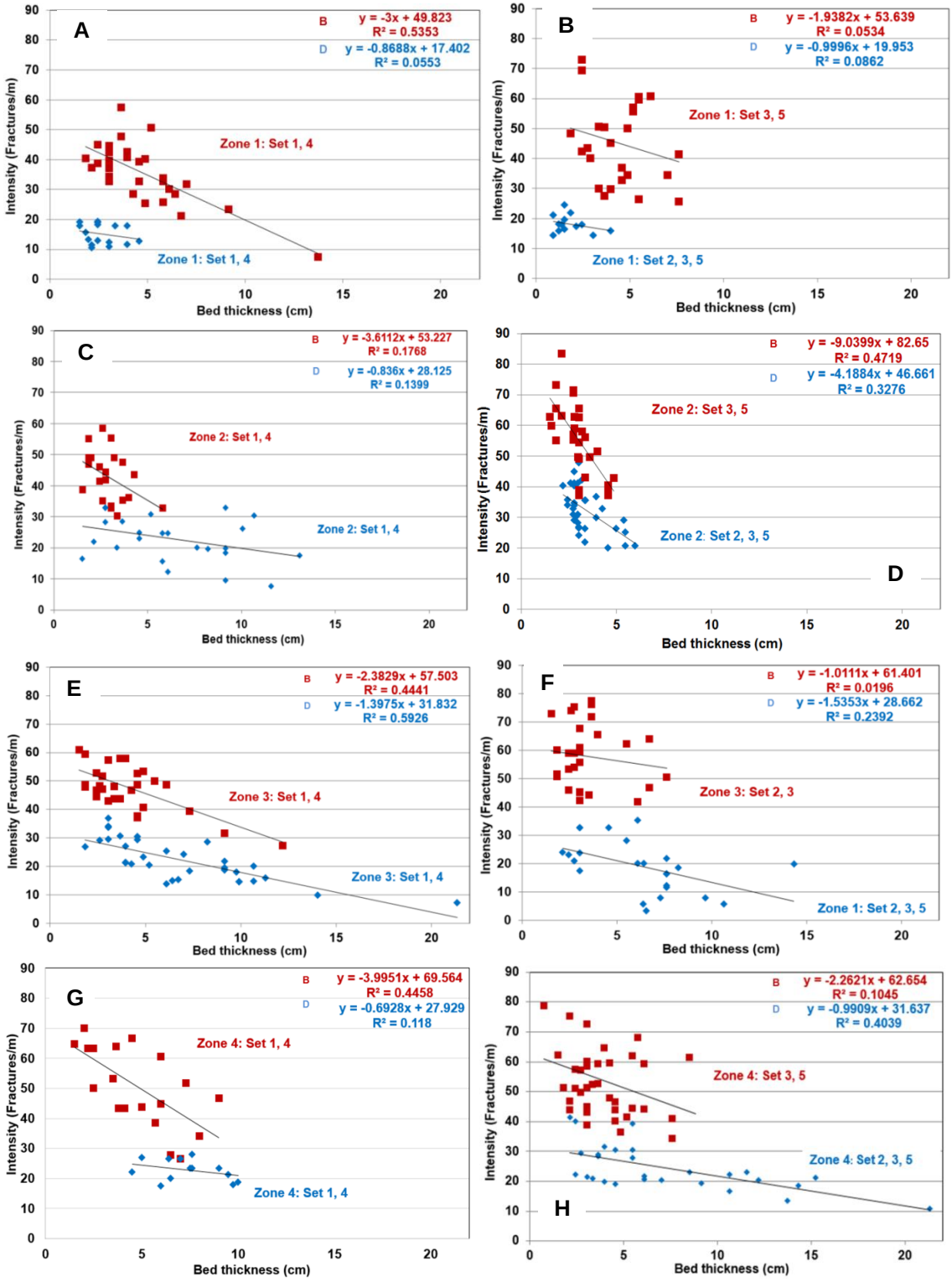

Figure 3.12: Variation in fracture intensity with bed thickness in the AWO. Larger squares and smaller diamonds show the brittle and ductile beds respectively. **A)** Zone 1 Set 1 and Set 4 fractures in the brittle and ductile beds. **B)** Zone 1 Set 3 and 5 fractures in the brittle beds; Set 2, 3, and 5 fractures in the ductile beds. **C)** Zone 2 Set 1 and Set 4 fractures in the brittle and ductile beds. **D)** Zone 2 Set 3 and 5 fractures in the brittle

beds; Set 2, 3, and 5 fractures in the ductile beds. **E)** Zone 3 Set 1 and Set 4 fractures in the brittle and ductile beds. **F)** Zone 3 Set 3 and 5 fractures in the brittle beds; Set 2, 3, and 5 fractures in the ductile beds. **G)** Zone 4 Set 1 and Set 4 fractures in the brittle and ductile beds. **H)** Zone 4 Set 3 and 5 fractures in the brittle beds; Set 2, 3, and 5 fractures in the ductile beds. Results from all measurable beds in Zone 4 are shown. **Abbreviations- B**: brittle, **D**: ductile (more + less ductile).

Upon calculation of the stratigraphic fracture densities (P20), three high-density areas within Zone 1, middle of Zone 2, lower Zone 2, and almost the entire Zone 3 is seen (Figure 3.13, Column 5). Column 5 shows the P20 values of the two set groups (Sets 2, 3, 5 [red] and Sets 1, 4 [dashed black]). The fracture densities of the two groups overlap at most places except Zone 3 and some parts of Zone 4. This similarity in fracture density between these two set groups is not apparent on direct bed face observations. Low GR values in Zone 1 is due to a much lower number of organic-rich argillaceous mudstones compared to chert beds. The fracture density is the lowest between 64-75 m (~ 210-245 ft) where there is a peak in the GR value.

Within curly brackets in Column 5, not all points have high fracture densities. However, the curly brackets represent a large number of high fracture density peaks and have an average of nearly 150 fractures/ft^2 (fractures/0.093 m^2). Further subdivision of high-density areas is possible within the curly bracketed areas depending on the interpreter. The high fracture density area in Zone 1 (column 5: red curly bracket) correlates to the low percentage of ductile beds (Column 2: red curly bracket [~ 25% on average]) or a high percentage of brittle beds per stratigraphic foot. The high fracture density area in the middle of Zone 2 (column 5: green curly bracket), is situated in areas with low thickness of ductile (average ~ 3-5 cm [~ 0.1-0.16 ft]) and brittle (average ~ 2.5 cm [~ 0.08 ft]) beds (Column 3: red and green curly brackets, Columns 4: black curly bracket). Most of the high fracture density area in the lower Zone 2 and entire

Zone 3 (column 5: black curly bracket) are situated in areas with lower percentage (~ 50% on average) of ductile beds (Column 2: green, purple, and brown curly brackets), low thickness (average ~ 5 cm [~ 0.16 ft]) of ductile beds (Column 3: orange curly bracket), and low thickness (average ~ 3 cm [~ 0.1 ft]) of brittle beds (Column 4: black curly bracket). Average bed thicknesses of both brittle and ductile beds are higher in Zone 4 compared to other zones leading to lower fracture densities.

Plotting GR values vs. calculated fracture density reveals a weak negative correlation between the two parameters (Figure 3.14). However, there is a considerable scatter from the best-fit line represented by a low R^2 value of 0.0119.

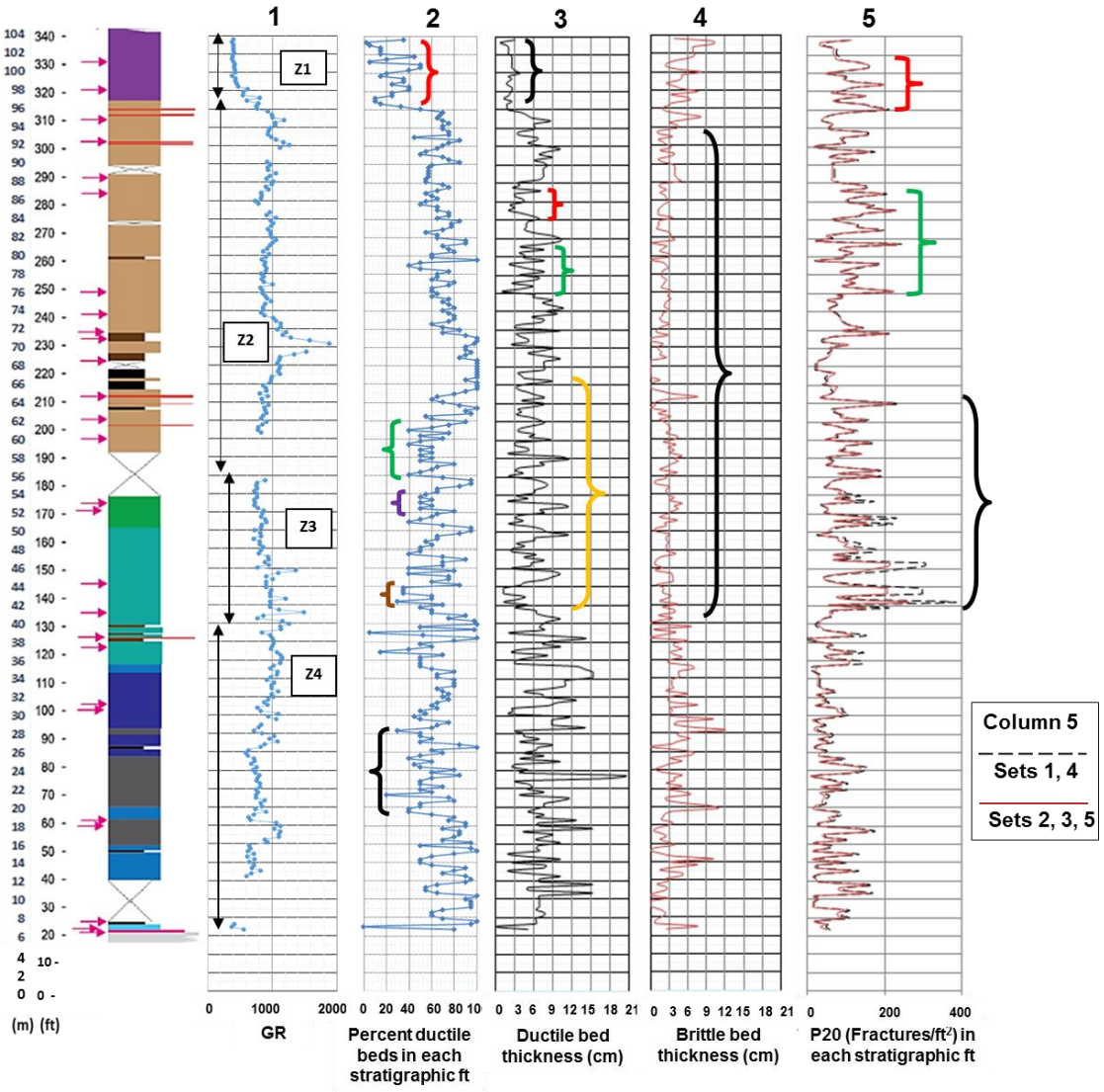

Figure 3.13: Stratigraphic summary along the entire section of the AWO. On the left are the stratigraphic height in meters and feet, and the lithologic column (shown earlier in Figure 3.3). Pink arrows to the left of the lithologic column show intervals from which thin sections were analyzed for lithologic description. Column 1 shows the GR log and the four zones (similar to Figure 3.3). Column 2 shows the percent stratigraphic height occupied by the ductile beds in each 1 ft interval. Intervals with a relatively small percentage of these beds are shown in curly brackets. Columns 3 and 4 show the average bed thicknesses of the ductile and brittle beds respectively in each 1 ft interval. Intervals with relatively low bed thicknesses are bracketed. Column 5 shows the number of fracture traces, including both brittle and ductile beds, in each 1 ft x 1 ft (0.305 m x 0.305 m) interval (P20: areal density). Regions with a relatively higher number of high fracture density peaks are shown in curly brackets.

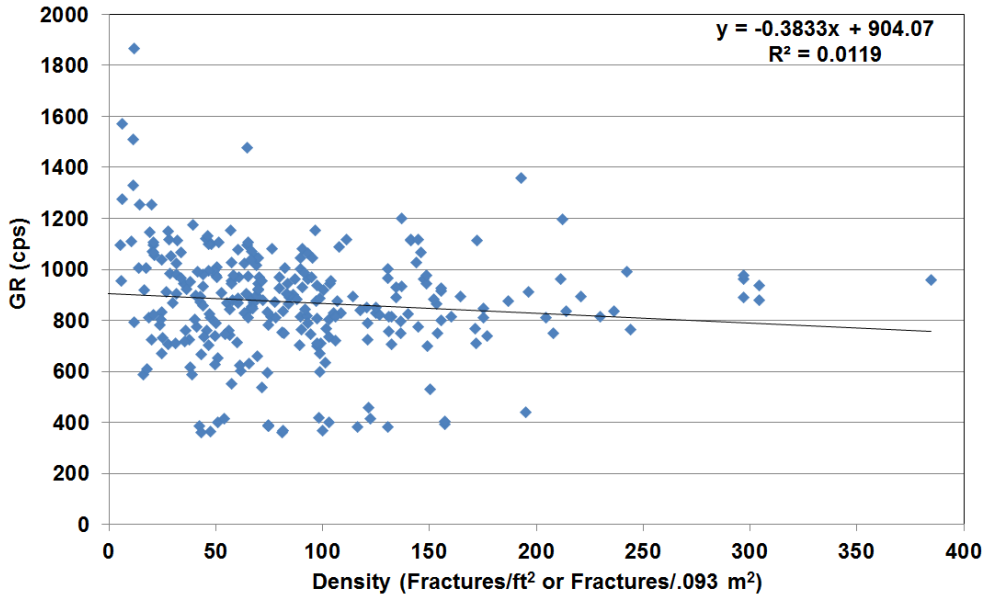

Figure 3.14: Fracture areal density (P20) vs. GR values for each stratigraphic foot of the AWO. Notice the gentle negative slope and a low R^2 value.

3.4.6 Fracture size and spacing

3.4.6.1 Aperture size and spacing

Most fractures opening displacements (kinematic apertures) measured at the outcrop fall in the ~ 0.05-1 mm (0.000164-0.00328 ft) range. Only brittle beds were used because of intact (not eroded or partially obscured) fracture presence. Exponential aperture distribution (characteristic distribution) is exhibited in most cases (Table 3.3 and Figures 3.15A, 3.15C, 3.15D through 3.15G, 3.15I, 3.15K, and 3.15L). This is true for both micro and macrofractures. However, other distributions such as lognormal (Table 3.3 and Figure 3.15B, 3.15J, 3.15M through 3.15P) distributions and power-law distributions (3.14H and 3.14Q) are also seen. Both exponential and lognormal distributions are characteristic size distributions (Hooker et al., 2014). The spacing between adjacent fractures is mostly uniform, indicated by $C_v < 1$ in all cases of outcrop scanlines (Table 3.3). In other words, fracture clustering was not observed in macrofractures. $C_v > 1$ was seen of all microfractures. No bed-parallel macrofractures were clearly visible, i.e., only bed-parallel microfractures (< 0.05 mm) were observed. Spots 1 and 2 (not shown on the outcrop photograph) in the US-77D mentioned in

Figures 3.15M through 3.15Q are two spots in the US-77D outcrops from where measurements were taken.

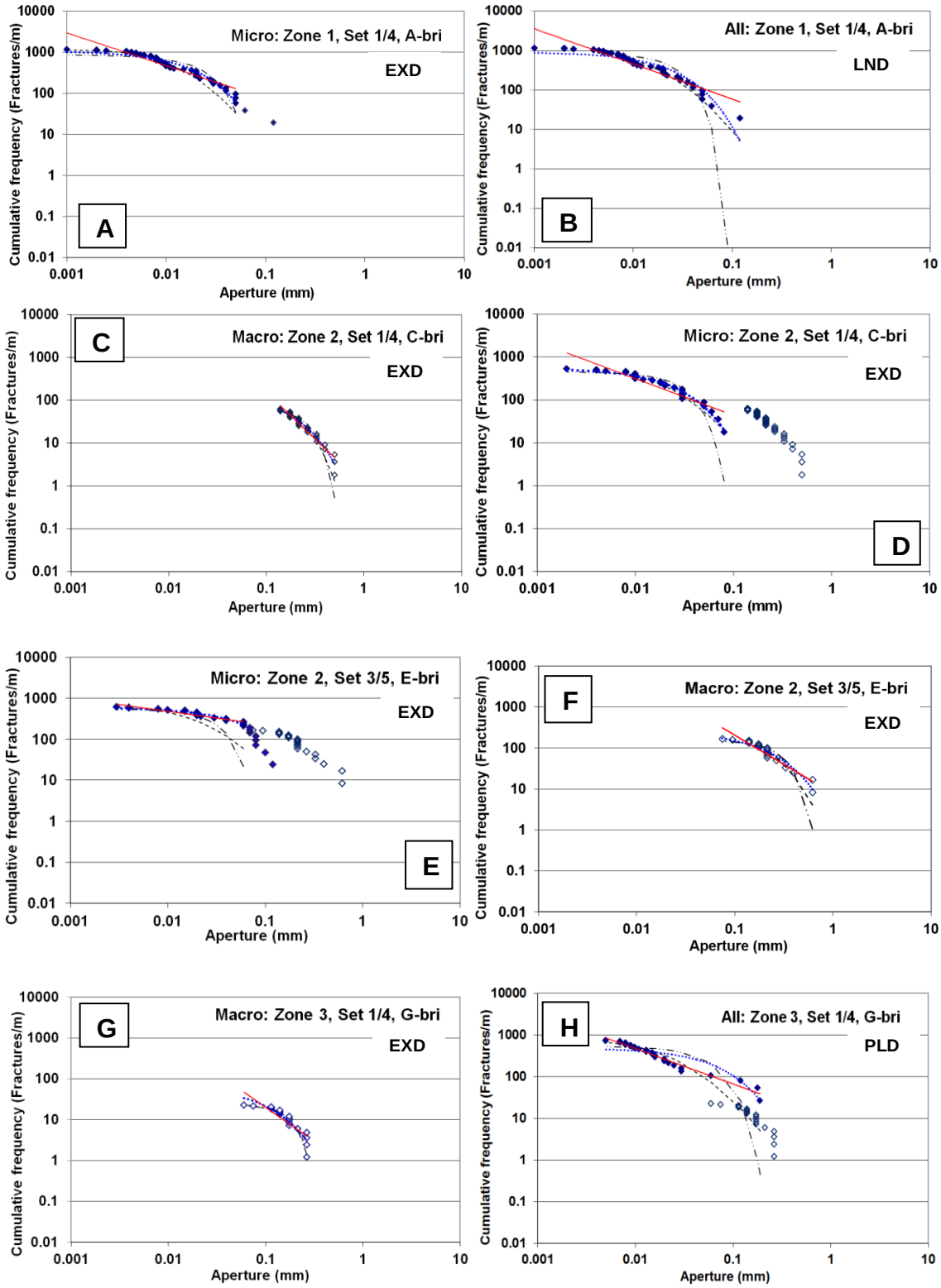

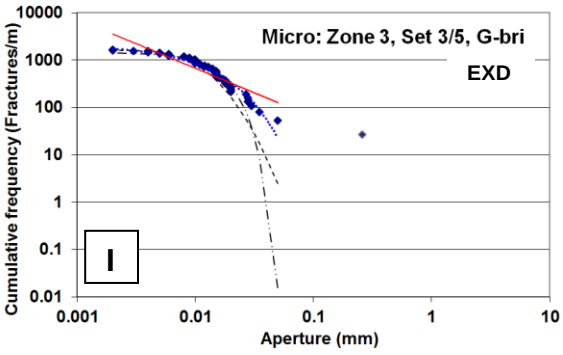
I
Micro: Zone 3, Set 3/5, G-bri
EXD
Cumulative frequency (Fractures/m)
Aperture (mm)
10000
1000
100
10
1
0.1
0.01
0.001
0.01
0.1
1
10

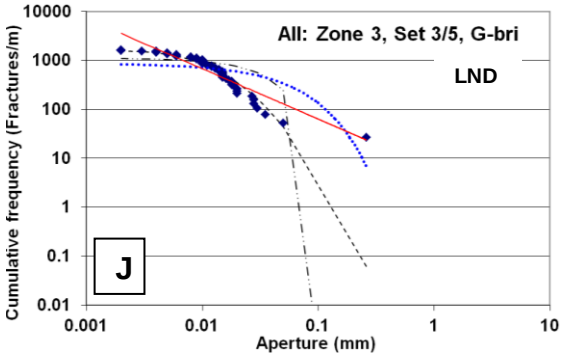
J
All: Zone 3, Set 3/5, G-bri
LND
Cumulative frequency (Fractures/m)
Aperture (mm)
10000
1000
100
10
1
0.1
0.01
0.001
0.01
0.1
1
10

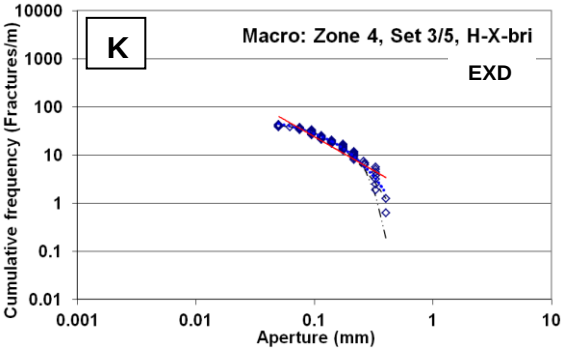
K
Macro: Zone 4, Set 3/5, H-X-bri
EXD
Cumulative frequency (Fractures/m)
Aperture (mm)
10000
1000
100
10
1
0.1
0.01
0.001
0.01
0.1
1
10

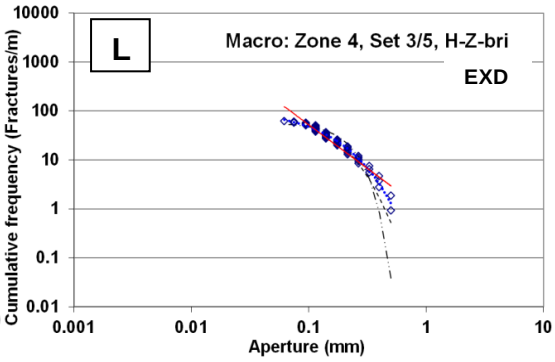
L
Macro: Zone 4, Set 3/5, H-Z-bri
EXD
Cumulative frequency (Fractures/m)
Aperture (mm)
10000
1000
100
10
1
0.1
0.01
0.001
0.01
0.1
1
10

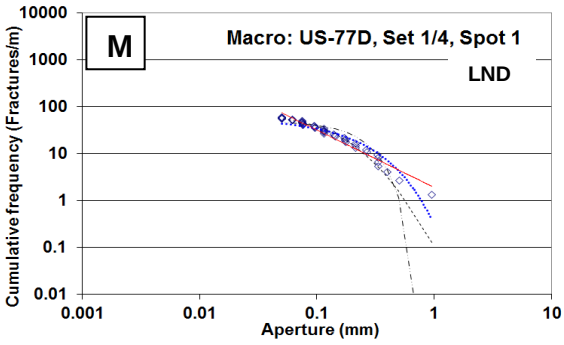
M
Macro: US-77D, Set 1/4, Spot 1
LND
Cumulative frequency (Fractures/m)
Aperture (mm)
10000
1000
100
10
1
0.1
0.01
0.001
0.01
0.1
1
10

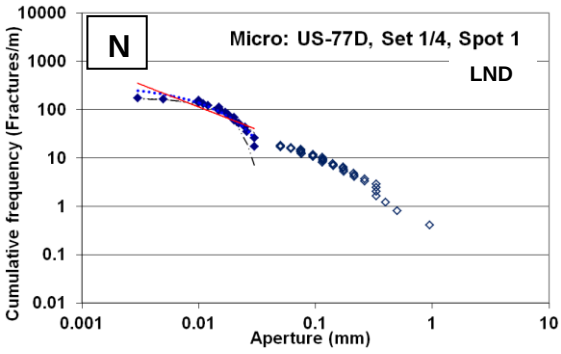
N
Micro: US-77D, Set 1/4, Spot 1
LND
Cumulative frequency (Fractures/m)
Aperture (mm)
10000
1000
100
10
1
0.1
0.01
0.001
0.01
0.1
1
10

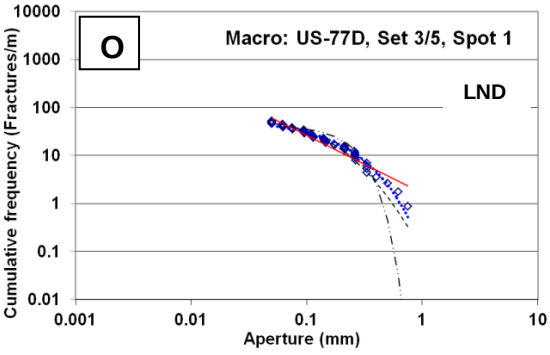
O
Macro: US-77D, Set 3/5, Spot 1
LND
Cumulative frequency (Fractures/m)
Aperture (mm)
10000
1000
100
10
1
0.1
0.01
0.001
0.01
0.1
1
10

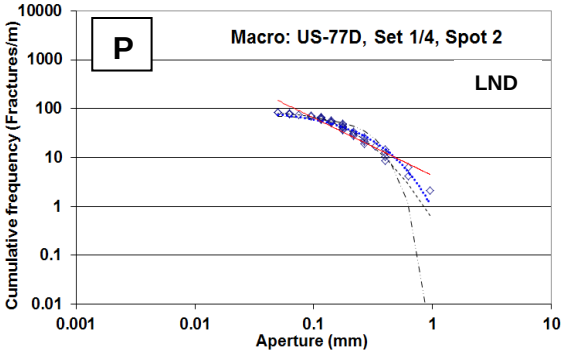
P
Macro: US-77D, Set 1/4, Spot 2
LND
Cumulative frequency (Fractures/m)
Aperture (mm)
10000
1000
100
10
1
0.1
0.01
0.001
0.01
0.1
1
10

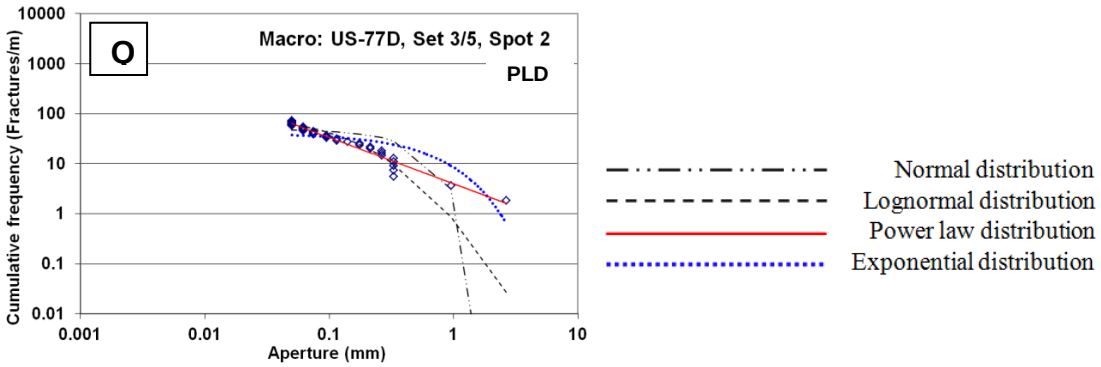

Figure 3.15: Cumulative-frequency distribution of macrofractures, microfractures or both (all) at the same time (in same thin section). Diamond shapes are the points which are fitted with different lines. Solid diamonds are apertures measured in a microscope. Open diamonds are fractures measured directly on the outcrops. Macro (Figures **C**, **F**, **G**, **K**, **L**, **M**, **O**, **P**, and **Q**), micro (Figures **A**, **D**, **E**, **I**, and **N**) and "all" fractures are mentioned in the graphs. In the "all" graphs (Figures **B**, **H**, and **J**), both the macro and microfractures statistical analysis are put together using the same regression line because both macro and microfractures were seen in the same thin section (i.e., on the same scanline). Best fit cumulative distributions (**EXD**: exponential; **LND**: lognormal, **PLD**: power-law) are mentioned in the figures. Notice that the number of macrofractures range between 10 and 50 fractures/m. While ~ 1000-2000 microfractures/m exist.

Table 3.3: Natural fracture parameters obtained from the Arbuckle Wilderness Outcrop. All values belong to direct observations in particular beds or thin sections obtained from these beds. The number of fractures (**NF**) used to calculate the parameters for both macro and microfractures are given individually. Macrofracture apertures were not measured on all beds mentioned due to lack of suitable fractures for that purpose. **Abbreviations- FS:** fracture aperture-size classification, **ND:** normal distribution χ^2 error, **LND:** lognormal distribution χ^2 error, **PLD:** power-law distribution χ^2 error, **EXD:** exponential distribution χ^2 error **(**distribution showing the lowest χ^2 error [best fit] is in bold),, **PLD exp**: exponent of the power-law distribution. **EXD exp**: exponent of the exponential distribution. **NF**: number of fractures, **AA**: average fracture aperture (mm), $\mathbf{C_v}$: coefficient of variation, **AS**: average fracture spacing (cm), **GR:** gamma ray (cps), **FD**: macrofracture density of the specific bed on which macrofracture apertures were measured (fractures/m), **BT**: bed thickness of the specific bed on which the macrofracture linear intensities were measured (cm).

		Bed-perpendicular fractures												**Bed-parallel fractures**			
Beds	**FS**	**ND**	**LND**	**PLD**	**EXD**	**PLD exp**	**EXD exp**	**NF**	**AA**	**C_v**	**AS**	**GR**	**BT**	**NF**	**AA**	**C_v**	**AS**
Zone 1, Set 1/4, A-bri	**Mac.**	-	-	-	-	-	-	2	0.09	-	-	440	-	-	-	-	-
	Mic.	2053	900	2497	**860**	-0.8	-58	58	0.01	1.07	0.081	-	-	-	-	-	-
	All	$6.4*10^6$	**400**	3516	1861	-0.89	-44	60	-	-	-	-	-	-	-	-	-
Zone 2, Set 1/4, B-bri	**Mac.**	-	-	-	-	-	-	3	0.34	-	-	610	1.3	-	-	-	-
	Mic.	-	-	-	-	-	-	2	0.018		-	-	-	-	-	-	-
	All	-	-	-	-	-	-	-	-	-	-	-	-	-	-	-	-
Zone 2, Set 3/5, B-bri	**Mac.**	-	-	-	-	-	-	2	0.25	-	1.8	610	1.3	-	-	-	-
	Mic.	-	-	-	-	-	-	-	-	-	-	-	-	-	-	-	-
	All	-	-	-	-	-	-	-	-	-	-	-	-	-	-	-	-
Zone 2, Set 1/4, C-bri	**Mac.**	102	41	33	**15**	-2	-8	35	0.247	0.49	1.68	975	3.6	-	-	-	-
	Mic.	735	107	808	**88**	-0.86	-41	29	0.023	1.48	0.17	-	-	14	0.013	0.81	0.26
	All	-	-	-	-	-	-	-	-	-	-	-	-	-	-	-	-
Zone 2, Set 3/5, E-bri	**Mac.**	335	69	141	**46**	-1.4	-5.2	21	0.239	0.85	0.57	760	3.3	-	-	-	-
	Mic.	6975	2747	90	**40**	-0.33	-16	18	0.025	1.1	0.12	-	-	-	-	-	-
	All	-	-	-	-	-	-	-	-	-	-	-	-	-	-	-	-

		Bed-perpendicular fractures												Bed-parallel fractures			
Beds	**FS**	**ND**	**LND**	**PLD**	**EXD**	**PLD exp**	**EXD exp**	**NF**	**AA**	**C_v**	**AS**	**GR**	**BT**	**NF**	**AA**	**C_v**	**AS**
Zone 3, Set 1/4, G-bri	**Mac.**	15	8	30	**12**	-1.7	-11.8	19	0.167	0.41	1.39	900	5.5	-	-	-	-
	Mic.	-	-	-	-	-	-	-	-	-	-	-	-	-	-	-	-
	All	6009	955	**117**	1400	-0.85	-15.3	28	0.031	0.96	0.113	-	-	6	0.019	0.95	0.54
Zone 3, Set 3/5, G-bri	**Mac.**	-	-	-	-	-	-	1	0.26	0.44	1	900	5.5	-	-	-	-
	Mic.	$2*10^5$	3490	6389	**603**	-1.04	-90	61	0.013	1.63	0.057	-	-	5	0.036	1.05	0.95
	All	1013	**104**	6786	14221	-1.03	-19	62	-	-	-	-	-	-	-	-	-
Zone 4, Set 3/5, H-X-bri	**Mac.**	77	20	113	**15.3**	-1.4	-9.5	69	0.154	0.79	2.27	550	6.1	-	-	-	-
	Mic.	-	-	-	-	-	-	2	0.023	-	-	-	-	-	-	-	-
	All	-	-	-	-	-	-	-	-	-	-	-	-	-	-	-	-
Zone 4, Set 3/5, H-Z-bri	**Mac.**	212	41	100	**22**	-1.78	-8.9	66	0.177	0.47	1.51	550	5.5	-	-	-	-
	Mic.	-	-	-	-	-	-	9	0.017	0.85	0.29	-	-	8	0.018	1.6	0.51
	All	-	-	-	-	-	-	-	-	-	-	-	-	-	-	-	-
US-77D, Set 1/4, Spot 1	**Mac.**	$6.2*10^4$	**27.7**	37	60	-1.22	-5.2	45	0.168	0.58	1.67	-	3	-	-	-	-
	Mic.	105	**29.3**	298	47.2	-0.94	-82	19	0.016	1.3	0.188	-	-	-	-	-	-
	All	-	-	-	-	-	-	-	-	-	-	-	-	-	-	-	-
US-77D, Set 3/5, Spot 1	**Mac.**	995	**23.1**	51	26	-1.2	-6.2	60	0.164	0.63	1.84	-	3	-	-	-	-
	Mic.	-	-	-	-	-	-	1	0.01	-	-	-	-	-	-	-	-
	All	-	-	-	-	-	-	-	-	-	-	-	-				
US-77D, Set 1/4, Spot 2	**Mac.**	1800	**19**	140	33	-1.18	-4.7	40	0.223	0.51	1.15	-	1.5	-	-	-	-
	Mic.	-	-	-	-	-	-	1	0.006	-	-	-	-	-	-	-	-
	All	-	-	-	-	-	-	-	-	-	-	-	-	-	-	-	-
US-77D, Set 3/5, Spot 2	**Mac.**	$8*10^6$	163	**21**	318	-0.92	-1.56	40	0.216	0.73	1.47	-	1.5	-	-	-	-
	Mic.	-	-	-	-	-	-	-	-	-	-	-	-	-	-	-	-
	All	-	-	-	-	-	-	-	-	-	-	-	-	-	-	-	-

3.4.6.2 Length aperture relations from US-77D

Except for Figure 3.16B, all other figures (3.16A, 3.16C, 3.16D) show a power-law curve best fit. In Figure 3.16B, the linear regression value fit is pretty close to the power-law regression value. Power-law exponents range 0.53-0.59.

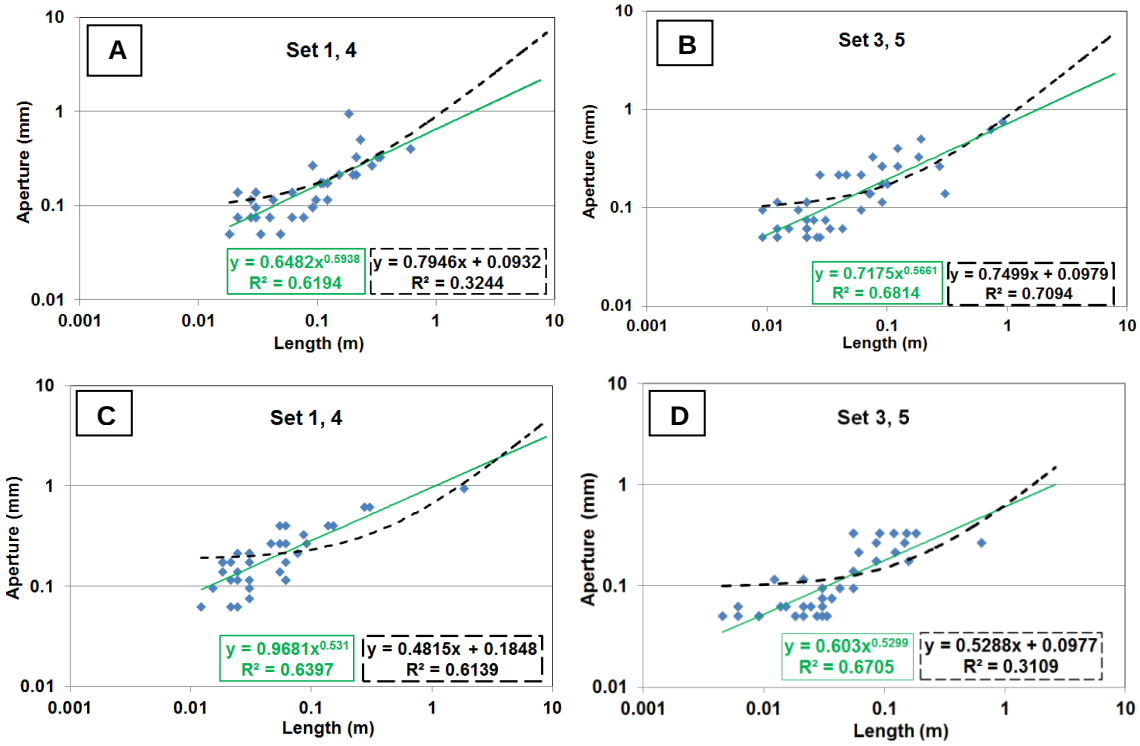

Figure 3.16: Fracture aperture-length relations from the US-77D Outcrop. **A)** Log-log plots of Set 1 and/or Set 4 fractures. **B)** Log-log plots of Set 3 and/or 5 fractures. **C**) Log-log plots of Set 1 and/or 4 fractures. **D)** Log-log plots of Set 3 and/or 5 fractures. Dashed line (black): linear fit; solid line (green): power-law fit.

3.5 Discussion

3.5.1 Fracture origin timing

In the AWO, in most cases, the presence of similar material in the cement (bitumen or calcite) as the matrix indicates that the cement was likely locally derived from the matrix or not too far from the cement deposition site. In the upper Woodford, apart from bitumen, most of the fractures are clay or quartz-filled. In the lower

Woodford apart from bitumen, most fractures are filled with calcite/dolomite in the AWO. Clay filled Set 5 fractures are present in the lower Woodford (Figure 3.11A), which could have been derived from a clay-rich bed. Evidence of bitumen derived from the adjacent matrix of Set 1 fractures exist in the US-77D (lower Woodford Shale wall) (Figure 3.11B). This observation suggests conversion of organics near the fracture wall into bitumen and escape through the Set 1 fractures.

The sinusoidal shape of bitumen-filled fractures in the AWO is partly due to their circumscribing the rigid quartz grain boundaries. However, part of the sinusoidal (wiggly) in shape may indicate early opening and subsequent vertical compaction. Evidence of early vertical compaction exists, such as the buckled fracture in Figure 3.10E and compacted bitumen-filled fractures (3.9E and 3.9F). It is also possible that few of these early compacted fractures gained a more stylolite-like shape due to later fracture-wall perpendicular horizontal compression (3.8G and 3.9H). Whether stylolitic or sinusoidal/compacted, the narrow, sinuous fractures are almost entirely bitumen-filled.

However, not all bitumen-filled fractures are sinusoidal, especially in Zone 1 (narrow bitumen-filled fractures in Figure 3.7D) of the AWO, where mostly narrow and planar bitumen-filled fractures, which are presumably younger (compared to the compacted ones), exist. In the same photograph, wide chalcedony-filled fractures are shifted along some of these planar bitumen-filled fractures indicating that some wide, non-bitumen cemented, fractures originated before the planar bitumen-filled ones. Sinusoidal fractures were found in all zones, most located in thin sections of both Sets 1/4 and 3/5 from the lower part of Zone 3 with high organic/clay content (high total

GR). This indicates that during the early stage of compaction, there was lower horizontal differential stress leading to fractures striking in many directions.

In many cases, the later fracture growth nucleation sites have been provided by the initial bitumen-filled fractures. If an older bitumen-filled fracture is not too sinuous, younger cement or bitumen-filled fractures tend to follow their weak surfaces (Figures 3.8G and 3.9H). Probably imperfect sealing (by bitumen) led to later reactivation (Holland and Urai, 2010) when some cement (non-bitumen) filled fractures happened to originate too close to the sinusoidal/compacted fractures, and therefore, found an easier path through them. However, at sharp corners in the older fractures, the younger fractures crosscut the older ones (Figure 3.9H). Therefore, the presence of early bitumen-filled fractures, non-bitumen cement-filled fractures, and bitumen-filled planar fractures indicate that fractures of different fill and shape even though sub-parallel have originated at different geologic times. The early bitumen-filled sinusoidal/compacted fractures are roughly contemporary to the compacted/buckling fracture in Zone 4 suggesting calcite cement in the lower Woodford was deposited early. Quartz or calcite cement in the zones above was likely deposited later by reopening of the bitumen-filled sinusoidal/compacted fractures or by creating new fractures.

Two type of bed-parallel fracture fill were seen. Ones filled with bitumen, and others filled with calcite. Calcite-filled bed-parallel fractures were also seen in the MCQ (mentioned in Chapter 2). Most observed bitumen-filled bed-parallel fractures occurred away from any significant bed boundary (Figures 3.8F and 3.8H) rather than at a bed boundary (Figure 3.8E). The observed calcite-filled bed-parallel fractures occurred away from bed boundaries (Figure 3.9F). This again indicates at least two phases of

bed-parallel fracture generation/fill. The often observed bitumen-filled bed-parallel microfractures terminating at bed-perpendicular ones (which are also bitumen-filled), and their presence away from significant bed boundaries (Figure 3.8F), i.e., away from any weakness plane, indicates that the bed-parallel bitumen-filled ones originated (not reactivated bed boundaries) during the compression phase when the minimum stress was in a sub-vertical direction. This also implies that these bed-parallel fractures came into place when the Woodford Shale was still in the oil window. In rare cases, doglegging of planar bed-perpendicular bitumen-filled fractures on bed-parallel bitumen-filled ones (Figure 3.8H) is also seen, implying some bed-parallel bitumen-filled fractures could have originated before the bed-perpendicular bitumen-filled fractures. The calcite-filled bed-parallel fractures could have originated later (similar to the MCQ). It is also possible that the calcite-filled bed-parallel fractures could have originated when the beds were rotated to vertical, i.e., the bed-parallel fracture actually could have opened against the sub-horizontal stresses. The presence of bitumen migration, which probably happened after shearing of the Woodford Shale beds is shown by the high concentration of bitumen in the porous and permeable sheared zones in the US-77D (Figure 3.11D). The shearing probably happened before the origin of calcite-filled bed-parallel fractures based on the thin-section observations that bitumen migration happened before the calcite deposition in bed-parallel fractures.

Set 1, 2, and 3 macrofractures observed at the US-77D and AWO (Figure 3.5) were also observed at the McAlister Cemetery Quarry. Set 1 and 2 were also observed in the Wyche Shale pit, the Clarita Shale pit, and the Jennings Quarry (Hunton Group). These poles to these fracture planes plot at similar spots after bed restoration. Set 1

fractures strike approximately E-W, Set 2 strike NE-SW, Set 3 strikes NW-SE. Set 3 fractures at the US-77D and the AWO are equivalent to Set 3P (Set 3 planar) fractures in the McAlister Cemetery Quarry (MCQ). Set 3S observed at the MCQ were not clearly observed at the AWO or MCQ.

Set 4 (fold related) fractures are fold parallel and observed at US-77D (Figure 3.6D), AWO (Figure 3.6H), and MCQ (Figure 2.6H) plot within the first quadrant of the stereonet after bed restoration, but not at the same location because folds strike in variable directions at different locations. Set 5 fractures, which are also fold related and sub-perpendicular to the fold strike, are prominent in the AWO and US-77D. These fractures were not seen in any of the outcrops discussed in the previous chapters. Both Sets 4 and 5 are likely related to the stress and strain generated during the mid-Virgilian Arbuckle Orogeny due to excessive tilting or overturning. At the microfracture scale, early bitumen-filled Set 1 fractures were later crosscut by clay-filled Set 3 or 5 fractures (Figure 3.11A). This confirms the early origin of Set 1 fractures, which was determined by the presence of crosscutting and bitumen fill in the McAlister Cemetery Quarry.

3.5.2 Fracture size and spacing

Mostly characteristic aperture cumulative-frequency distributions were observed. This is true for both micro- and macrofractures. Also, fracture cement observed in thin sections are either bitumen, quartz, calcite, or a combination of these types of cement but without crack-seal textures. It is possible, however, to have sampling bias leading to deviation from power-law best fit. Nevertheless, the characteristic distribution appears real since most of the cumulative plots lack a substantial straight-line portion (corresponding to power-law). Bed-bounded fracture

apertures are mostly < 1 mm wide, which agrees with observations by Gale et al. (2014). Wider than 1 mm fractures are seen on > 10 ft long Set 1 fractures in the US-77D Outcrop. However, these fractures were likely sheared during the bed folding, and therefore, wider apertures may have resulted due to dilation during shearing and accompanied weathering. It is also important to note that an overall similar (characteristic) aperture frequency distribution in the AWO was seen in both Sets 1/4 and 3/5. This might indicate that bed boundedness has a higher effect on fracture size distribution rather than fracture timing or fracture formation mechanism.

In addition to the characteristic distribution, uniform fracture spacing ($C_v < 1$), i.e., an absence of fracture clustering in macrofractures was seen along all outcrop scanlines. Mostly bed-bounded nature of the observed macrofractures and larger stress shadows is indicated by the higher uniformity in spacing compared to random spacing. Microfractures, on the other hand, exhibit clustering ($C_v > 1$ [Table 3.3]). Mostly non-bed-bounded nature of microfractures (as observed in the AWO), in combination with small stress shadows, may be related to their higher clustering than random spacing values.

A power-law relationship between aperture and length exists. On average, a slope of -0.55 and an intercept of 0.7 exists from equations in Figures 3.16A through 3.16D. Vermilye and Scholz (1995) reported similar power-law aperture-length slopes in the veins they studied. Table 3.4 shows that if a 22.5 m long E-W fracture (height > 1 m category) is considered, which is one of the longest E-W fractures observed in the Clarita Shale pit, an intercept of 0.7 and a slope of -0.55 would yield an aperture of 3.8 mm. This value is close to the maximum aperture (3.3 mm) value of the E-W fractures

in the Clarita Shale Pit (compare green values for E-W fractures). For the E-W fractures (height > 1 m category), the average measured aperture was 0.84 mm, while the calculated average aperture is 2.6 mm, which is around three times the measured average (compare red values for E-W fractures). On the other hand, for the NE-SW fractures, there is a considerable mismatch between maximum calculated and measured apertures (purple: 2.4 vs. 10 mm). The averages, however, show a good match (orange: 2.1 vs. 2.0). The linear relationships in Figures 3.16A through 3.16D, on the other hand, overestimate the apertures of the long fractures.

In summary, the power-law correctly predicts the maximum aperture and the average aperture for the E-W and NE-SW fractures respectively, but not the average and maximum for these sets respectively for fractures with height > 1 m. It is known that aperture is a function of not just the length but also the host rock mechanical properties, cement deposition, and pore pressure during opening among other factors. Therefore, the power-law relationship should only be used as a guideline rather than a rule. In addition, the power-law relation was constructed using fracture sets 1/4 and 3/5 separately, which may be a reason that the relationship does not predict the apertures exactly. However, given the debris/vegetation cover, and obscurity by the matrix itself, of the long macrofractures (E-W and NE-SW) in the Wyche and Clarita shale pit discussed in Chapter 1, it would be hard to construct a reliable relationship between the two variables for each fracture set. It must be extrapolated from an aperture-length relationship of smaller fractures whose tips are visible on both ends and apertures are uniform.

Table 3.4: Comparison of calculated apertures vs. measured apertures. E-W and NE-SW fracture measured height (Wyche Shale Pit), calculated lengths from power-law eq. from Figure 1.14H, calculated apertures using slopes and intercepts of 0.7 and -0.55, and measured apertures.

	Measured height (min. [m])	Measured height (max. [m])	Measured height (ave. [m])	Calculated length (min. [m])	Calculated length (max. [m])	Calculated length (ave. [m])	Calculated aper. (min. [mm])	Calculatd aper. (max. [mm])	Calculated aper. (ave. [mm])	Measured aper. (min. [mm])	Measured aper. (max. [mm])	Measured aper. (ave. [mm])
E-W	1	5	2.2	5.7	22.5	11	**1.8**	**3.8**	**2.6**	**0.27**	**3.3**	**0.84**
NE-SW	1	1.84	1.3	5.7	9.5	7.1	**1.8**	**2.4**	**2.1**	**0.27**	**10**	**2**

3.5.3 Stratigraphic fracture density and application to hydraulic fracturing

Fracture density decrease with increase in bed thickness was seen in both brittle and ductile beds in all four zones in the AWO. Also, significantly lower fracture intensities (~1.5-3 times) exist in the ductile beds compared to the brittle beds implying a relationship between mechanical and fracture stratigraphy in the studied area. However, even though these relationships commonly exist, they might not apply everywhere. Laubach et al. (2009) mentioned that mechanical and fracture stratigraphy may or may not coincide. In addition, lower slope values for the ductile beds (Figures 3.12A through 3.12H) indicate that intensity variation with bed thickness is lower in the ductile beds compared to the brittle beds. Also, there is considerable scatter in the linear fits (Figures 3.12A through 3.12H), similar to the observation made by Ladeira and Price (1981). Even though the scanlines are sub-orthogonal to the fracture strikes, some scanlines involve more than one fracture sets depending on minor lithologic variabilities. Therefore, a 20-30 degree deviation from an orthogonal scanline-fracture strike direction is expected in these cases, which makes the relationship sub-perpendicular, rather than orthogonal. In addition, there might be slight variation in scanline direction from layer to layer. The sub-orthogonally, in part, explains the scatter in the density-bed thickness relationship. The other reason for the scatter is that minor lithologic variability within the brittle and ductile beds, causing subtle changes in the mechanical rock properties, might influence fracture intensity. Structural influences have been minimized by measuring fracture linear intensities away from minor folds and faults.

However, these factors do not change the overall findings regarding the locations of the high fracture density zones (Figure 3.13, Column 5) because these

zones are located in areas with a higher number of brittle beds, thinner beds, or both. Galvis-Portilla et al. (2017), from outcrop measured sections in the upper Woodford Shale, reported a similar GR, stratigraphy, and fracture intensity trends ~ 10 km (~ 6 miles) south of the study area. In addition, based on the outcrop and subsurface GR correlations, they reported a similar GR trend nearly 25 km (~15 miles) east and west of their study area. Therefore, the relative densities for bed-bounded fractures can be extrapolated away from the outcrop into the subsurface.

However, exact fracture densities are likely lower in the flatter subsurface, where rocks are less deformed and fold related joints (Sets 1, 2, and 3) are likely rare. A strong relationship between GR values and fracture intensity does not exist. However, significantly low or high GR values can indicate areas with high and low fracture densities respectively. In the studied areas, one of the lowest GR zones showed one of the highest fracture intensities (Zone 1) and vice versa for the 64-75 m (~210-245 ft) interval (Figure 3.13, Column 5). The utility of understanding the fracture intensity trends lies in identifying landing sites for horizontal wells in brittle, silica-rich, areas for easier drilling and obtaining complex fracture network. Well landing location is one of the important issues when considering hydraulic fracturing in the Woodford Shale (Slatt et al., 2015). Higher natural fracture density invariably leads to more complex hydraulic fracturing (Maxwell, 2014). Moreover, the presence of these high fracture density zones within organic-rich intervals (recognized by relatively high GR values) is desirable due to the proximity of hydrocarbon bearing zones to the complex fracture networks. Therefore, the zone between 250-290 ft (Figure 3.13: Column 5, green

bracket) and 140-200 ft (Figure 3.13: Column 5 black bracket) might be considered as suitable landing spots.

3.6 Conclusions

Five fracture sets were identified which developed at different times. Set 1 (E-W) and Set 2 (NE-SW) are the oldest fractures and seen at all outcrops, including both US-77D and AWO. Sets 3, 4, and 5 are fold-related. Sets 4 and 5 have the highest effect of the Mid-Virgilian Arbuckle Orogeny. The sinusoidal, bitumen-filled fractures are the oldest microfractures. More than one phase or an extended period of bitumen/ oil flow is evident with bitumen presence observed in all fracture sets as seen under the thin section, including the bed-parallel, sinusoidal, planar ones.

The five fracture sets were divided into two groups for intensity, aperture and spacing measurements. Using bed thickness-fracture intensity relations for four different zones, the fracture density variation in an entire Woodford Shale section was defined. In all zones except Zone 1, the average thicknesses of brittle beds are lower compared to ductile beds. Zone 1 has overall high fracture density and low GR due to a high proportion of low TOC chert beds compared to the carbonaceous, argillaceous beds. Two high fracture density areas in the high GR zones of the upper and middle Woodford are due to low average thicknesses of both brittle and ductile beds, or relatively high percent of brittle beds, or both. These two zones might be appropriate for landing horizontal wells. The GR values showed a weak correlation considering the whole section. However, at the highest GR values, fracture intensities are the lowest and vice versa.

Mostly bed-bounded fractures with characteristic aperture cumulative-frequency distribution exist in the studied areas. Moreover, uniform spacing exists in all areas, i.e., fracture clustering was not observed in the macrofractures. The bed-bounded fracture apertures are mostly < 1 mm wide. A power-law aperture (mm)-length (m) relationship with an intercept of 0.7 mm and a slope of -0.55 can approximate the aperture given the length of a fracture. However, this relationship should only serve as a guideline. Field measurements should be used if available.

The subsurface fracture intensity can be expected to be lower than measured at the overturned outcrops since mostly Set 1 and 2 fractures will exist instead of all five sets. However, since a bed thickness and a mineralogical relationship exist between the fracture densities, a similar fracture density variation trend, at least for the bed-bounded fractures, can be expected in the subsurface, though with lower densities. In the folded subsurface, additional fracture sets, in addition to Sets 1 and 2, probably exists. Subject to availability, the stratigraphic fracture density profile, presented in this study, may be compared to profiles obtained from image logs or other outcrops exposing a substantial portion of the Woodford Shale section.

References

Badra, H., 2011. Field Characterization and Analog Modeling of Natural Fractures in the Woodford Shale, Southeast Oklahoma. Master's Thesis, University of Oklahoma, Norman, OK.

Bontempi, C.P., 2015. High resolution stratigraphy of thin bedded shales/radiolarites, Woodford Shale, Arbuckle Wilderness Area, Murray County, Oklahoma: A new correlation tool. Master's Thesis, University of Oklahoma, Norman, OK.

Gale, J.F.W., S.E. Laubach, J.E. Olson, P. Eichhubl, and A. Fall, 2014. Natural Fractures in Shale: A Review and New Observations. AAPG Bull., 98 (11), p. 2165–2216. http://dx.doi.org/10.1306/08121413151.

Galvis-Portilla, H., D. Becerra-Rondon, R. Slatt, 2017. Let's Make Outcrops Recover Their Value, Understanding the Rock on the Surface for Predicting the Subsurface: Woodford Shale Case Study, Ardmore Basin, Oklahoma: Search and Discovery Article#10907.

Ham, W. E., and M.E. McKinley, 1954; revised by Johnson K.S. (1990). Geologic Map and Sections of the Arbuckle Mountains, Oklahoma. Oklahoma Geological Survey, Norman, OK.

Holland, M., and J.L. Urai, 2010. Evolution of anastomosing crack–seal vein networks in limestones: Insight from an exhumed high-pressure cell, Jabal Shams, Oman Mountains, J. Struct. Geol., 32(9), p. 1279–1290, doi:10.1016/j.jsg.2009.04.011.

Hooker, J.N., S.E. Laubach, and R. Marrett, 2013. Fracture-aperture size—Frequency, spatial distribution, and growth processes in strata-bounded and nonstrata-bounded fractures, Cambrian Mesón Group: AAPG Bulletin, 54, 54–71. http://dx.doi.org/10.1016/j.jsg.2013.06.011.

Hooker, J.N., S.E. Laubach, and R. Marrett, 2014. A universal power-law scaling exponent for fracture apertures in sandstones: Geological Society of America Bulletin, doi: 10.1130/B30945.1.

Ladeira, F.L., and N.J. Price, 1981. Relationship between fracture spacing and bed thickness, J. Struct. Geol., 3 (2), p. 179–183.

Laubach, S.E., J.E. Olson, and M.R. Gross, 2009. Mechanical and fracture stratigraphy, AAPG Bulletin, 93 (11), p. 1413-1426. http://dx.doi.org/10.1306/07270909094.

Maxwell, S.C., 2014. Hydraulic-fracturing concepts, S.M., Maxwell, Microseismic Imaging of Hydraulic Fracturing: Improved Engineering of Unconventional Shale Reservoirs. Distinguished Instructor Series, No. 17. Tulsa, OK, SEG., p. 28.

Sanchez, J.D.A., 2012. Sequence Stratigraphy and Seismic Interpretation of the Upper Devonian- Lower Mississippian Woodford Shale in the Cherokee Platform: A Characterization Approach for Unconventional Resources. Master's thesis, University of Oklahoma.

Slatt, R.M., B. McCullough, C. Molinares, E. Baruch, F. Cardona, and B. Turner, 2015. Paleotopographic and Depositional Environment Control on "Sweet Spot" Locations in Unconventional Resource Shales: Woodford and Barnett Shale Examples. American Association of Petroleum Geologists, Search and Discovery Article, No. 10713.

Turner, B.W., C.E. Molinares-Blanco, and R.M. Slatt. 2015. Chemostratigraphic, palynostratigraphic, and sequence stratigraphic analysis of the Woodford Shale, Wyche Farm Quarry, Pontotoc County, Oklahoma: Interpretation, 3(1), p. 1-9, doi: 10.1190/INT-2014-0089.1.

Vermilye, J.M., and C.H. Scholz, 1995. Relation between vein length and aperture, J. Struct. Geol., 17(3), p. 423– 434.

Appendix A

Fracture density calculations (**T** = thickness, **N** = number of)

$T_{\_average\_brittle\_beds}$ in 1 ft interval (cm) = ($T_{1\_brittle\_bed}$ + $T_{2\_brittle\_bed}$ + ...$T_{N\_brittle\_bed}$)/ ($N_{\_brittle\_beds}$ in 1 ft interval)…….. ……..…….....**Eq. 3.1**

$T_{\_average\_ductile\_beds}$ in 1 ft interval (cm) = ($T_{1\_ductile\_bed}$ + $T_{2\_ductile\_bed}$ +….$T_{N\_ductile\_bed}$)/ $N_{\_ductile\_beds}$ in 1 ft interval……..…...….**Eq. 3.2**

Fracture linear intensity$_{\_brittle\_bed}$ (fractures/ft) in a hypothetical bed of thickness T_average_brittle_beds = (Slope*T$_{_average_brittle_beds}$ in 1 stratigraphic ft interval + intercept) /3.28 ……..……..……..…….…..…**Eq. 3.3**

Fracture linear intensity$_{\_ductile\_bed}$ (fractures/ft) in a hypothetical bed of thickness T$_{_average_ductile_beds}$ = (Slope*T$_{_average_ductile_beds}$ in 1 stratigraphic ft interval + intercept)/3.28 ……..……...…**Eq. 3.4**

Fracture areal density$_{\_brittle+dutile\_beds}$ (fractures/ft2) in a (1 ft x 1 ft) interval = (Fracture linear intensity$_{_brittle_bed}$*N$_{_brittle_beds}$ in 1 ft interval + *Fracture linear intensity*$_{\_ductile\_bed}$ *N$_{_ductile_beds}$ in the 1 ft interval) ……..**Eq. 3.5**

Observations were made for 1 ft interval rather than 1 m interval for higher resolution. Slopes and intercepts in equation 3 and 4 are taken from the linear regression lines for each lithology and fracture set groups. For example, Figure 3.12G shows that the slope and intercept for the brittle beds in Zone 4 for fracture Sets 1, 4 are -3.99 and 69.56 respectively. Similarly, for the ductile lithologies, these are -0.69 and 27.9

respectively. To obtain the fracture density values in fractures/ft, the conversion “3.28” is used in the denominator in equations 3 and 4.

CONCLUSIONS

This dissertation presents an example of implementing rigorous field observations to an idealized geologic model. This model is then used to understand the control of natural fracture on hydraulic fracturing. Field observations, including fracture timing and stratigraphic fracture density trends, were two other main focuses of this dissertation.

Stratigraphic fracture density based on different bed-bounded fracture sets was not studied before in any of the Woodford Shale outcrops. Even though large fractures control hydraulic fracturing, smaller bed-bounded fractures may play a role in hydrocarbon production. In this study, the stratigraphic density variation in smaller fractures was part of the focus since an entire section of the Woodford Shale was available.

It is preferable to vary the stratigraphic density including smaller, i.e., bed-bounded fractures in the discrete fracture network model. However, this would depend on the amount of information available about the smaller fractures from outcrops (assuming the non-fold related sets have been identified), well logs, and the lithology in which the fractures occur. Another concern regarding the number of discrete fractures that can be input into the DFN model is the capability of the software to handle the number of fractures. Therefore, the minimum size cut-off must be user determined as there is a larger number of small fractures compared to large fractures. For hydraulic fracture simulation, the key is to understand the size distribution of large fractures from outcrops and quarries with relatively large exposed areas so that traces of the largest fractures are visible.

However, whether large or relatively small fractures are used to build the geologic model, understanding natural fracture timing and causes (overpressure or fold-related) is of utmost importance to ascertain the presence of certain fracture sets in the subsurface. Certain fracture sets that are present at different Woodford Shale outcrop locations, along with their reported presence in the subsurface (in the literature), can reasonably be inferred to be ubiquitous in the Woodford Shale. Fold related fractures are likely to be present in more folded and tilted subsurface. Also, not only the fractures from the Woodford Shale but also from carbonates need to be predicted for the discrete fracture network model because stimulation takes place both in and out of the target formation (Woodford Shale).

The result of the combined approach (outcrop + simulation) used in this study is real-world conclusions regarding relative formation permeabilities, fluid efficiencies, and how the formation would behave under certain treatment conditions.